Science

Spliceosome
up close

A detailed view of the
RNA splicing machine
pp. 1182 & 1191

CONTENTS

1158

CONTENTS

11 SEPTEMBER 2015 • VOLUME 349 • ISSUE 6253

1202
Vortices in an egg crate

RESEARCH

ON THE COVER

Three-dimensional structure of a yeast spliceosome. In eukaryotes, genetic information stored in DNA is transcribed into precursor messenger RNA (pre-mRNA), which contains protein-coding exons interspersed with noncoding introns. The splicing of pre-mRNA, which entails removal of introns and covalent linkage of exons, is mediated by a multicomponent ribonucleoprotein complex—the spliceosome. See pages 1182 and 1191. *Illustration: C. Bickel/Science; structure based on the cryo-EM map of a yeast spliceosome (EMDB ID EMD-6413)*

Published by AAAS

Puerto Rico's future at stake

This week, Puerto Rico hosts scientists and other stakeholders in Caribbean science to discuss "Attaining Sustainability Through Science and Education."* This comes at the end of a summer that saw the island's economy "death spiral" into a first-ever default on a bond payment. Its more than $70 billion in debt, high unemployment, and a shrinking economy are causing Puerto Ricans to leave the island in droves in search of stability. This includes young scientists and biomedical professionals. Austerity measures being considered by the Puerto Rican government include reducing support for higher education, but this would only drive the brain drain, decimate the scientific enterprise, and reduce the capacity to confront the economic and environmental challenges: a perfect storm that would be devastating to Puerto Rico's future. Robust science and technology are needed now more than ever to avoid this catastrophe.

"...reducing support for higher education...would be devastating to Puerto Rico's future."

The economic crisis is partly the consequence of a history of neglected investment in science-based planning for sustainable development. Puerto Rico is still strongly dependent on fossil fuels, consuming more total barrels of petroleum per day than any of the seven Central American countries, while having a smaller population than six of them. Transitions from oil to natural gas and particularly to renewable energy resources have been slow. Decades of watershed mismanagement and an inefficient water distribution system have made coping with severe drought difficult. And even though the risks are evident, the island has not responded to the threats of climate change. The Puerto Rico Climate Change Council has projected up to 1.70m of sea-level rise by 2110, exceeding the upper limit of the global mean indicated by the Intergovernmental Panel on Climate Change. Yet most of the population, critical infrastructure, and economic activity are still concentrated in coastal plains within 1 km of the coast.

About 10 years ago, Puerto Rico recognized that the economy of the 21st century is strongly based on science, and the government formed the Puerto Rico Science, Technology and Research Trust (and Fund), supported by public and private sectors. Its goal has been to support research, development, and infrastructure projects. The trust recently awarded several $150,000 research grants to develop new products in biotechnology and life sciences, aerospace, medical devices, and information technology. The trust also completed a strategic plan to promote entrepreneurship and innovation through infrastructure- and capacity-building.

Puerto Rico also has made recent strides to build environments that not only retain science professionals but are fertile for international collaborations. The Turabo University's Technology Accelerator, the Bioprocess Development and Training Complex, the University of Puerto Rico Comprehensive Cancer Center, and the future Science City are all geared toward this end. The University of Puerto Rico's Molecular Sciences Research Center opened in 2011, supporting basic and translational biomedical research through interactions between academia and the biopharmaceutical industry and equipped to license and commercialize its intellectual property. The University of Puerto Rico's new joint science and biomedicine training and development programs for graduate students and faculty are in partnership with institutions including Stanford and Yale Universities. The island's scientific diaspora is involved in all of these efforts, particularly through Ciencia Puerto Rico, a network with over 7000 members interested in science and Puerto Rico.

In June, *Puerto Rico—A Way Forward*, a report by former International Monetary Fund economists (commissioned by the government), indicated that drastic cuts in public spending are needed, including education. Although restructuring the debt and eliminating the wasteful use of government resources are certainly necessary, slashing education is not a viable solution for an economy whose recovery relies on scientific innovation activities. Science investment in a time of economic turmoil might seem like a luxury. However, it is a gateway toward economic and social development.

– **Jorge Colón**

Jorge Colón is a professor in the Department of Chemistry at the University of Puerto Rico, San Juan, Puerto Rico, and a member of Ciencia Puerto Rico. E-mail: jorge.colon10@ upr.edu

NEWS

IN BRIEF

Polio resurfaces in West Africa and Ukraine

Low vaccination rates enabled two polio outbreaks, in Ukraine and in Mali; for each, the culprit was a virus derived from the live oral vaccine (shown here in Pakistan).

Countries in Ebola-ravaged West Africa are on high alert after polio was confirmed in a toddler in Bamako, Mali, on 7 September, just a week after two cases were reported in southwestern Ukraine. The outbreaks are unrelated, but in both instances the culprit is a vaccine-derived poliovirus (VDPV). Rare VDPVs arise when the weakened form of a virus used in the live vaccine regains its virulence—a danger when vaccination rates are low, which allows the strain to circulate and accumulate genetic mutations. In West Africa, a 19-month-old boy was paralyzed in Guinea on 20 July and traveled to Mali for treatment, where a type 2 VDPV was confirmed. With health systems and routine immunization in West Africa decimated due to the Ebola outbreak, the World Health Organization (WHO) deems the risk of spread high. In Ukraine, two children—a 4-year-old and a 10-month-old—were paralyzed on 30 June and 7 July. VDPV type 1 was confirmed 31 August. The risk of spread within Ukraine—where social tumult led to falling vaccination rates—is also high, WHO says, but the risk of international spread is low. Emergency efforts to fight the outbreaks with mass vaccination campaigns could begin this week. http://scim.ag/polioUkraineMali

AROUND THE WORLD

Grizzly obesity study retracted

THOUSAND OAKS, CALIFORNIA | Last year, researchers announced in *Cell Metabolism* that they had learned how grizzly bears gain weight prior to hibernation—without developing obesity-associated health problems like diabetes. But the journal retracted the paper last week after some of its authors at Amgen in Thousand Oaks, California, announced that the original paper contained falsified data. No one outside of Amgen knows who tampered with the findings, but the scientist has since been let go, according to a report in *The Wall Street Journal*. The academic co-authors on the study insist that the findings are still viable, and say they are currently replicating the falsified portion of the study to verify them.

Mekong forests dwindling fastest

WASHINGTON, D.C. | Earth lost 18 million hectares of trees in 2014, according to a report last week by the Global Forest Watch (GFW)—but not in the most expected places. Economic factors and new laws have slowed the forests' demise in Brazil and Indonesia, the top tree-clearing countries, reducing their share of global forest loss from 53% in 2001 to 38% in 2014. Meanwhile, the rate of tree cover loss is increasing in Cambodia, Vietnam, and other Mekong Delta countries, at rates five times faster than in other tropical countries. Sierra Leone and Madagascar are not far behind, in part because of the development of oil palm plantations. And dry tropical forests in Paraguay, Argentina, and Bolivia are also in trouble. GFW's estimate of total hectares lost roughly agrees with an estimate of 15 billion trees per year reported last week in *Nature*. But critics note that neither number factors in new trees being replanted or growing back naturally.

Human subject rules revamped

WASHINGTON, D.C. | Sixteen U.S. agencies, including the Department of Health and Human Services (HHS), are moving to tighten rules intended to protect human research subjects. A notice released last

week fleshes out intended changes to the Common Rule, a set of ethical requirements that apply to studies funded by the federal government as well as many private entities. One change would require the consent of participants prior to any analyses of their stored blood and tissue samples for additional studies unrelated to the original research, even if the samples are stripped of identifying information. Another change would simplify the often sprawling informed consent forms by moving all but the most essential components into an appendix. The new rules would also require that a research project spanning multiple institutions be consolidated under a single institutional review board. HHS and 15 other agencies will accept public comments for 90 days before releasing a final rule. http://scim.ag/CommRule

Long-distance robot control

NOORDWIJK, THE NETHERLANDS | In video games, feeling the response of a simulated plane to a joystick or the recoil of an onscreen gun is called force feedback, or "haptic" technology. Haptic feedback is crucial for space robotics, too: The ability to "feel" helps controllers guide robot arms to do delicate tasks. This week, the European Space Agency (ESA) put this technology to the test, when Danish astronaut Andreas Mogensen drove a rover around the grounds of ESA's technology center—from the International Space Station, 400 kilometers above Earth. Mogensen took the wheel of Interact Centaur, a rover equipped with cameras, location sensors, and two robot arms. Signals from Mogensen's handheld controllers traveled through a geostationary satellite to the rover, a total journey of 90,000 kilometers. Mogensen directed the rover to do tasks with submillimeter precision, including finding a "task board" where it pulled out and reinserted a pin into a hole.

Trained monkeys destroy nests

BEIJING | In an effort to prevent damage to military aircraft due to accidental bird strikes, China's People's Liberation Army has trained a squadron of male rhesus macaques to find and destroy birds' nests. The effort, which focused on an airfield located along a major migration route for birds known as the East Asian-Australasian Flyway, was planned in advance of an airshow with jet fighters on 3 September, the 70th anniversary of Japan's surrender at the end of World War II. The macaques scramble up trees and dismantle nests by pulling out twigs; two

Pollution and invasive sea stars threaten the spotted handfish.

Help for the spotted handfish

The charmingly awkward spotted handfish (*Brachionichthys hirsutus*) isn't an avid swimmer; it prefers to clamber along the sandy bottom on its oddly shaped pectoral fins. Last month, the most comprehensive survey to date of this critically endangered species native to Tasmania, Australia, found just 79 handfish within its remaining habitat in the Derwent River and estuary, with three or fewer at several locations. Pollution and silt clouding the waters from farming and construction are partially responsible for its decline. But another major culprit is an invasive sea star that eats stalked sea squirts. That's a problem because the handfish like to lay their eggs around these squirts. Biologists with the Commonwealth Scientific and Industrial Research Organisation and the University of Tasmania are trying to recreate the handfish's habitat by putting pieces of plastic into the sediment to replace the eaten sea squirts. The scientists will meet with Australia's Department of the Environment next month to discuss setting up a captive breeding population in case the remaining wild fish go extinct.

monkeys dismantled about 180 nests over 1 month, a Chinese airbase commander told *China Daily* in May. Ornithologists, however, say the operation is misguided at best, and could cause stress and lead to higher mortality among migrating birds that stop in Beijing on their way south for the winter. http://scim.ag/monkeynests

China's People's Liberation Army Air Force has trained a group of macaques to drive away birds from airfields.

Alzheimer's protein: contagious?

From 1958 to 1985, 30,000 people worldwide—mostly children—received injections of human growth hormone extracted from the pituitary glands of human cadavers. The procedure was halted when researchers found that a small percentage of recipients had received contaminated injections and were developing Creutzfeldt-Jakob Disease (CJD), a fatal neurodegenerative condition caused by misfolded proteins called prions. This week, a study of the brains of eight deceased people who had contracted CJD from such injections suggests that the injections may also have spread amyloid-β, the neuron-clogging protein that is the hallmark of Alzheimer's disease. The study is the first evidence in humans that amyloid-β could be transmitted through invasive medical procedures such as brain surgery or blood transfusion, the team writes this week in *Nature*. Skeptics, however, note that the CJD prion itself often triggers unusual amyloid deposits; epidemiological

studies, they say, show no connection between the injections and increased risk of developing Alzheimer's disease. http://scim.ag/AlzheimersCJD

New light on Basque's origins

Many researchers have assumed that Basque—a language spoken by a group of people between Spain and France and with no known relationship to any other tongue—is a "relic language" spoken by the hunter-gatherers who occupied Western Europe before farmers moved in about 7500 years ago. But a new study this week in the *Proceedings of the National Academy of Sciences* contradicts this idea. The researchers sequenced the genomes of eight skeletons found in a Basque country cave called El Portalón in northern Spain. The skeletons date to between 5500 and 3500 years ago and thus belonged to the farmers. The team compared these genomes with genomes from other skeletons spanning hunter-gatherer to early farming periods in Western and Central Europe, from 8000 to 5000 years ago. They also compared the ancient DNA with more than 2000 genomes from modern Europeans. Today's Basques, the scientists found, were most closely related to those early farmers, who then became isolated from later migration waves. http://scim.ag/BasqueOrigins

NEWSMAKERS

Three Q's

Soumya Swaminathan, a pediatrician who has spent 2 decades working on HIV-associated tuberculosis, is the new head of the Indian Council of Medical Research (ICMR), India's premier biomedical research organization. She talked with *Science* about her plans for the council.

Q: What's India's biggest health challenge?
A: Getting quality health care to people who need it most—urban slum dwellers, tribal and remote rural populations. We have a high burden of communicable diseases, [including] tuberculosis, malaria, and diarrhea, with increasing rates of noncommunicable diseases [such as] hypertension, diabetes, mental health problems. Undernutrition is a major factor.

Q: How can ICMR make a difference?
A: We need to develop, test, and validate indigenous diagnostics for common diseases and use modern communications technology. For too long, we have ignored the role that communities and ordinary citizens can play in preventive and promotive health care. [ICMR] will focus on translational and implementation research to improve access to quality health care.

Q: What about funding levels?
A: Biomedical research definitely needs more funding from the government. We can [also] leverage existing resources more effectively by strengthening partnerships with other Indian science agencies and with international organizations like the NIH, CDC, and MRC. I also propose to explore partnerships with the private sector and philanthropic organizations.

A key mapping instrument on SMAP (artist's conception shown) failed just months after launch.

Satellite's high-resolution mapping instrument fails

A radar instrument on NASA's Soil Moisture Active Passive (SMAP) mission, designed for high-resolution mapping of the moisture content in the topmost 5 centimeters of Earth's soil, has failed because of a problem with its amplifier, the agency announced on 2 September. With an ability to map moisture in areas as small as 9 kilometers across, the radar was supposed to help improve forecast models for weather, drought, and flooding. But engineers have exhausted possibilities for resurrecting the instrument after it first stopped working on 7 July. The other main instrument on the $916 million mission, which launched in January (http://scim.ag/SMAPlaunch), is still operational, but that instrument, a passive radiometer, has lower resolution, at about 40 kilometers across. Scientists had wanted to use SMAP to understand how some storms seem to depend on alternating wet and dry patches of soil at distances of 10 kilometers.

BY THE NUMBERS

6190

Height, in meters, of Alaska's Denali, the tallest peak in North America, according to a new measurement by the U.S. Geological Survey. The previous accepted elevation, made using 1950s-era technology, was 6194 meters.

0

Number of HIV infections that occurred over 2 years in 657 people in San Francisco, California, who took a daily antiretroviral drug as prophylaxis.

300

Number of induced pluripotent stem cell lines—the largest publicly available collection—available through a new stem cell bank launched last week by the Coriell Institute for Medical Research in Camden, New Jersey.

ILLUSTRATION: NASA/JPL

Analyzing the more than 1500 fossils, representing more than 15 individuals, was a group effort at a workshop in South Africa.

PALEOANTHROPOLOGY

New human species discovered

Bizarre skeletons emerge from South African cave

By **Ann Gibbons**

From the moment in 2013 when paleoanthropologist Lee Berger posted a plea on Facebook, Twitter, and LinkedIn for "tiny and small, specialised cavers and spelunkers with excellent archaeological, palaeontological and excavation skills," some experts began grumbling that the excavation of a mysterious hominin in the Rising Star Cave in South Africa was more of a media circus than a serious scientific expedition. Daily blogs recorded the dangerous maneuvers of "underground astronauts" who squeezed through a long, narrow chute to drop 30 meters into a fossil-filled cavern, while Berger, who is based at the University of the Witwatersrand in Johannesburg, South Africa, became the "voice from the cave" in radio interviews.

When it came time to analyze the fossils, Berger put out a call for applications from "early career scientists" to study them at a workshop in Johannesburg in March 2014. Handing over much of the analysis of such potentially important specimens to inexperienced researchers didn't inspire confidence among Berger's colleagues either, though it did win him the nickname Mr. Paleodemocracy. Many thought the expedition "had more hype than substance," paleoanthropologist Chris Stringer of the Natural

History Museum in London writes in a commentary accompanying the fossils' official presentation this week in the journal *eLIFE*.

But the substance has now been unveiled, and few dispute that the findings are impressive. In their report, Berger and his team describe 1550 fossils representing more than 15 ancient members of a strange new kind of hominin, which they named *Homo naledi*. (Naledi means "star" in the Sotho language spoken in the region of the cave.) It is the largest trove of fossils of a hominin ever found in Africa—and more await excavation at the site, 50 kilometers northwest of Johannesburg. "Lee has to be congratulated for finding this stuff," says Fred Grine, a paleoanthropologist at the State University of New York at Stony Brook.

Although the fossils are still undated, making it hard to know where they sit in the human family tree, they already reveal a profoundly different way to be a member of our genus *Homo*. "There is no doubt in my mind that this is a new species," Grine says.

As soon as spelunkers led by Pedro Boshoff, a former student of Berger's, found

Cavers found 26 of the 27 bones in this hand, which has modern and primitive features.

a handful of ancient teeth and a jaw deep in the cave's Dinaledi Chamber in September 2013, it was clear that "something bizarre was going on," Berger says. This ancient individual had small front teeth like a modern human but larger molars like a more primitive human ancestor.

When the spelunkers brought up more remains, Berger's perplexity deepened. The skull was globular, like a member of our genus *Homo*, but the brain was small and primitive. The wrist suggested this species was an adept toolmaker, but its shoulder and fingers showed it still climbed in trees, like more primitive hominins. "We were facing something that was different from anything else that had been described," Berger says.

At first, he worried that something was wrong with the excavation or that the teeth came from more than one type of hominin. Much to his frustration, he couldn't check the dig for himself, because he couldn't squeeze down the 20-centimeter-wide natural chute that led into the cavern (see diagram, p. 1150). With a quick grant from the National Geographic Society, where he is an explorer-in-residence, Berger assembled a team of thin, young researchers and cavers to excavate further.

"As the teeth came up, you'd see this odd tooth; then the same thing in two, three, five, 10, 50, 100 teeth," Berger says. "No individual part varied." Other remains—skulls, hands,

and foot bones from infants, teens, and the elderly—also consistently showed the same unusual combination of modern and apelike traits. But although the similarity of the fossils convinced the researchers that they had uncovered a new species, analyzing all 1550 was a Herculean task. "No one had ever tried to publish more than 100 fossils of a single species at once," Berger says.

In the end, the work of more than 60 researchers yielded a picture of "a relatively tall, skinny hominid with long legs, human-like feet, with a core and shoulder that is primitive," Berger says. Some body parts have come into sharper focus than others. In an analysis of the remarkably complete hands, paleoanthropologist Tracy Kivell of the University of Kent in the United Kingdom found that bones in the wrist were shaped like those in modern humans, suggesting that the palm at the base of the thumb was quite stiff. That would allow forces to dissipate over a larger area of the hand than in more primitive humans—a trait associated with tool use. At the same time, *H. naledi* had a weird thumb and long, curving fingers, as if it still spent a lot of time climbing.

In a separate analysis of the foot, paleoanthropologist William Harcourt-Smith of the American Museum of Natural History in New York City and his colleagues noted that its proportions were modern and the big toe was aligned with the other toes, rather than diverging like an ape's grasping big toe. Taken together, the hand and foot suggest "you have a creature that would have walked upright really well but also would have been comfortable in the trees," Harcourt-Smith says. Harvard University paleoanthropologist Dan Lieberman agrees: "The foot is indeed strikingly modern … and suggests it walked and *possibly* ran much like modern humans."

No other animals were found in the subterranean chamber except a hapless owl and a few rodents. As a result, the team rules out the idea that animals dragged the human remains into the cave. Instead, they suggest that other humans, perhaps modern humans, deposited the bodies there—as in a crypt. But the team can't rule out alternate explanations—for example, that a group of *H. naledi* found their way into the cave but got lost or trapped.

Despite the wealth of data, the initial analysis invites more questions than it answers, Stringer writes, including "Where does *H. naledi* fit in the scheme of human evolution?" Determining the age of the bones or cave would help answer that, but caves are notoriously difficult to date, and the bones may be too old for radiocarbon dating.

Still, "it is absolutely essential that the remains be dated," says paleoanthropologist Curtis Marean of Arizona State University, Tempe. "For example, if they date to the last 300,000 years, then it is plausible that early modern humans killed them and stashed them in the cave as part of a ritual." A date would also illuminate whether the fossils represent an ancient population or an isolated relic that persisted until fairly recently, says paleoanthropologist Bernard Wood of George Washington University in Washington, D.C.

Berger says now that his team has described the fossils, they can focus on dating them, trying to extract DNA, and extending his exercise in paleodemocracy by recruiting still more young researchers to the effort. "The Rising Star expedition isn't a media stunt," Berger says. "I felt it was the first time in history to bring the entire world into a place where we discovered a hominid fossil." ∎

Treasure map

South Africa's Rising Star Cave yielded a trove of bones from what turned out to be a new *Homo* species. Excavating them was a task for small, slim cavers.

Spherical nucleic acids start rolling

Promise of cancer-seeking nanoparticles wins funding for research center

By **Robert F. Service**

The shape of gene therapy to come may be round. Last week, the U.S. National Cancer Institute (NCI) awarded Northwestern University in Evanston, Illinois, $11.7 million to pursue nanoparticles called spherical nucleic acids (SNAs) as a new avenue for treating everything from cancer to psoriasis. The particles, typically consisting of an inert core carpeted with DNA or RNA, have already proved biologically potent, able to switch genes on and off and kick the immune system into action.

The institute is one of six centers funded last week as part of NCI's third 5-year cancer nanotechnology program, but the only one devoted to SNAs. And the grant marks what could be a turning point for these versatile particles. After decades of test tube and animal experiments, they are now about to enter human trials.

SNAs found their way to the clinic through the back door. Northwestern chemist Chad Mirkin and colleagues made the first ones in 1996, from tiny gold nanoparticles, each festooned with about 100 identical short strands of DNA or RNA. At the time, Mirkin's team wanted to build new materials by harnessing nucleic acids' skills at binding complementary strands to assemble nanoparticles into 3D structures. The effort succeeded, but in the process, Mirkin says, "we discovered [SNAs] have other very unusual and interesting properties."

For starters, SNAs can seek out and bind to very low quantities of complementary DNA and RNA. They do that even better than linear nucleic acids because each SNA harbors so many nucleic acid copies. That knack has made them ideal as nucleic acid detectors. Nanosphere, a biotech company that Mirkin co-founded in Northbrook, Illinois, has exploited it to develop SNA tests that can identify pathogenic bacteria and viruses in blood and other samples without the need for the time-consuming
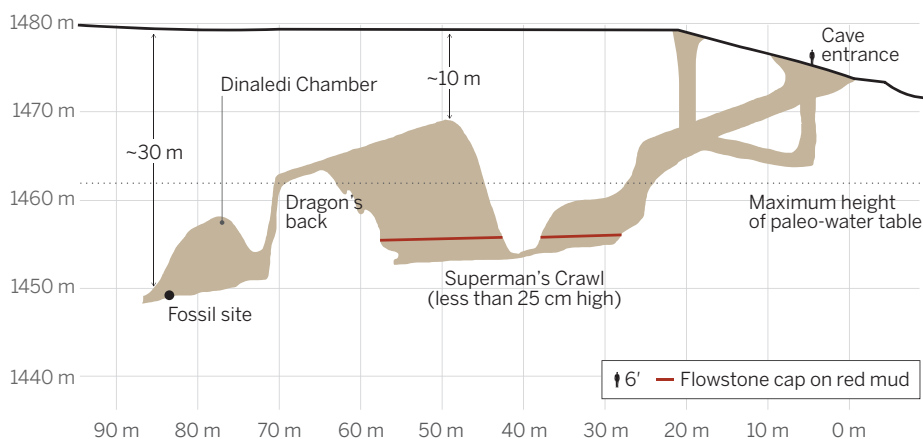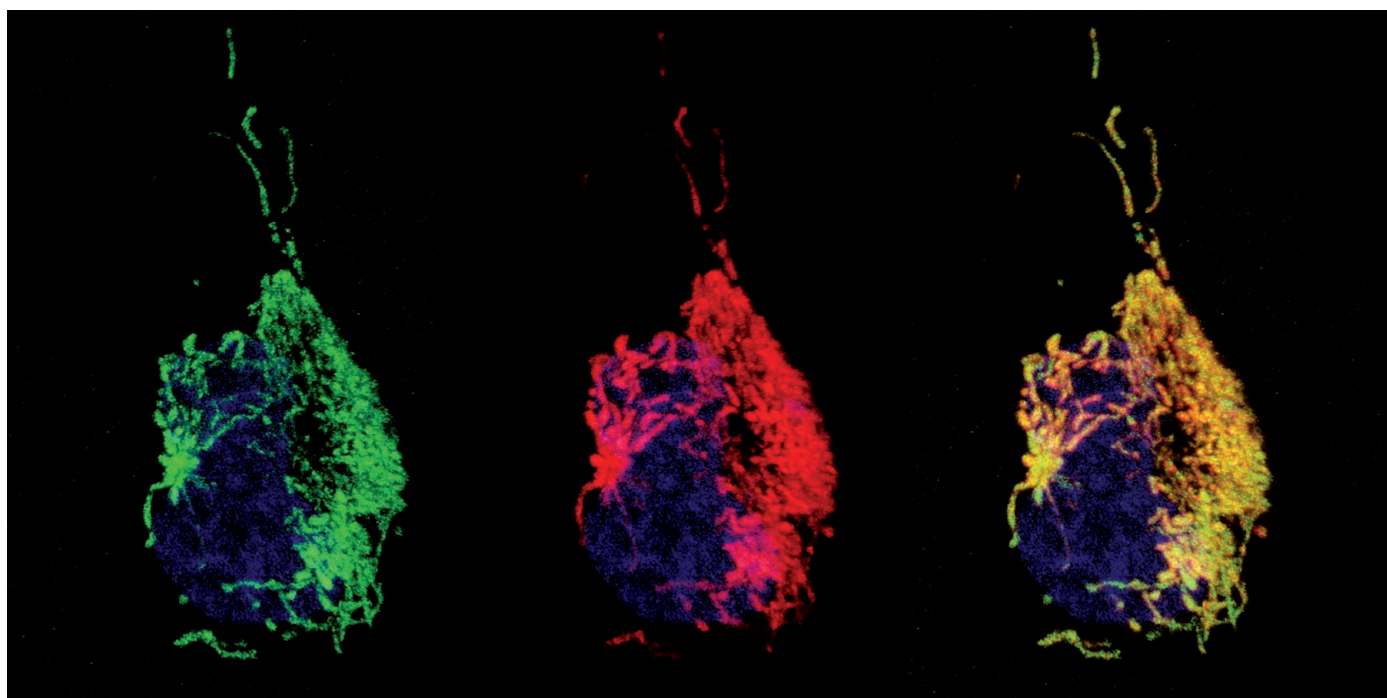
In a cell, an SNA (red) is as effective as a special stain (green) at highlighting DNA-containing mitochondria. Yellow shows where the methods overlap.

process of culturing microbes.

Mirkin's team also discovered that SNAs readily enter cells—a complete surprise, he says. Because DNA and cell membranes are both negatively charged, he assumed they would repel each other, as happens when free-floating linear DNA encounters a cell membrane. Yet nearly all cell types readily engulf SNAs in compartments called endosomes, which trap materials for possible destruction. Mirkin's team found that many SNAs manage to escape into the cell body, although researchers still don't understand just how they slip the net. Once there, an SNA's strands of DNA or RNA can bind to complementary DNA or RNA in the cell, detecting or even silencing genes involved in disease.

In 2012, for example, Mirkin and colleagues reported that when they applied SNAs to the skin of mice, skin cells readily took up the nanoparticles, which knocked down the expression of genes normally upregulated in psoriasis. A similar skin study showed promise for speeding wound healing.

The particles are proving equally adept when injected into the body. In one such study in *Science Translational Medicine* in 2013, SNAs were programmed to home in on specific RNAs in patients with glioblastoma multiforme, one of the deadliest forms of brain cancer. The targeted RNAs speed cancer growth by helping make proteins that turn off a tumor suppressor gene in the cancer cells. When injected into the tail veins of mice with glioblastoma, the SNAs crossed the blood-brain barrier, bound to their target

RNAs, and knocked down the expression of the antitumor suppressor protein, lengthening the life span of the mice.

More recently, the researchers have tested SNAs as cancer vaccines, which train immune cells to seek out and destroy malignancies. In the 31 March issue of the *Proceedings of the National Academy of Sciences*, Mirkin and his colleagues at Northwestern and AuraSense Technologies, a SNA drug startup company since renamed Exicure, reported that they had created SNAs that could bind to a cancer-cell protein and direct it to a key immune-cell receptor. The SNAs carried short fragments from a protein called ovalbumin (Ova), which is overexpressed in cells with lymphoma, a type of blood cell cancer. The particles were tailored to home in on so-called toll-like receptors, which are key to getting immune cells to target foreign peptides. In mice, the SNAs coaxed immune cells to attack Ova-containing cells, reduced the size of lymphoma tumors, and lengthened survival. "We found that the mice eventually do die of cancer. But when we took the tumors out, there were no Ova-containing cells left," Mirkin says.

Lately, the Northwestern team has tried combining immune-stimulating SNAs with a new class of cancer drugs called checkpoint inhibitors. These take aim at immune cell

Tendrils of nucleic acids enable SNAs to bind to genes or RNA in cells.

proteins called checkpoints, which inhibit immune responses. Disabling the checkpoints can unleash immune cells to destroy cancer (*Science*, 20 December 2013, p. 1432). At the American Chemical Society (ACS) meeting last month in Boston, Mirkin reported preliminary evidence that when he combined his immune-boosting SNAs with a conventional checkpoint inhibitor, they eliminated tumors in a small number of animals models of breast cancer and melanoma.

Such successes are "really exciting," says Karen Wooley, a chemist at Texas A&M University, College Station, who heard Mirkin detail his latest work at the ACS meeting. Robert Langer, a nanotechnology expert at the Massachusetts Institute of Technology in Cambridge, agrees. "Chad's work is excellent," he says.

Work funded by the NCI grant could soon extend such successes to human patients. Mirkin says human clinical trials with glioblastoma patients are expected to begin in the United States this fall. And by next spring, the team expects to begin similar trials with psoriasis patients in Europe.

If those prove successful, Mirkin says his team could roll out a host of new trials in short order. After all, Mirkin says, "to target novel diseases we don't need to come up with new molecules, we just need to change the [nucleic acid] sequence." ■

IMAGES: (TOP TO BOTTOM) W. BRILEY ET AL., PNAS, 112, 9591–9595, 2015; J. CUTLER ET AL., AMERICAN CHEM. SOC. 134, 1376–1391, 2012

CLIMATE CHANGE

A cold, creeping menace

In Alaska, frozen debris lobes threaten a key lifeline

*By **Eli Kintisch**, in Fairbanks, Alaska*

Barack Obama last week became the first sitting U.S. president to visit the nation's Arctic territory, using a sojourn in this vast state to highlight the risks posed by climate change. They include, Obama said, the accelerated thawing of the frozen permafrost that sits beneath "the earth on which 100,000 Alaskans live, threatening homes [and] damaging transportation and energy infrastructure."

It was a familiar warning to geological engineer Margaret Darrow of the University of Alaska, Fairbanks. Just before Obama arrived, she had spent a week in the field with a research team seeking to better understand one emerging hazard caused by thawing permafrost: a massive, slow-motion landslide that threatens the Dalton Highway, the only land route into Alaska's lucrative North Slope oil fields and arguably the state's most important road. Researchers have so far identified 43 of these frozen debris lobes (FDLs) along the highway's route through the rugged Brooks Range—including a 20-meter-high slide that has bulldozed its way to within 40 meters of the northbound lane. If the slide, dubbed FDL-A, reaches the road, it would dump some 45 metric tons of debris daily—more than enough to fill a dump truck.

The slides create what looks "like a war zone," Darrow says: cracked earth, toppled trees, and layers of moss and debris wrapped into jelly rolls. When it's quiet, she adds, you can hear trees straining as the mass creeps along at an average of 1.4 centimeters a day. As Alaska's warming softens their icy underpinnings, FDLs are now "a serious impending geohazard," Darrow says, noting that FDL-A's speed has increased by 40% in the past 7 years.

FDL's didn't get much attention in 1974, when engineers built the gravel, 666-kilometer-long Dalton Highway from outside Fairbanks to Deadhorse, near the Arctic Ocean, in order to service the Trans-Alaska Pipeline System, which parallels the road. Geologists knew the FDLs existed on adjacent slopes, but they were barely moving. Then, in 2008, satellite photos revealed that a mass of frozen earth about 260 meters wide and 1200 meters long had inched to within 150 meters of the road at milepost 219, near the town of Coldfoot. Soon, state and federal officials were asking researchers to take a closer look at FDL-A, and others like it—and to consider ways of stopping them in their tracks.

Since then, scientists have used airborne radar and other sensors to create 3D maps of the slides and estimate how fast they are moving. On the ground, they're drilling cores through the FDLs to see inside. In a bid to understand why some lobes are moving faster than others, they have measured slope angles and identified soil types.

There have been plenty of surprises. One was the liquid water that gurgled up from under FDL-A in 2012, as scientists probed the critical "shear zone" in the permafrost beneath the slide. "You see water coming out and you're like: 'What the heck?'" recalls Darrow, who says the liquid likely seeps in from the surrounding soil and remains supercooled in the frozen ground. Its high pressure—155,000 kilograms per square meter—enables it to lubricate the

Scientists are unsure how to stop massive frozen landslides inching toward Alaska's Dalton Highway.

FDL's downhill slide, in the same way a thin layer of water enables a hockey player's skate blade to slide across the ice, says state geohydrologist Ronald Daanen in Fairbanks. As Arctic soil temperatures rise, basic physics holds that the pressure—and the lubrication—will increase, he adds. "Just a little more [water] pressure and [the lobes] will be floating," allowing them to slide faster, Daanen says.

That worrying scenario could also hold true for other permafrost formations found in Alaska on steep slopes. Daanen says vegetation often holds in place these piles, which are slower moving, but "I'm afraid with warming temperatures there's a tipping point after which gravity takes over."

In the meantime, researchers are mulling ways to defend the Dalton Highway from FDL-A. (The pipeline, some 800 meters away, is not at risk in the near-term.) Digging a trench to funnel water away from the lubricating shear zone is one idea. But researchers aren't sure how to best configure the ditch, because they have data only from the 2012 borehole. Engineers have also envisioned a buttress wall to block the slide, but Darrow fears it might be little more than "a speed bump" for the massive lobe. A more radical idea is to install underground cooling pipes to freeze the slide in place. But the immense forces could rip apart the pipes, and they may not work as intended, Daanen says. For starters, the state plans to simply reroute the road "to buy some time," says Michael Coffey of Alaska's Transportation Department in Juneau.

Coffey estimates that, at current movement rates, it could take 10 years for FDL-A to reach the highway. But researchers say it could speed up given the unpredictable behavior of other FDLs, which have moved as much as 10 times as fast. ∎

BIOSECURITY

Flu study raises questions about U.S. ban

A new viral "backbone" could speed up production of influenza vaccines

By **Jon Cohen**

When the U.S. government temporarily halted a class of risky experiments on influenza, SARS, and Middle East respiratory syndrome last year, some researchers warned that the move could harm public health rather than help it. The far-reaching moratorium, which targeted studies that make the viruses more transmissible or pathogenic, would also impede low-risk research that could help fight pandemics, they argued.

Now, one of the researchers whose work triggered the moratorium has published a paper that he says underscores that point. In the new study, published online in *Nature Communications* on 2 September, Yoshihiro Kawaoka of the University of Wisconsin, Madison, engineered heartier influenza viruses to streamline vaccine production, which he says could help bring future pandemics under control.

The study, which was partly funded by the U.S. National Institute of Allergy and Infectious Diseases (NIAID), was completed before the moratorium took effect. But Kawaoka says it couldn't have been done today—even though it carried little risk.

NIAID Director Anthony Fauci disputes the argument. "It is very likely" that Kawaoka's group would have been granted an exemption—and would have continued to receive NIAID support—because the study specifically aims to improve vaccines against influenza, Fauci says. But others say the cumbersome exemption process could deter such work. One lab that received an exemption for similar work told *Science* that the process took 3 months.

Kawaoka published one of two highly controversial papers in 2012 that showed how so-called gain-of-function (GOF) mutations made the highly lethal H5N1 avian influenza virus more transmissible, and hence potentially more capable of causing a pandemic. The ensuing furor contributed to the U.S. government's decision to announce a 1-year funding pause in October 2014 of GOF experiments that could be "reasonably anticipated" to increase transmissibility or pathogenicity. Laboratories were also asked to halt ongoing GOF studies.

Before the moratorium, Kawaoka's team had set out to address a perennial problem in the production of influenza vaccines: the scramble to produce them in time for each year's flu season. To keep up with the ever-mutating flu virus, researchers have to create new vaccines each year, tailor-made to combat the strains they expect to dominate—and rush them into production.

The viruses used to make vaccines typically contain a "backbone" of six genes plus two variable genes that code for the proteins studding the viral surface. These surface proteins are critical for provoking a protective immune response, so vaccine-

A better vaccine virus

Flu vaccine viruses contain a "backbone" of six genes that remain the same (grey) and two variable genes encoding surface proteins (red and blue). Researchers improved virus growth by making mutations to the backbone.

Surface proteins

Backbone genes

makers combine the surface proteins currently in circulation with a standard backbone. The companies then grow these viruses in eggs or in mammalian cells.

In the new study, Kawaoka's team randomly mutated the backbone genes to create a large library of variants and then tested them with many different surface proteins. They found a novel backbone that—for reasons they have not been able to pin down—increased the yield of the viruses in eggs and mammalian cells, by more than 200-fold in some cases.

The study "tackles a question that is of great pragmatic importance," says virologist Gary Nabel, chief scientific officer at flu vaccine producer Sanofi in Cambridge, Massachusetts. "If you can't make enough vaccine at an acceptable cost, it won't be available to many who need it."

Fauci notes the new work is especially relevant because it sped up growth in mammalian cells. That's a faster vaccine production system than chicken eggs, and it avoids mutations that occur when the virus adapts to eggs, which can compromise vaccine effectiveness.

Kawaoka stresses that the experiment did not create dangerous viruses. Flu viruses with the new backbone only marginally increased the severity of disease in mice, the team found—and manufacturers routinely kill the virus as part of the vaccine production process in any case. Nor could anyone glean information from the paper that might help construct more deadly human influenza viruses, Kawaoka says. "We have no idea whether these mutations would make other influenza viruses more pathogenic or transmissible," he says. "I don't think people who are seriously concerned about [GOF studies] are concerned about this type of work," he says. "The net was cast too wide."

Fauci's support for studies such as Kawaoka's does not address a broader issue, says former National Science Advisory Board for Biosecurity (NSABB) member Arturo Casadevall, an immunologist at the Johns Hopkins Bloomberg School of Public Health in Baltimore, Maryland. "Moratoriums and pauses are blunt instruments," Casadevall wrote in an email. "I worry that even if exclusions are made for certain experiments so that they continue, the GOF controversy combined with its pauses/moratoriums has already created an environment where scientists may be discouraged from experimental work that is clearly in the public interest."

The U.S. government has asked NSABB to review the risks and benefits of GOF research and hired Gryphon Scientific of Takoma Park, Maryland, to conduct an analysis. NSABB will discuss the review on 28 September, and Casadevall wrote, "I hope that the NSABB takes notice of this paper as an example of the potential value of these experiments."

Carrie Wolinetz, a policy official at the U.S. National Institutes of Health in Bethesda, Maryland, says NSABB does not plan to recommend any changes to the moratorium until next spring. ∎

GLOBAL PAYER

As head of the $29 billion Wellcome Trust, Jeremy Farrar took the stage during the Ebola epidemic. Now, he wants to make the trust a world leader

By **Kai Kupferschmidt**

Some appointments seem prescient in retrospect. On 1 October 2013, Jeremy Farrar took over the reins of the Wellcome Trust. Three months later, an 18-month-old boy in the tiny village of Meliandou in Guinea developed a fever and started vomiting. He died 2 days later, the first victim in the largest Ebola outbreak the world has ever seen.

As the epidemic grew into an international crisis, the topics that had dominated Farrar's career—pandemic preparedness, international cooperation, fighting infectious diseases in poor countries, clinical studies in the midst of an emergency—became global priorities. And as the brand-new head of the world's second-largest private funder of medical research, Farrar became determined to make a difference.

Even before the scale of the disaster had sunk in, the Wellcome Trust started providing millions of dollars to conduct clinical trials. Farrar chastised the world for not acting more decisively, lobbied for making experimental therapies available, and joined high-level panels to guide the R&D response to the drama.

Farrar had previously worked far from the media spotlight, heading a Wellcome Trust research group in Ho Chi Minh City, Vietnam, for 18 years. Now, almost overnight, his name became widely known. *Fortune* magazine named him among the "50 greatest leaders of the world," ahead of people like Facebook founder Mark Zuckerberg. "The trust had a lot of influence before, of course, in the U.K.," says James Wilsdon, a science policy specialist at the University of Sussex in the United Kingdom. "But in the Ebola outbreak they really stepped onto the international stage and became much more vocal and visible."

The research push paid off. On a recent Wednesday morning, Farrar stood wearing jeans and a blue and white shirt in front of several hundred staff members of the Wellcome Trust assembled on the sixth floor of the trust's modern office in central London.

"I appreciate that all of you go to bed with a copy of *The Lancet* every Thursday," he said. "But if you don't, make sure you do so this week." The journal was about to publish the results of an Ebola vaccine trial funded by the trust, Farrar revealed, and they were "very good, probably even better than that."

Indeed, the paper made headlines around the world. The vaccine, produced by Merck & Co., had been 100% effective in a trial set up by the World Health Organization (WHO) in Guinea. It was the first time ever that an Ebola vaccine had been shown to protect humans, raising hopes that future outbreaks can be contained much faster—and the trust's role had been essential. "If we hadn't been supported by Jeremy and the Wellcome Trust, we would not have been able to do anything apart from convening a meeting," says Marie-Paule Kieny, WHO's assistant director-general for health systems and innovation.

Still, Farrar was not happy. A few days after the trial results came out, he concluded

in *The Guardian* that the world had failed the people in West Africa. "The vaccine could and should have begun testing much more quickly," he wrote. Governments, companies, and philanthropies need to form a global fund to develop a series of vaccines for testing in the next deadly epidemic, he argued. "Ebola should change how the world reacts to such outbreaks," Farrar says.

The Wellcome Trust, whose assets top £18 billion ($29.2 billion), can help bring about that change, Farrar says. He also plans to make the trust more international and dynamic; give younger scientists a leg up; coordinate more closely with another public health behemoth, the Bill & Melinda Gates Foundation; and focus on areas where Wellcome can have a major impact. "It's not just about giving money," Farrar says. "It's shifting the Wellcome Trust from being just a funder into being a sort of thought leader."

THE WELLCOME TRUST is the legacy of an eccentric American-British businessman with a nose for marketing. Henry Wellcome was born in 1853 in a log cabin in Wisconsin, then part of the Wild West. At age 16 he marketed his first product, "Wellcome's magic ink," almost certainly lemon juice. Wellcome studied pharmacy in Chicago, Illinois, and Philadelphia, Pennsylvania, and moved to London in 1880, where he and a former classmate, Silas Burroughs, founded a pharmaceutical business.

At the time, most drugs in the United Kingdom were produced locally by pharmacists, using pestle and mortar, but Burroughs Wellcome and Company started importing an American novelty: compressed pills, which were safer because they contained a standardized dose. The pills became an instant success; later, the company started making them itself. Wellcome coined the trademarked name "tabloids," which turned out to be a marketing boon. As a publicity stunt, Wellcome gave some of the empire's big explorers medicine chests stocked with tabloids—Robert Scott took one with him on his ill-fated expedition to the South Pole. (Only later was the term tabloid adopted by newspapers filled with condensed, easily digestible stories.)

Wellcome's private life was less successful. In 1901, he married Syrie Barnardo, a friend's daughter, who was less than half his age. There were allegations that he beat her, and the couple separated and divorced after Barnardo had a child with celebrated author William Somerset Maugham. Wellcome became more reclusive, concentrating on his company and his collection of medical and historical artifacts. When he died in 1936 at age 82, it included hundreds of thousands of pieces, including Peruvian mummies, Japanese sex aids, and Napoleon's toothbrush.

He had also built a worldwide business, which his will converted into a foundation whose shares were owned exclusively by a new trust. The Wellcome Trust was charged with "the advancement of medical and scientific research to improve mankind's wellbeing."

Henry Wellcome made his fortune by selling compressed pills, which he called "tabloids."

AFTER HIS STAFF MEETING, Farrar settles into a rhythm of half-hour and one-hour meetings in his large corner office, a glass box on the fourth floor. His day includes a strategy meeting on how to convince the U.K. government to save science from spending cuts, a phone call with WHO's Kieny to discuss the *Lancet* paper, an interview for the World Economic Forum's annual risk report, and a call with a scientist at the U.S. National Institutes of Health. The next day, Farrar is scheduled to fly to Seattle, Washington, to meet with Bill Gates; the week after he has a meeting at the White House.

It wasn't always obvious that the trust would grow into a global force. Wellcome's company had contracted before his death, and the trust initially didn't have much to invest. A 1956 report showed that it had donated about £1 million in the first 20 years. But in the following decades, Wellcome scientists developed important drugs, such as the leukemia compound 6-mercaptopurine and azidothymidine, the first antiviral to treat HIV infections. The company grew richer and so did the trust.

In 1986, the trust started selling off Wellcome shares to become less dependent on just one company. Many of the remaining shares were sold to rival Glaxo in 1995, enabling that company to take over Wellcome. Some of the newfound wealth was wiped out in the stock market crash of 2000, but investments in Facebook, Twitter, and other companies more than made up for the losses. "We went from an organization that was spending maybe a million pounds a month to about a million pounds a day," says Clare Matterson, the trust's director of strategy.

On average, the trust's coffers have swelled by 14% annually since 1986. But some of the gains are controversial. "With increased visibility has come increased scrutiny," Wilsdon says. "The trust is certainly not used to that." *The Guardian* launched a campaign last year urging the trust to pull its money from oil giants BP and Shell. Farrar has argued that money buys influence and that it's better to promote change as a shareholder than to divest.

The trust is planning to spend roughly $1.3 billion on medical research in 2016, more than the U.K. government's Medical Research Council and more than any other charity in the world except the Gates Foundation. Currently, some 75% of its money is spent in the United Kingdom, but Farrar plans to fund more science abroad. "Jeremy is an internationalist," Matterson says.

That's hardly a surprise considering Farrar's upbringing. His father, whom he calls a "rabid socialist" and "a huge influence," was an expatriate who taught English in Singapore, where Farrar was born, and later in Libya, New Zealand, and Cyprus. Early in life, Farrar dreamed of working at the foreign office. His wife is Austrian and their three children were born in Vienna. "Delighted & proud that I & my whole family are part of the 8 million foreign born 'migrant' population," Farrar recently tweeted when immigration became a major topic in the United Kingdom.

In the competitive domain of world-class research and billion-dollar funding agencies, it's hard to lead without making enemies. But Farrar seems to have few. Soft-

spoken, he exudes an easy confidence and listens attentively, frequently sitting on the edge of his chair, chin propped on his hand, when a colleague talks. He decides quickly, but does not micromanage. "He just understands people very well," says Nick White, a tropical medicine researcher at Mahidol University in Bangkok.

FARRAR REJECTED the top job at Wellcome when headhunters first approached him in 2012 after then-director Mark Walport announced his departure to become the United Kingdom's chief science adviser. "The next morning I woke up feeling really good about that decision," he recalls. When the trust failed to find a suitable candidate and asked him again, Farrar said yes: "It was genuinely a sense of this very important organization that had supported me for a long time being without leadership." His decision marked the end of a long sojourn in Asia.

Farrar had trained as a neurologist in London, Edinburgh, and Oxford. At a conference one day, he decided he could not imagine spending the rest of his life in the company of the neurologists assembled there. "Neurologists have to be very precise in medicine and that is not me, actually," Farrar says. "I'm not good at that." He applied to a position, spotted by a friend, as head of a University of Oxford research group set up by the Wellcome Trust at a hospital in Ho Chi Minh City. "He is ex-

tremely bright and very motivated," says White, who had started the unit and helped pick Farrar. "Those things outweighed any lack of tropical medicine or infectious disease experience."

Farrar built up the unit and did research on dengue fever, typhoid, and other tropical diseases. He's most proud of a study in patients whose tuberculosis infections had spread to their brain, a condition that is fatal in half of all cases. In a large trial, Farrar showed that steroids could dramatically in-

> *"We need to be bolder in the stuff we fund. If we don't use our independence, what's the point of having it?"*
>
> **Jeremy Farrar**

crease survival. But international health isn't just a matter of good science, White says; it's also about understanding people, cultures, and organizations. "Jeremy is very good on the big picture, he is extremely broad in his thinking and imaginative too," he says.

In Vietnam, Farrar learned how frightening an emerging disease can be. In January 2004, on the eve of Tết, the Vietnamese new year, Farrar received a phone call from his colleague Tran Tinh Hien. A young girl in another hospital had come down with flulike symptoms, but Hien had a hunch that something unusual was go-

ing on. Could Farrar run some tests? Farrar called his wife, Christiane Dolecek, also a tropical medicine researcher, to run the diagnostics—"because I am useless in the lab"—and Hien brought samples on the back of his motorbike. In the early hours of the morning, it became clear that they were dealing with H5N1, a deadly avian influenza strain. "That was a very scary moment," Farrar says.

The fate of his friend Carlo Urbani was fresh in Farrar's mind. The Italian parasitologist had been working for WHO in Hanoi a year earlier when he was called to the bedside of an American businessman with flulike symptoms. Urbani realized he was probably looking at a new and dangerous disease, and was one of the first to raise the alarm. Severe acute respiratory syndrome, or SARS, as it became known, is now believed to have jumped from civets to humans; it soon spread to 37 countries and killed more than 800 people. Urbani, married with three children, persuaded the Vietnamese government to quarantine the hospital—"a brave decision," Farrar says. He became infected and died.

Now, Farrar was facing a little-known emerging pathogen himself. H5N1 had caused an enormous outbreak in Hong Kong poultry in 1997 that also sickened 18 people and killed six. "Is this virus transmissible between people? We didn't know that," Farrar says. The hospital lacked the

Sharing the wealth

The Wellcome Trust's charitable expenditure has increased sharply since the 1980s.

£775,000,000

£536,000,000

£60,000

£2,890,000

£31,000,000

No annual data available for 1936–1956; average annual spending was about £60,000.

Annual spending (millions of pounds)

1936 Henry Wellcome dies; Wellcome Trust established. It holds the entire share capital of his company, Wellcome Foundation.

Late 1950s Several successful drugs boost foundation's revenues.

1986 Wellcome Foundation goes to the stock market as Wellcome plc. The trust sells 25% of its shares for £211 million.

1992 The trust sells another £2.3 billion in Wellcome plc shares. The Welcome Trust Limited takes over as the only trustee.

1993 Sanger Institute opens with trust as main funder; becomes largest contributor to the Human Genome Project.

1995 Most of remaining shares in Wellcome plc sold to Glaxo.

2002 Most Glaxo-SmithKline shares sold for almost £1.8 billion.

2013 Jeremy Farrar becomes director; trust's assets reach £16.3 billion ($26.5 billion).

Farrar led a research unit at a hospital in Ho Chi Minh City, Vietnam, for 18 years. "Of course, I miss Asia," he says.

kind of protective equipment that Western hospitals have. "Should you go home in the evening to your family? Should you stay in the hospital?"

In the following months, Farrar's team treated many patients and made the best of the scientific opportunity. They described the disease and its various symptoms, analyzed which factors predicted survival, and showed that oseltamivir helped some patients—although some H5N1 strains were resistant to it. "The research element was done extremely well," White says. "That got him and the unit noticed."

THE EBOLA OUTBREAK wasn't detected until March 2014, 3 months after it started. By mid-July, more than 1000 people had become sick and hundreds had died; cases were doubling every 3 weeks or so. It reminded Farrar not of SARS or H5N1, but of something far worse: the start of the HIV pandemic in the 1980s. As a medical student at St. Stephen's Hospital in London, he had tended many early AIDS patients. "I still remember this now, the power of things you have no capacity to treat."

WHO and many public health experts initially said the world knew how to deal with Ebola outbreaks: by isolating patients, burying the dead safely and quickly, and monitoring patients' contacts. Farrar wanted to do more. On 5 August, 3 days before WHO declared Ebola a Public Health Emergency of International Concern, he published a *Wall Street Journal* op-ed with global health veterans David Heymann

and Peter Piot calling for experimental therapies to be made available for testing and compassionate use. The Wellcome Trust announced a multi–million-dollar package to fund clinical Ebola research 2 weeks later.

The trust ended up funding the Guinean vaccine trial and studies of two experimental drugs, brincidofovir and TKM-Ebola. Both of those trials were stopped early because of disappointing results—not what scientists had hoped for, WHO's Kieny says, "but they managed to eliminate two products that were highly regarded."

"The world changed after SARS because it demonstrated in a very powerful way that these viruses could go between animals and humans quite easily and then spread through the world," Farrar says. Ebola has changed the world again, he says: "It showed that you can actually do research in these situations."

ONE OF FARRAR'S DEAREST possessions is an old, worn anthology of poems, a gift from his father that sits on his desk. On one of the first pages, his mother has scribbled a quote from Robert Browning, the Victorian poet: "Ah, but a man's reach should exceed his grasp, Or what's a heaven for?" It could be Farrar's slogan at Wellcome. He wants to use the trust's $29 billion capital to reach further. "We need to be bolder in the stuff we fund," he says. "If we don't use our independence, what's the point of having it?"

In his first year at the trust, Farrar moved to double the number of grants for early-

and mid-career researchers. "Most of the great changes that have happened over the last 50 years have been led by people in their 20s and 30s, and yet I think on the whole science has moved away from that population," he says. Farrar also wants to focus the trust's efforts on areas where it can have a major impact. One example is understanding what makes pathogens like Ebola so good at jumping from animals to people and becoming established in the human population, he says.

Farrar has strengthened his ties to the Gates Foundation; the two organizations now have meetings every 6 months to coordinate and identify areas where they could work together. The two traditionally have had different models: "We fund projects, Wellcome funds people," says Chris Wilson of the Gates Foundation. Today, they more often adopt each other's approach. "We are influencing each other," Wilson says.

Farrar has also used his independence to express his own opinions. In a *Wall Street Journal* piece earlier this year, he criticized WHO, which he said had been "held back by deep structural flaws and a chronic refusal to lead." "If WHO doesn't change now, it will never change," Farrar says.

He's well aware that the Ebola crisis has given Wellcome and himself more clout, and he seems comfortable using it. Yet there are moments when he regrets leaving his job at the hospital and his life in Ho Chi Minh City. "I certainly miss being a clinician, and I miss being a clinical researcher," Farrar says. "And, of course, I miss Asia." ∎

Tailpipe to tank

Researchers are vying to use renewable energy to suck
carbon dioxide out of the air and turn it back into fuel

By **Robert F. Service**

Stuart Licht has designed the ultimate recycling machine. The solar reactor that he and colleagues built in his lab at George Washington University in Washington, D.C., takes carbon dioxide (CO_2) from the atmosphere—a byproduct of fossil fuel combustion—and uses the energy in sunlight to turn it back into fuel. There are a few steps in between. Water is also involved in the reaction, which produces hydrogen (H_2) and carbon monoxide (CO); they in turn can be stitched into liquid hydrocarbon fuels. But Licht's is one of the most efficient devices of its type ever constructed.

It is only one of the solar fuel technologies taking shape in labs around the world. They embody a dream: the prospect of one day bypassing fossil fuels and generating our transportation fuels from sunlight, air, and water—and in the process ridding the atmosphere of some of the CO_2 that our fossil fuel addiction has dumped into it.

These schemes are no threat to the oil industry yet. In Licht's device, parts of the reactor run at temperatures approaching 1000°C, high enough to require specialized materials to hold the components. Other researchers are pursuing an alternative approach, developing catalysts that could carry out the same chemical reactions at

or near room temperature, using electricity from sunlight or other renewables to power the chemical knitting process.

The bigger hurdle is economic. Oil is cheap, for the moment, and there is little incentive to adopt cutting-edge, costly alternatives. But the relentless march of climate change, and the elegance of the concept, have drawn researchers around the globe to the pursuit of solar fuels. "This is a very hot area right now," says Omar Yaghi, a chemist at the University of California (UC), Berkeley. And as Licht's reactor demonstrates, the research is making progress. "We're not there yet, but we're moving in the right direction," says Andrew Bocarsly, a chemist

at Princeton University who is developing low-temperature catalysts.

Enthusiasts even see a glimmer of hope for making the technology economical: the steady spread of renewable electricity sources, such as wind farms and solar plants. Already, windmills and solar cells sometimes generate more power than locals can absorb. If this oversupply could be stored in chemical fuels, experts argue, utility providers might be able to save their power for use anytime and anywhere—and make extra money on the side.

THE NEED FOR LIQUID FUELS is unlikely to go away despite concerns about climate change. The high energy density and ease of transport of gasoline and other liquid hydrocarbons have made them the mainstay of the world's transportation infrastructure. Researchers continue to pursue the use of low-carbon gases, such as methane and hydrogen, as transportation fuels, and electric cars are proliferating. But for long-distance trucks and other heavy vehicles, as well as aviation, there is no good alternative to liquid fuels. Solar fuel proponents argue that finding a way to brew them from readily available compounds such as water and CO_2 could make a sizable dent in future CO_2 emissions.

The task essentially boils down to running combustion in reverse, injecting energy from the sun or other renewables into chemical bonds. "It's a very challenging problem, because it's always an uphill battle," says John Keith, a chemist at the University of Pittsburgh in Pennsylvania. It's what plants do, of course, to make the sugars they need to grow. But plants convert only about 1% of the energy that hits them into chemical energy. To power our industrial society, researchers need to do far better. Keith likens the challenge to putting a man on the moon.

The trouble is that CO_2 is a very stable, unreactive molecule. Chemists can force it to react by pumping in electricity, heat, or both. The first step in this process is usually ripping off one of CO_2's oxygen atoms to make CO. That CO can then be combined with H_2 to make a combination known as syngas, which can be converted into methanol, a liquid alcohol that can be either used directly or converted into other valuable chemicals and fuels. Massive chemical plants do just that, but they make their syngas not from air, but from plentiful and cheap natural gas. So the challenge for chemists is to create syngas from renewables more cheaply than current sources can match.

Licht, who calls his solar-generated mixture of CO and H_2 "sungas," says he's

taking aim at that challenge by using both heat and electricity from the sun. His setup, which he details in a paper accepted at *Advanced Science*, starts with a high-end commercially available solar cell called a concentrated photovoltaic. It focuses a broad swath of sunlight onto a semiconductor panel that converts 38% of the incoming energy into electricity at a high voltage. The electricity is shunted to electrodes in two electrochemical cells: one that splits water molecules and another

Powered by geothermal energy, this plant in Iceland turns carbon dioxide into syngas and ultimately methanol fuel.

that splits CO_2. Meanwhile, much of the remaining energy in the sunlight is captured as heat and used to preheat the two cells to hundreds of degrees, a step that lowers the amount of electricity needed to split water and CO_2 molecules by roughly 25%. In the end, Licht says, as much as 50% of the incoming solar energy can be converted into chemical bonds.

It's unclear whether that process will produce syngas that's as cheap as that made from natural gas. But Licht notes that a 2010 economic analysis of his solar water splitting setup alone, which he first described in 2002, concluded that his approach could generate a kilogram of H_2—the energy equivalent of 4 liters of gasoline—at a cost of $2.61.

Yet it may be hard for Licht's sungas setup to lower the price further. Licht's charge-conducting electrolyte uses lithium, a somewhat rare and costly metal whose limited supplies could prevent a massive scale-up. Licht also faces competition from other researchers who also use high temperatures to ease the splitting of water and CO_2, but rely entirely on electricity instead of solar heating. But like sungas, those schemes, called solid oxide electrolysis cells, face the longevity challenges of running at high temperatures.

GIVEN THESE HURDLES, Bocarsly and others continue to try to split CO_2 at lower temperatures. One such approach is already commercial. In Iceland, a company called Carbon Recycling International opened a plant in 2012 that uses renewable energy to create syngas. The company harnesses the island's abundant geothermal energy to produce electricity, which drives electrolysis machines that split CO_2 and water. The resulting syngas is then turned into methanol.

Of course, most regions of the globe lack Iceland's abundant geothermal power needed to drive the process, so researchers are hunting for new catalysts that can split CO_2 with less energy. These catalysts typically sit on the cathode, one of two electrodes in an electrolytic cell containing water. At the opposite electrode, water molecules are split into electrons, protons, and oxygen, which bubbles away. The electrons and protons pass to the cathode, where CO_2 molecules split into CO and oxygen atoms that combine with the electrons and protons to make more water.

Today, the gold standard for such catalysts is, well, gold. In the 1980s, Japanese researchers found that electrodes made from gold had the highest activity for splitting CO_2 to CO of all the low-temperature setups. Then in 2012, Matthew Kanan, a chemist at Stanford University in Palo Alto, California, and colleagues discovered something even better: Making their electrode from a thin layer of gold divided into nanosized crystallites, they reported in the *Journal of the American Chemical Society*, slashed the electricity needed by more than 50% and increased the catalyst's activity 10-fold. The boundaries between the gold crystallites appear to promote the reaction.

At some $36,000 per kilogram, gold is still far too expensive for use on a mas-

Conjuring chemical cornucopias out of thin air *By* **Robert F. Service**

A fill-up at the gas station may seem expensive, but fuels are relatively cheap commodities. So would-be makers of solar fuels are looking for ways to apply their technology to making more valuable materials.

Last month, for example, Stuart Licht, a chemist at George Washington University in Washington, D.C., and colleagues reported in *Nano Letters* that they had developed a version of their solar reactor technology (see main story, p. 1158) that can take CO_2 out of the air and convert it into solid carbon nanofibers. The researchers found that when they added trace amounts of either nickel, copper, cobalt, or iron to their electrolysis cell, the metals form tiny islands on the cathode that then serve as landing sites for thousands of split-off carbon atoms to insert themselves and quickly grow into long, thin fibers. Licht's team had previously shown they could turn CO_2 into a solid carbon material called amorphous carbon, which is worth some $1000 per metric ton. But carbon nanofibers could be worth far more, perhaps as much as $25,000 per metric ton, because they are widely used in making lightweight, high-strength composites for applications such as car bumpers and airplane parts. "We
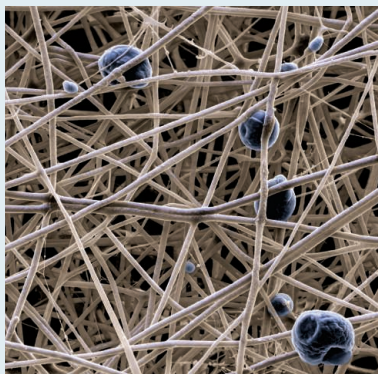
Pricey carbon nanofibers can be made from CO_2.

are making a valuable commodity that we hope will produce a driving force for using this technology," Licht says.

Others are pursuing the same strategy. A small New Jersey–based company called Liquid Light is working to commercialize technology for converting CO_2 into ethylene glycol, a commodity chemical with a $27 billion annual market. Another company, Skyonic, recently opened a demonstration plant in Texas that turns CO_2 into baking soda, hydrochloric acid, and bleach.

Such commodities aren't manufactured on a scale anywhere near that of gasoline and other transportation fuels. So making them with CO_2 siphoned off a smokestack or pulled from the air isn't likely to make a sizable impact on global atmospheric CO_2 levels, says Matthew Kanan, a chemist at Stanford University in Palo Alto, California, who is working to convert CO_2 into plastics and other higher value commodities. However, he says, "Perhaps we can use that as a stepping stone." With time and experience, companies may then find way to improve their processes, lower their costs, and begin to make high-volume, low-cost compounds such as fuels. "I'm a technology optimist," Kanan says. ∎

sive scale. Last year, however, researchers led by Feng Jiao, a chemist at the University of Delaware (UD), Norwalk, reported in *Nature Communications* that catalysts made from silver nanoparticles do almost as well. And this year, they reported in *ACS Catalysis* that even cheaper catalysts made from tiny zinc spikes called dendrites are also proving highly effective at churning out CO.

Catalysts that could be even cheaper are in the works. Researchers at UC Berkeley, for example, reported last month that they had made a highly porous crystalline material out of organic ring-shaped compounds with a combination of cobalt and copper atoms at their core. When layered atop an electrode and dunked in a water-based solution, the porous materials split CO_2 molecules into CO at a rate of 240,000 per hour—a furious pace compared with most other room-temperature catalysts. And last year, Kanan and his colleagues reported that electrodes made of nanocrystalline copper could bypass the need for syngas, allowing them to directly synthesize a variety of more complex liquid fuels, such as ethanol and acetate, at unprecedented efficiencies.

Researchers worldwide are also pur-

suing another rich vein: driving the low-temperature electrolysis of CO_2 and H_2O with energy directly from sunlight. Most efforts center on using light-absorbing semiconductors, such as titanium dioxide–based nanotubes, to churn out CO, methane, or other hydrocarbons. So far, such setups aren't very efficient; typically they convert less than 1% of the incoming solar energy into chemical bonds. Bocarsly and others have done better using the sun's ultraviolet light, which makes up only a tiny part of the spectrum. But at the American Chemical Society meeting in Boston last month, Joel Rosenthal, a chemist at UD Newark, reported that his team has developed a bismuth-based photocatalyst that converts 6.1% of incoming visible light energy to chemical bonds in CO.

Despite progress on all these fronts, Kanan cautions that solar fuels still have a long way to go to compete directly with liquid fossil fuels, especially now that the price of oil has fallen below $50 per barrel. And barring a concerted push from governments worldwide to cap or tax carbon emissions, solar fuels may never be able beat oil-derived fuels on cost alone. "It's a tall order," he says.

But Paul Kenis, a solar fuels researcher at

the University of Illinois, Urbana-Champaign, argues that the broad penetration of solar and wind power offers hope. Denmark, for example, already produces some 30% of its electricity from wind farms and is on pace to reach 50% by 2020. On a particularly blustery day in July, the nation's wind turbines generated as much as 140% of the country's electrical requirements. The excess was sent to its neighbors, Germany, Norway, and Sweden. But the oversupply added to utilities' fears that in times of peak renewable power production, the value of electricity could fall to zero or even below, as producers would have to pay others to take it so as not to damage their grid.

That's where solar fuel producers could stand to benefit, Kenis says: By absorbing that power and using it to make fuels and other commodities, they could essentially act as energy banks and perhaps earn some cash as well. For now, Kanan argues, it still makes the most economic sense simply to shunt excess renewable power into the grid, displacing fossil energy. But someday, if renewable power becomes widespread enough and the technology for making renewable fuels improves, we may be able to guzzle gas without guilt, knowing we are just burning sunlight. ∎

PERSPECTIVES

Megathrust aftermath. Tsunami produced by the 2011 magnitude 9 Tohoku subduction earthquake.

GEOPHYSICS

Weak subduction makes great quakes

Small earthquakes reveal low stress levels at megathrust zones and in surrounding crust

By **Roland Bürgmann**

The world's greatest earthquakes, producing catastrophic shaking and tsunamis, occur in subduction zones. Here oceanic plates dive below adjoining regions along megathrust faults (see the figure). The recent magnitude ~9 megathrust earthquakes in Sumatra, Chile, and Japan, with fault displacements of several tens of meters, were stark reminders of the destructive power of these events. On page 1213 of this issue, Hardebeck (*1*) uses the orientations of fault planes of thousands of smaller earthquakes near and above the world's megathrusts to evaluate the state of stress driving these great events. The general conclusion made is that all faults in sub-

duction zones, including the megathrusts, are unusually weak.

Plate tectonic forces drive the subduction process and earthquakes. Stress at a particular point can be fully described by the orientations and magnitudes of three mutually perpendicular, principal (maximum, intermediate, and minimum) compressive stresses. By definition, shear stress is zero on planes perpendicular to the principal stresses. As Earth's free surface cannot support shear stress, the principal stresses in the shallow crust are expected to be parallel and perpendicular to the surface, a state of stress referred to as Andersonian (*2*).

The magnitude of stresses in the brittle crust is bounded by the frictional strength of faults. The coefficient of friction determines the strength of a fault as a linear

function of the fault-perpendicular normal stress. Laboratory-derived estimates of friction coefficients for most rock types suggest that fault strength and stress will linearly increase with increasing rock overburden within Earth, reaching several hundred megapascals (MPa) at depths where subduction earthquakes occur (*3*).

Our knowledge of the actual stresses driving earthquake faulting remains limited and is based on indirect or incomplete measures of stress. It is nearly impossible to directly measure absolute stress where earthquakes occur, as this requires observations in costly deep boreholes (*4*). A number

Department of Earth and Planetary Science, University of California, Berkeley, CA 94720, USA. E-mail: burgmann@ seismo.berkeley.edu

of geophysical studies in some subduction zones have suggested that fault friction values and stress may be much lower than expected from laboratory experiments. Such studies have relied on estimates of frictional heat generated by faulting (5, 6), the orientation of stresses estimated from the geometry of aftershock fault planes (7), as well as the apparent large rotation in principal stress orientations from before to after the 2011 Tohoku earthquake in Japan (8, 9).

Hardebeck focuses on using the fault plane geometry of small earthquakes near and above the megathrust of global subduction zones to determine the orientations of the principal stresses and constrain their magnitudes. The orientation of the maximum principal stress with respect to the megathrust provides information about the relative strength of the fault and surrounding crust. If the megathrust is weak (low friction) in an otherwise strong crust,
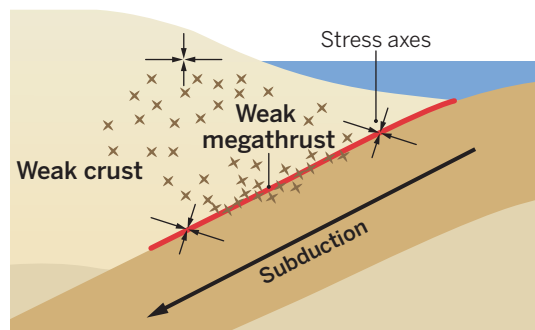
Weak subduction zones. The orientation of compressive stress inferred from the geometry of many small earthquake fault planes suggests a weak megathrust in a weak surrounding crust.

we would expect the principal stresses to be nearly perpendicular and aligned with the fault, similar to the case for the free Earth's surface. If both the megathrust and surrounding material are either weak or strong, we would expect the maximum compressive stress to be oriented at an oblique angle (20° to 60°) from the fault.

Contrary to expectations, Hardebeck finds that the orientation of maximum compressive stress near most subduction thrusts plunges toward the trench at angles of 10° to 50°. This indicates that the state of stress is not Andersonian and that the maximum compressive stress is oriented roughly 30° from the megathrust. This orientation is expected for faults with frictional strength similar to that of the surrounding crust; that is, they are either both strong or both weak. Using evidence of absolute megathrust weakness from studies documenting low frictional heat production (5, 6), stress rotations due to great earthquakes (8, 9), and high fluid pressures in fault zones (10), Hardebeck argues that both the megathrust and

surrounding crust must be weak, with only a few exceptions. Stresses are likely no higher than a few tens of MPa, rather than hundreds of MPa expected from standard friction theory. Apparently, not that much stress is required to make a great earthquake fault slip, and when it does, it drops the ambient stress to extremely low levels.

Hardebeck suggests that most faults in the world's subduction zones are weak. What might produce such weakness? Possible explanations include intrinsically low friction of fault zone materials composed of clays and talc (11), high fluid pressures that push against the normal stress on faults (10), and dynamic shear weakening during earthquake fault slip (12). It is important to remember that the inference of stress is indirect and depends on the accuracy of the fault plane orientations and various assumptions made when inferring stress orientations from the fault slip data. To improve our knowledge of the magnitude and orientation of stress in subduction zones and the factors determining their variations in space and time, we need much-improved observations. More detailed observations of small earthquakes and their fault plane orientations near the megathrust require seafloor seismic sensors. Seafloor geodetic measurements can capture the strain associated with evolving stress (13). Improved in situ observations are possible by drilling into a megathrust at greater depths to directly observe the composition, stress, and conditions in the fault zone (14). The distribution of absolute stress in space and time is probably the most important quantity in solid earth sciences that we know the least about. The analysis reported in Hardebeck's paper takes an important step toward changing that. ∎

REFERENCES

1. J. Hardebeck, *Science* **349**, 1213 (2015).
2. E. M. Anderson, *The Dynamics of Faulting and Dyke Formation with Application to Britain* (Oliver & Boyd, Edinburgh, 1951).
3. J. Byerlee, *Pure Appl. Geophys.* **116**, 615 (1978).
4. M. Brudy, M. D. Zoback, K. Fuchs, F. Rummel, J. Baumgärtner, *J. Geophys. Res.* **102**, 18453 (1997).
5. P. M. Fulton *et al.*, *Science* **342**, 1214 (2013).
6. X. Gao, K. Wang, *Science* **345**, 1038 (2014).
7. M. E. Magee, M. D. Zoback, *Geology* **21**, 809 (1993).
8. A. Hasegawa, K. Yoshida, T. Okada, *Earth Planets Space* **63**, 703 (2011).
9. J. Hardebeck, *Geophys. Res. Lett.* **39**, 21313 (2012).
10. P. Audet *et al.*, *Nature* **457**, 76 (2009).
11. D. E. Moore, M. J. Rymer, *Nature* **448**, 795 (2007).
12. G. Di Toro *et al.*, *Nature* **471**, 494 (2011).
13. R. Bürgmann, C. D. Chadwell, *Annu. Rev. Earth Planet. Sci.* **42**, 509 (2014).
14. W. Lin *et al.*, *Science* **339**, 687 (2013).

10.1126/science.aac9625

How single cells work together

Are single-celled symbioses organelle evolution in action?

By **Jonathan P. Zehr**

Symbiotic interactions are fundamental to life on Earth and were critical for the evolution of organelles that led to the success of eukaryotes on the planet. Such mutualistic interactions between unicellular microorganisms and multicellular plants and animals are pervasive in natural and agricultural ecosystems (1). In contrast, very little is known about symbiotic interactions between unicellular partners. Recent studies have revealed single-celled nitrogen-fixing symbioses that require different mechanisms to maintain symbiosis than seen in multicellular systems.

In aquatic environments, there are many examples of protists that acquire endosymbionts or plastids (2). These types of symbioses are analogous to the evolution of organelles, such as the photosynthetic organelle of the unicellular eukaryote *Paulinella* (3). Other unicellular mutualistic associations are nitrogen-fixing symbioses—for example, between filamentous cyanobacteria and marine diatoms (see the figure, panel A) (4). The filamentous cyanobacteria in these associations develop specialized cells (heterocysts) that allow them to separate the oxygen generated by photosynthesis from the oxygen-sensitive nitrogen fixation enzymes. In these symbioses, the intracellular cyanobacteria coordinate growth and division and are transmitted through different life stages (5). More recent studies have found evidence for nitrogen-fixing symbioses between unicellular cyanobacteria and single-celled protists that do not involve the development of specialized cells.

One example is a nitrogen-fixing symbiosis between the single-celled cyanobacterium UCYN-A (unicellular cyanobacteria nitrogen-fixing "group A") and a prymnesiophyte microalga (see the figure, panel B)

Department of Ocean Sciences, University of California, Santa Cruz, Santa Cruz, CA 95064, USA. E-mail: zehrj@ucsc.edu

(6, 7). This symbiosis is one of a few documented symbioses with a prymnesiophyte (a group of protists) and the only known nitrogen-fixing symbiosis with a haptophyte. Furthermore, the nitrogen-fixing cyanobacterial partner exhibits dramatic genomic reductions that have led to a very high degree of metabolic streamlining (8). A second

Examples of unicellular symbioses. (**A**) Marine diatom with heterocyst-forming filamentous cyanobacterium. (**B**) Fluorescent in situ hybridization micrograph of UCYN-A (red) and its symbiotic partner, the prymnesiophyte *Braarudosphaera bigelowii* (green). Blue, DAPI (4′,6-diamidino-2-phenylindole)-stained nucleus. Two types of this cyanobacterium are now known: UCYN-A1 (left) and UCYN-A2 (right). (**C**) Rhopaloid freshwater diatom showing spheroid body.

example is a similar symbiosis between a freshwater diatom and a nitrogen-fixing cyanobacterium (simply called spheroid bodies; see the figure, panel C) with a small and metabolically streamlined genome (9, 10). Both of these cyanobacterial genomes are greatly reduced compared to those of other cyanobacteria. Although UCYN-A retains a complete photosystem I, it does not evolve oxygen and may instead allow for energy or reductant production. The spheroid bodies have completely lost both photosystem I and photosystem II. Both genomes have also lost part or all of the TCA (tricarboxylic acid) cycle, and have lost the ability to fix carbon dioxide into organic matter. They thus lack the defining characteristics of cyanobacteria and are only cyanobacteria

in the sense that they evolved within the cyanobacteria lineage.

These single-celled symbioses are intriguing models of nitrogen-fixing symbiosis in general, but are perhaps even more interesting as models of the evolutionary events that led to eukaryotic organelles. The genome reduction implies that the cyanobacterium must be obligate and implies an evolutionary "luggage" strategy of the host (11), because it must always carry the symbiont even if is not physiologically advantageous at all times.

It is curious that these single-celled symbioses did not ultimately give rise to a nitrogen-fixing organelle, given the importance of nitrogen as a nutrient that limits the productivity of terrestrial and aquatic ecosystems. The unicellular cyanobacterial symbiotic partners are as close to being such nitroplasts as anything yet known. Indeed, some features of the UCYN-A reduced genome are very reminiscent of the features of algal chloroplast genomes: For example, it exists in the cell in two different forms that are caused by rearrangements of the chromosome bracketed by inverted sequence repeat regions. Perhaps UCYN-A and similar microorganisms (4, 9) effectively serve as such nitrogen-fixing organelles.

The nature of single-celled symbiosis is important for understanding how organelles evolved and what the minimum constraints for symbiosis are. Symbiotic interactions with multicellular plants or animals have additional needs beyond the metabolic exchanges that form the core of nutritional, or syntrophic, mutualistic interactions. Signaling, mobility, cell and tissue development, entrance through tissue or cell walls, tissue modifications, or structure development are likely all unnecessary for a symbiosis that involves just two cells, or a small number of cells. By contrast, transmission of the symbiotic partner to future generations of host cells may be critical in the dilute ocean environment where concentrations of cells are low, and growth and cell division must be highly coordinated to ensure that the growth of one partner does not outstrip that of the other.

In single-celled symbioses, both partners' growth and cell division must be coordinated. The UCYN-A prymnesiophyte host

was first visualized with a single cyanobacterial cell (6). A few observations have now been made of two UCYN-A cells on one host (12), suggesting that the cyanobacterial growth and division occur prior to the prymnesiophyte cell division. UCYN-A's close relative UCYN-A2 (13) forms a cluster of a few cells encased in a cellular pocket of the host prymnesiophyte. It is unclear how this group of cells grows and divides in synchrony with the attached host prymnesiophyte cell.

It is not certain whether the UCYN-A cyanobacteria are enclosed in a membrane. One observation of UCYN-A (UCYN-A2) suggests that the symbionts are intracellular (14). Regardless of its position inside or outside the cell, there must be channels or porters that allow exchange of fixed nitrogen for carbon, and perhaps even proteins, as in the photosynthetic organelle of *Paulinella* (3). There are now many international reports of UCYN-A, showing that the symbiosis is present at much wider geographic scales than is typical for the better-known oceanic nitrogen-fixing microorganisms (12, 15). Many similar symbioses probably exist in the environment, but are difficult to detect or study because they are small, not easily visualized or characterized, and difficult to manipulate experimentally. UCYN-A and the freshwater diatom symbionts offer a snapshot of what is likely to be found and provide motivation for looking harder in the environment for examples of microbial symbiosis and, perhaps, organellar evolution in action. ∎

REFERENCES AND NOTES

1. E. T. Kiers, S. A. West, *Science* **348**, 392 (2015).
2. D. K. Stoecker, M. D. Johnson, C. deVargas, F. Not, *Aquat. Microb. Ecol.* **57**, 279 (2009).
3. E. C. M. Nowack, A. R. Grossman, *Proc. Natl. Acad. Sci. U.S.A.* **109**, 5340 (2012).
4. T. A. Villareal, *Mar. Ecol. Prog. Ser.* **11**, 117 (1990).
5. T. A. Villareal, *Br. Phycol. J.* **24**, 357 (1989).
6. A. W. Thompson *et al.*, *Science* **337**, 1546 (2012).
7. J. P. Zehr, M. T. Mellon, S. Zani, *Appl. Environ. Microbiol.* **64**, 3444 (1998).
8. H. J. Tripp *et al.*, *Nature* **464**, 90 (2010).
9. T. Nakayama *et al.*, *Proc. Natl. Acad. Sci. U.S.A.* **111**, 11407 (2014).
10. C. Kneip, C. Voβ, P. J. Lockhart, U. G. Maier, *BMC Evol. Biol.* **8**, 30 (2008).
11. J. Wouters, J. A. Raven, S. Minnhagen, S. Janson, *Symbiosis* **49**, 61 (2009).
12. A. M. Cabello *et al.*, *ISME J.* 10.1038/ismej.2015.147 (2015).
13. D. Bombar, P. Heller, P. Sanchez-Baracaldo, B. J. Carter, J. P. Zehr, *ISME J.* **8**, 2530 (2014).
14. K. Hagino, R. Onuma, M. Kawachi, T. Horiguchi, *PLOS ONE* **8**, e81749 (2013).
15. M. Bentzon-Tilia *et al.*, *ISME J.* **9**, 273 (2015).

An increasing carbon sink?

Southern Ocean carbon uptake may have strengthened between 2002 and 2012, slowing climate change

By **S. E. Mikaloff-Fletcher**

Since 1870, Earth's oceans have absorbed more than one-quarter of the carbon dioxide emitted to the atmosphere from fossil fuel burning and other human activities, thereby dramatically slowing climate change (*1*). The Southern Ocean is responsible for ~40% of this global ocean carbon sink (*2*). Recent studies have suggested that the rate of carbon uptake by the Southern Ocean may be slowing (*3*, *4*). Such a positive climate feedback effect would reduce the Southern Ocean's capacity to slow climate change. On page 1221 of this issue, Landschützer *et al.* show that although the rate of carbon uptake by the Southern Ocean slowed between the 1980s and early 2000s, it began to strengthen again in 2002 and continued to do so until at least 2012 (*5*).

Air-sea fluxes of CO_2 are proportional to the difference in partial pressure of CO_2 between the atmosphere and the surface ocean, ΔpCO_2 (*6*). Therefore, increases in atmospheric CO_2 concentrations are expected to drive increases in ocean CO_2 uptake. In 2007, Le Quéré *et al.* suggested that Southern Ocean carbon uptake began leveling off in the early 1980s while atmospheric CO_2 continued to rise (see the figure) (*3*). The authors based their conclusions on an analysis of ocean models and an atmospheric inverse model that estimates air-sea and air-land CO_2 fluxes from atmospheric CO_2 measurements and atmospheric model simulations. They and others attributed this trend to the strengthening and poleward shift of the westerly winds that overlay the Southern Ocean, bringing carbon-rich waters to the surface and thus reducing ΔpCO_2 (*3*, *4*). Because the changes in the westerly winds are linked to climate change and ozone depletion, the rate of carbon uptake by the Southern Ocean would then be expected to continue to slow in response to future climate change (*3*).

National Institute of Water and Atmospheric Research (NIWA), Wellington, New Zealand. E-mail: sara.mikaloff-fletcher@niwa.co.nz

The hypothesized weakening of the Southern Ocean carbon sink has been the subject of vigorous debate, because many processes that play a critical role in the Southern Ocean are not well represented in coarse-resolution ocean models (*7*, *8*). Furthermore, estimates of trends in the Southern Ocean carbon sink from atmospheric inversion models are sensitive to data selection (*9*).
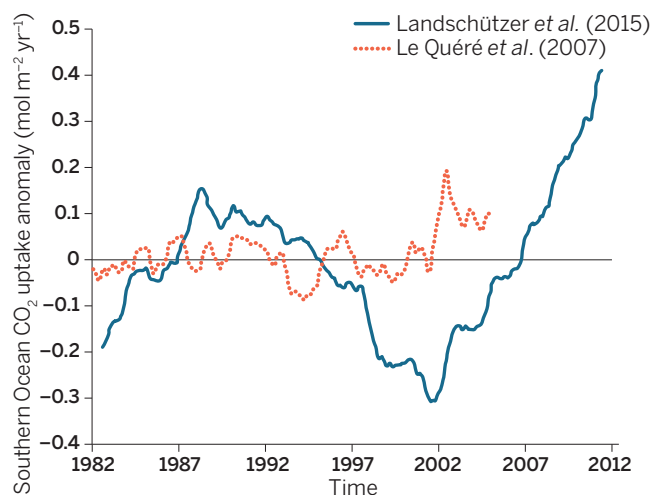
Beyond the slowdown. Southern Ocean CO_2 uptake anomalies from Le Quéré *et al.* (*3*) (red) and Landschützer *et al.* (*5*) (blue), averaged between 35°S and 90°S. Both studies found a flattening of the Southern Ocean carbon sink between the 1980s and early 2000s despite rising atmospheric CO_2 concentrations. On the basis of longer-term data, Landschützer *et al.* report a reinvigoration of this sink in the mid-2000s. Positive values reflect ocean uptake; anomalies are calculated relative to the 1980s average.

Landschützer *et al.* have now analyzed trends in a global data set of ΔpCO_2 measurements that includes 2.6 million observations in the Southern Ocean spanning 30 years (*10*). They used two novel statistical methods to interpolate ship data in space and time: a neural network approach that incorporates physical and biological observations, and a method that assimilates the ΔpCO_2 data into a mass budget of the mixed layer. As in the earlier study of Le Quéré *et al.* (*3*), they also compared their results with complementary estimates from atmospheric data. The analysis confirms that the rate of carbon uptake by the Southern Ocean slowed down between the early 1980s and the early 2000s. However, all three approaches reveal a striking reversal in this trend in 2002. From 2002 to

2012, Southern Ocean carbon uptake began to strengthen, a result that would not have been apparent during the time period studied by Le Quéré *et al.* (see the figure).

Further support for this finding comes from a coincident study by Munro *et al.* based on carbon measurements collected in the Drake Passage between 2002 and 2015 (*11*). Although focused on a single region, this study has a remarkable temporal coverage of more than 20 cruises per year. The results show a clear increase in ΔpCO_2 in the Drake Passage south of the Antarctic Polar Front from 2002 to 2015, implying a strengthening of the carbon sink in this region.

The reinvigoration of the ocean carbon sink demonstrated by the two studies (*5*, *11*) presents a puzzle. Between 2002 and 2012, there has been no reversal in the strengthening of westerly winds thought to have caused the slowdown between the early 1980s and the early 2000s (*5*). Landschützer *et al.* argue that the reinvigoration of the sink since 2002 may result from a combination of regional trends in sea surface temperature (which controls CO_2 solubility) and circulation-driven changes in the carbon balance at the sea surface.

Although these studies represent an intriguing new picture of the Southern Ocean sink in the recent past, it is not yet clear how this region will respond to future changes in climate. The Southern Ocean has long been undersampled, particularly during the austral winter, which may be a critical period for the reinvigoration of the carbon sink (*11*). An improved understanding of key processes controlling this important carbon sink will require more observations with higher spatial and temporal resolution of carbon and other physical and biogeochemical properties in the Southern Ocean and the overlying atmosphere. ∎

REFERENCES AND NOTES

1. C. Le Quéré *et al.*, *Earth Syst. Sci. Data* **7**, 47 (2015).
2. T. L. Frölicher *et al.*, *J. Clim.* **28**, 862 (2015).
3. C. Le Quéré *et al.*, *Science* **316**, 1735 (2007).
4. N. S. Lovenduski, N. Gruber, S. C. Doney, *Global Biogeochem. Cycles* **22**, GB3016 (2008).
5. P. Landschützer *et al.*, *Science* **349**, 1221 (2015).
6. R. Wanninkhof, *J. Geophys. Res.* **97**, 7373 (1992).
7. T. Ito, M. Woloszyn, M. Mazloff, *Nature* **463**, 80 (2010).
8. K. B. Rodgers *et al.*, *Biogeosciences* **11**, 4077 (2014).
9. R. M. Law *et al.*, *Science* **319**, 570a (2008).
10. D. C. E. Bakker *et al.*, *Earth Syst. Sci. Data* **6**, 69 (2014).
11. D. R. Munro *et al.*, *Geophys. Res. Lett.* 10.1002/2015GL065194 (2015).

IMMUNOLOGY

Viruses carry antiviral cargo

Infected cells generate a factor that is incorporated into viruses and transferred to other cells

By **John W. Schoggins**

I n the molecular arms race between viruses and their host cells, each side employs multiple strategies to deal with the other. Whereas the host has sophisticated antiviral signaling programs to combat viral infection, viruses use their own proteins to subvert these host defenses. Viruses are often lauded for these clever evasion tactics. However, the host may also have its own brand of molecular chicanery. On pages 1232 and 1228 of this issue, Gentili *et al.* (*1*) and Bridgeman *et al.* (*2*), respectively, show that during infection, a host cell–derived antiviral molecule is packaged inside viral particles. As a stowaway, the antiviral factor is poised to trigger immune defense pathways upon infection of another host cell.

During a viral infection, the host cell uses specialized proteins to sense viral nucleic acids. For viruses with double-stranded DNA genomes or DNA-based intermediates (e.g., retroviruses), a major sensor is the cytosolic cyclic guanosine monophosphate (GMP)–adenosine monophosphate (AMP) synthase (cGAS) (*3*, *4*), a DNA binding protein that catalyzes the formation of the heterodinu-cleotide cyclic GMP-AMP (cGAMP) in response to DNA (*5*). Signaling by cGAMP, the founding member of a family of metazoan cyclic heterodinucleotides, parallels analogous second messenger functions of cyclic dinucleotides in bacteria (*6*). In mammalian cells, cGAMP binds to the protein stimulator of interferon genes (STING), which triggers the production of interferons, cytokines that establish an antiviral state.

The importance of the cGAS-cGAMP pathway has been demonstrated clearly in vivo. Mice that lack cGAS are highly susceptible to multiple DNA viruses (*7*, *8*). Moreover, cGAMP function does not appear to be limited just to the infected cell, as it can passively diffuse across cellular membranes to trigger antiviral signaling in neighboring cells (*9*). Gentili *et al.* and Bridgeman *et al.* find that cGAMP can also transmit antiviral signals by moving as cargo inside newly formed viruses.

To demonstrate this novel mode of cGAMP transmission, both studies used HIV-1–based lentiviral vectors in cell culture models of infection. When the viruses were produced in cells overexpressing cGAS, the authors could detect transmission of an antiviral signal into newly infected cells. Furthermore, STING ex-pression was required for the transmitted signal to stimulate interferon production in the newly infected cells. Gentili *et al.* and Bridgeman *et al.* also confirmed, using mass spectrometry, that cGAMP was indeed inco-porated into viral particles.

Gentili *et al.* and Bridgeman *et al.* extended their studies to other enveloped viruses and cell types. For example, HIV-1–based vectors bearing envelope proteins from diverse viruses, including vesicular stomatitis virus, influenza A virus, and thogotovirus, could transmit the cGAMP signal through this stowaway mechanism. HIV-2–based vectors, specific HIV-1 strains, and murine leukemia virus, did too. Importantly, two enveloped viruses with double-stranded DNA genomes—vaccinia virus and murine cytomegalovirus—also incorporated cGAMP into the viral particles. Both studies further show that endogenous concentrations of cGAS were sufficient for cGAMP inclusion in viral particles. Also, primary dendritic cells showed enhanced activation (reflected as the production of cytokines) by lentiviral vectors when cGAMP was preloaded into the viral particles. Together, these findings suggest that this mechanism of cGAMP cell-to-cell transport may exist in nature and may be harnessed for therapeutic applications such as vaccination.

But is cGAMP loaded into viral particles in a natural setting? HIV-1 normally evades

Department of Microbiology, University of Texas Southwestern Medical Center, Dallas, TX 75390, USA. E-mail: john.schoggins@utsouthwestern.edu
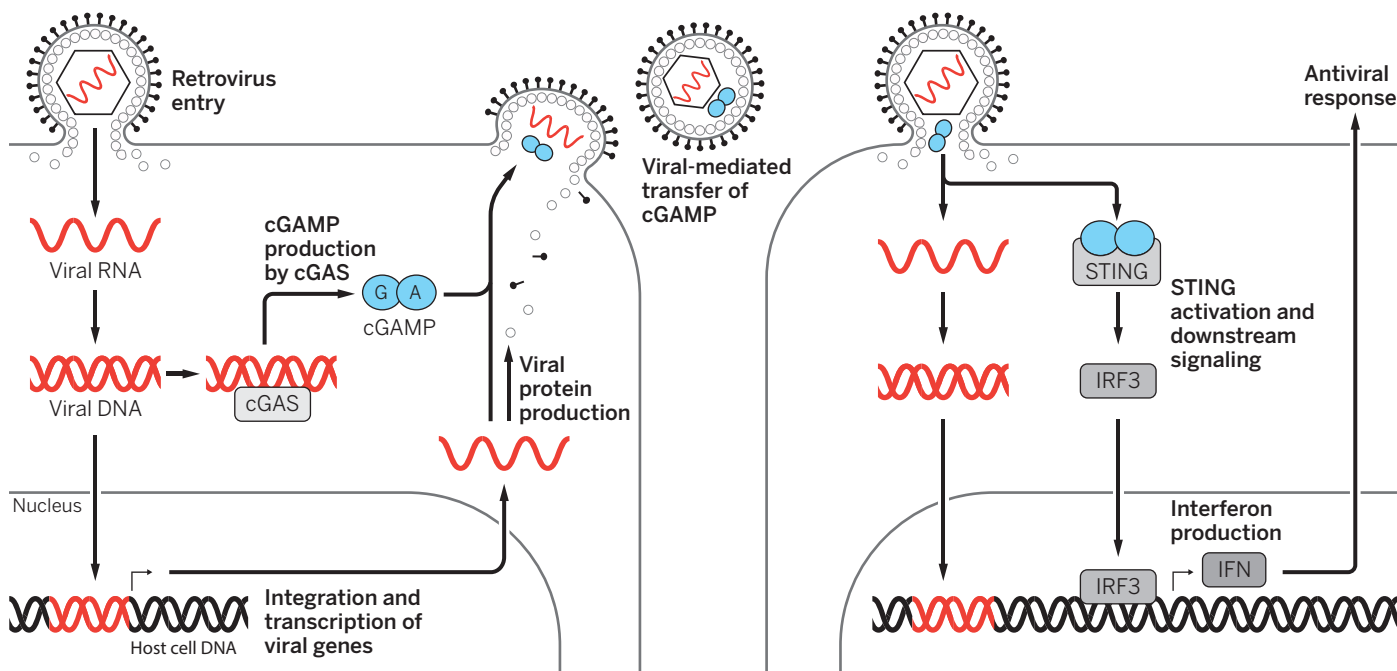
Stowaway. Viral DNA generated during a viral infection is sensed by cGAS, which produces the cGAMP dinucleotide. cGAMP is incorporated as cargo into newly formed virions that exit the cell and infect nearby cells. cGAMP is released into the cytosol of the newly infected cell, binds STING, and triggers downstream antiviral signaling. IRF3, interferon regulatory factor 3.

cGAS-mediated detection, suggesting that the viral particles that emerge from an infected cell would likely not incorporate cGAMP (10). However, Gentili et al. and Bridgeman et al. show that a poxvirus and a herpesvirus (both double-stranded DNA viruses) can take up cGAMP into viral particles. Perhaps the stowaway mechanism is restricted to certain classes of DNA viruses or retroviruses that lack sophisticated evasion tactics.

Another question is whether cGAMP incorporation into virions is a host-directed strategy or simply a consequence of stochastic fluid-phase uptake of cytosolic material into viral particles. By necessity, enveloped viruses must use host membranes to complete the virus assembly and maturation process. Viruses incorporate a variety of host molecules into their virions such as histocompatibility proteins, tetraspanins, or even antiviral molecules like apolipoprotein B messenger RNA editing enzyme, catalytic polypeptide-like 3G (APOBEC3G) in the case of HIV-1 (11). Yet, it is not clear if this process is regulated by the host. It is tantalizing to speculate that the host is as wily an adversary as the virus, with the ability to sneak an antiviral molecule into outbound viral particles.

What are the biological implications of cGAMP incorporation into viral particles? The host might benefit on multiple levels. A virus carrying cGAMP may promote long-distance transmission of antiviral signals to cells and tissues located far from the initial site of infection. Similarly, a cGAMP-loaded virion could serve as a sentinel of innate immune signaling during transmission of the virus from one host to another, potentially even crossing species barriers. The main benefit to the host could be rapid initiation of cGAMP-mediated signaling, even in cells that cannot mount antiviral responses due to poor cGAS expression. It is not yet clear, however, whether cGAMP loading is a propagating mechanism. Further studies will be needed to determine whether cells activated into an antiviral state by incoming virus carrying cGAMP also produce virions that carry cGAMP. ∎

REFERENCES

1. M. Gentili *et al.*, *Science* **349**, 1232 (2015).
2. A. Bridgeman *et al.*, *Science* **349**, 1228 (2015).
3. L. Sun, J. Wu, F. Du, X. Chen, Z. J. Chen, *Science* **339**, 786 (2013).
4. D. Gao *et al.*, *Science* **341**, 903 (2013).
5. V. Hornung, R. Hartmann, A. Ablasser, K. P. Hopfner, *Nat. Rev. Immunol.* **14**, 521 (2014).
6. A. Camilli, B. L. Bassler, *Science* **311**, 1113 (2006).
7. X. D. Li *et al.*, *Science* **341**, 1390 (2013).
8. J. W. Schoggins *et al.*, *Nature* **505**, 691 (2014).
9. A. Ablasser *et al.*, *Nature* **503**, 530 (2013).
10. X. Lahaye, N. Manel, *Curr. Opin. Virol.* **11**, 55 (2015).
11. D. E. Ott, *Rev. Med. Virol.* **18**, 159 (2008).

10.1126/science.aad0942

Plant precursor. Epotoside is a commonly used chemotherapy drug that is derived from a natural compound in mayapple plants.

PLANT BIOCHEMISTRY

Fighting cancer while saving the mayapple

The genes required for synthesizing a plant-derived anticancer compound are identified

By **Sarah E. O'Connor**

Plants synthesize an abundance of metabolites that can be exploited for pharmacological purposes (1). The pool of plant metabolites that can be considered medicinally important is greatly expanded when considering that many plant natural products can be used as a scaffold for derivatization, with the resulting unnatural analogs often having either improved or novel medicinal activity. Typically, unnatural analogs are made semisynthetically by chemically modifying natural biosynthetic intermediates. However, on page 1224 of this issue, Lau and Sattely (2) report the discovery of a set of biosynthetic enzymes in mayapple (*Podophyllum*) plants that can produce a compound that is a direct precursor to etoposide, an "unnatural" anticancer agent. Moreover, Lau and Sattely

John Innes Centre, Department of Biological Chemistry, Norwich NR4 7UK, UK. E-mail: sarah.o'connor@jic.ac.uk

show that the genes encoding these enzymes can be expressed in a different plant species to produce this etoposide precursor. The study clearly demonstrates the power of metabolic pathway discovery and genetic engineering to make not only naturally occurring compounds, but also natural product analogs with enhanced pharmacological value.

Derivatizing unnatural analogs from natural plant compounds has had successful outcomes in the development of anticancer drugs. For example, camptothecin, which is produced by the Chinese "happy tree" (*Camptotheca*), is a potent inhibitor of topoisomerase, an enzyme that controls DNA integrity during the cell division cycle. However, camptothecin is too insoluble for clinical use. Its derivatization with an amino group yields topotecan, an anticancer agent currently used in the clinic to treat ovarian, cervical, and small-cell lung cancer (3). Even when natural compounds are clinically important, chemical derivatization can broaden the spectrum of applications or mitigate side

effects. Derivatives of the plant-derived anti-cancer agent taxol [isolated from the Pacific yew tree (*Taxus brevifolia*)] and vinblastine [isolated from the Madagascar periwinkle (*Catharanthus roseus*)] are used in the clinic in addition to the natural compounds (*4*, *5*).

Etoposide is chemically synthesized from the natural metabolite podophyllotoxin, a liganin that is produced in mayapple plants (*6*). The potent cytotoxic activity of podophyllotoxin suggested that it could be developed into an anticancer drug, but in practice, the compound proved to be too toxic for clinical use. In the 1950s, a program was launched to synthesize and screen semisynthetic podophyllotoxin derivatives that exhibited less toxic side effects. Etoposide, which was eventually discovered from this effort, showed excellent results in clinical trials and was introduced to the United States drug market in 1983 (*6*). Etoposide has a different mode of cytotoxicity compared to the podophyllotoxin precursor. Chemical derivatization is typically used to enhance pharmacological properties such as water solubility, but etoposide reflects how subtle chemical modifications can also dramatically change the biological mode of action.

> *"...biosynthetic enzymes in mayapple...produce a... precursor to...an 'unnatural' anticancer agent."*

Medicinally useful plant metabolites, including podophyllotoxin, are usually isolated from the producer plant and are often produced in low yields. Furthermore, many medicinal plants are difficult to grow or are endangered, as is the case for a number of *Podophyllum* species (*7*). Development of a renewable plant cell culture that generates sufficient yields of podophyllotoxin has been unsuccessful (*8*). An emerging approach for sustainable production of plant-derived compounds is reconstitution of the biosynthetic genes in a heterologous host to recreate a functional pathway. Many challenges must be overcome to reconstitute these complex biosynthesis pathways, but perhaps the largest hurdle is finding the relevant genes within a large, uncharacterized plant genome.

Lau and Sattely identified missing steps in podophyllotoxin biosynthesis by tracking the expression levels of mayapple genes. Because podophyllotoxin increases in response to leaf wounding, comparison of RNA sequence data sets from wounded and unwounded leaf tissue pinpointed appropriately upregulated genes. Lau and Sattely filtered the pool of gene candidates by considering only up-regulated genes that encode four enzyme classes that are predicted to carry out specific types of chemical reactions required for podophyllotoxin biosynthesis. Once this set of candidates was identified, the genes could be transformed into the heterologous host *Nicotiana benthamiana,* a fast-growing relative of tobacco for which a robust protein expression system has been developed (*9*). Lau and Sattely expressed multiple gene candidates at once in this host plant and identified the resulting compounds in leaf tissue by mass spectrometry. This untargeted metabolite profiling approach, in which all compounds resulting from candidate gene expression are identified, proved critical for characterizing unexpected, but highly valuable, chemical reactions that are catalyzed by these candidate gene products. Expression of one candidate gene consumed the biosynthetic intermediate (−)-deoxypodophyllotoxin, but the expected hydroxylated product was not detected, and instead, a demethylated product was observed. A second candidate gene did hydroxylate (−)-deoxypodophyllotoxin in the predicted position but yielded unexpected stereochemistry. Lau and Sattely realized that these unpredicted enzymatic reactions could be used to produce a more direct precursor for etoposide. Expression of these two genes, plus an additional eight biosynthetic genes and a small-molecule precursor, in the *N. benthamiana* host produced (−)-4′-desmethylepipodophyllotoxin, a compound that can be converted to etoposide in fewer chemical steps than are required for the podophyllotoxin precursor.

Although discovery of biosynthetic genes from plant metabolic pathways remains a challenging prospect, the elucidation of this pathway by Lau and Sattely demonstrates how far the field has come. The use of a heterologous host as a gene discovery tool ensures that gene candidates can be examined in the context of other pathway enzymes, which in this case was critical for revealing unexpected chemistry carried out by biosynthetic enzyme candidates. Rather than produce podophyllotoxin, Lau and Sattely used a specific combination of enzymes to synthesize a molecule more valuable than the initial target. ∎

REFERENCES

1. J. D. McChesney *et al.*, *Phytochemistry* **68**, 2015 (2007).
2. W. Lau, E. S. Sattely, *Science* **349**, 1224 (2015).
3. E. L. Chazin *et al.*, *Mini Rev. Med. Chem.* **14**, 953 (2014).
4. Y. Fu *et al.*, *Curr. Med. Chem.* **16**, 3966 (2009).
5. P. Keglevich *et al.*, *Molecules* **17**, 5893 (2012).
6. H. F. Stähelin, A. von Wartburg, *Cancer Res.* **51**, 5 (1991).
7. A. Nag *et al.*, *AoB Plants* **7**, plu076 (2014).
8. S. Farkya *et al.*, *Appl. Microbiol. Biotechnol.* **65**, 504 (2004).
9. F. Sainsbury, G. P. Lomonossoff, *Curr. Opin. Plant Biol.* **19**, 1 (2014).

10.1126/science.aad1801

QUANTUM MECHANICS

Interference of atomic clocks

The time dilation of gravity is mimicked with atomic clocks in magnetic fields

By **Markus Arndt** *and* **Christian Brand**

When de Broglie predicted that we need to associate a periodic phenomenon with any isolated portion of matter or energy (*1*), this idea became the basis of Schrödinger's wave equation and modern matter-wave interferometry. It has stood the test of time and inspired intriguing discussions on the relation between quantum physics, classicality (*2*), and general relativity theory (GRT) (*3*–*5*). It also inspired the recent work on page 1205 of this issue by Margalit *et al.* (*6*), who demonstrated that the internal clock of a delocalized atom can be used as a witness of the atom's path through a matter-wave interferometer. The study shows Bohr's complementarity principle in action and how dephasing in an external potential may mimic "classicality" even though the underlying quantum correlations can be erased and reversed.

In 1908, Einstein predicted that the proper time of any clock on Earth will change with the local gravitational potential by one part in 10^{16} per meter height difference. This effect is tiny, but it already needed to account for the comparison of optical clocks with a height separation of 5 cm (*7*). If we take de Broglie's idea of a periodic phenomenon in any lump of matter literally, does that imply that even "a rock is a clock?" Could this boost precision measurements of gravitational time dilation in an atom interferometer where the center-of-mass wave function of an atom is delocalized over a certain height (*3*)?

Although it has been argued that time dilation will remain unobservable in experiments with simple "rocks" as probe particles (*4*), interesting effects are expected (*5*) when the rock is replaced by a clock, i.e., a particle with internal dynamics (see the figure, panel A). Even if the two center-of-mass wave functions of the same atom are perfectly in phase and suitable for high-contrast matter-wave interference, the internal atomic clocks may still tick at different rates in each arm.

University of Vienna, Faculty of Physics, VCQ and QuNaBioS, Boltzmanngasse 5, 1090 Vienna, Austria. E-mail: markus.arndt@univie.ac.at
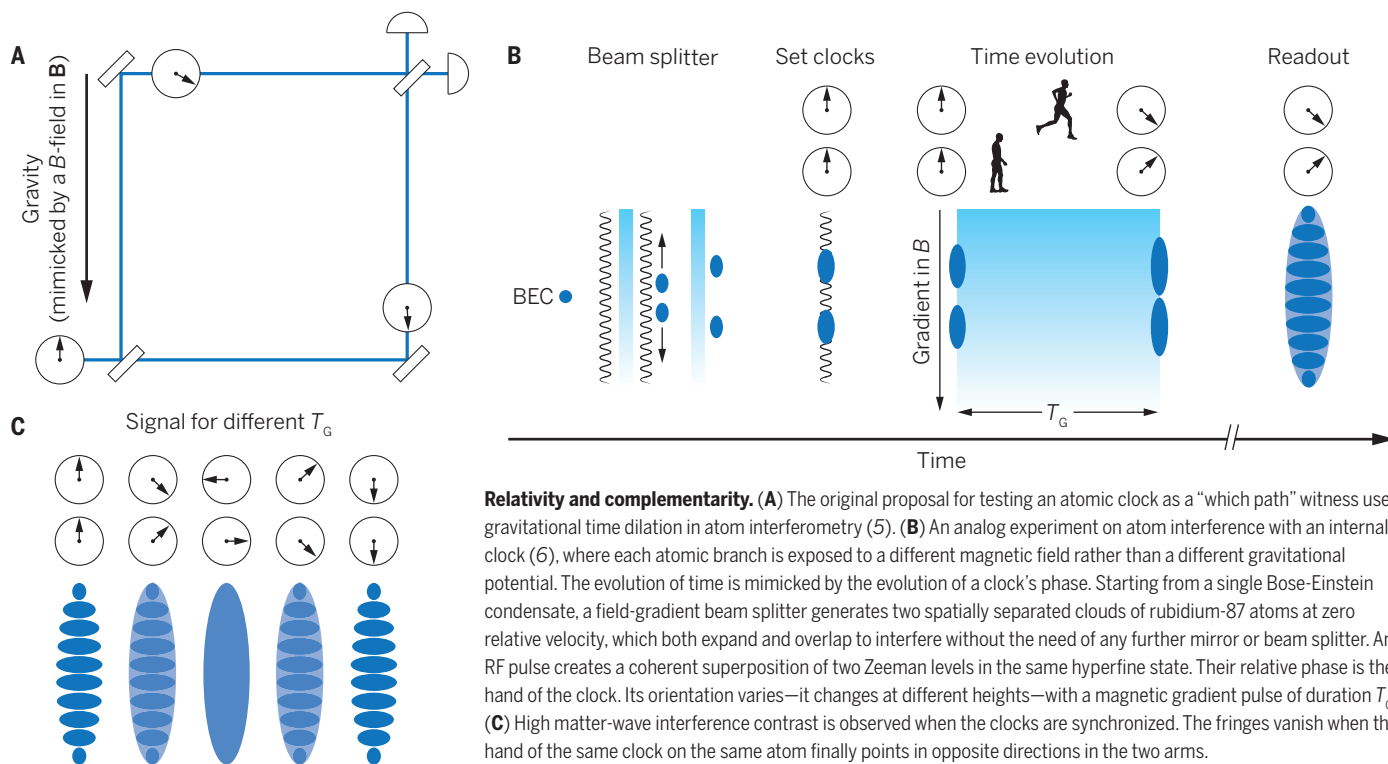
Relativity and complementarity. (**A**) The original proposal for testing an atomic clock as a "which path" witness uses gravitational time dilation in atom interferometry (5). (**B**) An analog experiment on atom interference with an internal clock (6), where each atomic branch is exposed to a different magnetic field rather than a different gravitational potential. The evolution of time is mimicked by the evolution of a clock's phase. Starting from a single Bose-Einstein condensate, a field-gradient beam splitter generates two spatially separated clouds of rubidium-87 atoms at zero relative velocity, which both expand and overlap to interfere without the need of any further mirror or beam splitter. An RF pulse creates a coherent superposition of two Zeeman levels in the same hyperfine state. Their relative phase is the hand of the clock. Its orientation varies—it changes at different heights—with a magnetic gradient pulse of duration T_G: (**C**) High matter-wave interference contrast is observed when the clocks are synchronized. The fringes vanish when the hand of the same clock on the same atom finally points in opposite directions in the two arms.

Because the total atomic wave function is the product of both the internal and the center-of-mass state, the overall interference will vanish if the internal states along two interferometer branches evolve to be orthogonal. In agreement with established decoherence theory (8), the internal clock gets entangled with the position of the atom and acts as a witness of the path the atom takes in the field. This mathematically expresses Bohr's complementarity principle, that an experiment can reveal high-contrast interference or unambiguous which-path information, but not both. Dephasing by gravitational time dilation is only expected to be maximally destructive if an atomic clock of frequency ω can be delocalized over a vertical separation H in the gravitational acceleration g over time T, with $\omega \cdot H \cdot T \geq \pi c^2 / g \simeq 3 \times 10^{16}$ m (5), where c is the speed of light and $g = 9.81$ m/s² is the Earth's gravitational acceleration. Although modern atom interferometers already achieve spectacular coherence times and beam separations (9), the predicted effect is still too small to be measurable today.

This challenge inspired Margalit et al. to build an experimental analogy that can illustrate the underlying complementarity principle, as well as the role of a clock as a which-path witness in atom interferometry (see the figure, panel B). They start from a small Bose-Einstein condensate (BEC) of rubidium-87 atoms. A sequence of radio-frequency (RF) and magnetic-field gradient pulses allows the ensemble to split coherently into two. The naturally expanding ultracold atomic clouds then expand further

to finally overlap and interfere. Because the atomic locations within these two clouds are fundamentally indistinguishable, the atomic matter-wave amplitudes can interfere to create a characteristic set of fringes in the atom number density.

This indistinguishability and interference may, however, be broken if path information is available in the internal atomic state. For that to happen, Margalit et al. used an RF pulse to start the clock by creating an identical superposition of the sublevels $m_F = 1$ and $m_F = 2$ of the same hyperfine state $F = 2$ in both arms. Their clock (6) ticks about 10 orders of magnitude more slowly than modern optical clocks (7) and cannot test GRT. However, its low frequency provides excellent control over the internal state, which is important here to visualize the essential role of the path witness.

Both branches see the same proper time, but to simulate aspects of the envisioned future tests of GRT, a vertical magnetic-field gradient provides different magnetic fields at different heights to drive the magnetic clocks out of phase. When the clock hands point in opposite directions, matter-wave interference vanishes. A longer interaction time in the external magnetic field allows the clocks to rephase. The path information is erased, the witness eliminated, and matter-wave interference is restored (see the figure, panel C).

Complementing earlier demonstrations in neutron (10) and atom interferometry (11), the experiment of Margalit et al. shows the periodic and reversible dephasing of mat-

ter waves that occurs when an atomic clock is used for which-path labeling. It could be argued that the underlying importance of quantum indistinguishability can even be visualized in a Mach-Zehnder interferometer with light—if the atomic clock in panel A of the figure was replaced by polarized light and the polarization was rotated in one arm with the magnetic field in a Faraday rotator. However, a superposition of a massive clock in each interferometer arm has a much farther-reaching potential, in principle. In the long run, it may test the role of time as a universal parameter in quantum mechanics, in contrast to GRT, where it is a dynamical variable. Furthermore, also the original proposal for matter-wave interference as a witness for time dilation in the Earth's potential (5) may be tested. For that to happen, experiments will have to be pushed by many orders of magnitude over the current state-of-the-art in coherence time, path splitting, and clock frequency by combining the best optical clocks (running at 3×10^{15} s⁻¹) with beam separations and coherence times on the order of 1 m and 10 s. ∎

REFERENCES

1. L. De Broglie, *Nature* **112**, 540 (1923).
2. M. Arndt, K. Hornberger, *Nat. Phys.* **10**, 271 (2014).
3. H. Müller, A. Peters, S. Chu, *Nature* **463**, 926 (2010).
4. P. Wolf et al., *Nature* **467**, E1 (2010).
5. M. Zych et al., *Nat. Commun.* **2**, 505 (2011).
6. Y. Margalit et al., *Science* **349**, 1205 (2015).
7. B. J. Bloom et al., *Nature* **506**, 71 (2014).
8. W. H. Zurek, *Phys. Today* **44**, 36 (1991).
9. S. M. Dickerson et al., *Phys. Rev. Lett.* **111**, 083001 (2013).
10. H. Rauch et al., *Phys. Lett. A* **54**, 425 (1975).
11. S. Dürr, T. Nonn, G. Rempe, *Nature* **395**, 33 (1998).

ILLUSTRATION: P. HUEY/SCIENCE

CLIMATE CHANGE

Winning coalitions for climate policy

Green industrial policy builds support for carbon regulation

By **Jonas Meckling**,[1,2*] **Nina Kelsey**,[3,2,4] **Eric Biber**,[5,2] **John Zysman**[6,2,3]

T he gap is wide between the implications of climate science and the achievements of climate policy. Natural sciences tell us with increasing certainty that climate change is real, dangerous, and solvable; social sciences report that key constituencies largely support action. But current and planned

POLICY policy remains weak and will allow a long-term increase in temperature of 3.6°C (*1*). How can we address the gap between science and policy? From the political successes of climate policy leaders, we identify key strategies for building winning coalitions for decarbonization of domestic economies. Green industrial policy provides direct incentives for growth of green industries, which builds political support for carbon regulation.

Policy-makers and scholars increasingly think that global climate agreements emerge from aggregating bottom-up, domestically driven policies rather than from top-down negotiations (*2*). But research does not explain what drives bottom-up approaches. How do we create and maintain political and entrepreneurial will for the fundamental transformations in our economy, infrastructure, and institutions needed to decarbonize our energy systems?

Empirical research on actual decarbonization strategies gives an answer: Providing economic benefits supports effective policy-making in a way that penalizing industrial polluters does not (*3–6*). Green industrial policy creates and enhances low-carbon industries, which brings economic constituencies into

coalitions for decarbonization, as well as giving feedback that drives progress toward more comprehensive climate policy.

CARBON PRICING, MARGINAL CHANGE. This dynamic forces us to re-evaluate assumptions underlying carbon emissions policy-making through the lens of coalition-building. Economists favor directly regulating emissions by putting a price on greenhouse gas (GHG) emissions. Pricing carbon through a tax or a cap-and-trade scheme is, theoretically, the most efficient solution. But there are political barriers to implementing an effective carbon price. To date, one regional, 38 national, and 21 subnational jurisdictions have, are scheduled to implement, or are considering a carbon price (*7*). Although half of these schemes are operating, realizing all of them would cover

Sequencing in climate policy. Of the 54 countries and subnational entities that adopted a carbon pricing scheme by 2013, nearly two-thirds installed a FIT or RPS before setting up the pricing regime. Data from (*7, 11*).

GIP precedes carbon pricing CP	GIP → CP	**35** 24 national 11 subnational
GIP and CP in same year	CP / GIP	**2*** 2 national 0 subnational
CP precedes GIP or CP with no subsequent GIP	CP → GIP	**17*** 13 national 4 subnational

GIP GIP = Green Industrial Policy (FIT/RPS)   **CP** CP = Carbon pricing mechanism such as tax or cap and trade

*Of these 19, 13 are either late entrants to the EU that "inherited" carbon pricing when they joined, or countries that already had naturally low-carbon energy mixes (percentage of nuclear + hydroelectric power substantially above global share).

only 12% of global GHG emissions.

Progress is slow because carbon regulation imposes costs on the powerful few—well-organized energy and energy-intensive manufacturing firms—and provides dispersed benefits to the weak many—the broader public (*8*). The few regulatory losers have greater incentives and capacity to organize politically and prevent policy implementation. So policies focused on imposing a cost on carbon often fail. Even when carbon pricing schemes are created, they accommodate the demands of polluters (*9*), which renders them only marginally effective. Without political support, carbon pric-

ing tends to be a weak instrument at best.

As such, carbon pricing may be ineffective for cultivating coalitions for stronger low-carbon policy. It favors least-cost changes, but costly moves, like major new capital investments, underlie corporate interest realignment. Current (weak) pricing schemes tend to effect marginal changes, such as supplementary equipment and fuel switching in existing infrastructure, although there is also a modest increase in patenting (*10*). Strong carbon pricing would likely drive more fundamental changes but is politically costly, whereas more direct measures, such as renewable portfolio standards (RPSs), have had more support.

COALITIONS AND FEEDBACK. Unlike carbon pricing, green industrial policies have proliferated since the late 1980s. Such policies provide concentrated benefits to the few and well-organized, such as renewable energy firms, low-carbon industries, and investors. By 2013, at least 132 countries and subnational entities had enacted a feed-in tariff (FIT), an RPS, or both (*11*).

Economists view such measures as third- or fourth-best options for efficiency (*12*). But research in political science and law suggests that green industrial policy nurtures a political landscape of interests and coalitions that benefit from a transformation to low-carbon energy use—even when polluting industries might oppose it. The widespread adoption of FITs and RPSs and the fact that they often precede carbon pricing, confirms this (see the figure). Green industries are political allies in the development of more stringent climate policy that subsequently penalizes incumbent polluters. Carrots buy sticks. In contrast, Canada and the United States both failed to create cap-and-trade schemes and lacked strong, prior federal renewable energy policy.

Winning coalitions thrive on positive feedback (*13*). The more green industries form or expand, the stronger coalitions for decarbonizing energy systems become, and the easier it gets to install stronger or more

[1]Department of Environmental Science, Policy, and Management, University of California, Berkeley, CA 94720, USA. [2]Berkeley Roundtable on the International Economy, University of California, Berkeley, CA 94720, USA. [3]Center for Information Technology Research in the Interest of Society, University of California, Berkeley, CA 94720, USA. [4]Institute of Governmental Studies, University of California, Berkeley, CA 94720, USA. [5]School of Law, University of California, Berkeley, CA 94720, USA. [6]Department of Political Science, University of California, Berkeley, CA 94720, USA. *Corresponding author. E-mail: meckling@berkeley.edu

comprehensive regulatory strategies. Policy leaders have used feedback processes before implementing carbon pricing. For instance, German policies began with funding for research and development, then subsidies for demonstration projects during the 1970s and 1980s, and continued to larger-scale market formation programs, including a feed-in law after the 1986 Chernobyl disaster. These policies led to industrial expansion in wind and, later, solar energy production; these developments helped create and expand a coalition of interests that fought to defend existing measures and supported further measures (14). California, too, demonstrates feedback effects (15): Early measures responding to pollution and oil crises led to (i) the creation of a strong regulatory infrastructure; (ii) efficiency regulations; (iii) decoupling of profits from sales volume for utilities; and (iv) early support for renewables. Those measures created tolerance for regulation and set the stage for the passage of a renewable portfolio standard and GHG reduction legislation that ultimately resulted in an emissions trading scheme. Denmark has a similar story (4).

A political strategy that emphasizes green industries may raise concerns that it is vulnerable to costs from rent-seeking (obtaining economic gain from others without benefitting others) and regulatory capture. However, a feedback-based strategy broadens political support, which can effectively lead energy systems out of carbon lock-in. And as Rodrik (16) convincingly argues, rent provision can be managed to prevent capture of policy-makers by winners. Moreover, it is possible that these "third-best" policy options may avoid future costs, by speeding up progress toward more ambitious emission cuts.

POLICY IMPLICATIONS. Although some governments have—often unintentionally—built winning coalitions, policy-makers should use the approach more strategically to cut emissions across power, transport, and heating sectors and as other countries adopt their initial climate policies. We propose three key strategies: (i) adopt initial policy suites of targeted sector-specific policies; (ii) send direct, high-leverage policy signals rather than broad, shallow ones; and (iii) sequence policies strategically.

First, multiple policies—narrow sector, technology, and region-specific—are effective for initiating a trend toward decarbonization because they provide concentrated benefits and can link climate policies with local issues. Targeted green industrial policies—like subsidies, tax rebates, and renewable energy standards—provide concrete benefits to firms and households. Specificity

makes them politically bounded and relatively easy to understand—unlike broader, more systemic strategies, such as carbon pricing or urban planning reform. They can be tailored to provide side benefits and to balance different demands. Linking issues allows for greater leverage in policy-making (4). For example, the European Union's (EU's) climate policy mix aimed at reducing emissions and also played to concerns about energy security and national competitiveness. The broad policy suite allowed policy-

> "*The more green industries form or expand, the stronger coalitions for decarbonizing energy systems become.*"

makers to link emission cuts to other key energy-related policy goals, such as reducing dependence on Russian gas and creating export opportunities. In early phases of policy-industry feedback, when political will for climate policy per se is still limited, all these qualities are important.

Second, policy signals need to have high leverage, directly tied to concrete, meaningful changes in industry investment or structure. Relative to weak carbon pricing, policy instruments like FIT or RPS provide comparatively strong direct incentives for growth of cohesive green industry groups and, thus, are most likely to drive initial shifts in investment and revenues that can realign interests in industries (17). This realignment expands coalitions for low-carbon policy and provides support for experimentation with policy and technology, as well as progress toward systems transformation. Marginal changes encouraged by weak economy-wide signals like carbon-pricing will not accomplish this goal.

Third, strategic sequencing of policies matters. Initially, climate policy must create constituencies that provide the support for subsequent policy moves. Early high-leverage measures are particularly likely to mobilize support. They also prove to be politically stable and lasting given support from the constituencies and coalitions they create. For instance, several efforts in U.S. states to roll back RPSs have failed in recent years, in part owing to political opposition from beneficiaries of those policies. Over time, broader policy signals targeted at polluters, like carbon prices, can be introduced and strengthened. The more carbon policy is politically entrenched, the more discretion there is for less-targeted policy that is more efficient. Strategic sequencing

requires adaptive policy design—focused on knowledge exchange, discipline, and accountability (16)—to prevent lock-in of technical-institutional paths that fail to increase political support and/or to decarbonize the energy system (e.g., ethanol policy).

Future research needs to note the context of successful strategies and to specify potential policy interventions, particularly as they vary by locale. For instance, what type of policy sequences work in different types of political or energy systems? How can policy-makers avoid dead ends and maintain flexibility for adjusting policy measures? How can policy-makers best balance needs for politically salient and economically efficient policy interventions? When are policy-makers likely to retrench from decarbonization trajectories? How will opposing "brown" coalitions adapt over time to strategies based on these concepts?

Over the past year, climate change has risen on the global agenda. The U.S. climate action plan, the United States–China deal, and the EU's 2040 targets are key developments. The December climate meeting in Paris may deliver more. The real test for effective climate policy will be the extent to which governments are capable of building and growing domestic coalitions for low-carbon energy that support implementation and strengthening of those international commitments over time. ∎

REFERENCES AND NOTES

1. International Energy Agency, "World Energy Outlook 2014" (IEA, Paris, 2014).
2. D. G. Victor, J. C. House, S. Joy, *Science* **309**, 1820 (2005).
3. J. Meckling, *Wiley Interdiscip. Rev. Clim. Chang.* **5**, 569 (2014).
4. J. Zysman, M. Huberty, Eds., *Can Green Sustain Growth? From the Religion to the Reality of Sustainable Prosperity* (Stanford Business Books, Stanford, CA, 2014).
5. M. Aklin, J. Urpelainen, *Am. J. Pol. Sci.* **57**, 643 (2013).
6. P. Newell, M. Paterson, *Climate Capitalism: Global Warming and the Transformation of the Global Economy* (Cambridge Univ. Press, Cambridge, 2010).
7. World Bank, "State and trends of carbon pricing" (World Bank, Washington, DC, 2014).
8. K. A. Oye, J. H. Maxwell, *J. Theor. Polit.* **6**, 593 (1994).
9. J. Meckling, *Carbon Coalitions: Business, Climate Politics, and the Rise of Emissions Trading* (MIT Press, Cambridge, MA, 2011).
10. R. Calel, A. Dechezleprêtre, *Rev. Econ. Stat.* http://dx.doi.org/10.1162/REST_a_00470 (2015).
11. Renewable Energy Policy Network for the 21st Century, "Renewables 2014: Global status report" (REN21, Paris, 2014).
12. C. Fischer, R. G. Newell, *J. Environ. Econ. Manage.* **55**, 142 (2008).
13. K. Levin et al., *Policy Sci.* **45**, 123 (2012).
14. F. N. Laird, C. Stefes, *Energy Policy* **37**, 2619 (2009).
15. E. Biber, *Vand. L. Rev.* **66**, 399 (2013).
16. D. Rodrik, *Oxf. Rev. Econ. Policy* **30**, 469 (2014).
17. N. Kelsey, *The Green Spiral: Policy-Industry Feedback and the Success of International Environmental Negotiation* (Univ. of California, Berkeley, CA, 2014).

MICROBIOME

Rethinking heritability of the microbiome

How should microbiome heritability be measured and interpreted?

By **Edward J. van Opstal**[1]
and **Seth R. Bordenstein**[1,2]

For almost a century, heritability has been routinely used to predict genetic influences on phenotypes such as intelligence, schizophrenia, alcoholism, and depression (1). However, there has been relatively little work on heritability of the human microbiome—defined here as the number and types of microorganisms and viruses present in or on the human body. This question has become increasingly more interesting as research reveals that humans and their microbial communities interact in complex and often beneficial networks. An underlying question is the degree to which environment versus human genotype influences the microbiome. A central goal of quantifying microbiome heritability is to discern genetic from environmental factors that structure the microbiome and to potentially identify functionally important microbial community members.

Twin-based studies provide one method for quantifying heritability (h^2) of microbial taxa. In such analyses, heritability is measured by comparing variation in microbial taxon abundances that is attributable to human genetics. This approach simplifies microbial abundances to continuously varying phenotypes, comparable to human height, weight, and eye color. In 2009 and 2012, studies of twins conducted in this manner concluded that there are no heritable gut microbial members (2), or low overall gut microbiome heritability (3), respectively. But in 2014, the largest twin cohort to date examined members of the gut microbiome and found that the bacterial family *Christensenellaceae* has the highest heritability (h^2 = 0.39), and associates closely with other heritable gut bacterial families (4). The groundbreaking discovery of a high heritability for members of the human microbiome raises specific questions about understanding the genetics of human-microbe symbioses: How

[1]Department of Biological Sciences, Vanderbilt University, Nashville, TN 37232, USA. [2]Department of Pathology, Microbiology, and Immunology, Vanderbilt University, Nashville, TN 37232, USA. E-mail: s.bordenstein@vanderbilt.edu

should we interpret what heritability means for microbiome studies? Can microbiome heritability be viewed in a more comprehensive manner? Is h^2 the only term to measure and denote microbiome heritability?

Under a heritability analysis with standard statistical approaches [such as the Additive Genetics, Common Environment, Unique Environment (ACE) model], the abundance of each human-associated microbe is presented as a continuously varying, quantitative "trait" that is affected by host genetics—in other words, the host genome significantly dictates the abundance of a microbe. Although a suitable starting point, this host-centric interpretation of microbiome heritability tends to consider the human-microbiome interaction as unidirectional, in which the host regulates colonization. This view, however, is only half of the story. The microbiome is a collection of different organisms with genotypes that interact with each other as well as with the host to achieve colonization. A more comprehensive view is advisable in which both the host and the microbiome play a role in heritability. This view, based on community genetics principles, requires that studies adopt a conceptual foundation of interspecies (genotype-by-genotype) interactions that drive the assembly of the host and microbial consortia. It also necessitates the use of a measure—"community heritability" (H^2_C)—that reflects genetic variation underlying interactions with the entire (or portions of the) community—in this case, the microbiome together with its human host.

Human-associated microbes contain distinct genetic, transcriptomic, metabolic, and proteomic features that can reciprocally influence their own colonization of specific human genotypes. These features span competitive nutrient acquisition, mechanisms to evade the host immune system, and niche construction, among others. Thus, heritable taxa such as *Christensenellaceae* may be "recruited" by the human genome to perform beneficial functions in the microbial community, but they also may encode traits that enable them to circumvent host defenses and colonize susceptible genotypes. For example, commensal bacteria tolerate or evade human immune responses by modifying surface

ILLUSTRATION: CHARIS TSEVIS

components in their cell walls and outer membranes (5). Other microbes proactively subvert the immune system by injecting effector proteins into host immune cells to kill them (6). Microbes may alter the expression of genes involved in regulating immune, developmental, and metabolic functions (7–10). Communities of microbes can also alter their human environment by forming internal biofilms. Biofilms can provide protection against the host immune response, afford stability in fluctuating environments, and promote the survival of a microbial community (11). Put simply, microbiome heritability can represent three outcomes: host control of the microbiome, host susceptibility to the microbiome, or a combination of host control and susceptibility. Interspecies interactions (host-microbe and microbe-microbe) thus underlie the emergent property of microbiome heritability.

Standard heritability h^2

Genetic relatedness among twins

Microbial species abundance

Community heritability H^2_C

Genetic relatedness among individuals

Microbial community structure
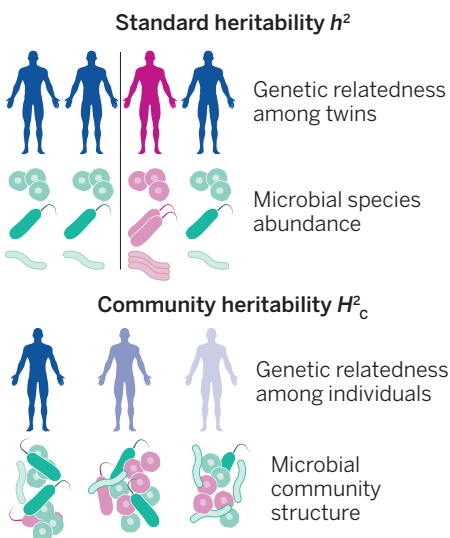
Analyzing heritability. Under standard heritability (h^2) analysis, each microbe is a quantitative "trait" that is encoded by host genetics. Comparing monozygotic versus dizygotic twins allows an indirect estimate of the additive genetic factors affecting that microbe's abundance. Community heritability (H^2_C) emphasizes that the host is part of the ecosystem and measures the extent to which whole community phenotype variation is due to genetic variation in the host. It specifies that host genetic variation will have predictable effects on microbial community assembly.

Human-microbiome interactions tend to be viewed through the lens of host regulation. A key point when discussing community-wide symbiotic interactions is that heritability denotes host involvement rather than control of microbiome assembly. Thus, human genetic effects on the microbiome are most easily understood as genotype-by-genotype (i.e., hologenomic) interactions between the host and other microbial members (12). Without knowing the mechanisms underlying the heritability of a certain microbial member, we must be cautious in interpreting whether a highly heritable microbe in any symbiosis is harmful, harmless, or beneficial to the whole system.

In addition to taking a comprehensive view of microbiome heritability, it is important to understand the ecological genetics principle of broad-sense community heritability (H^2_C) (13). H^2_C emphasizes that the host is part of an ecosystem and measures the extent to which variation in "whole-community" phenotype is due to genetic variation in the foundation (i.e., host) species of the community. It therefore specifies that host genetic variation will have predictable effects on microbial community assembly (14), in addition to having effects on specific members of the microbiome, as measured by h^2.

The whole-community phenotype is measured by ordination methods that cluster microbial community data into single scores used to compare compositional differences (i.e., β diversity) between the communities of various hosts. One such data clustering method is nonmetric multidimensional scaling (NMDS). Analysis of NMDS scores (by ANOVA, which tests whether there is significant variation in means among groups, among subgroups, within groups, etc.), would then identify the fraction of total variation in whole community phenotype that relates to genetic variation in the host (14).

The utility of this approach in addition to conventional heritability measurements is that it incorporates the vast interspecies interactions that contribute to a whole community phenotype, instead of considering individual microbial members as phenotypic extensions of the host. If these interactions have a heritable component (H^2_C), then the assembly of the community is nonrandom (i.e., via ecological selection). For host-microbiome symbioses, this has been referred to as "phylosymbiosis" (15). Given a signficant H^2_C, selection as an evolutionary force can potentially act on the community.

Presently, community heritability measurements have only been applied to ecological systems analyzing plant genetic influences on soil microbe, arthropod, bird, and mammal community structures (14). Human microbiome studies could adopt H^2_C to determine whether human genetic variation across the whole genome, or certain functional categories of genes, affects microbial community assembly. Twin-based microbiome studies could derive a NMDS score for the whole microbial community or from specific taxonomic levels to test if there is a significant association with human genetic relatedness across the cohort of twins. Further, transcriptomes, metabolomes, and proteomes could potentiate identification of the candidate genes that affect microbiome heritability. Data integration from large "omics" data sets holds the potential to move the community genetics view of host and microbes from unspecified genetic effects on interacting species to precise gene-by-gene interactions.

The products of host genes work in intimate association with the products of microbial genes to enable functioning of the whole holobiont (14). Strong degrees of microbiome heritability could therefore have profound consequences for the ecology and evolution of human and all animal and plant holobionts. A crucial outcome of this community heritability view is to underscore the deterministic and predictable interactions between hosts and microbes. Further studies also need to consider the relative roles of vertical and horizontal transmission of microbial communities in heritability assessments. Thus, genetic analysis of whole community organization is an important frontier in the life sciences, particularly for fusing the fields of ecology and evolution and the taxonomic disciplines of zoology and botany with microbiology. The repurposing of community heritability from traditional macroecological systems (i.e., gardens) to microecological systems (i.e., human gut) will provide a more comprehensive view to studies of microbiome heritability. This view looks outwards, beyond the phenotype, to examine links at higher interspecies levels and holds the potential to unify community ecology and evolution concepts. In the words of the microbiologist Carl Woese: "Biologists now need to reformulate their view of evolution to study it in complex dynamic-systems terms." ∎

REFERENCES AND NOTES

1. T. J. Bouchard Jr., M. McGue, *J. Neurobiol.* **54**, 4 (2003).
2. P. J. Turnbaugh *et al.*, *Nature* **457**, 480 (2009).
3. T. Yatsunenko *et al.*, *Nature* **486**, 222 (2012).
4. J. K. Goodrich *et al.*, *Cell* **159**, 789 (2014).
5. T. W. Cullen *et al.*, *Science* **347**, 170 (2015).
6. G. H. Palmer, K. A. Brayton, *Cell. Microbiol.* **15**, 1969 (2013).
7. N. D. Lewis *et al.*, *J. Immunol.* **186**, 3632 (2011).
8. B. B. Finlay, G. McFadden, *Cell* **124**, 767 (2006).
9. N. A. Broderick, N. Buchon, B. Lemaitre, *MBio* **5**, e01117-14 (2014).
10. L. M. Cox *et al.*, *Cell* **158**, 705 (2014).
11. L. Hall-Stoodley, J. W. Costerton, P. Stoodley, *Nat. Rev. Microbiol.* **2**, 95 (2004).
12. S. R. Bordenstein, K. R. Theis, *PLOS Biol.* **13**, e1002226 (2015).
13. S. M. Shuster, E. V. Lonsdorf, G. M. Wimp, J. K. Bailey, T. G. Whitham, *Evolution* **60**, 991 (2006).
14. T. G. Whitham *et al.*, *Nat. Rev. Genet.* **7**, 510 (2006).
15. R. M. Brucker, S. R. Bordenstein, *Science* **341**, 667 (2013).

ILLUSTRATION: P. HUEY/SCIENCE

Symmetry, proportion, and economy are common features of art and of naturally occurring structures.

BOOKS *et al.*

AESTHETICS

Beautiful minds

A physicist and a philosopher contemplate the nature of beauty and the value of art

By **Giovanni Frazzetto**

As living beings with curious, sophisticated minds, we marvel at nature and ponder our relationship with it. To make our investigation stimulating, we endlessly develop and refine methods of discovery. Art, science, and philosophy are a few such methods that occasionally intersect, as they do in two eloquent books that aptly complement each other: physicist Frank Wilczek's *A Beautiful Question* and philosopher Alva Noë's *Strange Tools*.

A vivid, at times dense, journey through physics from Pythagorean geometry and Newton's laws of dynamics to Einstein's relativity theory, quantum particles, and Wilczek's own discovery of asymptotic freedom, *A Beautiful Question* seeks to determine whether the world embodies beautiful ideas. The question itself is not new, but Wilczek tackles it with remarkable audacity, bringing vast, compelling evidence for symmetry, proportion, and economy in nature's own design as well as in science's endeavors to expose it.

Wilczek's search for beauty in nature begins with a discussion of the natural philosophers of ancient Greece, who pursued the belief that matter is built from products of the mind and argued that beautiful forms reflect mathematical order. Indeed, some of the simplest creatures in our biosphere mirror the basic solid shapes described by Plato.

For instance, HIV and the herpes virus are perfect icosahedra. Radiolarians, ocean life-forms of ancient origins, equally incarnate those symmetrical structures. Wilczek further relishes the ineffable beauty in Maxwell's electromagnetism equations, which he visualizes as a balanced "dance of concepts through space and time," a movement he says is more easily experienced than explained.

Wilczek's enthusiasm in the book is palpable and contagious, in resonance with some of the concluding lines from his Nobel Prize lecture: "It is truly awesome to discover … that we humans can come to comprehend Nature's deepest principles, even when they are hidden in remote and alien realms." If you ask Wilczek, a physicist's work is surely driven by logical consistency. But that is not enough: Beauty is also needed to guide us toward truth.

With incisive arguments and in crisp and engaging prose, *Strange Tools* brings the discourse on the function of art and beauty to a different level. Central to Noë's book is the idea that, like philosophy, art is a tool to understand how we live. It is a practice—a technique—that, in his words, organizes and reorganizes us.

Although it involves fundamental biological qualities such as vision and other forms of perception, Noë argues that art is much more than biology. The act of seeing is a basic or, as Noë calls it, first-order activity. On the contrary, art is a second-order activity. Although it cannot be disentangled from a biological substrate, it is enriched with meanings that emerge from an identifiable cultural background.

Contemplating a work of art can be a physical experience as well as an intellectual one. For example, visiting a sculpture by artist Richard Serra, who is famous for erecting labyrinth-like structures of steel and massive size, can be a disorienting experience. It is difficult to distinguish front, back, or side and impossible to tell where the piece starts and ends. The disturbance is visceral. Noë argues that stepping into such spaces represents a "certain kind of enlightenment" that is akin to entering an entirely new intellectual world.

Noë's examples extend beyond the visual world, arguing that music, too, elicits reactions in light of educated knowledge. That is why, for instance, the complexity of Beethoven may leave the musically unversed indifferent—or why we often tend to have a privileged connection to the music of our own time.

Against popular trends, Noë sides decidedly against using neuroscience to elucidate art—a position he lucidly upholds in a dedicated chapter. Neuroscience, he argues, is not to be taken as an "intellectual readymade" that is pertinent to all phenomena—and especially not to art. Art, as he emphasizes several times in the book, is not a phenomenon like digestion or eyesight. It is itself a mode of investigation.

Noë's book begins with a revealing episode that ties the overall argument in his book with the leitmotiv of Wilczek's investigation. Asked by an artist about the science of visual perception, Noë responded that a vision scientist wonders how we get to see endless beauty in the world when it reaches us as warped upside-down images projected on our retinas. In other words, what a scientist asks is How do we see so much based on so little? For the artist—who we later find out is Noë's dad—the right question to ask is exactly the opposite: Why are we so blind, when there is so much to see?

The reviewer is the author of Joy, Guilt, Anger and Love (Penguin Books, New York, 2014) and a visiting research fellow at Trinity College Dublin. E-mail: gio@giovannifrazzetto.com

POLICY

A new chemical economy

Better living through (sustainable) chemistry

By **Megan R. Schwarzman**

The United States has a big problem when it comes to our production and consumption of chemicals—and we've been thinking about it all wrong. So argues Ken Geiser in his sweeping new tome, *Chemicals Without Harm.* Instead of decrying (and attempting to regulate) the health and environmental impacts of hazardous chemicals, Geiser argues that we need to see hazardous chemicals as the symptom of a much larger problem: a whole chemical economy gone awry. In addressing this new version of the problem, he issues a far-reaching scientific, technical, and cultural challenge: retool the material basis of our society toward a system that produces and uses dramatically safer chemicals.

What starts as a thorough survey of key U.S. statutes governing the landscape of chemicals and products becomes a thoughtful investigation of how those laws have performed (mostly poorly) in the face of political maneuvering, procedural limitations, and small budgets. In search of solutions, Geiser places the chemicals problem within its technical context, examining the complex system of feedstocks, processing steps, and product-manufacturing supply chains. He further implicates the current political climate, which he sees as hostile toward business regulation, as well as America's cultural tradition of permissiveness toward new technologies.

Although jaded about the potential for the federal government to play a central role in the transformation to an economy based on safer chemicals ("The government that I studied and engaged with for some forty years has changed dramatically. There are no big visions and grand gestures now"), Geiser sees tremendous potential in a rich tapestry of other actors: nongovernmental organizations that aim to shift market forces, trade unions trying to improve workplaces, consumer goods manufacturers working on safer products, and state legislatures adopting new chemical policies. In fact, optimism and possibility run so continuously through the book that if it were a song, its refrain might be "We can do it." Geiser

clearly believes that although a monumental transformation in the chemical economy is ambitious and runs counter to powerful and entrenched interests, a well-meaning society can and should make it a reality.

Citing examples primarily from Europe, but also Asia, Geiser describes new, more comprehensive chemical policies that offer solid models, supported by chemical data, on which we might base our own programs. He argues that such policies are becoming de facto global standards.

Geiser gathers examples of best practices from around the world and in so do-

A technician collects water samples near the site of a chemical warehouse explosion in Tianjin, China, in August.

ing has created a terrific resource. Want to catalog every chemical in commerce? Look to the European chemicals agency, where companies have registered more than 100,000 substances. Think we need a consumer-facing system for rating the chemical hazards in products? He points to GoodGuide, a free iPhone application that offers environmental ratings of over 200,000 food items, toys, and household products. Geiser offers a vision of how each of these pieces might fit together to create a new, better functioning chemical economy.

Although Geiser's "yes, and" approach is welcome in the face of a challenge as apparently intractable as the current chemical economy, some of his suggestions seem

improbable. His substitute for government action—the blossoming of a million flowers, or in this case, crowd-sourced chemical policy—is not always convincing. For example, he suggests that chemical manufacturers could classify the hazard level of their own chemicals and that if the information were posted on the Internet, "its veracity could be managed by comments and critiques from the hundreds of contributors it most certainly would attract." He notes that companies that make and distribute chemicals will need to reenvi-

sion themselves as "valued agent[s] of environmental and health protection." Particularly in light of the many stories Geiser tells of industry's role in blocking much-needed change to existing industrial systems, the reader could be forgiven for mumbling, "Fat chance."

In the expanse of the book, though, we can tolerate some overly aspirational ideas. Geiser has gathered a wealth of information and applies it to the problem at hand in an imaginative way: offering a framework for how to reorient a hazardous and resource-intensive industry toward safety and sustainability. It is an impressive contribution—and a call to action.

The reviewer is at the School of Public Health, University of California, Berkeley, Berkeley, CA 94720, USA. E-mail: mschwarzman@berkeley.edu

10.1126/science.aac9931

Planted forests (left), invasion by forestry and horticultural tree species (center), and native forest (right) in New Zealand.
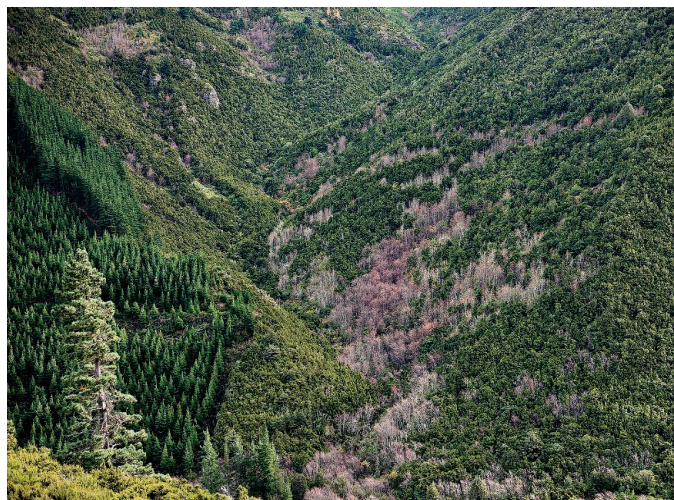
LETTERS

Edited by **Jennifer Sills**

Commercial forests: Native advantage

THE REVIEW "PLANTED forest health: The need for a global strategy" (M. J. Wingfield *et al.*, 21 August, p. 832) suggests that preventing future forest pest problems requires integrating management approaches globally. We agree, but with caveats.

First, the dominant species used in plantation forestry (such as *Pinus*, *Acacia*, and *Eucalyptus*) rank among some of the worst biological invaders worldwide (*1*, *2*). Efforts to improve plant performance by reducing pest and pathogen impacts will likely make those species more problematic and must therefore go hand-in-hand with approaches to mitigate their spread beyond plantations. The use of genetic modification to improve pest and pathogen resistance should be developed alongside techniques to ensure seed sterility for these species. Second, commercial forestry often requires the co-introduction of mutualistic organisms such as root-associated fungi and bacteria, which form symbiotic relationships with surrounding plants. These mutualists can themselves become invasive or interact with additional invasive species creating novel complex interactions (*3*, *4*). Third, an increasing number of native insects and pathogens have shifted their host preference onto introduced plantation tree species (*5*) and attempts to manage these through biological control will face considerable regulatory hurdles. Fourth, the expansion of planted forests globally will increase the likelihood that new pests and pathogens will emerge in regions where commercial trees have been introduced and will pose new and uncertain risks to these trees in their native range. For example, myrtle rust is a significant pathogen of *Eucalyptus* plantations in Brazil that has now spread to Australia, potentially threatening a wide range of threatened native eucalypts (*6*).

We suggest that rather than commercial forestry relying on a relatively small set of plantation species and genotypes, more effort should be invested in developing native species as commercial alternatives to *Pinus*, *Acacia*, and *Eucalyptus*. Not only will this lessen the threat of biological invasion, but such planted forests will be established with the entire contingent of pests and their predators that might pose an ecological barrier to the invasion of alien pests and pathogens. Experiences with planted forests based on native species in Europe, Asia, and North America suggest that a strategy based on diverse native species adapted to local conditions may lead to a more robust long-term outlook for forestry, rather than a single global strategy reliant on a limited genetic diversity.

Duane A. Peltzer,¹* Peter J. Bellingham,¹ Ian A. Dickie,² Philip E. Hulme²

¹Landcare Research, Lincoln, 7640, New Zealand. ²Bio-Protection Research Centre, Lincoln University, Lincoln, 7640, New Zealand.

*Corresponding author. E-mail: peltzerd@ landcareresearch.co.nz

REFERENCES

1. F. Essl *et al.*, *Divers. Distrib.* **16**, 911 (2010).
2. M. Rejmánek, *Biol. Inv.* **16**, 483 (2014).
3. J. R. Wood *et al.*, *J. Ecol.* **103**, 121 (2015).
4. E. M. Wandrag *et al.*, *J. Ecol.* **101**, 1103 (2013).
5. T. D. Paine *et al.*, *Ann. Rev. Entomol.* **56**, 181 (2011).
6. A. J. Carnegie, *Plant Disease.* **99**, 161 (2015).

Bringing science to prisons is not enough

C. J. LEROY describes her experience teaching science behind bars to improve cross-boundary science outreach ("Outside the tower: Bringing science inside prison walls," Letters, 1 May, p. 511) and the importance of educating prisoners in environmental science (*1*). I established a science outreach course at the Champaign County Juvenile Detention Center (JDC) in Urbana, IL, that has since attracted several other graduate students who lead lecture discussions on neuroscience, evolutionary biology, and game theory, to name a few topics popular among the 13- to 17-year-old students. We can all agree on the importance of bringing STEM to marginalized populations (*2*), but what good is a positive attitude or an interest in engaging science to marginalized populations of students who are systematically excluded from higher education? The social stigma of imprisonment will follow these students, and the obstacles present before incarceration will not be removed after release, regardless of how engaged and thoughtful their comments are in class. The hunger for knowledge that LeRoy notes is inspiring, and I find hope in my students' thoughtfulness, but no aspect of outreach can alone compensate for the lack of alternatives they experience on the outside and will once again face upon release.

It is difficult to commit to STEM enrichment without collaterally working to affect social change in the institutions that contribute to educational segregation and the policies that disproportionately cause harm. Until we broadly address these injustices, some students will be able to mature along a path to success paved by their communities, while others who have been shunted from school to prison, regardless of potential, will be out of luck.

A collaboration of scientists and social activists built around the central issue of equality is needed to develop a system of inclusion that addresses the educational needs of all students, regardless of privilege or economic (dis)advantage. Collaterally, we should all continue to bring science to where it is needed most, and to learn what I quickly learned at the JDC: Concrete and steel separate my students from me, not the capacity to think like a scientist.

Ian Traniello

Carl R. Woese Institute for Genomic Biology, University of Illinois at Urbana-Champaign, Champaign, IL 61801, USA. E-mail: traniel2@illinois.edu

REFERENCES

1. Sustainability in Prisons Project; http://sustainabilityinprisons.org/.
2. K. Adams *et al.*, *Prison J.* **74**, 433 (1994).

Illuminating next steps for NEON

IN HIS 7 August In Depth News story "The dimming of NEON" (p. 574), J. Mervis

reported cuts to the National Science Foundation's (NSF's) National Ecological Observatories Network (NEON) program. NEON is a highly ambitious research program that attempts to observe biological and ecological phenomena at unprecedented scales (1). We served as science advisers, evaluating a series of budget and technical problems that compromised the envisioned capabilities of the Observatory. We recommended changes that will leave an Observatory of extraordinary value, provide continental coverage, and deliver transformational science (2).

Mervis focused on STREON, one of the most important conceptual components of NEON despite accounting for only a few percent of the budget. The STREON design adds an otherwise missing element to NEON by altering stream ecosystems, and NSF should identify a funding path to restore it. Deferment of STREON places crucial science at risk.

Despite his generally upbeat appraisal of the Observatory, Mervis raised serious concerns of a broader nature, including "high staff turnover and conflicts created by giving scientists what they felt was insufficient authority." NSF's model for project management emphasizes early science involvement in the design, but execution by project management professionals (3). This approach limited NEON's ability to adapt scientifically as unforeseen technical and scientific challenges arose.

Many of the challenges that derailed NEON were evident long ago, and some could have been addressed by peer-to-peer engagement between science and project management. Re-engaging the scientific community at this time will provide benefits for NSF, NEON, and the broader ecological community. A renewal of science leadership, and scientific peer review, are required to lead to final project success, allowing NEON to realize its benefits to science and society.

Todd Dawson,[1] Serita Frey,[2] Eugene F. Kelly,[3] Susan Stafford,[4] David Schimel[5]*

[1]Department of Integrative Biology, University of California, Berkeley, Berkeley, CA 94720, USA. [2]Department of Natural Resources, University of New Hampshire, Durham, NH 03824, USA. [3]Department of Soil and Crop Sciences, Colorado State University, Fort Collins, CO 80523, USA. [4]Department of Forest Resources, University of Minnesota, St. Paul, MN 55108, USA. [5]Jet Propulsion Laboratory, Pasadena, CA 91101, USA.

*Corresponding author. E-mail: dschimel@jpl.nasa.gov

REFERENCES

1. M. Keller, D. S. Schimel, W. W. Hargrove, F. M. Hoffman, *Front. Ecol. Environ.* **6**, 282 (2008).
2. K. Sand, "Special report: Recommendations related to NSF Scope Management Directives" (2015); www.neoninc.org/updates-events/update/special-report-recommendations-response-nsf-scope-management-directives.
3. D. Schimel, M. Keller, *Oecologia* **177**, 925 (2015).

RESEARCH

IN *SCIENCE* JOURNALS

Edited by **Stella Hurtley**

NEUROSCIENCE

How crickets communicate by sound

Sound patterns present a computational challenge in all animals that communicate by sound. Schöneich unraveled the processing of male calling songs by female crickets. A local network of only five neurons in the brains of the females forms an auditory feature detector circuit, with a response tuning that matches the selectivity of the female behavioral responses to the calls. — PLY

Sci. Adv. 10.1126/ sciadv.1500325 (2015).

Female crickets need only five neurons to recognize male songs

CRITICAL PHENOMENA

Vortices in a superconducting egg crate

Near equilibrium phase transitions, physical systems that bear no resemblance to one another can behave in a very similar way. For example, thermodynamic functions follow the same scaling behavior in a magnetic transition as in the seemingly unrelated gas-liquid transition. Does such universality exist in nonequilibrium phase transitions? Poccia *et al.* fabricated a square array of superconducting islands on a metallic surface. They applied a magnetic field, which caused vortices to form in between the islands, and induced a transition from a state in which vortices were stuck to their positions to one where they were able to move. They observed the same scaling behavior that applies to some equilibrium transitions. — JS

Science, this issue p. 1202

STRUCTURAL BIOLOGY

Structure and function of the spliceosome

When RNA is transcribed from DNA in the eukaryotic cell nucleus, the initial transcript includes noncoding introns that must be spliced out. This splicing is done by a complex macromolecular machine, the spliceosome, which comprises five small nuclear RNAs and more than 100 associated proteins. Now, two papers reveal insights into the structure and function of the yeast spliceosome. Yan *et al.* describe a high-resolution structure determined by electron microscopy of a spliceosome complex comprising four RNAs and 37 proteins. Hang *et al.* focus on the catalytic site and show how protein components anchor the transcribed RNA and allow sufficient flexibility to deliver RNA components involved in catalyzing the splicing reaction. — VV

Science, this issue pp. 1182 and 1191

PLANT SCIENCE

Transplanting the wisdom of the mayapple

Etoposide, a topoisomerase inhibitor, is used to treat various cancers. However, etoposide isn't that easy to get. Its precursor comes from the very slow-growing mayapple plant. Lau and Sattely used bioinformatics, heterologous enzyme expression, and kinetic characterization, to work out the pathway that makes the precursor in mayapple (see the Perspective by O'Connor). They then successfully transplanted the full biosynthetic pathway into tobacco plants. — PJH

Science, this issue p. 1224; see also p. 1167
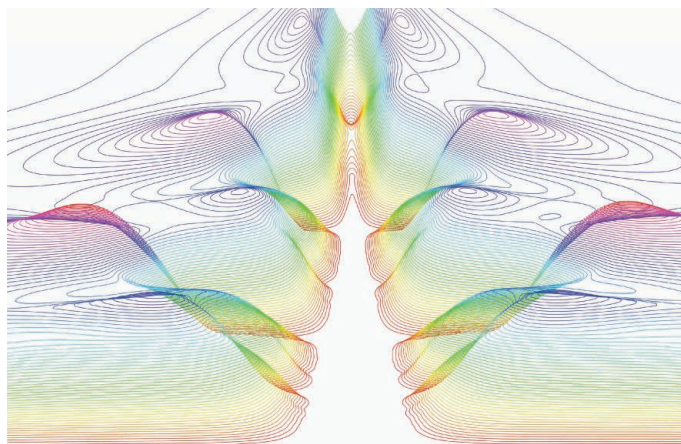
Three-dimensional image of the dynamic resistance as a function of the driving current and the applied magnetic field

GLOBAL CARBON CYCLE
Uptake uptick

Has global warming slowed the uptake of atmospheric CO_2 by the Southern Ocean? Landschützer *et al.* say no (see the Perspective by Fletcher). Previous work suggested that the strength of the Southern Ocean carbon sink fell during the 1990s. This raised concerns that such a decline would exacerbate the rise of atmospheric CO_2 and thereby increase global surface air temperatures and ocean acidity. The newer data show that the Southern Ocean carbon sink strengthened again over the past decade, which illustrates the dynamic nature of the process and alleviates some of the anxiety about its earlier weakening trend. — HJS

Science, this issue p. 1221; see also p. 1165

ELECTROCHEMISTRY
Improving cobalt catalysts

Tethering molecular catalysts together is a tried and trusted method for making them easier to purify and reuse. Lin *et al.* now show that the assembly of a covalent organic framework (COF) structure can also improve fundamental catalytic performance. They used cobalt porphyrin complexes as building blocks for a COF. The resulting material showed greatly enhanced activity for the aqueous electrochemical reduction of CO_2 to CO. — JSY

Science, this issue p. 1208

NEURONAL IDENTITY
Changing properties of interneurons

Neuronal identity is determined early during development. It is assumed that once a neuron has adopted its identity, this remains stable throughout life. However, Dehorter *et al.* investigated the mechanisms controlling the specification of fast-spiking interneurons. They found that the transcription factor Er81 is crucial for the normal specification of these cells by regulating the expression of a potassium channel subunit. — PRS

Science, this issue p. 1216

ANTIVIRAL IMMUNITY
Viruses pack antiviral mediators

Viruses often hijack host proteins for their own use, turning host cells into virion-spewing machines. However, Bridgeman *et al.* and Gentili *et al.* now report a sneaky way that the host can fight back (see the Perspective by Schoggins). Host cells that expressed the enzyme cGAS, an innate immune receptor that senses cytoplasmic DNA, packaged the cGAS-generated second messenger cGAMP into virions. Virions could then transfer cGAMP to neighboring cells, triggering an antiviral gene program in these newly infected cells. Such transfer of an antiviral mediator may help to speed up the immune response to put the brakes on viral spread. — KLM

Science, this issue pp. 1228 and 1232; see also p. 1166

CANCER
Shutting off cancer's motor

Glioblastoma is a difficult-to-treat common and aggressive brain tumor. Two mechanisms that contribute to its lethality are proliferation of the tumor cells and their invasion into normal brain tissue. Although these two processes are usually believed to be independent, Venere *et al.* show that a molecular motor, KIF11, plays a role in both. Inhibiting KIF11 with a small molecule blocked the proliferation and invasion of glioblastoma cells and prolonged survival in mouse models of the disease. These findings, together with the availability of a KIF11 inhibitor that is safe for human use, suggest KIF11 as a viable therapeutic target for treating glioblastoma. — YN

Sci. Transl. Med. **7**, 304ra143 (2015).

CLIMATE
Explaining the last glacier retreat

Between 19,000 and 11,500 years ago, glaciers around the globe retreated as Earth emerged from the last glacial period. Efforts to identify the main drivers of this retreat have been hampered by dating uncertainties. Shakun *et al.* have recalculated the ages of over 1000 glacial boulders from almost 200 sites around the world, using an improved calibration that provides more accurate dates. They find that although there are regional variations, most glacier retreats coincided with the rise in atmospheric carbon during the deglaciation. The high sensitivity of alpine glaciers to carbon dioxide increases has implications for future glacier loss as a result of climate change. — JFU

Nat. Commun. 10.1038/ncomms9059 (2015).
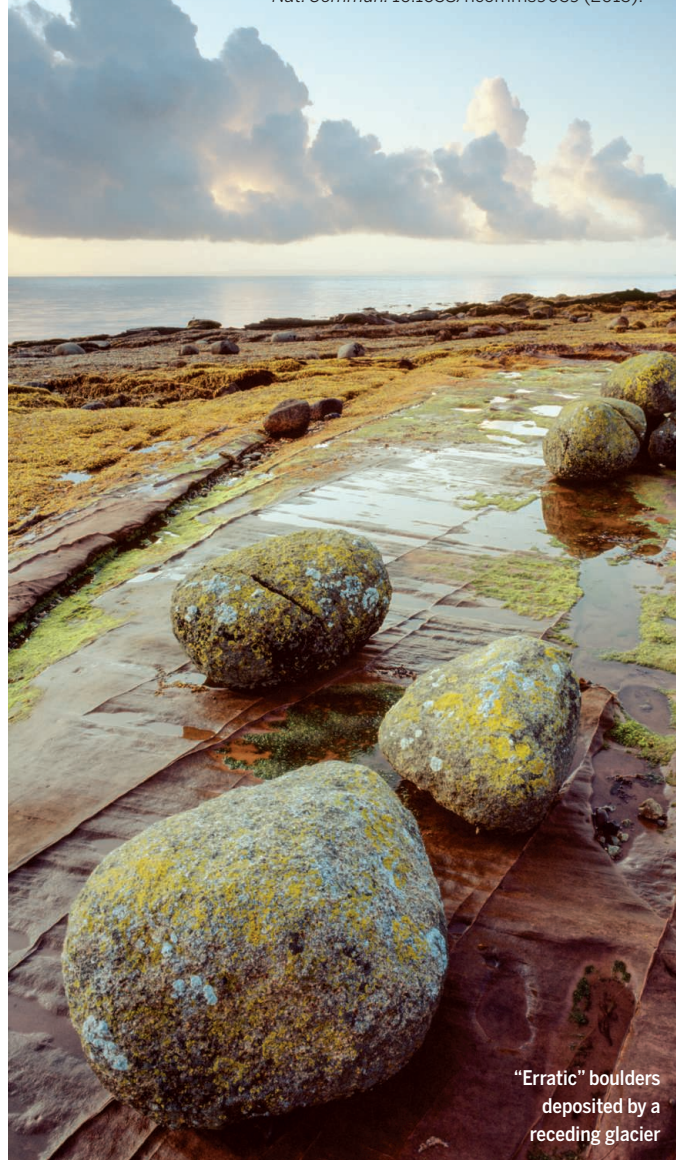
"Erratic" boulders deposited by a receding glacier
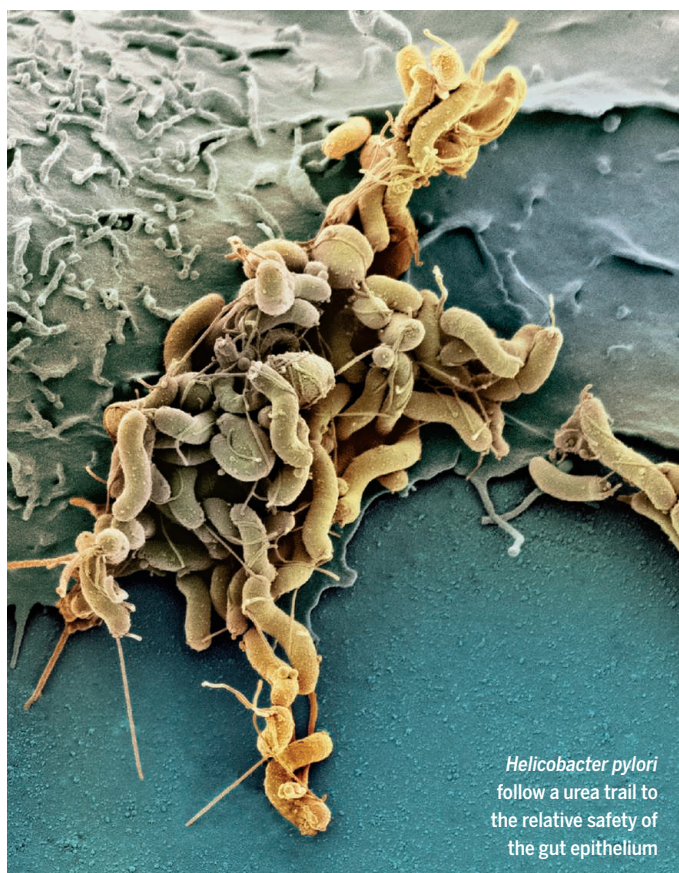
Helicobacter pylori follow a urea trail to the relative safety of the gut epithelium

MICROBIOLOGY

Stomach microbe finds a safe haven

Helicobacter pylori causes stomach ulcers and is linked to gastric cancer. How does this microbe survive in the destructive environment of the stomach? Huang *et al.* looked at how *H. pylori* manages to make its way to the gastric epithelium, where it can reside relatively unscathed by the stomach's defenses. *H. pylori* express a protein chemoreceptor, TlpB, that sniffs out urea released by the gut epithelium. The bugs follow a urea trail to the epithelium and simultaneously degrade the urea to generate ammonia and bicarbonate, which can help to buffer the microbe from the stomach acids. The authors watched how the bacteria locate and swim toward epithelia within seconds, attracted by minute amounts of urea. — SMH

Cell Host Microbe **18**, 147 (2015).

PROTEIN DESIGN

Switching off protein production

Controlling protein production is desirable, but current methods are complex, inefficient, difficult to generalize, or not quickly reversible. Chung *et al.* describe a small-molecule–assisted shutoff (SMASh) tag that is genetically added to a target protein and allows reversible shutoff of various proteins in multiple cell types. The tag includes a site that is cut by a protease and a degron sequence that targets the protein for rapid destruction. Active protease cuts the tag from newly synthesized protein so that it does not disrupt protein function. However, inhibiting the protease with a clinically approved drug protects the tag, and the degron sequence causes the protein to be rapidly degraded. Stopping the drug restores protein production. — VV

Nat. Chem. Biol 10.1038/nchembio.1869 (2015).

MATERIALS SCIENCE

Brushing up on being soft and squishy

Polymer gels can be thought of as a netlike structure of cross-linked linear polymer chains swollen with solvent. Because these materials are mostly liquid, they can be quite soft and squishy, but this means that solvent loss, which makes the gels sticky, also is a concern. Cai *et al.* fabricated very long poly(dimethylsiloxane) chains with a bottle-brush structure: long backbone macromolecules heavily decorated with short side chains (a bit like a hairy caterpillar), which prevent the long chains from entangling. When crosslinked, these chains formed soft gellike materials with a tunable elastic modulus that was dependent on the crosslink density. — MSL

Adv. Mater. 10.1002/adma.201502771 (2015).

METABOLOMICS

Terroir quantified

Wines are characterized not only by year but by vineyard. Anesi *et al.* used chromatography and microarrays to analyze the metabolomes of one variety of the Corvina grape variety grown in different settings in Italy. The study spanned 3 years in order to average effects due to variation in temperature, sunlight, and rainfall. Shifts in the composition of volatile and nonvolatile compounds that correlate with altitude, viticultural practices, and characteristics of the soil revealed the signatures attributable to terroir. — PJH

BMC Plant Biol. 10.1186/s12870-015-0584-4 (2015).

NEURODEVELOPMENT

Brain development hamstrung

Mutations in a zinc-finger transcription factor known as Zic2 cause problems in cortical development and can result in schizophrenia symptoms. Studying embryonic mice, Murillo *et al.* show that this protein supports migrations of several types of neural cells during brain development. The loss of Zic2 hobbled Cajal-Retzius cells, which lay the groundwork for further brain development, as well as cells destined to build key relay and integrative centers in the brain. Normal in number, the stranded Cajal-Retzius cells release their signaling molecule reelin in the wrong places. The migration problems may also range through neural development, affecting cells from the prechordal plate to the neural crest that emigrate from the neural tube. — PJH

J. Neurosci. **35**, 32 (2015).

EDUCATION

Assessing chemistry one class at a time

Before changes in a curriculum can be proposed, it is necessary to assess the current state of the course. Fox and Roehrig did exactly that when surveying undergraduate physical chemistry courses in the United States. Data were collected about issues such as depth versus breadth of content, types of assessments, teacher preparation, and beliefs about the challenging nature of physical chemistry, allowing more-informed decisions to be made about the future of physical chemistry education. Two main themes uncovered by the survey, "how can instructors clearly translate learning goals into assessments" and "how can instructors gain more teacher preparation experience," are relevant to all science disciplines and can be used as a starting point for future science education research. — MM

J. Chem. Edu. 10.1021/acs.jchemed.5b00070 (2015).

PHOTO: SPL/SCIENCE SOURCE

ALSO IN *SCIENCE* JOURNALS

Edited by **Stella Hurtley**

HUMAN GENOMICS
Duplications and deletions in the human genome

Duplications and deletions can lead to variation in copy number for genes and genomic loci among humans. Such variants can reveal evolutionary patterns and have implications for human health. Sudmant *et al*. examined copy-number variation across 236 individual genomes from 125 human populations. Deletions were under more selection, whereas duplications showed more population-specific structure. Interestingly, Oceanic populations retain large duplications postulated to have originated in an ancient Denisovan lineage. — LMZ

Science, this issue p. 1181

MESOSCOPIC PHYSICS
Making and manipulating a weak-link qubit

In superconductors, single particles cannot have energies smaller than the superconducting gap. Yet when two superconductors are separated by a thin nonsuperconducting bridge (the "weak link"), quasiparticles can occupy states that are inside the gap, the so-called Andreev bound states (ABSs). Janvier *et al*. fabricated such a structure out of superconducting aluminum and manipulated the occupation of a pair of ABSs. They observed oscillations in population between two of the energy levels, forming a type of qubit, which they dubbed the Andreev qubit. The results may

lead to applications in quantum information processing. — JS

Science, this issue p. 1199

GEOPHYSICS
Faults well oriented for failure

A deck of cards will remain motionless while pressed on from above, but easily separates when sheared. Similarly, the ease by which geological faults rupture depends on the geometry of the fault relative to the size and direction of stress. Hardebeck finds that faults are well oriented for failure in subduction zones worldwide, suggesting a low-stress environment (see the Perspective by Bürgmann). Subduction zone faults unleash powerful earthquakes. These estimates on the state of stress constrain potential generation mechanisms of destructive subduction zone earthquakes. — BG

Science, this issue p. 1213;
see also p. 1162

CHROMOSOMES
A misstep in the chromosomes' dance

The chromosomes of most cancer cells are unstable, suffering breaks and rearrangements. These aberrations perturb normal gene-regulatory programs and contribute to cancer progression. Tanno *et al.* studied several human cell lines that show chromosome instability. Homologous chromosomes did not pair very well with each other during cell

division. These chromosomes had lost a specific chromatin covalent modification, methylation of histone H3 lysine 9, and/or the protein "glue" cohesin at the chromosomes' centromeres. Either of these losses interfered with the binding of the shugoshin-like protein 2, which is required for proper chromosome pairing and segregation. — GR

Science, this issue p. 1237

CANCER
RNF43 halts Wnt at the nucleus

Wnt signaling, which triggers the transcriptional activity of β-catenin, is critical during development and is often reactivated in cancer. Loregger *et al*. found that RNF43 inhibited Wnt–β-catenin signaling by sequestering TCF4, a β-catenin partner and transcription factor, at the nuclear membrane. Wnt signaling was increased in frog embryos that expressed forms of RNF43 with mutations such as those found in human gastrointestinal tumors. Furthermore, coexpression of wild-type RNF43 suppressed Wnt signaling even in cells with a constitutively active mutant of β-catenin. — LKF

Sci. Signal. **8**, ra90 (2015).

EVOLUTION
Symbioses between single-celled organisms

Examples abound of long-term mutually beneficial relationships between microorganisms and plants or animals. In contrast,

only a few examples of such symbioses between unicellular partners are known. In a Perspective, Zehr highlights recent reports of unicellular symbioses in marine and freshwater systems. In both cases, the cyanobacterial partner in the symbiosis has a much reduced genome and must thus always carry their symbiont. These systems resemble organelle evolution and may help to understand the evolutionary events that led to organelle formation in eukaryotic cells. — JFU

Science, this issue p. 1163

QUANTUM MECHANICS
Interfering with time

The interference pattern arising from light or particles passing through a double slit is a simple experiment that belies the subtleties of interpretation when attempting to describe and understand the effect. For example, determining "which path" the light or particles travel can result in the interference pattern disappearing. Margalit *et al*. present a new take on interferometry using time (see the Perspective by Arndt and Brand). A clock—i.e., the internal state of a cold atom condensate—was coherently split and brought back together to interfere. Making one-half of the clock tick at a different rate resulted in a change in the interference pattern, possibly as a consequence of the time being a "which path" witness. — ISO

Science, this issue p. 1205;
see also p. 1168

RESEARCH ARTICLE SUMMARY

HUMAN GENOMICS

Global diversity, population stratification, and selection of human copy-number variation

Peter H. Sudmant, Swapan Mallick, Bradley J. Nelson, Fereydoun Hormozdiari, Niklas Krumm, John Huddleston, Bradley P. Coe, Carl Baker, Susanne Nordenfelt, Michael Bamshad, Lynn B. Jorde, Olga L. Posukh, Hovhannes Sahakyan, W. Scott Watkins, Levon Yepiskoposyan, M. Syafiq Abdullah, Claudio M. Bravi, Cristian Capelli, Tor Hervig, Joseph T. S. Wee, Chris Tyler-Smith, George van Driem, Irene Gallego Romero, Aashish R. Jha, Sena Karachanak-Yankova, Draga Toncheva, David Comas, Brenna Henn, Toomas Kivisild, Andres Ruiz-Linares, Antti Sajantila, Ene Metspalu, Jüri Parik, Richard Villems, Elena B. Starikovskaya, George Ayodo, Cynthia M. Beall, Anna Di Rienzo, Michael F. Hammer, Rita Khusainova, Elza Khusnutdinova, William Klitz, Cheryl Winkler, Damian Labuda, Mait Metspalu, Sarah A. Tishkoff, Stanislav Dryomov, Rem Sukernik, Nick Patterson, David Reich, Evan E. Eichler*

INTRODUCTION: Most studies of human genetic variation have focused on single-nucleotide variants (SNVs). However, copy-number variants (CNVs) affect more base pairs of DNA among humans, and yet our understanding of CNV diversity among human populations is limited.

RATIONALE: We aimed to understand the pattern, selection, and diversity of copy-number variation by analyzing deeply sequenced genomes representing the diversity of all humans. We compared the selective constraints of deletions versus duplications to understand population stratification in the context of the ancestral human genome and to assess differences in CNV load between African and non-African populations.

RESULTS: We sequenced 236 individual genomes from 125 distinct human populations and identified 14,467 autosomal CNVs and 545 X-linked CNVs with a sequence read-depth approach. Deletions exhibit stronger selective pressure and are better phylogenetic markers of population relationships than duplication polymorphisms. We identified 1036 population-stratified copy-number–variable regions, 295 of which intersect coding regions and 199 of which exhibit extreme signatures of differentiation. Duplicated loci were 1.8-fold more likely to be stratified than deletions but were poorly correlated with flanking genetic diversity. Among these, we highlight a duplication polymorphism restricted to modern Oceanic populations yet also present in the genome of the archaic Denisova hominin. This 225–kilo-base pair (kbp) duplication includes two micro-RNA genes and is almost fixed among human Papuan-Bougainville genomes.

The data allowed us to reconstruct the ancestral human genome and create a more accurate evolutionary framework for the gain and loss of sequences during human evolution. We identified 571 loci that segregate in the human population and another 2026 loci of fixed-copy 2 in all human genomes but absent from the reference genome. The total deletion and duplication load between African and non-African population groups showed no difference after we account for ancestral sequences missing from the human reference. However, we did observe that the relative number of base pairs affected by CNVs compared to single-nucleotide polymorphisms is higher among non-Africans than Africans.

CONCLUSION: Deletions, duplications, and CNVs have shaped, to different extents, the genetic diversity of human populations by the combined forces of mutation, selection, and demography. ∎
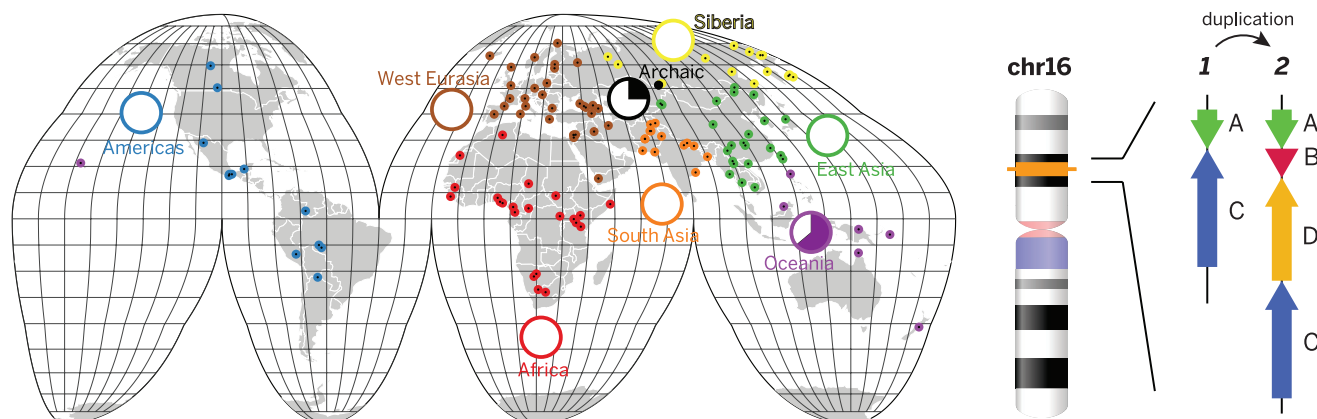
Global human CNV diversity and archaic introgression of a chromosome 16 duplication. (**Left**) The geographic coordinates of populations sampled are indicated on a world map (colored dots). The pie charts show the continental population allele frequency of a single ~225-kbp duplication polymorphism found exclusively among Oceanic populations and an archaic Denisova. (**Right**) The ancestral structure of this duplication locus (1) and the Denisova duplication structure (2) are shown in relation to their position on chromosome 16. We estimate that the duplication emerged ~440 thousand years ago (ka) in the Denisova and then introgressed into ancestral Papuan populations ~40 ka.

RESEARCH ARTICLE

HUMAN GENOMICS

Global diversity, population stratification, and selection of human copy-number variation

Peter H. Sudmant,[1] Swapan Mallick,[2,3] Bradley J. Nelson,[1] Fereydoun Hormozdiari,[1] Niklas Krumm,[1] John Huddleston,[1,39] Bradley P. Coe,[1] Carl Baker,[1] Susanne Nordenfelt,[2,3] Michael Bamshad,[4] Lynn B. Jorde,[5] Olga L. Posukh,[6,7] Hovhannes Sahakyan,[8,9] W. Scott Watkins,[10] Levon Yepiskoposyan,[9] M. Syafiq Abdullah,[11] Claudio M. Bravi,[12] Cristian Capelli,[13] Tor Hervig,[14] Joseph T. S. Wee,[15] Chris Tyler-Smith,[16] George van Driem,[17] Irene Gallego Romero,[18] Aashish R. Jha,[18] Sena Karachanak-Yankova,[19] Draga Toncheva,[19] David Comas,[20] Brenna Henn,[21] Toomas Kivisild,[22] Andres Ruiz-Linares,[23] Antti Sajantila,[24] Ene Metspalu,[8,25] Jüri Parik,[8] Richard Villems,[8] Elena B. Starikovskaya,[26] George Ayodo,[27] Cynthia M. Beall,[28] Anna Di Rienzo,[18] Michael F. Hammer,[29] Rita Khusainova,[30,31] Elza Khusnutdinova,[30,31] William Klitz,[32] Cheryl Winkler,[33] Damian Labuda,[34] Mait Metspalu,[8] Sarah A. Tishkoff,[35] Stanislav Dryomov,[26,36] Rem Sukernik,[26,37] Nick Patterson,[2,3] David Reich,[2,3,38] Evan E. Eichler[1,39]*

In order to explore the diversity and selective signatures of duplication and deletion human copy-number variants (CNVs), we sequenced 236 individuals from 125 distinct human populations. We observed that duplications exhibit fundamentally different population genetic and selective signatures than deletions and are more likely to be stratified between human populations. Through reconstruction of the ancestral human genome, we identify megabases of DNA lost in different human lineages and pinpoint large duplications that introgressed from the extinct Denisova lineage now found at high frequency exclusively in Oceanic populations. We find that the proportion of CNV base pairs to single-nucleotide–variant base pairs is greater among non-Africans than it is among African populations, but we conclude that this difference is likely due to unique aspects of non-African population history as opposed to differences in CNV load.

I n the past decade, genome sequencing has provided insights into demography and migration patterns of human populations (*1–4*), ancient DNA (*5–7*), de novo mutation rates (*8–10*), and the relative deleteriousness and frequency of coding mutations (*11*, *12*). Global human diversity, however, has only been partially sampled, and the genetic architecture of many populations remains uncharacterized. To date, the majority of human diversity studies have focused on single-nucleotide variants (SNVs), although copy-number variants (CNVs) have contributed significantly to hominid evolution (*13*, *14*), adaptation, and disease (*15–18*). Much of the research into CNV diversity has been performed with single-nucleotide polymorphism (SNP) microarray and array comparative genomic hybridization (aCGH) platforms (*19–22*), which provide limited resolution. In addition, comparisons of population CNV diversity with heterogeneous discovery platforms may lead to spurious population-specific trends in CNV diversity (*22*, *23*). Although there are many other forms of structural variation (e.g., inversions or mobile element insertions), in this study we focused on understanding the population genetics and normal pattern of copy-number variation by deep sequencing a diverse panel of human genomes.

Results
CNV discovery

We sequenced to high coverage a panel of 236 human genomes representing 125 diverse human populations from across the globe (Fig. 1 and table S2). Sequencing was performed to a mean genome coverage of 41-fold from libraries prepared by using a standard polymerase chain reaction–free protocol on the HiSeq 2000 Illumina (San Diego, CA) sequencing platform (*24*). The panel includes representation from a broad swathe of human diversity, including individuals from across Siberia, the Indian subcontinent, and Oceania. We also analyzed the high-coverage archaic Neanderthal (*25*) and Denisova (*26*) as well as three ancient human genomes to refine the evolutionary origin and timing of CNV differences (*24*). We applied a read-depth–based digital comparative genomic hybridization (dCGH) approach (*13*, *24*) to identify 14,467 autosomal CNVs and 545 X-linked CNVs among individuals relative to the reference genome (Table 1 and table S1), which we estimate provides breakpoint resolution to ~210 base pairs (bp) (*24*). CNV calls were validated with SNP microarrays and a custom aCGH microarray that targeted all CNVs identified in 20 randomly selected individuals (*24*).

The median CNV size was 7396 bp, with 82.2% of events (n = 12,338) less than 25 kbp (*24*). CNVs mapping to segmental duplications were larger on average (median of 14.4 kbp) than CNVs mapping to the unique portions of the genome (median of 6.2 kbp). Almost one-half of CNV base pairs mapped within previously annotated segmental

[1]Department of Genome Sciences, University of Washington, Seattle, WA 98195, USA. [2]Broad Institute of Massachusetts Institute of Technology (MIT) and Harvard, Cambridge, MA 02142, USA. [3]Department of Genetics, Harvard Medical School, Boston, MA 02115, USA. [4]Department of Pediatrics, University of Washington, Seattle, WA 98119, USA. [5]Department of Human Genetics, University of Utah School of Medicine, Salt Lake City, UT 84112, USA. [6]Institute of Cytology and Genetics, Siberian Branch of Russian Academy of Sciences, Novosibirsk 630090, Russia. [7]Novosibirsk State University, Novosibirsk 630090, Russia. [8]Estonian Biocentre, Evolutionary Biology Group, Tartu 51010, Estonia. [9]Laboratory of Ethnogenomics, Institute of Molecular Biology, National Academy of Sciences of Armenia, Yerevan 0014, Armenia. [10]Department of Human Genetics, Eccles Institute of Human Genetics, University of Utah, Salt Lake City, UT 84112, USA. [11]Raja Isteri Pengiran Anak Saleha (RIPAS) Hospital, Bandar Seri Begawan, Brunei Darussalam. [12]Laboratorio de Genética Molecular Poblacional, Instituto Multidisciplinario de Biología Celular (IMBICE), Centro Científico y Tecnológico–Consejo Nacional de Investigaciones Científicas y Técnicas (CCT-CONICET) and Comisión de Investigaciones Científicas de la Provincia de Buenos Aires (CICPBA), La Plata B1906APO, Argentina. [13]Department of Zoology, University of Oxford, Oxford OX1 3PS, UK. [14]Department of Clinical Science, University of Bergen, Bergen 5021, Norway. [15]National Cancer Centre Singapore, Singapore. [16]Wellcome Trust Sanger Institute, Wellcome Trust Genome Campus, Hinxton, Cambridgeshire CB10 1SA, UK. [17]Institute of Linguistics, University of Bern, Bern CH-3012, Switzerland. [18]Department of Human Genetics, University of Chicago, Chicago, IL 60637, USA. [19]Department of Medical Genetics, National Human Genome Center, Medical University Sofia, Sofia 1431, Bulgaria. [20]Institut de Biologia Evolutiva [Consejo Superior de Investigaciones Científicas–Universitat Pompeu Fabra (CSIC-UPF)], Departament de Ciències Experimentals i de la Salut, UPF, Barcelona 08003, Spain. [21]Department of Ecology and Evolution, Stony Brook University, Stony Brook, NY 11794, USA. [22]Division of Biological Anthropology, University of Cambridge, Fitzwilliam Street, Cambridge CB2 1QH, UK. [23]Department of Genetics, Evolution and Environment, University College London, WC1E 6BT, UK. [24]University of Helsinki, Department of Forensic Medicine, Helsinki 00014, Finland. [25]University of Tartu, Department of Evolutionary Biology, Tartu 5101, Estonia. [26]Laboratory of Human Molecular Genetics, Institute of Molecular and Cellular Biology, Siberian Branch of Russian Academy of Sciences, Novosibirsk 630090, Russia. [27]Center for Global Health and Child Development, Kisumu 40100, Kenya. [28]Department of Anthropology, Case Western Reserve University, Cleveland, OH 44106-7125, USA. [29]Arizona Research Laboratories Division of Biotechnology, University of Arizona, Tucson, AZ 85721, USA. [30]Institute of Biochemistry and Genetics, Ufa Research Centre, Russian Academy of Sciences, Ufa 450054, Russia. [31]Department of Genetics and Fundamental Medicine, Bashkir State University, Ufa 450074, Russia. [32]Integrative Biology, University of California, Berkeley, CA 94720-3140, USA. [33]Basic Research Laboratory, Center for Cancer Research, National Cancer Institute, Leidos Biomedical Research, Incorporated, Frederick National Laboratory, Frederick, MD 21702, USA. [34]Centre Hospitalier Universitaire (CHU) Sainte-Justine, Département de Pédiatrie, Université de Montréal, QC H3T 1C5, Canada. [35]Departments of Biology and Genetics, University of Pennsylvania, Philadelphia, PA 19104, USA. [36]Department of Paleolithic Archaeology, Institute of Archaeology and Ethnography, Siberian Branch of Russian Academy of Sciences, Novosibirsk 630090, Russia. [37]Altai State University, Barnaul 656000, Russia. [38]Howard Hughes Medical Institute, Harvard Medical School, Boston, MA 02115, USA. [39]Howard Hughes Medical Institute, University of Washington, Seattle, WA 98195, USA.
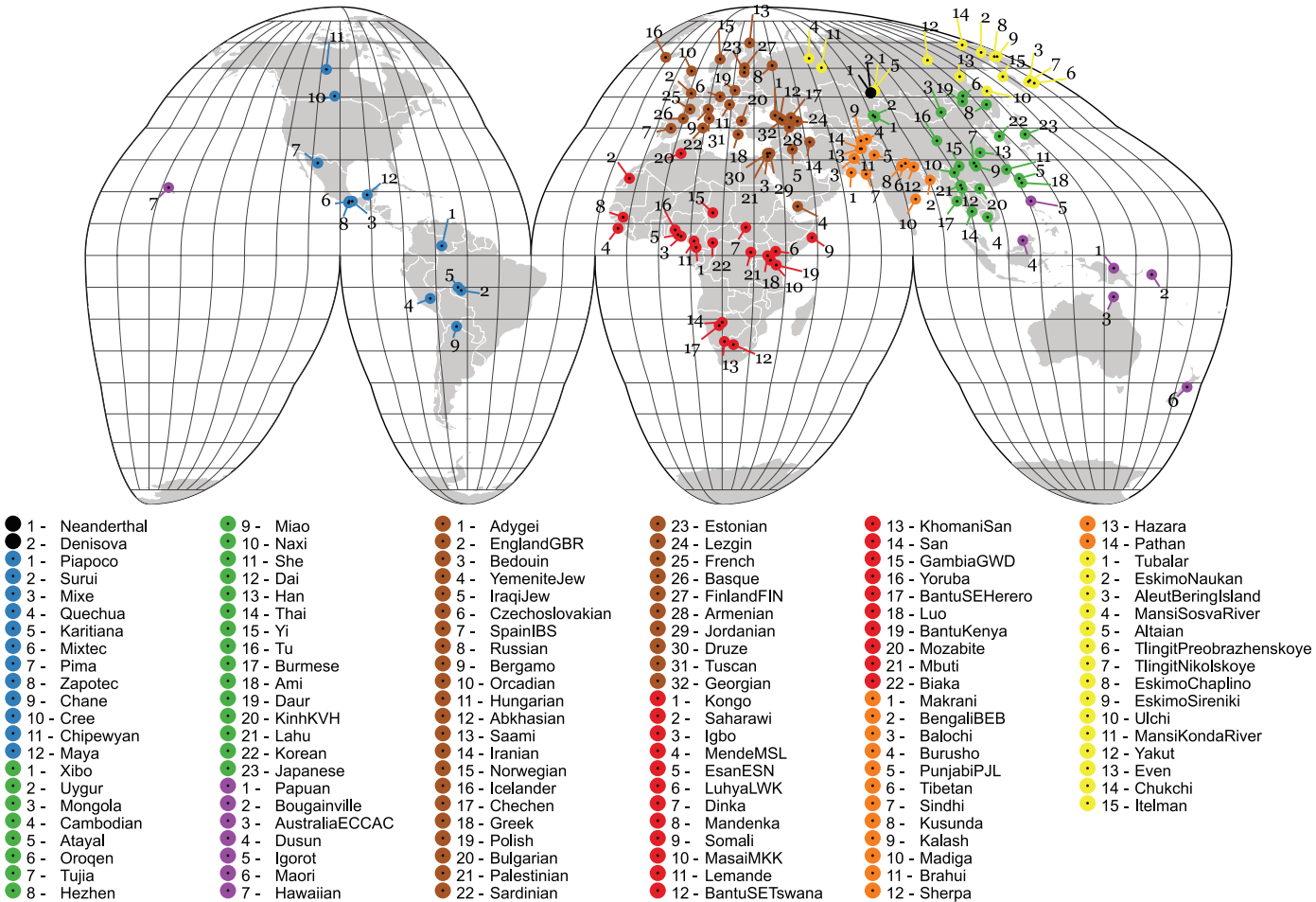*Corresponding author. E-mail: eee@gs.washington.edu

Fig. 1. Analysis of CNVs in several world populations. The geographical locations of the 125 human populations, including two archaic genomes, assessed in this study. Populations are colored by their continental population groups, and archaic individuals are indicated in black.

Table 1. CNVs and SNVs broken down by their intersection with genomic region. The number of mega–base pairs of exonic and segmentally duplicated CNVs reflects the amount of exonic and segmental duplication sequences affected, respectively, not the total sum of the intersecting CNVs.

Class	Autosomal (Mbp)	X chromosome (Mbp)	Exonic (Mbp)	Segmentally duplicated (Mbp)
Deletions	7,233 (78.99)	278 (6.61)	636 (0.32)	331 (8.47)
Duplications	7,234 (129.62)	267 (6.46)	2,093 (1.56)	4,462 (96.93)
Subtotal	14,467 (204.54)	545 (12.61)	2,729 (1.84)	4,793 (99.84)
SNVs	32,630,650 (32.63)	1,175,170 (1.18)	314,872 (0.31)	1,559,158 (1.56)
All	32,645,117 (237.17)	1,175,715 (13.79)	317,601 (2.15)	1,563,951 (101.4)

duplications (a 10-fold enrichment) (Table 1). In total, 217.1 Mbp (7.01%) of the human genome are variable because of CNVs, in contrast to 33.8 Mbp (1.1%) resulting from single-nucleotide variations (Table 1). Deletions (loss of sequence) were less common (representing 85.6 Mbp or 2.77% of the genome) compared with duplications (gain of sequence, 136.1 Mbp or 4.4% of the genome). Furthermore, comparing our data set with other studies of CNVs (21, 27), 67 to 73% of calls we report are unique to our study, whereas we captured 68 to 77% of previously identified CNVs (24).

CNV diversity and selection

African populations are broadly distinguished from non-African populations by a principal component analysis (PCA) for either deletions (Fig. 2A and fig. S20) (24) or duplications (Fig. 2B). In this analysis, we limited the variants to biallelic deletions or biallelic duplications (dip-

loid genotypes of two, three, or four) to eliminate difficulty of inferring phase from multicopy CNVs. For deletions, PC1 (6.8% of the variance) and PC2 (3.94%) distinguish Africans, West Eurasians, East Asians, and Oceanic populations. PC3 and PC4, describing 2.8% and 2.0% of the total variance, cluster Papuans and populations of the Americas, respectively. Many other populations were predictably distributed along clines between these clusters (e.g., Northern Africans, Siberians, South Asians, Amerindians, and indigenous peoples of Philippines and North Borneo). PCAs generated from SNVs showed patterns similar to those from deletions. Africans also show much greater heterozygosity (Fig. 2C and Table 2), for instance, ~25% more heterozygous biallelic deletions and more than a twofold difference when compared with Amerindians (θ_{African} = 535 versus θ_{Americas} = 209). The archaic Neanderthal and Denisova genomes form an out-group to all humans (24).

Duplication heterozygosity and PCA in general show similar trends (Fig. 2D), albeit with far less definition. Oceanic populations, especially those from Papua New Guinea, Australia, and Bougainville, showed the greatest separation on PC1
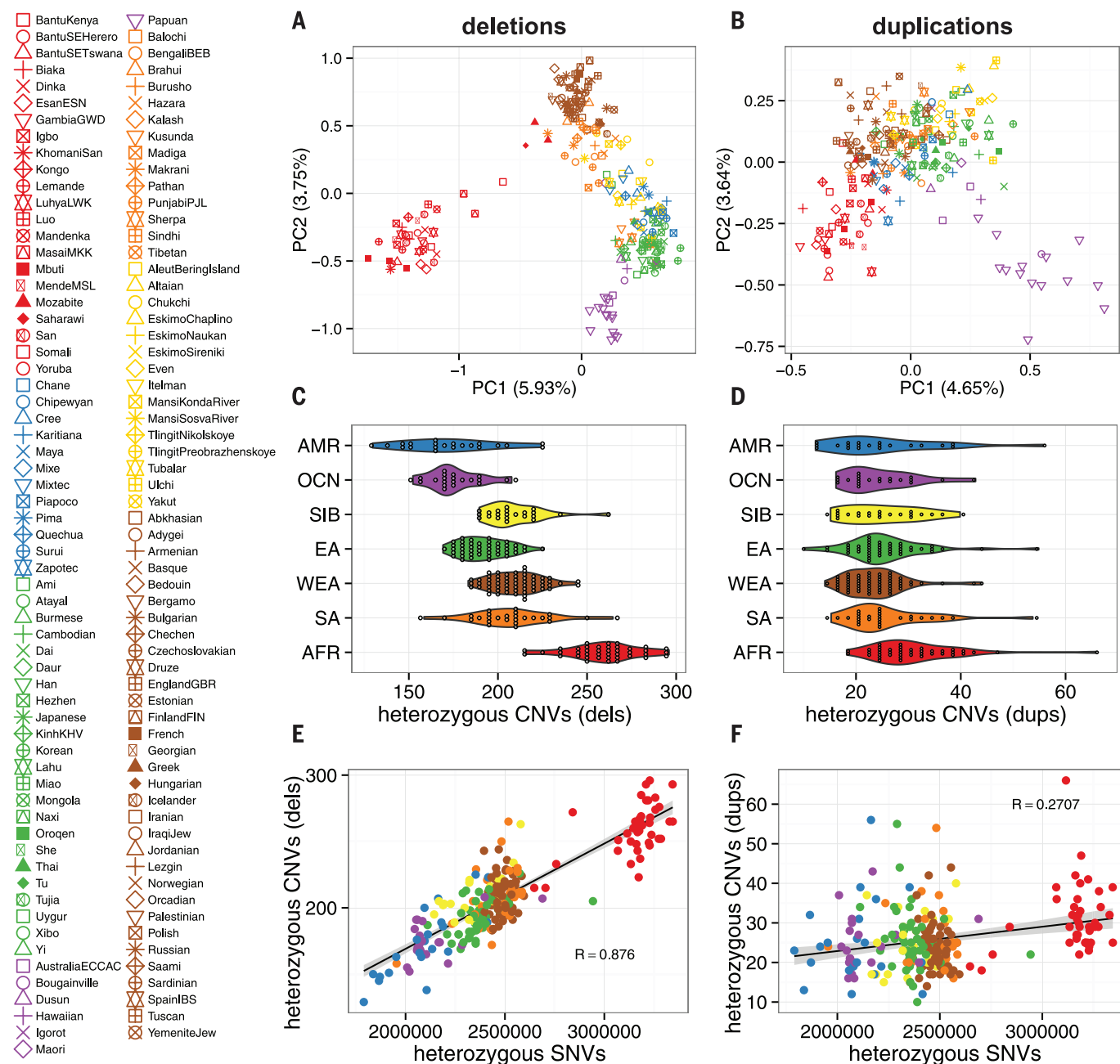
Fig. 2. Population structure and CNV diversity. PCA of individuals assessed in this study plotted for biallelic deletions (**A**) and duplications (**B**) with colors and shapes representing continental and specific populations, respectively. Individuals are projected along the PC1 and PC2 axes. The deletion (**C**) and duplication (**D**) heterozygosity plotted and grouped by continental population. The relationship between SNV heterozygosity and deletion (**E**) or duplication (**F**) heterozygosity is compared.

by duplication. Biallelic duplications appear to be somewhat less-informative markers of human ancestry, in contrast to SNVs, which provide the greatest resolution (e.g., SNV PCs 1 to 4 describe 5.8, 3.4, 2.6, and 1.7% of the variance, respectively). This difference is also seen when comparing SNV and CNV heterozygosity (Fig. 2, E and F). Whereas heterozygous biallelic deletions were strongly correlated ($R = 0.88$) with SNV heterozygosity, the correlation between SNVs and duplications was much weaker ($R = 0.27$). We compared this correlation for duplications lo-

cated adjacent to segmental duplications (within or proximal 150 kbp) in contrast to those occurring in unique regions of the genome and therefore less likely to be subject to recurrent mutation. Heterozygous duplications occurring in unique regions were better correlated with heterozygous SNVs ($r = 0.29$) than those adjacent or within segmental duplications ($r = 0.17$), although the difference was not significant (two-sided Williams' test $P < 0.1$).

Studies of larger (>100 kbp) deletion and duplication events indicate that deletions are more

deleterious than duplications (*28*). We reasoned that this may be reflected in the allele frequency spectrum (AFS) of normal genetic variation and compared the AFS of genic versus intergenic deletions and duplications for smaller events (Fig. 3, A and B). Genic deletions were significantly rarer than intergenic deletions (Wilcoxon rank sum test, $P = 1.84 \times 10^{-9}$), but genic duplications showed no such skew (Wilcoxon rank sum test, $P = 0.181$). Size also had a significant impact on the AFS of CNVs. Deletions increased in rarity as a function of size (F test, $P = 5.02 \times 10^{-11}$)

Table 2. Summary statistics of biallelic CNV deletions versus SNVs by continental population group.

| Continental population group	n	Segregating SNVs	Segregating CNVs	CNVs/individual (median)	Heterozygous CNVs/individual (median)	Continental population group-specific CNVs (allele count ≥ 2)	θ_{CNV}/genome
West Eurasian (WEA)	58	13610715	1728	279.0	209.0	688 (89)	324.42
Oceanic (OCN)	21	9467426	1022	263.0	173.0	353 (84)	237.51
East Asian (EA)	45	17452049	1463	271.0	191.0	525 (59)	288.48
Siberian (SIB)	23	9644914	1102	285.0	205.0	214 (30)	250.74
South Asian (SA)	27	11308883	1405	279.0	208.0	418 (43)	308.32
Americas (AMR)	21	8127639	899	266.0	169.0	208 (25)	208.93
African (AFR)	41	21698517	2663	319.0	261.0	1772 (702)	534.97
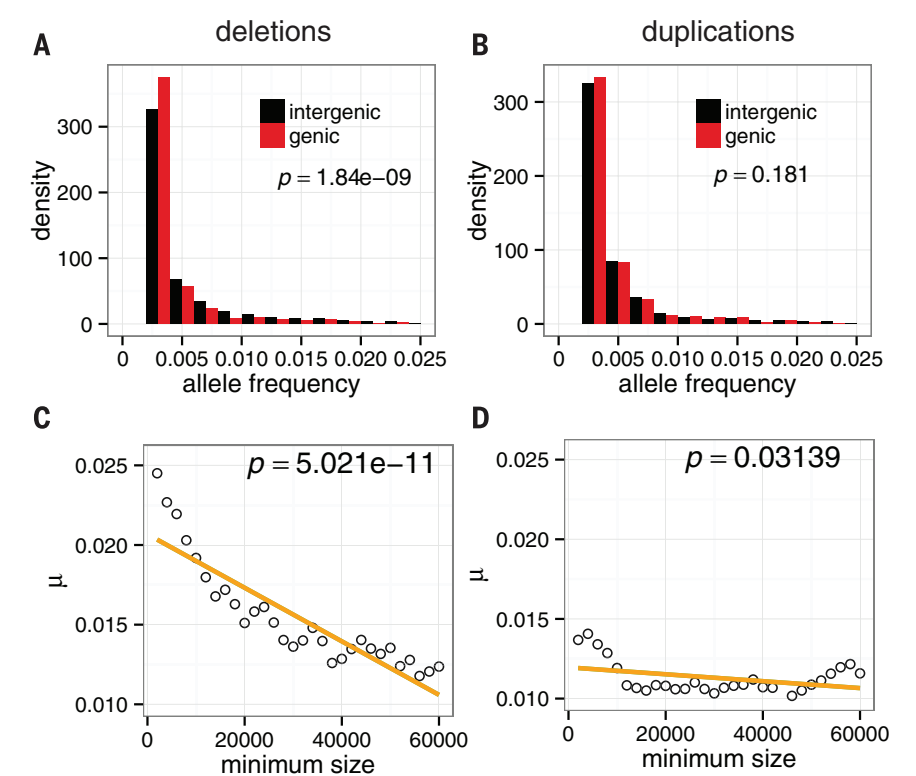
Fig. 3. Selection on CNVs. Folded allele-frequency spectra of exon-intersecting deletions (**A**) and duplications (**B**). Whereas deletions intersecting exons are significantly rarer than intergenic deletions, exon-intersecting duplications show no difference compared to intergenic duplications. The mean frequency of CNVs beyond a minimum size threshold is plotted for deletions (**C**) and duplications (**D**). A strong negative correlation between size and allele frequency is observed for deletions but less so for duplications.

(Fig. 3C), but only a nominally significant trend was observed for duplications ($P = 0.031$) (Fig. 3D). These data suggest that selection has shaped the extant diversity of deletions and duplications differently during human evolution.

Population stratification

Because population stratification can be indicative of loci under adaptive selection, we calculated V_{st} statistics for each CNV among all pairs of continental population groups, a metric analogous to F_{st} (the fixation index) (29). V_{st} and F_{st} statistics compare the variance in allele frequencies between populations, with V_{st} allowing comparison of multiallelic or multicopy CNVs. We

identified 1036 stratified copy-number–variable regions (CNVRs with maximum population $V_{st} > 0.2$, ~10% of the total), 295 of which intersected the exons of genes and 199 that exhibited extreme stratification ($V_{st} > 0.5$) (table S3). After correcting for copy number, duplicated loci were 1.8-fold more likely to be stratified than deletions. This finding is more remarkable in light of the fact that duplications were less discriminatory by PCA, suggesting that a subset of multiallelic duplicated CNVs show large allele frequency differences between different populations (see discussion below). The V_{st} of stratified duplicated CNVs was weakly correlated with the F_{st} of flanking SNVs ($R^2 = 0.03$, $P = 3.27 \times 10^{-12}$)

in contrast to deletions ($R^2 = 0.2$, $P < 2 \times 10^{-16}$). Stratified duplication loci, thus, are far less likely to be tagged by adjacent SNPs through linkage disequilibrium.

Many of the population-differentiated loci were multiallelic and mapped to segmental duplications, including the repeat domain of *ANKRD36* and the DUF1220 domain of *NBPF* (24) (Table 3). Several of these population differences involve genes of medical consequence, such as the multiallelic duplication of *CLPS*, a pancreatic colipase involved in dietary metabolism of long-chain triglyceride fatty acids (Fig. 4A). Increased expression in mouse models of this gene is negatively correlated with blood glucose levels (30). A duplication of the haptoglobin and haptoglobin-related (*HP* and *HPR*) genes expanded exclusively in Africa. The duplication has recently been associated with a possible protective effect against trypanosomiasis in Africa, although only copy 3 and 4 alleles were reported (31). We find this locus has further expanded to five and six copies in Esan, Gambian, Igbo, Mandenka, and Yoruban individuals (Fig. 4A). We also compared the location of our CNVs with disease loci identified by genome-wide association study (GWAS) (32) and sites of potential positive selection (33). Although only a small fraction of our CNVs (1 to 6%) overlapped such functional annotation, we note that 21% of putative adaptive loci intersected with a CNV when compared with 6% of disease GWAS loci (table S4). Because many of the intervals are large, further refinement and investigation are needed to determine the importance of such overlaps.

Denisovan CNVs are retained and expanded in Oceanic populations

We further searched for highly stratified population-specific CNVs sharing alleles with the archaic Neanderthal and Denisovan individuals assessed in our study. Although no Neanderthal-shared population-specific CNVs were identified, five Oceanic-specific CNVs were identified that shared the Denisova allele at high frequency (24). Papuan genomes have previously been reported to harbor 3 to 6% Denisovan admixture (6, 26). CNVs of putative Denisovan ancestry were at remarkably high frequency in Papuan individuals (all >0.2 allele frequency), with one ~9-kbp deletion

Table 3. CNVs differentiated between human populations. CNVs intersecting genes that show dramatic difference in copy number (as measured by V_{st}) between human populations (see Fig. 1 for definition of populations).

Locus	Genes	V_{st}	Copy range	Description
chr2:97849921–97899292	*ANKRD36*	0.49 (OCN-WEA)	30–41	Repeat domain expanded to 45 copies in Papuans.
chr1:144146792–144224420	*NBPF*	0.32 (AFR-EA)	185–271	Expansion of the *DUF1220* repeat domain in Africans and Amerindians. Copy number associated with cognitive function and autism severity (*47*).
chr6:35749042–35767153	*CLPS*	0.29 (AMR-SA)	2–6	Pancreatic colipase involved in dietary metabolism of long-chain triglyceride fatty acids. Increased expression is negatively correlated with blood glucose in mice (*30*).
chr16:72088031–72119241	*HP, HPR*	0.25 (AFR-WEA)	1–6	Haptoglobin and haptoglobin-related genes are expanded exclusively in Africa and associated with a possible protective effect against trypanosomiasis (*31*).
chr12:64011854–64015265	*DPY19L2*	0.32 (OCN-SA)	5–7	*DPY* genes are required for sperm head elongation and acrosome formation during spermatogenesis, and *DPY19L2* homozygous deletions have been identified as a major cause of globozoospermia (*48*).
chr1:74648583–74664195	*LRRIQ3*	0.23 (AMR-WEA)	2–3	*LRRIQ3* is duplicated exclusively in Siberian and Amerindian populations.
chr17:43692284–43708692	*CRHR1*	0.25 (EA-WEA)	4–7	Deletions of corticotropin-releasing hormone receptor 1 result in reduced anxiety and neurotransmission impairments in mice (*49*).
chr5:150201231–150223428	*IRGM* promoter	0.25 (AFR-WEA)	0–2	The *IRGM* promoter CNV is a Crohn's disease risk factor (*50*).
chr3:195771149–195776591	*TFRC* promoter	0.57 (AFR-EA)	0–2	Transferrin receptor is a cellular receptor for New World hemorrhagic fever arenaviruses (*51*).

lying 2 kbp upstream of the long noncoding RNA *LINC00501*, another 5-kbp duplication lying 8 kbp upstream of the *METTL9* methyltransferase gene, and a 73.5-kbp duplication intersecting the *MIR548D2* and *MIR548AA2* microRNAs (Fig. 4B).

We determined that the latter two are part of a larger composite segmental duplication that appears to have almost fixed among human Papuan-Bougainville genomes [allele frequency (AF) = 0.84] but has not been observed in any other extant human population (Fig. 4, B and C). We noted three additional duplications proximal to this locus exhibiting strikingly correlated copy number, despite being separated by >1 Mbp in the reference genome (Fig. 4C) (*24*). We suggest that these constitute a single, larger (~225 kbp) complex duplication composed of different segmental duplications. By using discordantly mapping paired-end reads, we resolved the organization of two duplication architectures not represented in the human reference (Fig. 4D). The first of which (architecture A/C) is present in all individuals assessed in this study (5625 discordant paired-end reads supporting) but not in the human reference genome. The second (B/D) corresponds to the Denisova-Papuan–specific duplication and is only present in these individuals and the Denisova genome. Seventy paralogous sequence variants [mark-

ers distinct to paralogous locus (*34, 35*)] distinguish the Papuan duplication, of which 65/70 (92.9%) were shared with the archaic Denisova genome. On the basis of single-nucleotide divergence, we estimate that the duplication emerged ~440 thousand years ago (ka) and rose to high frequency in Papuan (>0.80 AF) but not Australian genomes, probably over the past 40,000 years after introgression from Denisova (Fig. 4E). This polymorphism represents the largest introgressed archaic hominin duplication in modern humans.

The ancestral human genome

The breadth of the data set allowed us to reconstruct the structure and content of the ancestral human genome before human migration and subsequent gene loss. To identify ancestral sequences potentially lost by deletion, we identified a set of sequences present in chimpanzee and orangutan reference genomes but absent from the human reference genome (20,373 nonredundant loci corresponding to 40.7 Mbp of sequence). Of these, 9666 (27.6 Mbp) were unique (i.e., not composed of common repeats). Because of the inability to accurately genotype copy number for unique segments less than 500 bp by read-depth analysis, we limited our ancestral reconstruction to nonrepetitive sequences greater

than this length threshold. Although the majority represented deletions specifically lost in the human lineage since divergence from great apes (6341 loci) or else referenced genome artifacts (2026 loci fixed-copy 2 in all individuals assessed, 6.2 Mbp), a small subset of these ($n = 571$ or 1.55 Mbp) segregate as biallelic polymorphisms in human populations (Fig. 5A). As expected, Africans were more likely to show evidence of these ancestral sequences compared with non-African populations, because the latter have experienced more population bottlenecks and thus retained less of the ancestral human diversity. A comparison to archaic genomes allowed us to identify sequences (50 loci or 104 kbp) that were present in Denisova or Neanderthal but lost in all contemporary humans as well as ancestral sequences present in all humans but not found in Denisova or Neanderthal (17 loci or 33.3 kbp).

No difference in the CNV load between Africans and non-Africans

The high coverage and uniformity allowed us to contrast putatively deleterious, exon-removing CNVs among human populations, which are of interest in disease studies (*36–38*). In our call set, we identified 2437 CNVRs intersecting exons. The distribution of allele counts of these tended
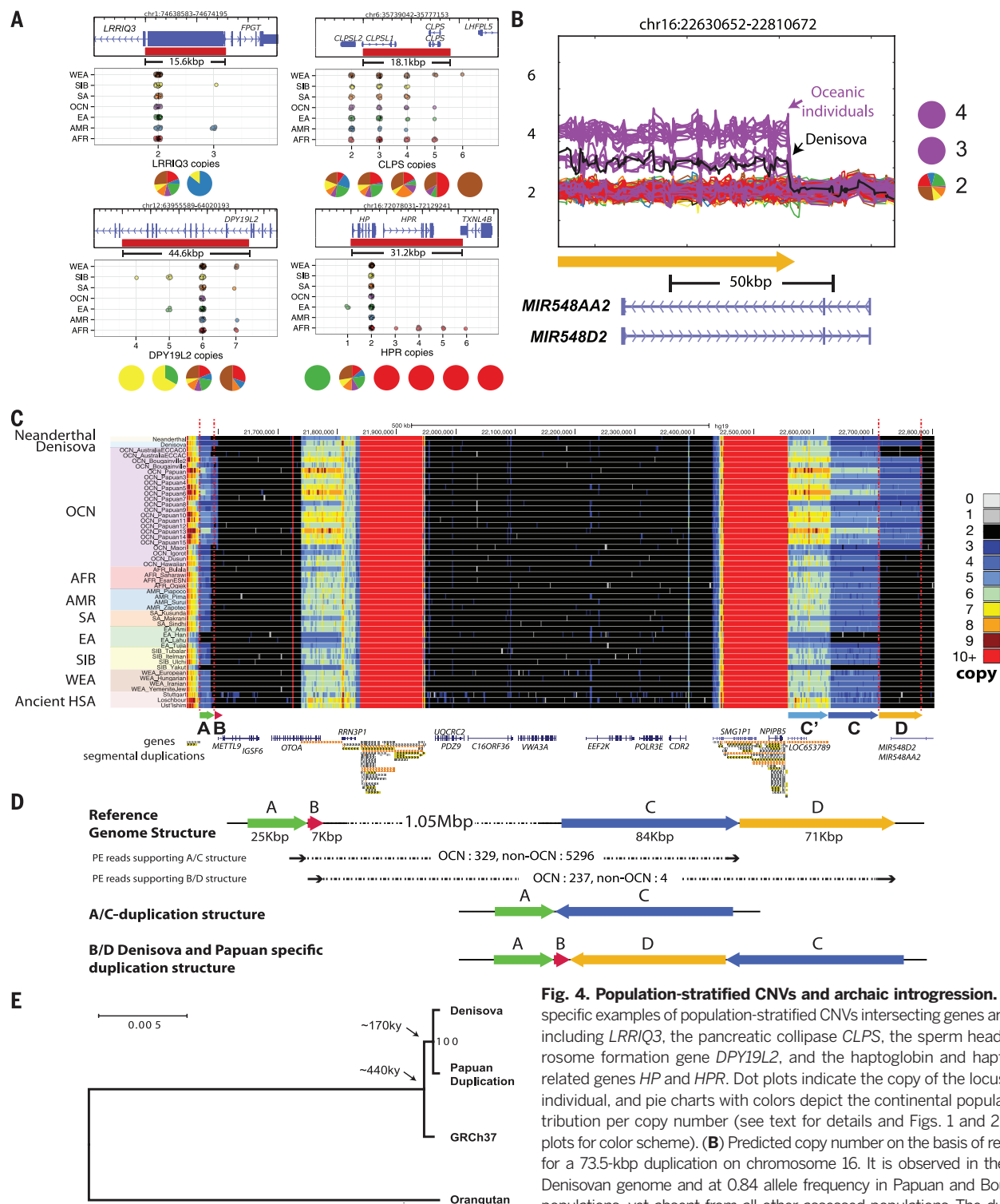
Fig. 4. Population-stratified CNVs and archaic introgression. (**A**) Four specific examples of population-stratified CNVs intersecting genes are shown, including *LRRIQ3*, the pancreatic collapase *CLPS*, the sperm head and acrosome formation gene *DPY19L2*, and the haptoglobin and haptoglobin-related genes *HP* and *HPR*. Dot plots indicate the copy of the locus in each individual, and pie charts with colors depict the continental population distribution per copy number (see text for details and Figs. 1 and 2 and dot plots for color scheme). (**B**) Predicted copy number on the basis of read depth for a 73.5-kbp duplication on chromosome 16. It is observed in the archaic Denisovan genome and at 0.84 allele frequency in Papuan and Bougainville populations, yet absent from all other assessed populations. The duplication intersects two microRNAs. The orange arrow corresponds to the position and orientation of this duplication as further highlighted in (C) and (D). (**C**) A heat map representation of a ~1-Mbp region of chromosome 16p12 (chr16:21518638–22805719). Each row of the heat map represents the estimated copy number in 1-kbp windows of a single individual across this locus. Genes, annotated segmental duplications, arrows highlighting the size and orientation in the reference of the Denisova/Papuan-specific duplication locus (locus D), and three other duplicated loci (A, B, and C) of interest are shown below. (**D**) The structure of duplications A, B, C, and D [as shown in (C) over the same locus] in the reference genome and the discordant paired-end read placements used to characterize two duplication structures. Structure A/C is found in all individuals, although not present in the reference genome, whereas structure B/D is only found in Papuan and Bougainville individuals, indicating a large (~225 kbp), complex duplication composed of different segmental duplications. Both the A/C and B/D duplication architectures exhibit inverted orientations compared with the reference. The number of reads in all Oceanic and non-Oceanic individuals supporting each structure are indicated. (**E**) Maximum likelihood tree of the 16p12 duplication locus [duplication D in (B) to (D)] constructed from the locus in orangutan, Denisova, the human reference, and the inferred sequence of the Papuan duplication (*24*). All bootstrap values are 100%.
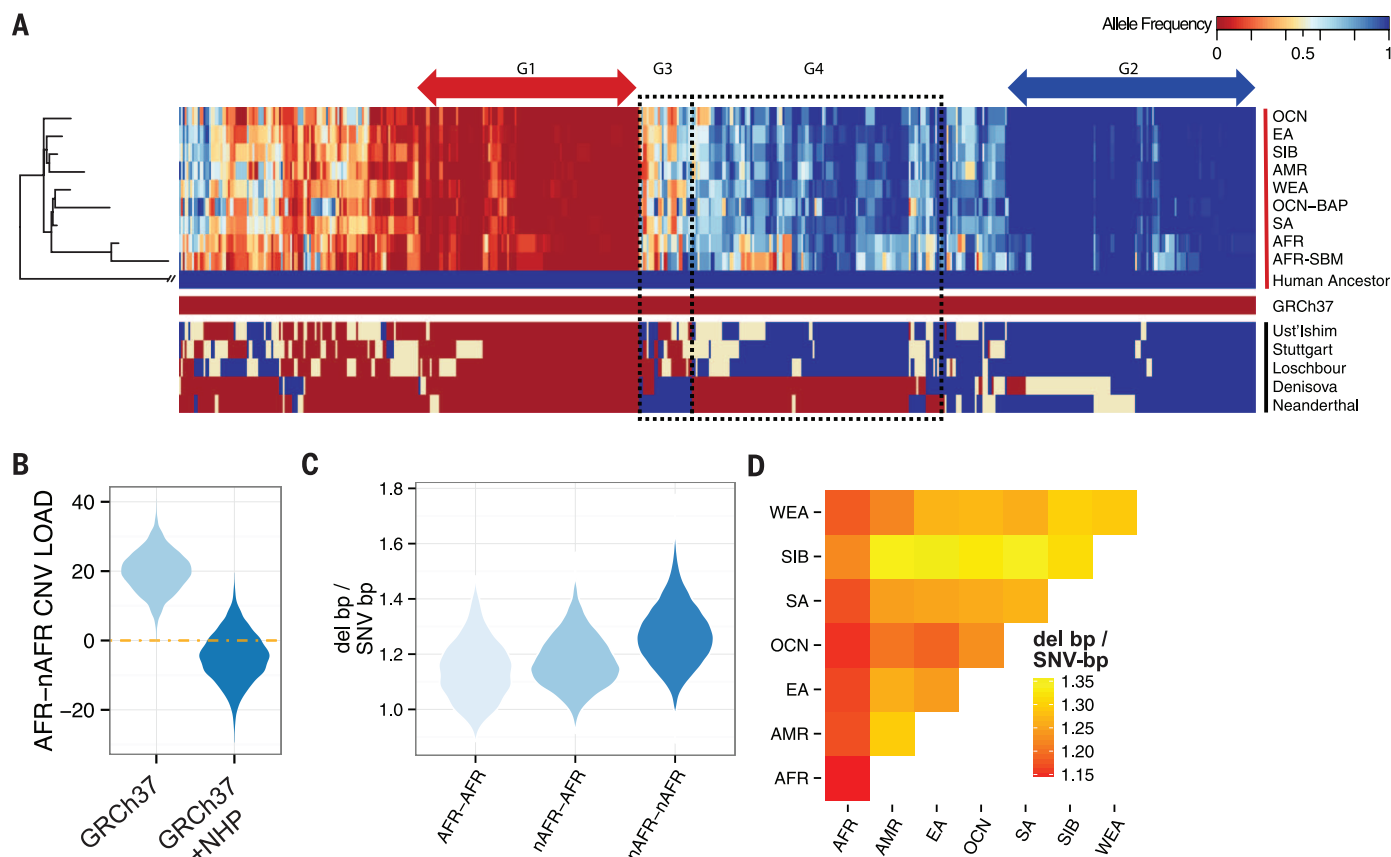
Fig. 5. The ancestral human genome and CNV burden. (**A**) A heat map of the allele frequency of 571 (1.55 Mbp) nonrepetitive sequences absent from the human reference genome yet segregating in at least one population ordered in humans by a maximum likelihood tree (*49*). Four groups of interest are highlighted: G1, ancestral sequences that have almost been completely lost from the human lineage; G2, ancestral sequences that are largely fixed but rarely deleted (also absent in human reference); G3, ancestral sequences that have become copy-number variable since the divergence of humans and Neanderthals/Denisovans ~700 ka; and G4, sequences potentially lost in Neanderthals and Denisovans since their divergence from humans. (**B**) The resulting distributions of 10,000 block-bootstrapped estimates of the difference in load between African (AFR) and non-African (nAFR) populations considering only the reference genome (GRCh37) and supplemented by sequence absent from the human reference genome (GRCh37 + NHP) included (see text for details). (**C**) Violin plots of the distribution of the ratio of deletion base pairs to SNV base pairs differing between every pair of African individuals (AFR-AFR), all pairs of non-African individuals (nAFR-nAFR), and every non-African, African pair (nAFR-AFR). (**D**) Heat map representation of the mean ratio of deletion to SNV base pairs differing between individuals from pairs of populations.

toward lower-frequency events with, again, deletions more rare than duplications (Wilcoxon rank sum test, $P = 1.25 \times 10^{-5}$). Collectively, individuals harbor a mean of 19.2 exon-intersecting deletions per genome (22.8 per diploid genome), with African individuals exhibiting, on average, a mean of 22.4 deletions compared with 18.6 in non-Africans (26.1 and 22.1 per diploid genome, respectively), consistent with the increased diversity of African populations and consistent with data observed for loss-of-function SNVs [(*12*, *39*), ~122 LoF SNVs in Africans versus ~104 in non-Africans].

Whereas non-African individuals exhibited more homozygous deletion variants compared with Africans, among exon-intersecting deletions no such pattern was observed. Exon-intersecting duplications were much more balanced, with African populations showing only a slight excess when compared to non-Africans (98.4 versus 95.2 events per genome). Studies of SNVs have not found consistent evidence of a difference in load between African compared to non-African populations (*40–42*). We compared the difference in load between African and non-African populations for deletions and duplications, respectively. Here, we defined the difference in load as the difference in the sum of derived allele frequencies between African and non-African populations,

$$L(\text{Afr}) - L(\text{nAfr}) = \sum_{\forall i} P_{\text{Afr}}(i) - \sum_{\forall i} P_{\text{nAfr}}(i) \text{ where}$$

$P_{\text{Afr}}(i)$ is the derived allele frequency of a variant i. Prima facie Africans exhibited an apparent higher deletion load than non-African populations (Fig. 5B) ($P = 0.0003$, block bootstrap test), although there was only a nominal difference in the load of exonic deletions ($P = 0.0482$). Duplications showed no such effect.

We reasoned that this difference might potentially be driven by high-frequency–derived alleles, absent from the human reference genome, which was enriched for clone libraries of non-African ancestry (*5*). Approaches that rely on identifying CNVs based on read placements to the reference genome would necessarily miss these CNVs, decreasing the number of variants identified in individuals more closely resembling the reference, i.e., non-Africans. To test this hypothesis, we incorporated the biallelic 571 nonrepetitive human CNV loci described above. Copy numbers were estimated for these sequences in each of the individuals and assessed by remapping raw reads against an ancestral human reference genome. As expected, the deletion allele of this sequence was at a high frequency (mean derived allele frequency, DAF = 0.58). After including these sequences, we observed no difference in the CNV load between Africans and non-Africans (95% confidence interval –18.4 to 8.8 load difference as defined above) (Fig. 5B), underscoring the importance of an unbiased human reference for such population genetic assessments.

Although we found no CNV or SNV load differences between populations, we examined whether the relative proportion of base pairs differing among individuals derived from CNVs versus SNVs showed any population-specific trends. We calculated the number of base pairs varying between all pairs of individuals assessed in our study contributed either from SNVs or from deletions,

calculating the DEL-bp/SNV-bp ratio. As expected, the number of base pairs differing between individuals by deletions or by SNVs independently was always higher among African individuals when compared with other populations. Unexpectedly, the ratio of deletion-bp to SNV-bp was substantially higher within non-African populations (mean of 1.27 compared to 1.14; Fig. 5, C and D). This relative increase in deleted base pairs was most pronounced among non-African populations, which have experienced more recent genetic bottlenecks (e.g., Siberian and Amerindian). Given the absence of a significant difference in the deletion load comparing African and non-African populations, there is no reason to believe that this finding is due to differences in the effectiveness of selection against deletions since the populations separated. However, selection places a downward pressure on the allele frequencies of both deletions and SNVs, with the pressure being stronger for deletions because the selection coefficients are stronger on average. As has been previously shown for SNVs, different allele-frequency spectra for deletions in contrast to SNVs have the potential to interact with the differences in demographic history across populations—even without differences in the effectiveness of selection after population separation—to contribute to observed differences in the apportionment of genetic variation among human populations (*41*).

Discussion

Although the mutational properties and selective signatures of SNVs have been explored extensively, similar analyses of CNVs have lagged behind. As a class, duplications show generally poor correlations with SNV density, have poor linkage disequilibrium to SNVs (*43*, *44*), and are less informative as phylogenetic markers but are more likely to be stratified than deletions among human populations. This observation may be explained by the fact that directly orientated duplications show a gradient of elevated mutation rates resulting from nonallelic homologous recombination and, as such, can change their copy-number state more dynamically over short periods of time. This property also makes this class of variation, similar to highly mutable loci such as minisatellites (*45*), particularly susceptible to homoplasy—that is, identity by state as opposed to identity by descent. Deletions, in contrast, recapitulate most properties of SNVs because they are more likely to exhibit identity by descent as a result of single ancestral mutation event.

We have provided here sequencing data for the study of human diversity and used this resource to explore patterns of human CNV diversity at a fine scale of resolution (>1 kbp). As expected, human genomes differ more with respect to CNVs than SNVs, and almost one-half of these CNV differences map to regions of segmental duplication. Both deletion and duplication analyses consistently distinguish African, Oceanic, and Amerindian human populations. Africans show the greatest deletion and duplication diversity and have the lowest rate of fixed deletions with respect to ancestral human in-

sertion sequences. Oceanic and Amerindian, in contrast, show greater CNV differentiation, likely as a result of longer periods of genetic isolation and founder effects (*46*). Among the Oceanic, the Papuan-Bougainville group stands out in sharing more derived CNV alleles in common with Denisova, including a massive interspersed duplication that rose to high frequency over a short period of time.

We find that duplications and deletions exhibit fundamentally different population-genetic properties. Duplications are subjected to weaker selective constraint and are four times more likely to affect genes than deletions (Table 1), indicating that they provide a larger target for adaptive selection. After controlling for reference genome biases, we find no difference in CNV load between human populations when measured on a per-genome basis, which is what matters to disease risk, assuming that CNVs act additively. However, we find that the proportion of human variation that can be ascribed to CNVs rather than to SNVs is greater among non-Africans than among Africans. The biological significance of this difference should be interpreted cautiously and will require association studies to determine its relevance to disease and other phenotypic differences.

REFERENCES AND NOTES

1. S. C. Schuster *et al.*, Complete Khoisan and Bantu genomes from southern Africa. *Nature* **463**, 943–947 (2010). doi: 10.1038/nature08795; pmid: 20164927
2. K. M. Steinberg *et al.*, Structural diversity and African origin of the 17q21.31 inversion polymorphism. *Nat. Genet.* **44**, 872–880 (2012). doi: 10.1038/ng.2335; pmid: 22751100
3. S. Gravel *et al.*, Reconstructing Native American migrations from whole-genome and whole-exome data. *PLOS Genet.* **9**, e1004023 (2013). pmid: 24385924
4. M. Raghavan *et al.*, The genetic prehistory of the New World Arctic. *Science* **345**, 1255832 (2014). doi: 10.1126/science.1255832; pmid: 25170159
5. R. E. Green *et al.*, A draft sequence of the Neandertal genome. *Science* **328**, 710–722 (2010). doi: 10.1126/science.1188021; pmid: 20448178
6. D. Reich *et al.*, Genetic history of an archaic hominin group from Denisova Cave in Siberia. *Nature* **468**, 1053–1060 (2010). doi: 10.1038/nature09710; pmid: 21179161
7. M. Rasmussen *et al.*, Ancient human genome sequence of an extinct Palaeo-Eskimo. *Nature* **463**, 757–762 (2010). pmid: 20148029
8. D. F. Conrad *et al.*, Variation in genome-wide mutation rates within and between human families. *Nat. Genet.* **43**, 712–714 (2011). doi: 10.1038/ng.862; pmid: 21666693
9. C. D. Campbell *et al.*, Estimating the human mutation rate using autozygosity in a founder population. *Nat. Genet.* **44**, 1277–1281 (2012). doi: 10.1038/ng.2418; pmid: 23001126
10. A. Kong *et al.*, Rate of de novo mutations and the importance of father's age to disease risk. *Nature* **488**, 471–475 (2012). doi: 10.1038/nature11396; pmid: 22914163
11. W. Fu *et al.*, Analysis of 6,515 exomes reveals the recent origin of most human protein-coding variants. *Nature* **493**, 216–220 (2013). doi: 10.1038/nature11690; pmid: 23201682
12. J. A. Tennessen *et al.*, Evolution and functional impact of rare coding variation from deep sequencing of human exomes. *Science* **337**, 64–69 (2012). doi: 10.1126/science.1219240; pmid: 22604720
13. P. H. Sudmant *et al.*, Evolution and diversity of copy number variation in the great ape lineage. *Genome Res.* **23**, 1373–1382 (2013). doi: 10.1101/gr.158543.113; pmid: 23825009
14. T. Marques-Bonet *et al.*, A burst of segmental duplications in the genome of the African great ape ancestor. *Nature* **457**, 877–881 (2009). pmid: 19212409
15. R. A. Kumar *et al.*, Recurrent 16p11.2 microdeletions in autism. *Hum. Mol. Genet.* **17**, 628–638 (2008). doi: 10.1093/hmg/ddm376; pmid: 18156158

16. A. J. Sharp *et al.*, A recurrent 15q13.3 microdeletion syndrome associated with mental retardation and seizures. *Nat. Genet.* **40**, 322–328 (2008). pmid: 18278044
17. J. Sebat *et al.*, Large-scale copy number polymorphism in the human genome. *Science* **305**, 525–528 (2004). doi: 10.1126/science.1098918; pmid: 15273396
18. L. A. Weiss *et al.*, Association between microdeletion and microduplication at 16p11.2 and autism. *N. Engl. J. Med.* **358**, 667–675 (2008). doi: 10.1056/NEJMoa075974; pmid: 18184952
19. S. A. McCarroll *et al.*, Common deletion polymorphisms in the human genome. *Nat. Genet.* **38**, 86–92 (2006). doi: 10.1038/ng1696; pmid: 16468122
20. S. A. McCarroll *et al.*, Integrated detection and population-genetic analysis of SNPs and copy number variation. *Nat. Genet.* **40**, 1166–1174 (2008). doi: 10.1038/ng.238; pmid: 18776908
21. D. F. Conrad *et al.*, Origins and functional impact of copy number variation in the human genome. *Nature* **464**, 704–712 (2010). doi: 10.1038/nature08516; pmid: 19812545
22. M. Jakobsson *et al.*, Genotype, haplotype and copy-number variation in worldwide human populations. *Nature* **451**, 998–1003 (2008).pmid: 18288195
23. A. Itsara *et al.*, Population analysis of large copy number variants and hotspots of human genetic disease. *Am. J. Hum. Genet.* **84**, 148–161 (2009). doi: 10.1016/j.ajhg.2008.12.014; pmid: 19166990
24. Materials and methods are available as supplementary materials at *Science* Online.
25. K. Prüfer *et al.*, The complete genome sequence of a Neanderthal from the Altai Mountains. *Nature* **505**, 43–49 (2014). doi: 10.1038/nature12886; pmid: 24352235
26. M. Meyer *et al.*, A high-coverage genome sequence from an archaic Denisovan individual. *Science* **338**, 222–226 (2012). pmid: 22936568
27. R. E. Mills *et al.*, Mapping copy number variation by population-scale genome sequencing. *Nature* **470**, 59–65 (2011). doi: 10.1038/nature09708; pmid: 21293372
28. G. M. Cooper *et al.*, A copy number variation morbidity map of developmental delay. *Nat. Genet.* **43**, 838–846 (2011). doi: 10.1038/ng.909; pmid: 21841781
29. R. Redon *et al.*, Global variation in copy number in the human genome. *Nature* **444**, 444–454 (2006). doi: 10.1038/nature05329; pmid: 17122850
30. J. Zhang, K. Kaasik, M. R. Blackburn, C. C. Lee, Constant darkness is a circadian metabolic signal in mammals. *Nature* **439**, 340–343 (2006). doi: 10.1038/nature04368; pmid: 16421573
31. R. J. Hardwick *et al.*, Haptoglobin (HP) and Haptoglobin-related protein (HPR) copy number variation, natural selection, and trypanosomiasis. *Hum. Genet.* **133**, 69–83 (2014). doi: 10.1007/s00439-013-1352-x; pmid: 24005574
32. L. A. Hindorff *et al.*, Potential etiologic and functional implications of genome-wide association loci for human diseases and traits. *Proc. Natl. Acad. Sci. U.S.A.* **106**, 9362–9367 (2009). doi: 10.1073/pnas.0903103106; pmid: 19474294
33. S. R. Grossman *et al.*, Identifying recent adaptations in large-scale genomic data. *Cell* **152**, 703–713 (2013). doi: 10.1016/j.cell.2013.01.035; pmid: 23415221
34. J. E. Horvath, S. Schwartz, E. E. Eichler, The mosaic structure of human pericentromeric DNA: A strategy for characterizing complex regions of the human genome. *Genome Res.* **10**, 839–852 (2000). doi: 10.1101/gr.10.6.839; pmid: 10854415
35. J. Cheung *et al.*, Genome-wide detection of segmental duplications and potential assembly errors in the human genome sequence. *Genome Biol.* **4**, R25 (2003). doi: 10.1186/gb-2003-4-4-r25; pmid: 12702206
36. N. Krumm *et al.*, Copy number variation detection and genotyping from exome sequence data. *Genome Res.* **22**, 1525–1532 (2012). doi: 10.1101/gr.138115.112; pmid: 22585873
37. M. Fromer *et al.*, Discovery and statistical genotyping of copy-number variation from whole-exome sequencing depth. *Am. J. Hum. Genet.* **91**, 597–607 (2012). doi: 10.1016/j.ajhg.2012.08.005; pmid: 23040492
38. Deciphering Developmental Disorders Study, Large-scale discovery of novel genetic causes of developmental disorders. *Nature* **519**, 223–228 (2015). pmid: 25533962
39. D. G. MacArthur *et al.*, A systematic survey of loss-of-function variants in human protein-coding genes. *Science*

335, 823–828 (2012). doi: 10.1126/science.1215040; pmid: 22344438

40. W. Fu, R. M. Gittelman, M. J. Bamshad, J. M. Akey, Characteristics of neutral and deleterious protein-coding variation among individuals and populations. *Am. J. Hum. Genet.* **95**, 421–436 (2014). doi: 10.1016/j.ajhg.2014.09.006; pmid: 25279984

41. R. Do *et al.*, No evidence that selection has been less effective at removing deleterious mutations in Europeans than in Africans. *Nat. Genet.* **47**, 126–131 (2015). doi: 10.1038/ng.3186; pmid: 25581429

42. Y. B. Simons, M. C. Turchin, J. K. Pritchard, G. Sella, The deleterious mutation load is insensitive to recent population history. *Nat. Genet.* **46**, 220–224 (2014). doi: 10.1038/ng.2896; pmid: 24509481

43. C. D. Campbell *et al.*, Population-genetic properties of differentiated human copy-number polymorphisms. *Am. J. Hum. Genet.* **88**, 317–332 (2011). doi: 10.1016/j.ajhg.2011.02.004; pmid: 21397061

44. D. P. Locke *et al.*, Linkage disequilibrium and heritability of copy-number polymorphisms within duplicated regions of the human genome. *Am. J. Hum. Genet.* **79**, 275–290 (2006). doi: 10.1086/505653; pmid: 16826518

45. A. J. Jeffreys, V. Wilson, S. L. Thein, Hypervariable 'minisatellite' regions in human DNA. *Nature* **314**, 67–73 (1985). doi: 10.1038/314067a0; pmid: 3856104

46. A. T. Duggan *et al.*, Maternal history of Oceania from complete mtDNA genomes: Contrasting ancient diversity with recent homogenization due to the Austronesian expansion. *Am. J. Hum. Genet.* **94**, 721–733 (2014). doi: 10.1016/j.ajhg.2014.03.014; pmid: 24726474

47. J. M. Davis, V. B. Searles Quick, J. M. Sikela, Replicated linear association between DUF1220 copy number and severity of social impairment in autism. *Hum. Genet.* **134**, 569–575 (2015). doi: 10.1007/s00439-015-1537-6; pmid: 25758905

48. I. Koscinski *et al.*, DPY19L2 deletion as a major cause of globozoospermia. *Am. J. Hum. Genet.* **88**, 344–350 (2011). pmid: 21397063

49. D. Refojo *et al.*, Glutamatergic and dopaminergic neurons mediate anxiogenic and anxiolytic effects of CRHR1. *Science* **333**, 1903–1907 (2011). pmid: 21885734

50. S. A. McCarroll *et al.*, Deletion polymorphism upstream of IRGM associated with altered IRGM expression and Crohn's disease. *Nat. Genet.* **40**, 1107–1112 (2008). doi: 10.1038/ng.215; pmid: 19165925

51. S. R. Radoshitzky *et al.*, Transferrin receptor 1 is a cellular receptor for New World haemorrhagic fever arenaviruses. *Nature* **446**, 92–96 (2007). doi: 10.1038/nature05539; pmid: 17287727

RESEARCH ARTICLES

STRUCTURAL BIOLOGY

Structure of a yeast spliceosome at 3.6-angstrom resolution

Chuangye Yan,[1]* Jing Hang,[1]* Ruixue Wan,[1]* Min Huang,[2]
Catherine C. L. Wong,[2] Yigong Shi[1]†

Splicing of precursor messenger RNA (pre-mRNA) in yeast is executed by the spliceosome, which consists of five small nuclear ribonucleoproteins (snRNPs), NTC (nineteen complex), NTC-related proteins (NTR), and a number of associated enzymes and cofactors. Here, we report the three-dimensional structure of a *Schizosaccharomyces pombe* spliceosome at 3.6-angstrom resolution, revealed by means of single-particle cryogenic electron microscopy. This spliceosome contains U2 and U5 snRNPs, NTC, NTR, U6 small nuclear RNA, and an RNA intron lariat. The atomic model includes 10,574 amino acids from 37 proteins and four RNA molecules, with a combined molecular mass of approximately 1.3 megadaltons. Spp42 (Prp8 in *Saccharomyces cerevisiae*), the key protein component of the U5 snRNP, forms a central scaffold and anchors the catalytic center. Both the morphology and the placement of protein components appear to have evolved to facilitate the dynamic process of pre-mRNA splicing. Our near-atomic-resolution structure of a central spliceosome provides a molecular framework for mechanistic understanding of pre-mRNA splicing.

P recursor messenger RNA (pre-mRNA) splicing, which involves the removal of the noncoding introns and the ligation of neighboring exons, is a defining feature for all eukaryotes (*1*). Aberrant splicing contributes to numerous debilitating diseases (*2*). The yeast spliceosome is a multi-megadalton ribonucleoprotein (RNP) complex and consists of U1, U2, U4, U5, and U6 small nuclear RNPs (snRNPs), NTC (nineteen complex; known as the Prp19-CDC5L complex in mammals), NTC-related proteins (NTR), and numerous other enzymes and cofactors (*3*, *4*). The spliceosome exhibits exceptional compositional dynamics and conformational flexibility, which is consistent with its function of splicing introns with diverse sequences (*5–7*).

At the beginning of a splicing reaction cycle, the 5′-splice site (5′SS) of an intron is recognized by U1 snRNP, and the branch point sequence (BPS) and 3′SS are bound by U2 snRNP, forming the spliceosomal A complex. Recruitment of the U4/U6.U5 tri-snRNP leads to assembly of the pre-catalytic B complex. RNP rearrangement causes displacement of U1 and U4 snRNPs and recruitment of NTC and NTR, generating the activated B complex (B^act). The B^act spliceosome is converted into the catalytically competent B* complex,

which catalyzes the first step of trans-esterification. The end product is the C complex, also known as the catalytic step I spliceosome, which contains the cleaved 5′-exon and an intron lariat-3′-exon intermediate (hereafter, intron lariat). The second step of trans-esterification results in the ligation of two exons, forming the post-catalytic P complex. Subsequently, the ligated exon is released, but the intron lariat remains associated with the intron-lariat spliceosomal (ILS) complex. Last, the intron lariat is dissociated, and the snRNPs, NTC, and NTR are recycled. The RNP rearrangements are driven by eight evolutionarily conserved DExD/H-type, RNA-dependent adenosine triphosphatases (ATPases)/helicases (*8*, *9*).

Biochemical studies during the past few decades have provided valuable insights into the mechanism of pre-mRNA splicing by the spliceosome. Analysis of thioester substitutions in pre-mRNA identified the spliceosome as a metalloenzyme (*10–12*), with the intramolecular stem loop of U6 small nuclear RNA (snRNA) coordinating the catalytic magnesium ions (*13*, *14*). The spliceosomal active site is centered around loop I of U5 snRNA, the U2/U6 duplex, and a catalytic cavity in Prp8 (*15*). Structural investigations of the spliceosomal components—exemplified by the crystal structures of Prp8 (*16*), Brr2 (*17*, *18*), and the Sm and like-Sm (Lsm) rings (*19–23*)—have also improved our understanding of pre-mRNA splicing.

Elucidating the molecular mechanisms of the spliceosome and the splicing reaction requires detailed structural information on the intact spliceosome at different stages of its action. The large size of the spliceosome and its extraordi-

nary conformational and compositional diversity have made this task a challenge for structural biologists (*24*). These features contrast with the other central RNP complex, the ribosome, which contains two relatively stable subunits that are more amenable to structural investigation (*25–27*). RNA accounts for more than 50% of the total molecular mass in the bacterial or mammalian ribosome, but less than 10% in the spliceosome. The constant flux of protein factors during each cycle of the splicing reaction has prevented crystallization of the spliceosome.

In the past decade, electron microscopy (EM) has been used to visualize various spliceosomal complexes, yielding a series of structures at resolutions ranging from 20 to 50 Å (*28–44*). Most recently, the cryogenic EM (cryo-EM) structure of the spliceosomal U4/U6.U5 tri-snRNP from *Saccharomyces cerevisiae* was determined at 5.9 Å resolution (*45*). Here, we report the cryo-EM structure of a yeast spliceosome at 3.6 Å resolution. We describe the overall structure of the spliceosome and its protein components in this Research Article and discuss the structural insights into snRNA recognition and pre-mRNA catalysis in (*46*).

Spliceosome isolation and characterization

We sought to purify the spliceosomal C complex because of its central role of bridging the two steps of a splicing reaction and catalyzing the second step. We modified a published purification protocol for the C complex (*36*, *47*) and obtained approximately 500 μg of spliceosome from 4 liters of *Schizosaccharomyces pombe* culture (fig. S1A and supplementary materials, materials and methods). The purified yeast spliceosome exhibited excellent solution behavior, as judged with gel filtration analysis (fig. S1B). The spliceosome contains three major RNA species—whose lengths are consistent with those of U2, U5, and U6 snRNAs from *S. pombe*—and a diverse array of RNA molecules with varying lengths, which probably includes the intron lariat (fig. S1C). In addition, the spliceosome contains a large number of protein components (fig. S1D).

To examine the identity of the spliceosome and to facilitate future structure assignment, we analyzed the sample using mass spectroscopy (MS). This approach detected ~80 spliceosomal proteins, with ~50 of these in high abundance (figs. S1E and S2). Most of these abundant spliceosomal proteins were components of U2 snRNP, U5 snRNP, NTC, and NTR (fig. S1E). These proteins are shared among the spliceosomal B^act, B*, C, P, and ILS complexes. To differentiate among these complexes, we performed reverse transcription polymerase chain reactions (RT-PCR) on the *cut6* gene using the purified spliceosome (fig. S3). The intron lariat was present in the spliceosome, suggesting completion of the first-step reaction. However, the unspliced *cut6* gene and the ligated exon were also detected, suggesting the presence of the B^act and/or B* and P complexes, respectively (fig. S3). We conclude that the purified spliceosome contains a mixture of the different complexes. Last, after

[1]Ministry of Education Key Laboratory of Protein Science, Tsinghua-Peking Joint Center for Life Sciences, Center for Structural Biology, School of Life Sciences, Tsinghua University, Beijing 100084, China. [2]National Center for Protein Science Shanghai, Institute of Biochemistry and Cell Biology, Shanghai Institutes of Biological Sciences, Chinese Academy of Sciences, Shanghai 200031, China.
*These authors contributed equally to this work. †Corresponding author. E-mail: shi-lab@tsinghua.edu.cn

chemical crosslinking, we uncovered by means of MS analysis 78 intermolecular interactions among the spliceosomal proteins (fig. S4), which proved important for structure assignment.

Structure determination

We first generated a low-resolution reconstruction of the yeast spliceosome by using negative staining (fig. S5). Then, we imaged the sample under cryogenic conditions with a K2 direct electron detector, mounted on a Titan Krios microscope operating at 300 kV. A total of 2246 micrographs were collected (Fig. 1A and table S1), and we subjected 224,450 particles, picked semi-automatically, to particle sorting and reference-free two-dimensional (2D) classification (Fig. 1B and figs. S6 and S7A). We performed 3D classification for 133,901 particles. The vast majority (112,795) of these particles produced a density map at an overall resolution of 3.9 Å, which was further improved by means of particle polishing to 3.6 Å on the basis of the gold-standard Fourier Shell Correlation (FSC) criteria (Fig. 1C). The actual resolution within the spliceosome ranged from 2.9 to 3.6 Å in the core region to 7 to 8 Å in the periphery (Figs. 1D, 2, and 3A). The quality and resolution of EM density for different regions of the spliceosome were improved by applying individual local masks (figs. S7B, S8, and S9).

Throughout the spliceosome, most secondary structural elements were clearly visible, and a large proportion of the amino acid side chains were well defined (figs. S10 to S17).

The spliceosome has an extended and asymmetric morphology, with the longest dimension exceeding 300 Å (Fig. 2). The bulk of the well-defined density can be attributed to a triangular Central Body (Figs. 1D and 2), which is connected to a Head group and two Arms (named I and II). The Head and Arm II in our structure appear to correspond to the "head-like" and "ridge" domains in the 29 Å cryo-EM structure of the *S. pombe* U5.U2/U6 complex (*36*). An elongated tubular EM density in Arm II, connected to a donut-shaped density, is visible at 20 Å resolution (Fig. 2A); at higher resolutions, this density can be assigned as a tetrameric assembly of Cwf8/Prp19, Cdc5 C-terminal fragment, and Cwf7. At 10 and 5 Å resolutions (Fig. 2, B and C), these structural features become more prominent, allowing identification of most secondary structural elements.

Identification of protein and RNA components

We combined de novo atomic model building and homologous structure modeling to generate an atomic model for the entire *S. pombe*

spliceosome (Fig. 3 and table S2). On the basis of the EM density, we identified the heptameric Sm ring and the WD40-repeat proteins Cwf1/Prp5, Cwf8/Prp19, and Cwf17 (fig. S18). The large proteins Spp42 (Prp8 in *S. cerevisiae*), Cwf10 (Snu114 in *S. cerevisiae*), and Cwf11, each with an available homologous structure (*16, 48, 49*), were docked into the EM density. Model building of Spp42 allowed assignment of U5 snRNA, which is mostly bound by the N-terminal 800 amino acids of Spp42. These procedures were followed by identification of the tetrameric assembly of Cwf8/Prp19, which resides in Arm II of the spliceosome; the superhelical proteins Cwf3/Syf1 and Cwf4/Syf3, which connect the Central Body to the Head and Arm I; and several other proteins, including Cdc5, Cwf2/Prp3, Cwf14, Prp45, Cwf19, Cwf5/Ecm2, and Prp17 (fig. S18). The EM density for Arm I is weak. A local mask refinement after two rounds of 3D classification generated an improved map and enabled subsequent identification of Lea1, Msl1, a portion of U2 snRNA, and the Sm ring for U2 snRNA (fig. S18). In addition to EM density, assignment of the U2 and U6 snRNAs was facilitated by the location of known interacting proteins, predicted secondary structures, and published base-pairing specifics (table S2). After identification of U2 and U6 snRNAs, the RNA lariat was located, and the BPS and 5′SS were tentatively assigned. Last, on the basis of EM density and MS identification of crosslinked proteins (fig. S4), we assigned Cwf7, Cwf15, and Cyp1.

Overall structure

The final refined atomic model of the yeast spliceosome contains 10,574 amino acids from 37 proteins, three snRNA molecules, and an intron lariat (Fig. 3B and tables S1 and S2), with a combined molecular mass of ~1.3 MD. Among the modeled amino acids, 9312 were assigned specific side chains, and the remaining 1262 residues were built into a poly(Ala) model. U2, U5, and U6 snRNAs contain a total of 405 nucleotides, of which 314 were tentatively assigned in our atomic model. We also modeled 18 nucleotides from the intron lariat. Some areas of very weak EM density, probably reflecting dynamic components of the spliceosome, remain unassigned. The protein components in the atomic model include all 10 core proteins of U5 snRNP (except Brr2), all nine core proteins of U2 snRNP, eight of the nine core proteins of NTC, and five of the eight core proteins of NTR. Nearly complete atomic models are now available for Spp42 (residues 47 to 2030), which, as a central component of the U5 snRNP, anchors the catalytic center of the spliceosome, and for Cwf10 (residues 68 to 971), which, as the only guanosine triphosphatase (GTPase) among the spliceosomal components, regulates the splicing reaction (*50*).

The U2 snRNP—comprising Lea1, Msl1, the heptameric Sm ring, and U2 snRNA—constitutes Arm I of the spliceosome. Arm I is linked to the Central Body through two associations: one with the superhelical proteins Cwf3/Syf1 and Cwf4/Syf3 and another through U2 snRNA, which
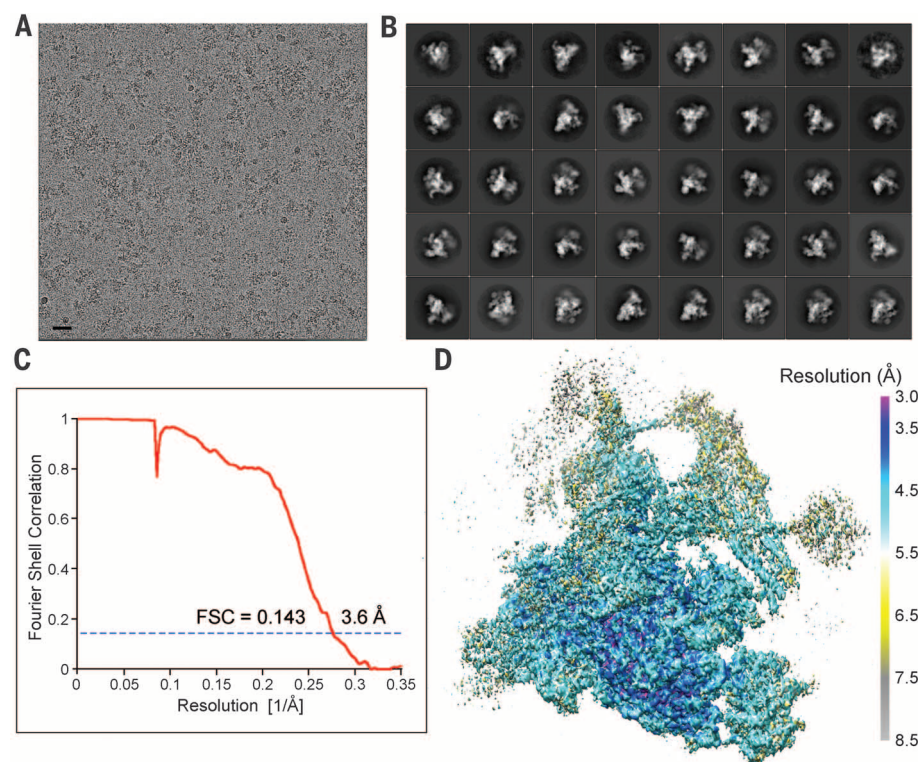
Fig. 1. Cryo-EM analysis of a yeast spliceosome. (**A**) A representative cryo-EM micrograph of the yeast spliceosomal complex. An entire micrograph is shown. Scale bar, 30 nm. (**B**) Representative 2D class averages of the yeast spliceosome. (**C**) The overall resolution is estimated to be 3.6 Å on the basis of the gold-standard FSC criteria of 0.143. (**D**) An overall view of the EM density for the yeast spliceosome. The resolution varies among different regions of the yeast spliceosome, as indicated by the different colors. The surface view of the spliceosome is shown here. The resolution reaches 2.9 to 3.2 Å in the center of the spliceosome.

enters the catalytic center (Fig. 3B). Arm II of the spliceosome consists of an elongated tetrameric assembly of Cwf8/Prp19 that is wrapped by Cwf7 and Cdc5 in their extended conformations (Fig. 3B). Cdc5, in turn, directly contacts Cwf3/Syf1, Cwf4/Syf3, the NTC component Cwf7, and the U5 snRNP protein Cwf17. The Head region comprises mainly Cwf11 and is connected to the triangular Central Body through the superhelical proteins Cwf3/Syf1 and Cwf4/Syf3. The base of the Central Body is mainly composed of U5 snRNP (Fig. 3B). All other proteins are located at the center of the Central Body, making direct or indirect contacts with the RNA molecules at the catalytic center.

The catalytic center, identified by the U2/U6 snRNA triplex, is located at the heart of the Central Body (Fig. 3B). The catalytic center is more than 100 Å away from the Head region, either Arm, and the corner of the Central Body (as defined by the 3′ end of U5 snRNA). The distance between the tip of the Head region and the far corner of the Central Body measures ~335 Å, whereas the two Arms are separated by a distance of up to 320 Å (Fig. 3B). The Head and two Arms of the spliceosome are linked to the Central Body through limited contacts, which may engender conformational flexibility. Both the large size and the extended organization of the spliceosome are likely to be functionally important for proper

splicing of pre-mRNAs with varying lengths and sequences.

Structure of Spp42

At 270 kD, Spp42 is the largest and most conserved component of all spliceosomal proteins (*51*), displaying 63 and 73% sequence identity with its functional ortholog Prp8 in *S. cerevisiae* and humans, respectively. As a major component of U5 snRNP, Spp42 serves as a central scaffold for pre-mRNA splicing. Except for the N-terminal 46 amino acids and the C-terminal Jab1/MPN domain, most of the Spp42 sequences have a well-defined EM density (fig. S10, A to H, and fig. S11A). The structure of Spp42
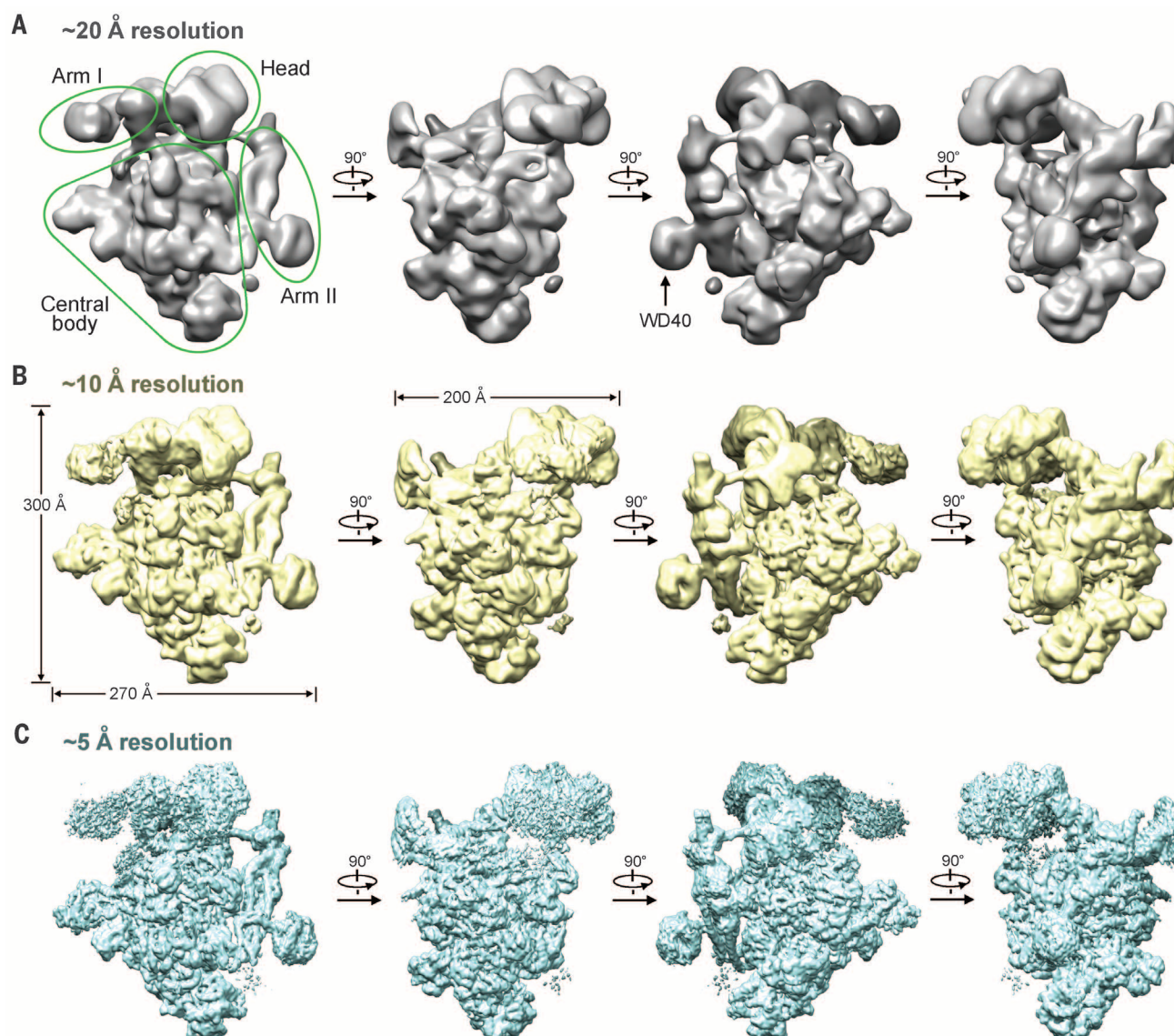

Fig. 2. Structural features of a yeast spliceosome at different resolution limits. (**A**) The EM density map of the yeast spliceosome at an averaged resolution of 20 Å. The spliceosome contains a triangular Central Body, a Head, and two Arms (I and II). The four perpendicular views illustrate the overall structural features. The same four views are shown in (B) and (C) for comparison. (**B**) The EM density map of the yeast spliceosome at an averaged resolution of 10 Å. The improved resolution of the structural features allows docking of homologous structures and assignment of many protein components. (**C**) The EM density map of the yeast spliceosome at an averaged resolution of 5 Å. Most secondary structural elements of the protein components can be assigned at this resolution. Connectivity between the adjacent secondary structural elements is mostly clear.

includes the following domains: N-terminal (residues 47 to 825), reverse transcriptase (RT) Palm/Finger (residues 826 to 1210), Thumb/X (residues 1211 to 1327), Linker (residues 1328 to 1602), endonuclease-like (residues 1603 to 1783), and ribonuclease (RNase) H–like (residues 1784 to 2030) (Fig. 4A).

Spp42 looks like a thick triangular plate, with the three sides measuring 175, 150, and 125 Å and a thickness of ~80 Å (Fig. 4A). The N-terminal domain of Spp42, the structure of which has not previously been described, binds the GTPase Cwf10 and recognizes the bulk of U5 snRNA (52, 53). In the structure, the N-terminal domain adopts an extended conformation, with three protruding structural elements reaching out to contact Cwf10, Cwf17, and the RT Palm/Finger domain of Spp42 (Fig. 4B). Spp42 can be superimposed onto Prp8 (16) with a root mean square deviation (RMSD) of 1.46 Å over 859 aligned Cα atoms in the RT Palm/Finger, Thumb/X, Linker, and endonuclease-like domains (Fig. 4, C and D). These four contiguous domains constitute a conserved structural scaffold between Spp42 and Prp8.

The reported Prp8 structure contains a C-terminal Jab1/MPN domain (Fig. 4C) (16). Placement of the Jab1/MPN domain depends on the U5 snRNP assembly factor Aar2, which contributes a pairing β strand between the RNase H–like and Jab1/MPN domains (16). Superposition of Spp42 and Prp8 revealed marked differences between the RNase H–like domains (Fig. 4D). Compared with Prp8, the RNase H–like domain in Spp42 undergoes a rotation of ~25° away from the RT Palm/Finger domain, resulting in a translation of up to 28 Å for its protruding β hairpin (Fig. 4E). The space vacated by the RNase H–like domain is in turn occupied by Cwf19, which interacts closely with both the RNase H–like and the RT Palm/Finger domains (Fig. 4A). The Jab1/MPN domain, responsible for binding the ATPase/helicase Brr2 (17, 18), is flexible and disordered in our structure. Consequently, despite its presence in the spliceosome (fig. S1E), Brr2 has no visible EM density, probably reflecting its highly dynamic
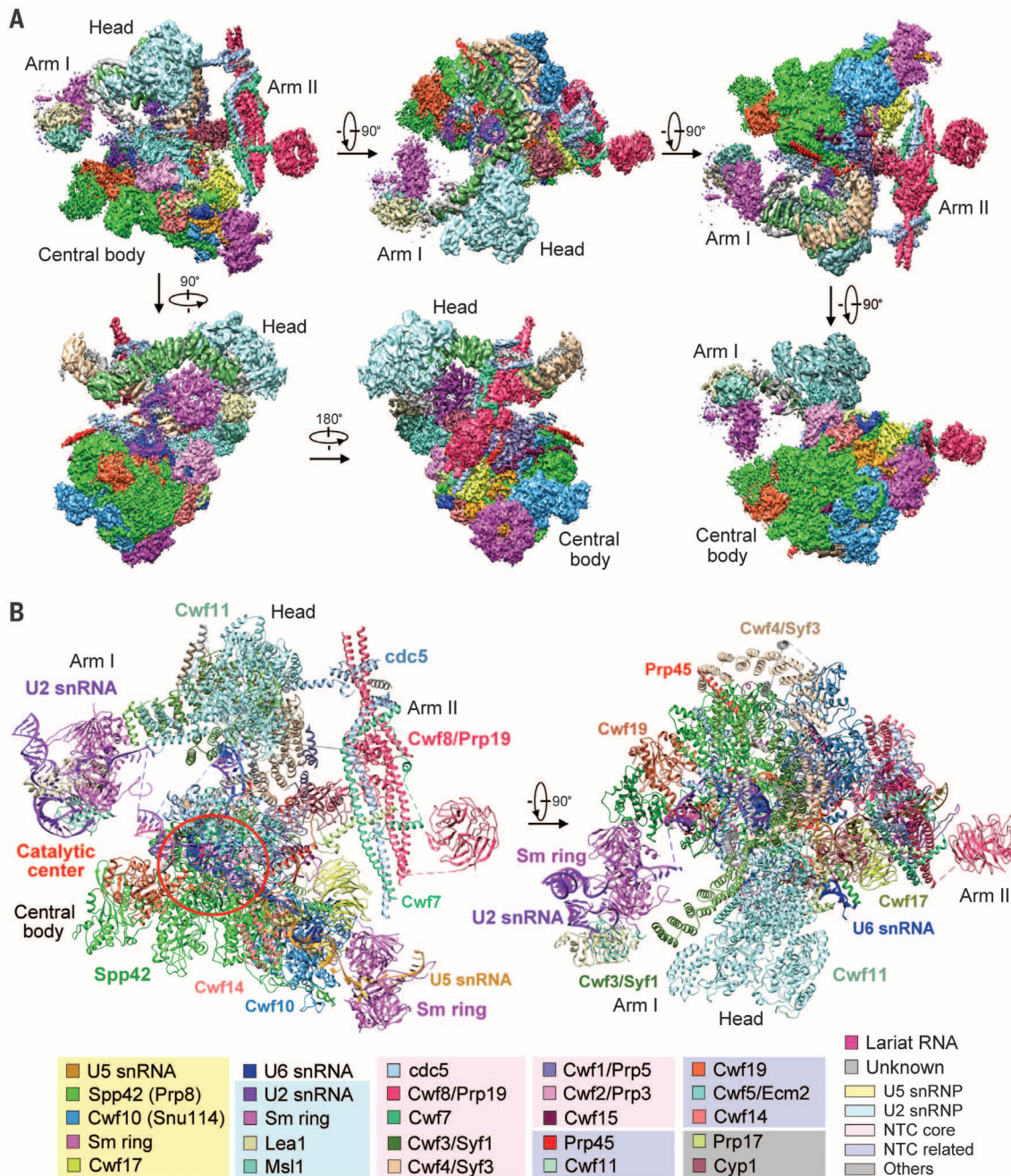

Fig. 3. Structure of a yeast spliceosome at 3.6 Å resolution. (**A**) The EM density map of the yeast spliceosome at an overall resolution of 3.6 Å. Four perpendicular views around the *x* axis and two additional views around the *y* axis show the color-coded protein and RNA components. (**B**) A representative illustration of the yeast spliceosome from two perpendicular views. The protein and RNA components are color-coded. This structure includes 37 proteins, three snRNAs, and one RNA lariat, with a combined molecular weight of ~1.3 MD. Among the modeled 10,574 amino acids, 9312 have been assigned side chains. All 332 RNA nucleotides were tentatively assigned.

state. This structural arrangement would place Brr2 in close proximity to the catalytic center and allow ample conformational freedom for Brr2 to apply its ATP-dependent RNP remodeling activity in both steps of the splicing reaction.
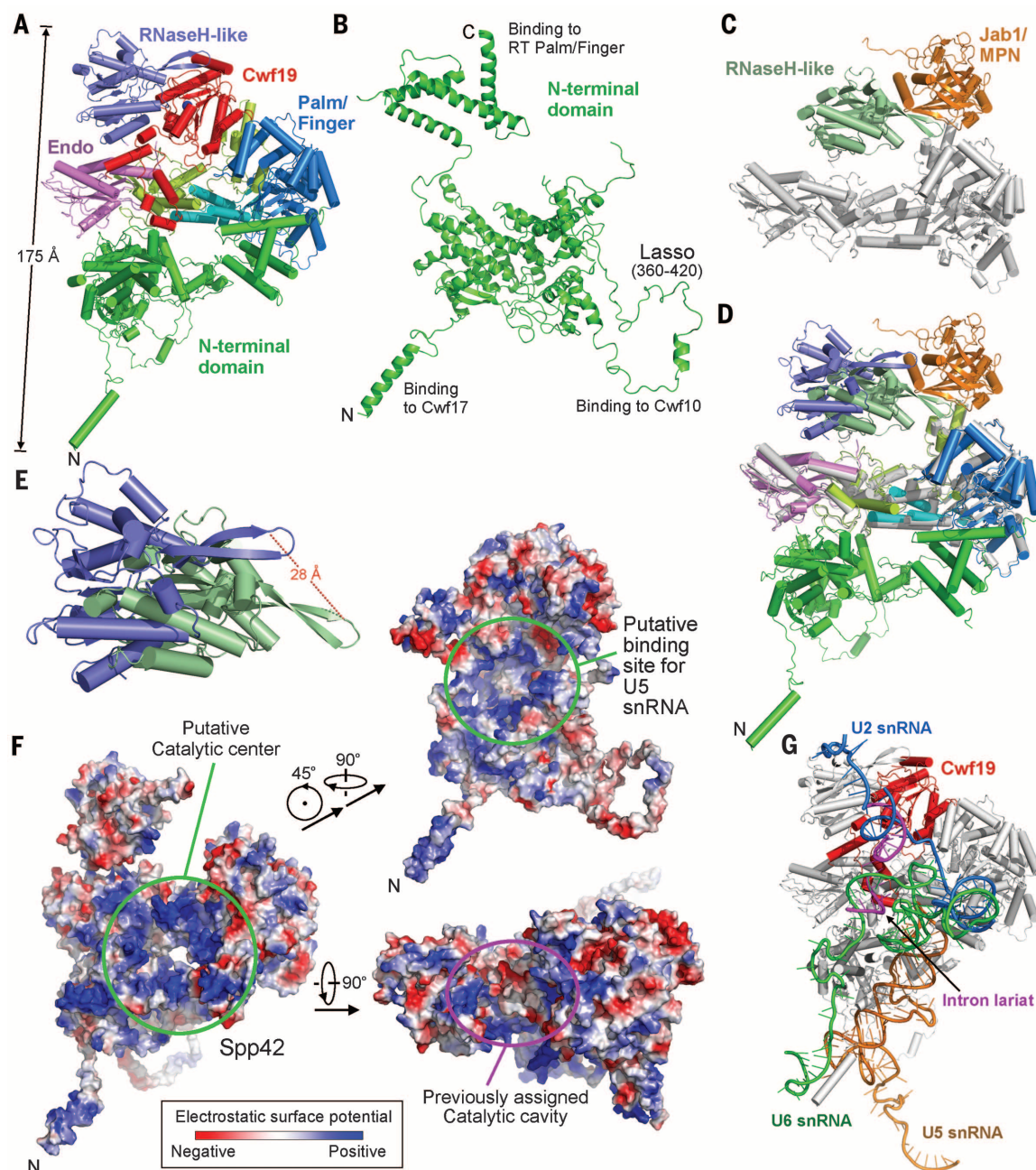
Catalytic cavity of the spliceosome

Spp42 plays a key role in pre-mRNA splicing. Splicing defects as a result of splice-site mutation can be suppressed by rescuing mutations in Prp8 (*54–56*). Based on examination of these mutation-targeted residues, the presence of a catalytic cavity on Prp8, formed mainly by the Linker and RNase H–like domains, has been proposed (*16*). Analysis of the electrostatic surface potential of Spp42 revealed a striking cavity that is highly enriched by positively charged amino acids (Fig. 4F) but differs from the proposed catalytic cavity

(*16*). Instead, this cavity is formed between the N-terminal domain and the Thumb/X–Linker region of Spp42 and hence can only be recognized in the full-length Spp42 protein. The RNA triplex of U2 and U6 snRNAs and the intron lariat are located in this cavity (Fig. 4G), making close contact with the positively charged amino acids. The positively charged residues in this catalytic cavity are invariant among *S. pombe*, *S. cerevisiae*, and

Fig. 4. Structure of the central protein component Spp42 (Prp8 in *S. cerevisiae*). (**A**) The overall structure of Spp42. The structure contains the following domains: N-terminal (green, residues 47 to 825), RT Palm/Finger (blue, residues 826 to 1210), Thumb/X (cyan, residues 1211 to 1327), Linker (pale green, residues 1328 to 1602), endonuclease-like (pink, residues 1603 to 1783), and RNase H–like (purple, residues 1784 to 2030). The Jab1/MPN domain (residues 2044 to 2363) is disordered, and its approximate position is occupied by Cwf19 (red). (**B**) The structure of the N-terminal domain of Spp42. The N-terminal helix is responsible for binding to Cwf17, and the lasso on the right corner interacts with Cwf10. (**C**) The structure of Prp8 (residues 885 to 2413) from *S. cerevisiae* (*16*). The RNase H–like and Jab1/MPN domains are colored light green and gold, respectively. (**D**) Structural comparison between Spp42 and Prp8. The structures from the Palm/Finger domain to the endonuclease-like domain are very similar. However, the RNase H–like domain exhibits a major conformational shift. (**E**) A close-up view of the RNase H–like domains of Spp42 and Prp8. The RNase H–like domain of Spp42 can be aligned to its counterpart in Prp8 by a translation of ~20 Å and a clockwise rotation of 25° around an axis perpendicular to the page. (**F**) Analysis of the electrostatic surface potential of Spp42 reveals a putative catalytic center. A central hole at the interface between the N-terminal domain and the Thumb/X and Linker domains is enriched by positively charged amino acids and probably represents the catalytic center (left). In contrast, the previously identified catalytic cavity lacks such positive potential (bottom right). Another region enriched by positive electrostatic potential (top right) represents the binding site for U5 snRNA. (**G**) U2 snRNA, U6 snRNA, and the intron lariat are bound at the catalytic center of Spp42.
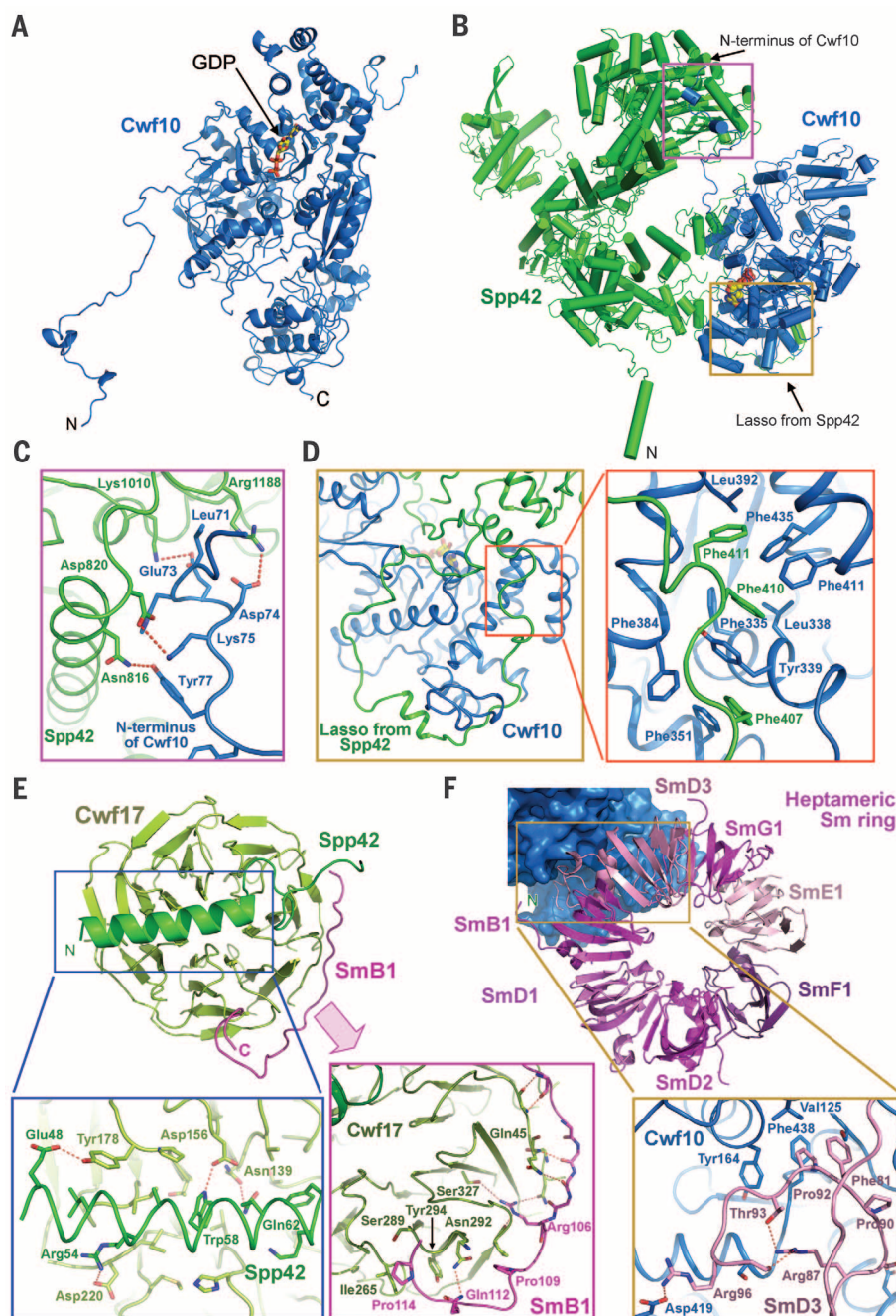
Fig. 5. Protein components in U5 snRNP. (**A**) Structure of the EF-2–family GTPase Cwf10. The bound GDP molecule is shown in stick representation. The extended N terminus binds Spp42. (**B**) An overall view of the interactions between Cwf10 and Spp42. The N-terminal sequences of Cwf10 recognize the Palm/Finger domain of Spp42, whereas the N-terminal domain of Spp42 forms a lasso over the back side of the nucleotide-binding domain of Cwf10. (**C**) A close-up view of the interface between the N-terminal sequences of Cwf10 and a shallow surface groove on the Palm/Finger domain of Spp42. (**D**) A close-up view of the Spp42 lasso over the N-terminal domain of Cwf10. In particular, three phenylalanine residues from Spp42 make a number of van der Waals contacts to hydrophobic amino acids on the surface of Cwf10. (**E**) Cwf17 and its interactions with Spp42 and SmB1. The N-terminal α-helix from Spp42 binds the bottom face of the Cwf17 WD40 propeller, whereas the C-terminal sequences of SmB1 interact with the outer surface of the propeller. Detailed interactions are shown in the two insets. (**F**) Structure of the heptameric Sm ring. The Sm ring directly interacts with the N-terminal domain of Cwf10 (blue in the background). Detailed interactions are shown in the inset. The Sm ring recognizes a stretch of U-rich RNA sequences at the 3′ end of U5 snRNA.

humans (fig. S19A), allowing modeling of a similar catalytic cavity in Prp8 (fig. S19B).

Other protein components in U5 snRNP

A major component of the U5 snRNP, Cwf10 (Snu114 in *S. cerevisiae* and U5-116K in humans), is a translation elongation factor 2 (EF-2)–like GTPase that regulates the RNP remodeling activity of Brr2 (*57*). The excellent EM density for Cwf10 allows atomic modeling of nearly the entire length of the protein and of a bound guanosine diphosphate (GDP) molecule (Fig. 5A and fig. S11, B and C). Cwf10 closely interacts with Spp42 through two discrete, reciprocal interfaces (Fig. 5B). Residues from the extended N-terminal sequences of Cwf10 bind to a surface groove on Spp42, making specific interactions with amino acids in the groove (Fig. 5C). In addition, an extended loop in the N-terminal domain of Spp42 forms a lasso over the nucleotide-binding domain of Cwf10 (Fig. 5D). In particular, three phenylalanine residues from the lasso (Phe[407], Phe[410], and Phe[411]) are nestled in a greasy surface pocket formed by hydrophobic amino acids in Cwf10 (Fig. 5D).

Cwf17/Spf38 (U5-40K in humans) is a WD40-repeat protein that is a core component of U5 snRNP. The functional ortholog of Cwf17/Spf38 in *S. cerevisiae* is yet to be identified. In the structure, an N-terminal α-helix of Spp42 associates with the bottom face of the WD40 repeats through specific hydrogen bonds and van der Waals contacts (Fig. 5E). The last core component of the U5 snRNP is the heptameric Sm ring, which orients the 3′ end sequences of U5 snRNA and specifically interacts with the N-terminal domain of Cwf10 (Fig. 5F). The extended C-terminal sequences of SmB1 reach out to contact the outer surface of the Cwf17 β propeller, forming a number of hydrogen bonds (Fig. 5E).

Protein components in NTC and NTR

A shared feature of the spliceosomal proteins is their extended architecture. This is best illustrated by the tetrameric assembly of Cwf8/Prp19, which measures up to 175 Å in length (Fig. 6A). Two molecules of Cwf8/Prp19 form an intertwined dimer through their elongated coiled-coil region, with the two U-boxes distant from each other. Two such Cwf8/Prp19 dimers use their respective U-boxes to further associate with each other (Fig. 6A). This structural arrangement may allow considerable conformational flexibility and markedly increase surface areas for potential interactions with other spliceosomal factors.

The extended architecture is also exemplified by Cwf3/Syf1 and Cwf4/Syf3. Both of these are superhelical proteins, containing 19 and 16 half-a-tetratricopeptide (HAT) repeats (*58*), respectively, and exhibiting a twisted C-shaped morphology (Fig. 6, B and C). The maximal intramolecular distance for these proteins exceeds 150 Å. The middle portion of the convex side of Cwf3/Syf1 associates with the central region of the concave surface of Cwf4/Syf3 (Fig. 6D). HAT-repeat proteins exhibit conformational plasticity (*58*); the presence of Cwf3/Syf1 and Cwf4/Syf3 in the

spliceosome probably ensures adequate conformational freedom for the splicing reactions and exchange of cofactors. Cwf8/Prp19, Cwf3/Syf1, and Cwf4/Syf3 are all core components of NTC,

supporting an important regulatory role for this complex.

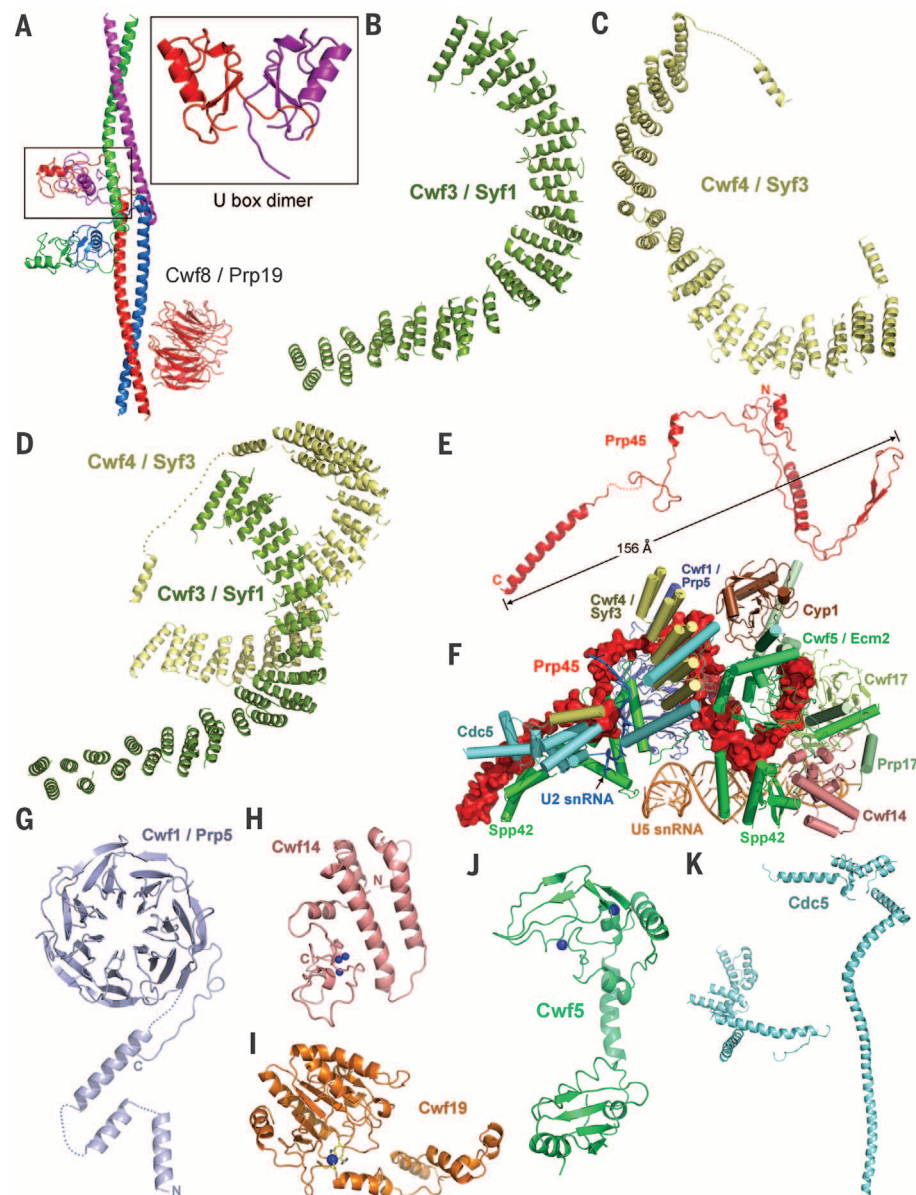Prp45, a core component of NTR, has been predicted to be intrinsically disordered (59). Our

structure confirms the prediction: Prp45 only contains extended secondary structural elements that span a distance of over 150 Å (Fig. 6E). Prp45 appears to promote spliceosome assembly by directly interacting with, and thus linking together, at least nine distinct proteins, including Spp42, Cwf17, and Cwf4/Syf3 (Fig. 6F and fig. S20). Prp45 also directly interacts with U2 and U6 snRNAs at the catalytic center. Such an arrangement allows the conformational changes at the catalytic center to be propagated to any distant corner of the spliceosome through the connection among Prp45, Cwf4/Syf3, and Cwf3/Syf1. Thus, similar to Cwf8/Prp19, Cwf3/Syf1, and Cwf4/Syf3, the morphology and the placement of Prp45 seem to have evolved to facilitate the dynamic process of pre-mRNA splicing.

Our structure includes a number of other NTC and NTR components. These include five NTC core components: (i) Cdc5, which plays an important role in pre-mRNA splicing by stabilizing the second-step spliceosome (60–62); (ii) Cwf7, which modulates interactions of Prp19 with other associated cofactors (63, 64); (iii) Cwf2/Prp3, which helps link NTC to the catalytic center; (iv) Cwf1/Prp5, which contains a 7-bladed β propeller; and (v) Cwf15, which interacts with U5 snRNA, Prp5, and Spp42. In addition, we modeled four NTR components: (i) Cwf5/Ecm2, which is involved in base-pairing interactions of U2/U6 helix II (65); (ii) Cwf11, which is an armadillo domain containing RNA helicase (49); (iii) Cwf14, which facilitates both steps of the splicing reaction (66); and (iv) Cwf19, the human ortholog of which is thought to be involved in the development of recessive ataxia syndrome (67). We also identified Prp17 and the prolyl isomerase Cyp1 in the EM density map. Structural mapping of these proteins in the spliceosome allows critical assessment of their functions in pre-mRNA splicing (Fig. 6, G to K, and fig. S21).

Assembly of snRNPs and NTC

The atomic model of the yeast spliceosome mainly comprises four subcomplexes—U2 snRNP, U5 snRNP, NTC, and NTR—which are intertwined with one another to form an asymmetric assembly (Fig. 7A). The U2/U6 duplex and the intron lariat are partially exposed on the surface of the spliceosome and accessible to the modifying enzymes, such as the ATPase/helicase Brr2. The U5 snRNP, located at the bottom of the triangular Central Body, serves as the base of the entire spliceosome (Fig. 7B). At the heart of the Central Body is an interconnected RNA assembly involving U2 snRNA, U6 snRNA, and the intron lariat. Loop I of U5 snRNA is located close to the U2/U6 duplex (Fig. 7B). NTC and NTR together form a supporting network above the U5 snRNP and the centrally located RNA molecules.

The NTC is characterized by a large and extended architecture, 200 Å in height and width and 170 Å in thickness (Fig. 8A). The eight identified protein components in NTC are mostly interconnected, constituting a large scaffold. In contrast, the five protein components of NTR are mostly unconnected (Fig. 8B) and only come together through interactions with the NTC
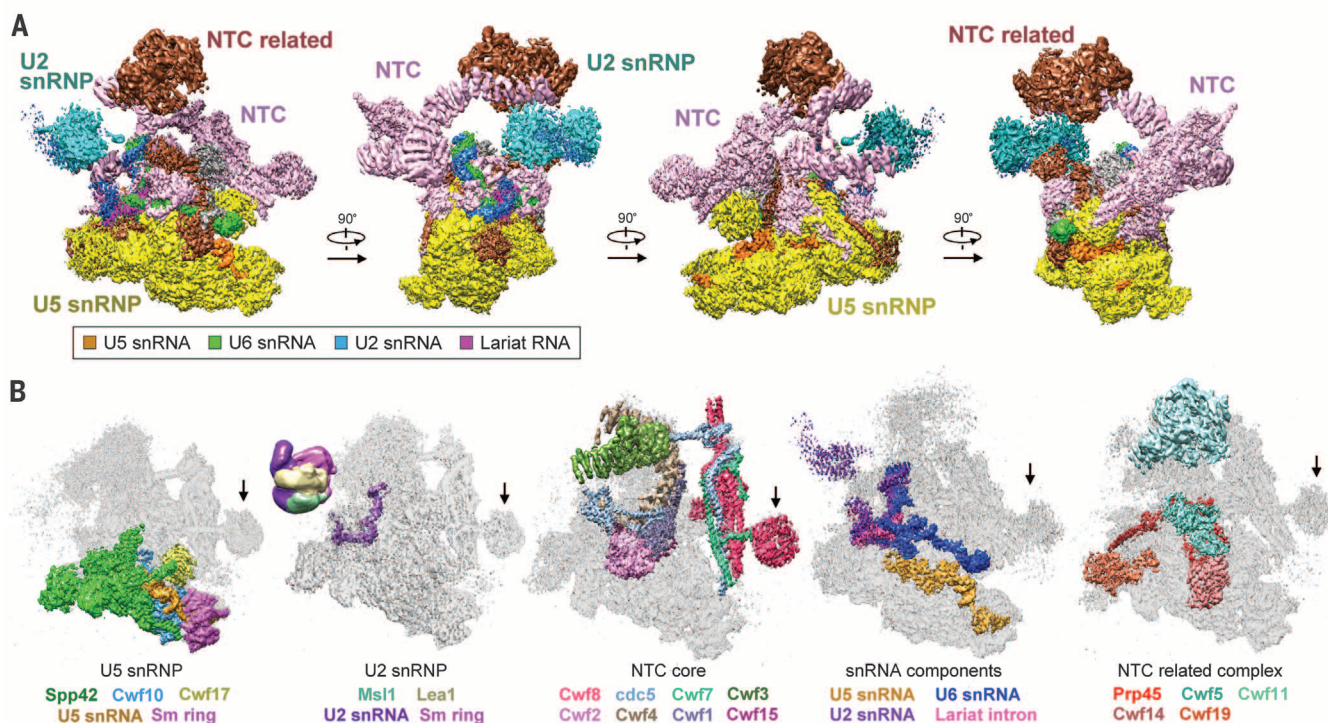

Fig. 6. Representative structures of individual protein components. (**A**) The tetrameric assembly of Cwf8/Prp19. The U-box dimer is highlighted in the inset. (**B**) The structure of the HAT-repeat superhelical protein Cwf3/Syf1. (**C**) The structure of the HAT-repeat superhelical protein Cwf4/Syf3. (**D**) Cwf3/Syf1 directly interacts with Cwf4/Syf3, both using HAT repeats in the middle portions of their respective structures. (**E**) The structure of Prp45. The 216 amino acids in Prp45 span 156 Å. (**F**) Prp45 interacts with at least nine protein components and two snRNAs. Prp45 is shown in surface view. (**G**) The structure of the WD40-repeat protein Cwf1/Prp5. (**H**) The structure of the NTR component Cwf14. Cwf14, which is thought to facilitate both steps of the splicing reaction, contains three zinc ions (blue spheres). (**I**) Structure of the functionally unknown NTR component Cwf19. (**J**) The NTR component Cwf5/Ecm2, which is thought to be involved in base-pairing interactions of U2/U6 helix II, exhibits an extended structure. (**K**) The structure of the NTC component Cdc5, which is thought to serve as a scaffold to recruit other protein factors. Of these proteins, no relevant structural information was previously available for Cwf19, Prp45, the N-terminal region of Cwf5, the N-terminal region of Spp42, or the C-terminal region of Cdc5. The other proteins have homologous structures, but this is the first time that they have been reported in *S. pombe*.

Fig. 7. The four multicomponent subcomplexes U5 snRNP, U2 snRNP, NTC, and NTR closely associate with one another to form the yeast spliceosome. (**A**) U5 snRNP forms a scaffold onto which the other three subcomplexes dock around the RNA molecules and the catalytic center. The protein components within the same snRNP are colored identically: yellow for U5 snRNP, cyan for U2 snRNP, light pink for NTC, and brown for NTR. The four RNA molecules are individually colored. (**B**) Relative positions of the four multicomponent subcomplexes and the RNA molecules within the spliceosome. The protein components within each subcomplex are differentially color-coded. These five views of the yeast spliceosome have the same general orientation as that of the first view in (A).

components (Fig. 8C). Together, NTC and NTR define a large central space, part of which is occupied by the catalytic center (Fig. 8C).

Dynamic conformation of the spliceosome

Most of the spliceosomal particles display a well-defined conformation, allowing us to obtain a 3D structure at an overall resolution of 3.6 Å. The high-resolution regions are largely restricted to the Central Body, which appears to have a rigid conformation. The peripheral regions occupied by components of NTC and NTR exhibit considerable conformational flexibility, which poses a challenge to any effort aimed at improving the local resolution. In addition to local conformational variations, large-scale structural changes are also associated with the spliceosome. We were able to obtain two conformational states, with 37,622 and 49,079 particles, through an additional round of 3D classification. We low-pass filtered both maps to 10 Å and compared the conformational changes (fig. S22A). Superposition of these two structures revealed a major movement of the Head region toward Arm I (fig. S22B). As a consequence of this movement, much of the already flexible U2 snRNP becomes disordered.

Discussion

Structure determination by means of x-ray crystallography has been focused on the individual components or subcomplexes of the spliceosome, yielding valuable information on a number of important proteins—namely, the structures of the core components of U1 snRNP (21–23), U2 snRNP (68–71), and U4 snRNP (19); two subcomplexes of the U6 snRNP (20, 72); a large fragment of Prp8 (16); and Brr2 (17, 18). These structures provide individual pieces of the spliceosome jigsaw puzzle. In the past decade, EM-based studies have produced structural insights into the intact spliceosome at various stages of the splicing reaction (73). These studies were performed on the mammalian spliceosomal A complex (29), B complex (31, 38, 40), B* complex (30), C complex (33, 35), and P complex (42), as well as on the yeast B complex (32), B^{act} complex (32), the U5.U2/U6 complex or C complex (32, 36), and the ILS complex (43). The highest resolution reported in these EM studies is 20 to 29 Å, which only allows description of general features of the spliceosome. After submission of this Research Article, the cryo-EM structure of the spliceosomal U4/U6. U5 tri-snRNP in *S. cerevisiae* was reported at 5.9 Å resolution (45), which allows domain identification and secondary-structure assignment for some components. The U4/U6.U5 tri-snRNP is an important complex for the assembly of functional spliceosomes.

Here, we report the cryo-EM structure of an intact *S. pombe* spliceosome at a near-atomic resolution of 3.6 Å. The resolution exceeds 3.2 Å in the core region of the spliceosome, which covers the bulk of the U5 snRNP and a number of other proteins from NTC and NTR. On the basis of the EM density, we have generated the first atomic model of an intact, functional spliceosome. We have provided an overall and preliminary analysis of the spliceosome structure. The enormous amount of information contained therein requires additional analysis. There are over 100 discrete protein-protein and protein-RNA interfaces among the 37 proteins and four RNA molecules of the spliceosome, involving a substantial amount of buried surface area. There are numerous other details that warrant attention; for example, Cwf5, Cwf14, and Cwf19 contain three different zinc-binding motifs (fig. S23). Determination of a near-atomic-resolution structure of an intact spliceosome represents a major milestone. Insights gained from structural analysis will greatly improve the mechanistic understanding of pre-mRNA splicing.

Although we intended to purify the spliceosomal C complex, the purified sample included a mixture of different spliceosomes, as judged by use of RT-PCR (fig. S3). Because Cdc5, which is recruited into the spliceosomal B^{act} complex, was used as the affinity tag for purification, the purified sample should be restricted to the B^{act}, B*, C, P, and ILS complexes. This finding is corroborated by the preponderance of NTC and NTR components (which are also recruited into the B^{act}

Fig. 8. Structures of the NTC and NTR. (**A**) The overall structure of the NTC. The color-coded NTC components are mostly interconnected through direct interactions. (**B**) Overall structure of the NTR. In contrast to NTC, components of the NTR make no direct contacts with each other and are mostly unconnected. (**C**) NTC and NTR surround the catalytic center. The catalytic center is identified by three intertwined RNA molecules: U6 snRNA (green), U2 snRNA (blue), and the intron lariat (magenta). The U5 snRNA (orange) is located next to the intertwined RNAs.
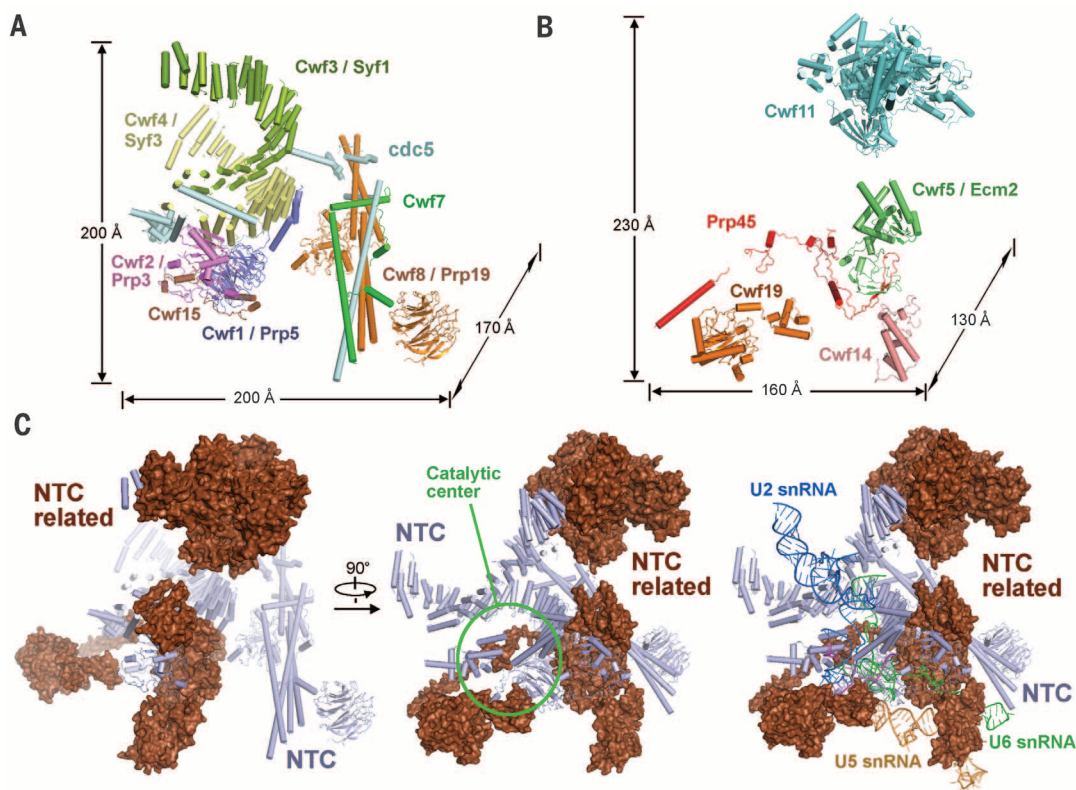
complex) (figs. S2 and S4). The EM density is well defined for the intron lariat, suggesting that the structure probably reflects the C, P, or ILS complex, or a mixture of the three complexes. The EM density for 5′-exon is weak, suggesting that either the ILS complex was a major species in the final EM sample or 5′-exon was lost during purification. These complexes share a large set of stable spliceosomal components, allowing determination of the cryo-EM structure at 3.6 Å resolution. The different spliceosomal complexes in the EM sample, major or minor, will probably be resolved upon collection and analysis of a larger set of micrographs.

Pre-mRNA splicing and protein translation, two central processes in eukaryotes, are each carried out by supramolecular protein-RNA machineries: spliceosome and ribosome, respectively. The 80S eukaryotic ribosome consists of two well-organized subcomplexes: the 60S large subunit and the 40S small subunit. In both subunits, the core protein components and the RNA molecules, in a mass ratio of approximately 1:1, form relatively stable RNP complexes. A flux of protein factors regulates the initiation, elongation, and termination of protein synthesis. In contrast to the ribosome, the spliceosome has a mass ratio of at least 10:1 in favor of the protein components and exhibits extreme dynamism in both composition and conformation. In the ribosome, the protein components are mainly located on the exterior, away from the catalytic center for peptide bond formation. In the spliceosome, the protein components surround and support the RNA-based catalytic center. The ribosome exhibits a generally isometric shape, whereas the spliceosome has a highly asymmetric morphology, with numerous surface cavities of varying sizes and cut-through spaces. Apparently, through evolution, two highly divergent strategies have been adopted for assembling RNPs to achieve complex functions in gene expression.

REFERENCES AND NOTES

1. C. B. Burge, T. Tuschl, P. A. Sharp, in *The RNA World, Second Edition: The Nature of Modern RNA Suggests a Prebiotic RNA World*, R. F. Gesteland, T. R. Cech, J. F. Atkins, Eds. (Cold Spring Harbor Laboratory Press, Cold Spring Harbor, NY, 1999), pp. 525–560.
2. T. A. Cooper, L. Wan, G. Dreyfuss, *Cell* **136**, 777–793 (2009).
3. D. A. Wassarman, J. A. Steitz, *Science* **257**, 1918–1925 (1992).
4. C. L. Will, R. Lührmann, *Cold Spring Harb. Perspect. Biol.* **3**, a003707 (2011).
5. M. C. Wahl, C. L. Will, R. Lührmann, *Cell* **136**, 701–718 (2009).
6. W. Chen, M. J. Moore, *Curr. Opin. Struct. Biol.* **24**, 141–149 (2014).
7. A. Hegele et al., *Mol. Cell* **45**, 567–580 (2012).
8. O. Cordin, D. Hahn, J. D. Beggs, *Curr. Opin. Cell Biol.* **24**, 431–438 (2012).
9. J. P. Staley, C. Guthrie, *Cell* **92**, 315–326 (1998).
10. T. A. Steitz, J. A. Steitz, *Proc. Natl. Acad. Sci. U.S.A.* **90**, 6498–6502 (1993).
11. E. J. Sontheimer, S. Sun, J. A. Piccirilli, *Nature* **388**, 801–805 (1997).
12. P. M. Gordon, E. J. Sontheimer, J. A. Piccirilli, *RNA* **6**, 199–205 (2000).
13. S.-L. Yean, G. Wuenschell, J. Termini, R.-J. Lin, *Nature* **408**, 881–884 (2000).
14. S. M. Fica et al., *Nature* **503**, 229–234 (2013).
15. T. W. Nilsen, in *RNA Structure and Function*, R. W. Simons, M. Grunberg-Manago, Eds. (Cold Spring Harbor Monograph vol. 35, Cold Spring Harbor Laboratory Press, Cold Spring Harbor, NY, 1998), pp. 279–307.
16. W. P. Galej, C. Oubridge, A. J. Newman, K. Nagai, *Nature* **493**, 638–643 (2013).
17. S. Mozaffari-Jovin et al., *Science* **341**, 80–84 (2013).
18. T. H. Nguyen et al., *Structure* **21**, 910–919 (2013).
19. A. K. Leung, K. Nagai, J. Li, *Nature* **473**, 536–539 (2011).
20. L. Zhou et al., *Nature* **506**, 116–120 (2014).
21. G. Weber, S. Trowitzsch, B. Kastner, R. Lührmann, M. C. Wahl, *EMBO J.* **29**, 4172–4184 (2010).
22. D. A. Pomeranz Krummel, C. Oubridge, A. K. Leung, J. Li, K. Nagai, *Nature* **458**, 475–480 (2009).
23. Y. Kondo, C. Oubridge, A. M. van Roon, K. Nagai, *eLife* **4**, e04986 (2015).
24. W. P. Galej, T. H. Nguyen, A. J. Newman, K. Nagai, *Curr. Opin. Struct. Biol.* **25**, 57–66 (2014).
25. N. Ban, P. Nissen, J. Hansen, P. B. Moore, T. A. Steitz, *Science* **289**, 905–920 (2000).
26. F. Schluenzen et al., *Cell* **102**, 615–623 (2000).
27. B. T. Wimberly et al., *Nature* **407**, 327–339 (2000).
28. M. Azubel, S. G. Wolf, J. Sperling, R. Sperling, *Mol. Cell* **15**, 833–839 (2004).
29. N. Behzadnia et al., *EMBO J.* **26**, 1737–1748 (2007).
30. S. Bessonov et al., *RNA* **16**, 2384–2403 (2010).
31. D. Boehringer et al., *Nat. Struct. Mol. Biol.* **11**, 463–468 (2004).
32. P. Fabrizio et al., *Mol. Cell* **36**, 593–608 (2009).
33. M. M. Golas et al., *Mol. Cell* **40**, 927–938 (2010).
34. M. Grote et al., *Mol. Cell. Biol.* **30**, 2105–2119 (2010).
35. M. S. Jurica, D. Sousa, M. J. Moore, N. Grigorieff, *Nat. Struct. Mol. Biol.* **11**, 265–269 (2004).
36. M. D. Ohi, L. Ren, J. S. Wall, K. L. Gould, T. Walz, *Proc. Natl. Acad. Sci. U.S.A.* **104**, 3195–3200 (2007).
37. B. Sander et al., *Mol. Cell* **24**, 267–278 (2006).
38. E. Wolf et al., *EMBO J.* **28**, 2283–2292 (2009).
39. E. M. Makarov et al., *Science* **298**, 2205–2208 (2002).
40. J. Deckert et al., *Mol. Cell. Biol.* **26**, 5528–5543 (2006).
41. M. S. Jurica, L. J. Licklider, S. R. Gygi, N. Grigorieff, M. J. Moore, *RNA* **8**, 426–439 (2002).

42. J. O. Ilagan, R. J. Chalkley, A. L. Burlingame, M. S. Jurica, *RNA* **19**, 400–412 (2013).
43. W. Chen *et al.*, *RNA* **20**, 308–320 (2014).
44. Z. Zhou, J. Sim, J. Griffith, R. Reed, *Proc. Natl. Acad. Sci. U.S.A.* **99**, 12203–12207 (2002).
45. T. H. Nguyen *et al.*, *Nature* **523**, 47–52 (2015).
46. J. Hang, R. Wan, C. Yan, Y. Shi, *Science* (2015).
47. M. D. Ohi *et al.*, *Mol. Cell. Biol.* **22**, 2011–2024 (2002).
48. R. M. Voorhees, I. S. Fernández, S. H. Scheres, R. S. Hegde, *Cell* **157**, 1632–1643 (2014).
49. I. De *et al.*, *Nat. Struct. Mol. Biol.* **22**, 138–144 (2015).
50. P. Fabrizio, B. Laggerbauer, J. Lauber, W. S. Lane, R. Lührmann, *EMBO J.* **16**, 4092–4106 (1997).
51. R. J. Grainger, J. D. Beggs, *RNA* **11**, 533–557 (2005).
52. S. Liu, R. Rauhut, H. P. Vornlocher, R. Lührmann, *RNA* **12**, 1418–1430 (2006).
53. I. Dix, C. S. Russell, R. T. O'Keefe, A. J. Newman, J. D. Beggs, *RNA* **4**, 1239–1250 (1998).
54. J. G. Umen, C. Guthrie, *Genetics* **143**, 723–739 (1996).
55. C. A. Collins, C. Guthrie, *Genes Dev.* **13**, 1970–1982 (1999).
56. L. Liu, C. C. Query, M. M. Konarska, *Nat. Struct. Mol. Biol.* **14**, 519–526 (2007).
57. E. C. Small, S. R. Leggett, A. A. Winans, J. P. Staley, *Mol. Cell* **23**, 389–399 (2006).
58. P. J. Preker, W. Keller, *Trends Biochem. Sci.* **23**, 15–16 (1998).
59. I. Korneta, J. M. Bujnicki, *PLOS Comput. Biol.* **8**, e1002641 (2012).
60. W. H. McDonald, R. Ohi, N. Smelkova, D. Frendewey, K. L. Gould, *Mol. Cell. Biol.* **19**, 5352–5362 (1999).
61. C. G. Burns, R. Ohi, A. R. Krainer, K. L. Gould, *Proc. Natl. Acad. Sci. U.S.A.* **96**, 13789–13794 (1999).
62. C. C. Query, M. M. Konarska, *RNA* **18**, 1001–1013 (2012).
63. H. R. Chen *et al.*, *Mol. Cell. Biol.* **18**, 2196–2204 (1998).
64. H. R. Chen *et al.*, *Proc. Natl. Acad. Sci. U.S.A.* **96**, 5406–5411 (1999).
65. D. Xu, J. D. Friesen, *Mol. Cell. Biol.* **21**, 1011–1023 (2001).
66. D. Saha, P. Khandelia, R. T. O'Keefe, U. Vijayraghavan, *J. Biol. Chem.* **287**, 5390–5399 (2012).
67. R. Burns *et al.*, *Neurology* **83**, 2175–2182 (2014).
68. S. R. Price, P. R. Evans, K. Nagai, *Nature* **394**, 645–650 (1998).
69. E. A. Sickmier *et al.*, *Mol. Cell* **23**, 49–59 (2006).
70. P. C. Lin, R. M. Xu, *EMBO J.* **31**, 1579–1590 (2012).
71. J. L. Jenkins, A. A. Agrawal, A. Gupta, M. R. Green, C. L. Kielkopf, *Nucleic Acids Res.* **41**, 3859–3873 (2013).
72. E. J. Montemayor *et al.*, *Nat. Struct. Mol. Biol.* **21**, 544–551 (2014).
73. R. Lührmann, H. Stark, *Curr. Opin. Struct. Biol.* **19**, 96–102 (2009).

Structural basis of pre-mRNA splicing

Jing Hang,* Ruixue Wan,* Chuangye Yan,* Yigong Shi†

Splicing of precursor messenger RNA is performed by the spliceosome. In the cryogenic electron microscopy structure of the yeast spliceosome, U5 small nuclear ribonucleoprotein acts as a central scaffold onto which U6 and U2 small nuclear RNAs (snRNAs) are intertwined to form a catalytic center next to Loop I of U5 snRNA. Magnesium ions are coordinated by conserved nucleotides in U6 snRNA. The intron lariat is held in place through base-pairing interactions with both U2 and U6 snRNAs, leaving the variable-length middle portion on the solvent-accessible surface of the catalytic center. The protein components of the spliceosome anchor both 5′ and 3′ ends of the U2 and U6 snRNAs away from the active site, direct the RNA sequences, and allow sufficient flexibility between the ends and the catalytic center. Thus, the spliceosome is in essence a protein-directed ribozyme, with the protein components essential for the delivery of critical RNA molecules into close proximity of one another at the right time for the splicing reaction.

In eukaryotic cells, the coding exons in a freshly transcribed precursor messenger RNA (pre-mRNA) are interdispersed by non-coding introns that must be removed before protein translation. Removal of the introns is carried out by the spliceosome, a dynamic ribonucleoprotein (RNP) machine that comprises more than 100 protein components and five small nuclear RNAs (snRNAs) (*1*). Pre-mRNA splicing occurs through two steps, which are both S_N2-type transesterification reactions (*2, 3*).

In the first step of pre-mRNA splicing, the 2′-OH group of a conserved RNA adenine nucleotide in the branch point sequence (BPS) of an intron initiates a nucleophilic attack on the phosphorous atom of the guanine nucleotide at the 5′ end of the intron, resulting in the release of 5′-exon and formation of an intron lariat–3′-exon intermediate (hereafter, intron lariat) (Fig. 1A). In the second step, the 3′-OH group of the RNA nucleotide at the 3′ end of the 5′-exon unleashes a second nucleophilic attack on the phosphorous atom of the RNA guanine nucleotide at the 5′ end of the 3′-exon, leading to joining of two exons and release of the intron lariat (Fig. 1A) (*3*). Although the nature of the two-step reaction has been clearly defined for decades, how the spliceosome facilitates such reaction remains largely enigmatic. How are the reacting pieces placed into close proximity of one another in the correct temporal order? Given the varying lengths of the exons and introns, how does the spliceosome accommodate pre-mRNA and hold the 5′-exon for both steps of the reaction?

The spliceosome is a metalloenzyme, and a number of conserved RNA nucleotides directly coordinate at least two magnesium ions (Mg^{2+}) that collectively catalyze the two-step reaction (*2, 4–7*). The reaction mechanism of pre-mRNA splicing is thought to closely resemble that of the group IIA or IIB self-splicing intron, each involving formation of an intron lariat, and differ from that of the group IIC intron, which splices by hydrolysis through a linear intron (*8, 9*). An in vitro reconstitution of U2 and U6 snRNAs revealed RNA splicing-like activity in the absence of the protein components, which strongly supports the ribozyme hypothesis (*10–13*). But the protein components of the spliceosome are obviously indispensable for pre-mRNA splicing to proceed because, for example, defective splicing due to a mutated RNA sequence can be rescued by mutations in Prp8 from *Saccharomyces cerevisiae* (Spp42 from *Schizosaccharomyces pombe*) (*14–18*). What are the functions of the protein components of the spliceosome during the two-step reaction? This Research Article addresses these interrelated questions through structural analysis of the yeast spliceosome from *S. pombe*, with a focus on the RNA components. The overall structure of the spliceosome and the features of the protein components are reported in (*19*).

Organization of the RNA components

The yeast spliceosome contains four distinct RNA molecules: U2 snRNA, U5 snRNA, U6 snRNA, and an intron lariat, which have been unambiguously located in the electron microscopy (EM) density map (Fig. 1B and figs. S1 and S2). U2, U5, and U6 snRNAs contain 186, 120, and 99 nucleotides (nt), respectively. In the structure, a nine-nucleotide fragment at the 3′ end of U6 snRNA (nt 91 to 99) and the middle and 3′ end portion of U2 snRNA (nt 44 to 92, 146 to 152, and 178 to 186) are flexible, exhibit poor EM density, and remain to be assigned. In addition, six nucleotides at the 5′ end and nine nucleotides at the 3′ end of U5 snRNA are disordered. All other 314 nucleotides from the snRNAs have been specifically assigned, representing ~80% of the total snRNA sequences. In addition, 18 nucleotides have been tentatively modeled for the intron lariat on the basis of conserved sequences for yeast (*1*).

Among the four RNA molecules, U5 snRNA is mostly buried in the structure (Fig. 1B). A large

Ministry of Education Key Laboratory of Protein Science, Tsinghua-Peking Joint Center for Life Sciences, Center for Structural Biology, School of Life Sciences, Tsinghua University, Beijing 100084, China.
*These authors contributed equally to this work. †Corresponding author. E-mail: shi-lab@tsinghua.edu.cn
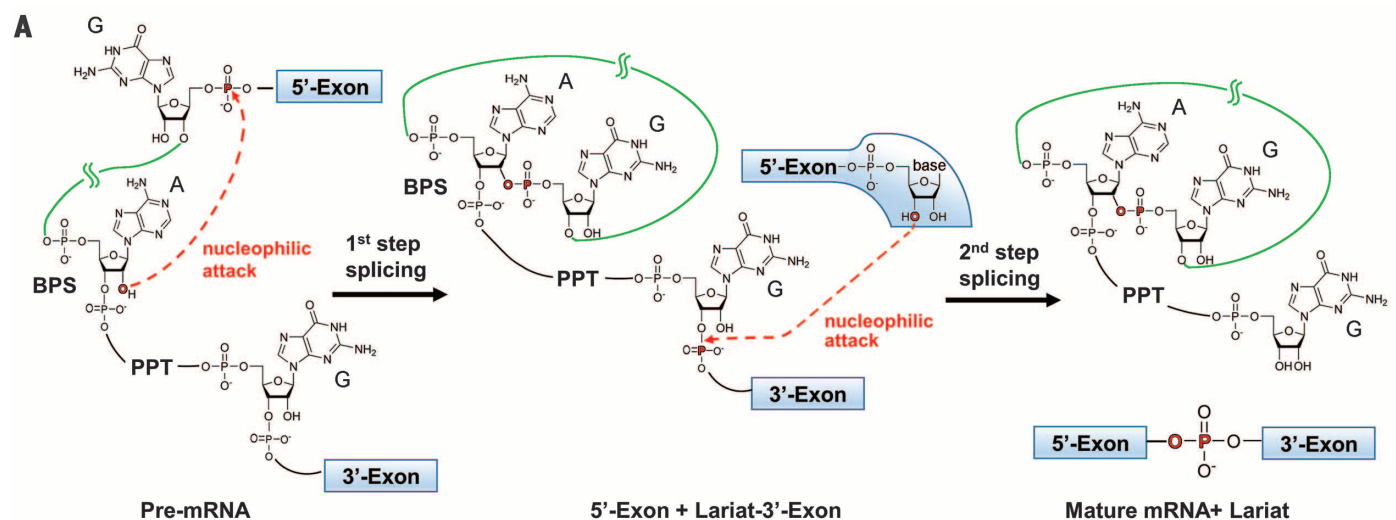
Fig. 1. Overall organization of the RNA components in the spliceosome. (**A**) A schematic diagram of the two-step splicing reaction. The intron sequences are indicated with thick green lines. The phosphorous and oxygen atoms that are directly involved in bond formation are highlighted in red. PPT, poly-pyrimidine tract. (**B**) Overall organization of the RNA components in the spliceosome. The EM density is displayed for the entire spliceosome, with the protein components shown in gray and the RNA molecules color-coded. U2, U5, and U6 snRNAs and the intron lariat are colored blue, gold, green, and purple, respectively. The RNA coloring scheme is preserved throughout this manuscript. A close-up view is shown to highlight the catalytic center and the U2/U6 duplex. (**C**) Overall organization of the RNA components in isolation. A surface view of the four pieces of RNA is displayed so as to indicate their overall dimension and relative orientation. Figures 1C; 2, A, B, D, and E; 3; 4; 5, A and C; 6, B and E; and 7, B and C, were prepared in PyMol (*48*). Figures 1B; 5B; and 6, A, C, and D, were made by use of CHIMERA (*49*).

proportion of the U2 and U6 snRNAs is surface-exposed, with a section of the U2/U6 duplex (known as Helix II) exposed at the tip of the Central Body. The 3′ end portion of U2 snRNA is anchored to Arm I and largely exposed, whereas the 5′ end portion is base-paired with the intron lariat and U6 snRNA (Fig. 1C). The catalytic center, as indicated by the intron lariat, is partially exposed to solvent and located at the heart of the Central Body on the side of Arm I (Fig. 1, B and C). Because of the endogenous nature of the yeast spliceosome, the intron is expected to vary in length and sequence. The intron is placed on the surface of the catalytic center, as

allowing its middle portion of variable length to reach into unrestricted space.

These RNA molecules form an extended and interconnected architecture (Figs. 1C and 2A). The longest dimension of the RNA architecture, as measured from the 3′ end of U2 snRNA to the 5′ end of U5 snRNA, exceeds 300 Å (Fig. 1C). Loop I of U5 snRNA is positioned close to the catalytic center and the Mg^{2+} ions (Fig. 2A). A large majority of the nucleotides in U5 snRNA, from G7 to C89, form a continuous duplex, except for three short stretches: Loop I (C47 to A53), Loop II (A26 to A31), and Loop III (U78 to A83) (Fig. 2B). The U5 snRNA duplex is divided

into Stems I, II, and III. The 5′ end portion of U2 snRNA and the 3′ end portion of U6 snRNA form an intermolecular duplex, known as Helix II (Fig. 2, A and C), with its tip located ~60 to 70 Å away from the nearest Mg^{2+} ion at the active site. The 3′ end portion of U2 snRNA and the 5′ end of U6 snRNA, each forming intramolecular duplexes, are separated from the spliceosomal active site by ~130 and 90 Å, respectively.

In contrast to their 5′ and 3′ ends, the middle portion of U2 or U6 snRNA pairs up with the intron lariat near the active site (Fig. 2, D and E). Specifically, the ACAGA box of U6 snRNA forms an intermolecular duplex with the 5′-splice site
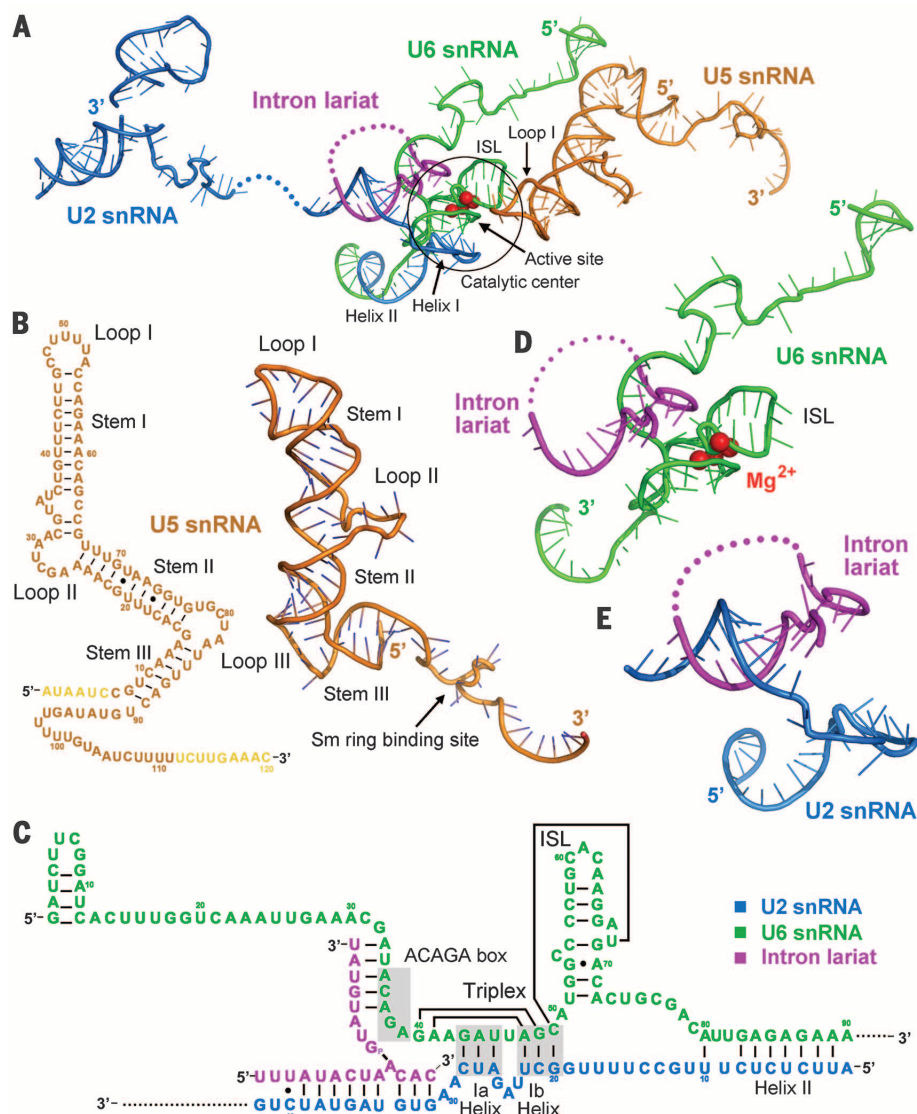
Fig. 2. Structures of individual RNA components in the spliceosome. (**A**) An overall illustration of the RNA architecture. The catalytic center—which comprises the ISL of U6 snRNA, Helix I of the U2/U6 duplex, Loop I of U5 snRNA, and the Mg^{2+} ions—is circled. The disordered RNA sequences are indicated with dotted lines. (**B**) Structure of U5 snRNA. An illustration of the U5 snRNA structure is shown at right, with its secondary structural elements indicated at left. The sequences in light color are invisible because of their intrinsic flexibility. (**C**) Overall base-pairing interactions among U2 snRNA, U6 snRNA, and the intron lariat. Base-pairing interactions in the RNA triplex between A41-G40, U68 and A47-G48-C49 are identified with solid lines. (**D**) Structure of U6 snRNA. The intron lariat is shown here to indicate its relative position to the active site. (**E**) Structure of U2 snRNA. The view in (D) and (E) is the same as that in (A).

(5′SS) of the intron, whereas a number of nucleotides from U2 snRNA interact with the BPS (Fig. 2, C and E). Intriguingly, the 2′-OH group of the invariant adenine nucleotide in BPS is located ~20 to 22 Å away from the reactive Mg^{2+} ions, suggesting that the catalytic Mg^{2+} ions may only be brought to the close proximity of BPS during the first-step reaction.

Catalytic center and the active site

The catalytic center of the spliceosome consists of Helix I of the U2/U6 snRNA duplex, the internal stem loop (ISL) of U6 snRNA, Loop I of

U5 snRNA, and Mg^{2+} ions (Fig. 3, A and B). A hallmark of the spliceosomal catalytic center is the triplex, which is formed through additional base-pairing interactions between the A47-G48-C49 triad of Helix Ib and three nucleotides, A41, G40, and U68 of U6 snRNA, respectively. The active site, featured by two Mg^{2+} ions and their coordinating phosphate groups, is located within the ISL of U6 snRNA and configured by the catalytic triplex (Fig. 3C). Both Mg^{2+} ions are coordinated by the phosphate group of U68, whereas the phosphate groups of A47, G48, and G66 also contribute to Mg^{2+} coordination (Fig. 3C). The

organization of the triplex brings the 5′SS close to the active site because the ACAGA box of U6 snRNA recognizes the 5′SS and immediately precedes G40 to A41 of the triplex (Fig. 2C). In the meantime, U2 snRNA recognizes the highly conserved BPS, which contains the bulged branch adenine nucleotide, just downstream of Helix I, thus bringing BPS and 5′SS together and priming the first catalytic step.

The two Mg^{2+} ions, known as M1 and M2, play distinct roles during the two steps of splicing (2). During the first step, M2 activates the nucleophile—the 2′-OH of the branch nucleotide adenine from BPS—whereas M1 stabilizes the leaving group, the 3′-OH of the 3′-end nucleotide in the 5′-exon. During the second step, the roles of M1 and M2 reciprocate, with M1 activating the nucleophile (3′-OH of the 3′ end nucleotide in the 5′-exon) and M2 stabilizing the leaving group (3′-OH of the 3′ end nucleotide in the intron). M1 is coordinated by both U and G of the UAG motif in the ISL of U6 snRNA, whereas M2 is only bound by the U nucleotide. Our structure is fully consistent with the proposed two-metal mechanism (Fig. 3C) (2). M1, coordinated by the phosphate groups of U68 and G66, is located close to Loop I of U5 snRNA, which is known to bind 5′-exon. This arrangement presumably places M1 in the proximity of the 3′ end of 5′-exon. In addition to M1 and M2, there are at least two additional Mg^{2+} ions near the active site, which likely help stabilize the active site conformation by neutralizing the negative charges from several closely spaced phosphate groups (fig. S3A).

Our structure provides direct experimental evidence that the spliceosome shares a generally similar catalytic mechanism with the self-splicing group II intron (2). However, important differences remain. Splicing of pre-mRNA, involving precise removal of numerous introns of variable length and distinct sequences, requires the participation of many dozens of protein components in the spliceosome. The spliceosomal catalytic center is anchored in the catalytic cavity on the surface of Spp42 (Fig. 3D). An inter-helical loop from the N-terminal domain of Spp42 follows a surface groove in the ISL of U6 snRNA, with the side chains of Arg^{681}, Arg^{686}, Lys^{693}, and Lys^{699} inserting into the groove, perhaps stabilizing the conformation of the ISL (fig. S3B).

U5 snRNA and U5 snRNP

As the central component of the spliceosome, U5 snRNP is the only invariant snRNP for both major and minor pre-mRNA splicing reactions and functions as a scaffold onto which the other snRNPs assemble (20). U5 snRNP in the structure consists of U5 snRNA and the protein components Spp42 (Prp8 in *S. cerevisiae*), Cwf10 (Snu114 in *S. cerevisiae*), Cwf17, and the heptameric Sm ring (Fig. 4A). The highly conserved Loop I and Stem I of U5 snRNA are bound predominantly by secondary structural elements from the N-terminal domain of Spp42 (Fig. 4B). Loop II and a portion of Stem III of U5 snRNA
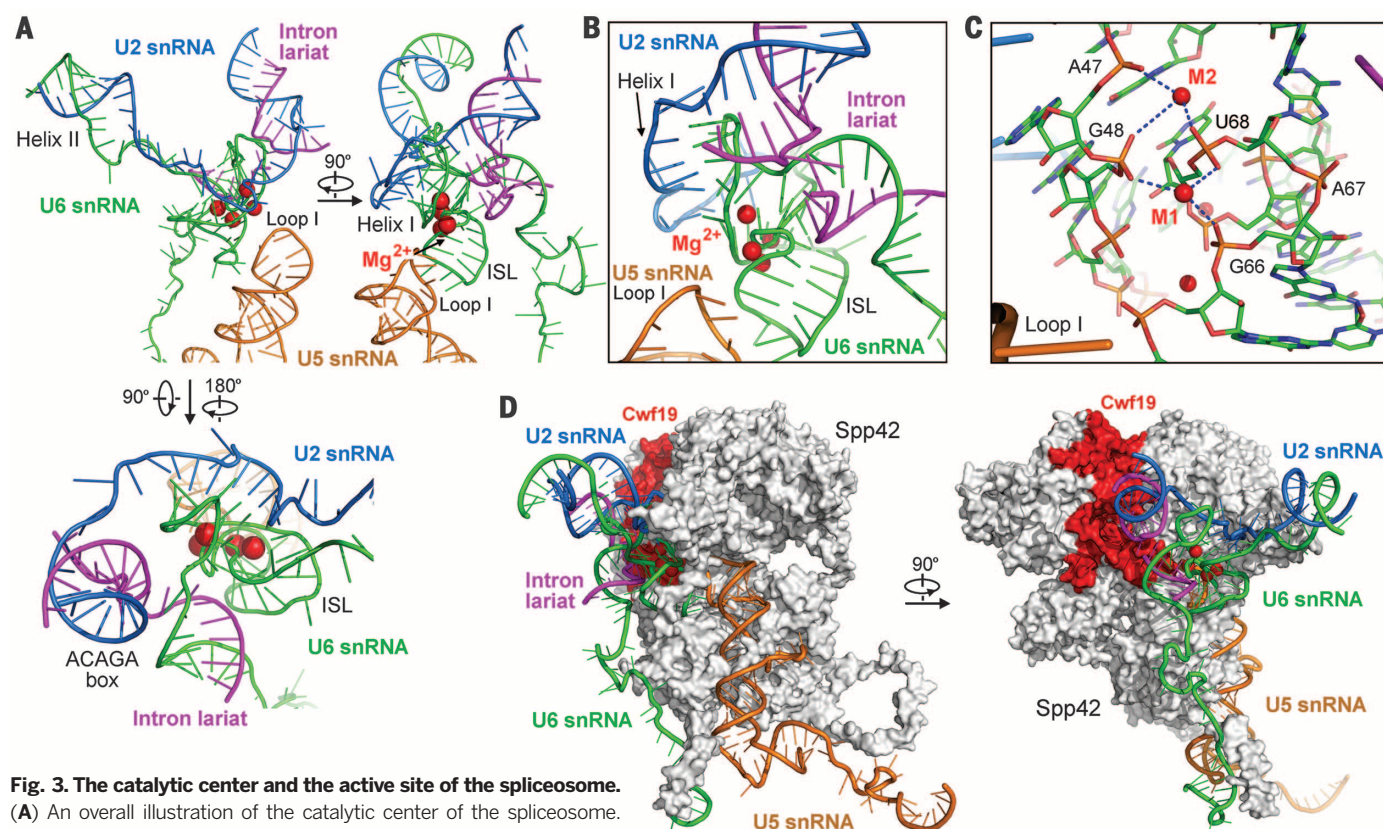
Fig. 3. The catalytic center and the active site of the spliceosome.
(**A**) An overall illustration of the catalytic center of the spliceosome. Three perpendicular views are shown. The intron lariat, Helix II of the U2/U6 duplex, and Stem I of U5 snRNA are included so as to indicate the relative orientation. (**B**) A close-up view on the catalytic center. Helix I of the U2/U6 duplex is placed to the left of the two catalytic Mg^{2+} ions, and the ISL of U6 snRNA is close to Loop I of U5 snRNA. (**C**) A close-up view on the active site. Among the two catalytic Mg^{2+} ions, the first (M1) is coordinated by phosphate groups from U68, G66, and G48 of U6 snRNA, and the second (M2) is bound by phosphates from U68, G48, and A47. A47 and G48 are part of the RNA triplex. (**D**) Both the catalytic center and U5 snRNA are anchored on Spp42. Two perpendicular views are shown. The catalytic center is placed into a positively charged, catalytic cavity on Spp42. Interactions between the active site and Loop I of U5 snRNA are mediated in a channel below the surface (left). This may allow retention of the 5′-exon after the first-step reaction.

are recognized by Cwf10, whereas Loop III is exposed to solvent in a surface cavity of the spliceosome. Cwf17 is placed in the close proximity of Stems II and III. The 3′ end U-rich sequences of U5 snRNA are specifically bound by the heptameric Sm ring (Fig. 4A).

As the largest and most conserved spliceosomal protein, Spp42 is a central component of U5 snRNP. Spp42 anchors U5 snRNA while simultaneously interacting with both U2 and U6 snRNAs. The N-terminal domain of Spp42 is entangled with U5 snRNA through an extensive interface, with an extended loop (residues 480 to 497) tracking the major groove between Stem I and Loop II and thus locking U5 snRNA into a relatively rigid conformation (Fig. 4B). Several positively charged amino acids from this loop, exemplified by Lys[488] and Arg[497], make hydrogen bonds to the phosphate groups of U5 snRNA (Fig. 4C). The imidazole side chain of His[490] appears to directly recognize G66 through a hydrogen bond. On the back side of the major groove bound by the extended loop, the RNA duplex is contacted by at least seven Arg and Lys residues from two α-helices (Fig. 4D). These basic residues mediate a number of hydrogen bonds to the phosphate backbone of U5 snRNA. The guanidinium group of Arg[665] reaches into the minor groove, donating three hydrogen bonds to U36 and C64 of U5 snRNA (Fig. 4E). The nucleotide sequences between Stem I and Loop I of U5 snRNA are located in the vicinity of an inter-helical loop (residues 786 to 791) from the N-terminal domain and an α-helix from the Thumb/X domain (Fig. 4F).

In addition to Spp42, at least five other proteins make specific interactions with U5 snRNA (fig. S4A). The side chains of Thr[119] and Arg[187] from Cwf10 donate two hydrogen bonds to the backbone phosphates of C28 and A30, respectively (fig. S4B), whereas four Lys residues of Cwf17 directly contact the phosphates of A12, A13, and G14 (fig. S4C). The bases G96 and U101 are each sandwiched by two aromatic and/or basic residues from the Sm proteins (fig. S4D). Last, Cwf1/Prp5 and Cwf15 associate with each other, whereas Lys[238] of Cwf1/Prp5 and His[32] of Cwf15 make specific hydrogen bonds to 2′-OH groups of G39 and A59, respectively (fig. S4E).

Placement of snRNA by protein components

Our structure clearly identifies the spliceosome as a ribozyme, with the active site in U6 snRNA well defined (Fig. 3). Yet, snRNAs only account for a very small fraction of the molecular mass in the spliceosome, with the rest contributed by a large number of spliceosomal proteins. These proteins can be divided into two general categories: enzymes exemplified by the RNA-dependent helicases/adenosine triphosphatases (ATPases) and structural components that lack enzymatic activities (1, 21). Functions of the enzymes in the splicing reaction have been relatively well understood because alteration of an enzymatic activity frequently leads to a splicing defect at a specific stage of the reaction. For example, mutations in the helicase Brr2 have a negative impact on the unwinding of the U4/U6 duplex, resulting in stalled activation of the spliceosome preceding the first-step reaction (22–26). In contrast, the structural components of the spliceosome are less well understood because their mutations may either disrupt the spliceosomal assembly or remain functionally silent. The organization of the protein components relative to that of snRNAs strongly suggests that an important function of the structural components is to direct the key snRNA elements to the catalytic center while anchoring the ends of these snRNA molecules away from the catalytic center (Fig. 5A). This arrangement may allow sufficient space for the enzymatic components,
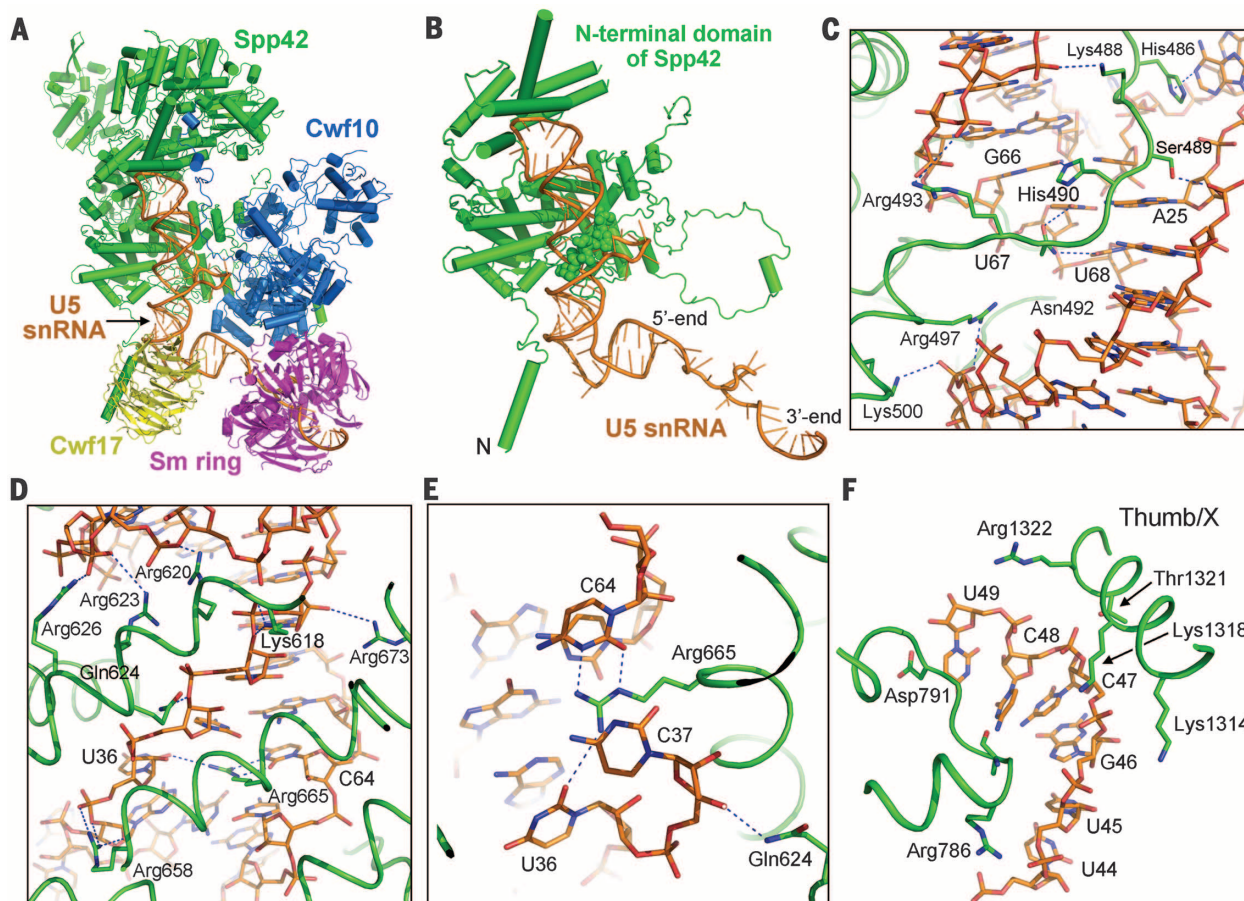
Fig. 4. Structure of U5 snRNP. (A) Overall structure of U5 snRNP. Except Brr2, all other core components of U5 snRNP are clearly identified in the structure. Brr2 is present in the spliceosome but is highly flexible and shows no clear EM density. **(B)** Recognition of U5 snRNA is mediated predominantly by the N-terminal domain of Spp42. An extended loop is inserted into the major groove between Stem I and Loop II, holding U5 snRNA into registry. **(C)** A close-up view on the specific interactions between residues from the extended loop and the major groove of U5 snRNA. His[490] and Asn[492] appear to recognize specific bases in the groove. Potential hydrogen bonds are represented by blue dotted lines. **(D)** Representative interactions between helical elements of Spp42 N-terminal domain and Stem I of U5 snRNA. **(E)** A close-up view on Arg[665] of Spp42. The guanidinium group of Arg[665] reaches deep into the minor groove, making three hydrogen bonds to U36 and C64. **(F)** A close-up view on Loop I of U5 snRNA. An α-helix from the Thumb/X domain and a helix-loop-helix motif are positioned close to Loop I for potential interactions.

such as the RNP remodeling proteins, to exert their functions.

The key elements that are essential for the splicing reaction are located in the middle portion of U6 and U2 snRNAs (Fig. 5A). Both the 5′ and 3′ ends of U6 or U2 snRNA are anchored by the structural protein components at sites that are distant from the catalytic center (Fig. 5B). This arrangement allows for considerable flexibility and regulatory space between the catalytic center and the ends of snRNAs. For example, the 5′ end of U6 snRNA is anchored by an N-terminal α-helix of Spp42 and the WD40 repeat protein Cwf17 (Fig. 5A and fig. S5A). The 3′ end portion of U2 snRNA is specifically recognized by the Lea1/Msl1 complex that is located ~130 Å away from the active site (Fig. 5C). This part of U2 snRNA is connected to the catalytic center through protein components including the half-a-tetratricopeptide (HAT) repeats containing proteins Cwf3/Syf1 and Cwf4/Syf3. The 5′ end of U2 snRNA base-pairs with the 3′ end of

U6 snRNA to form Helix II, with its tip positioned ~60 to 70 Å away from the active site. Helix II is held in place by Spp42, Cwf4/Syf3, and other structural protein components (Fig. 5B and fig. S5B). The intervening sequences between the ends and the catalytic center, such as those between Helix II and the catalytic center, are also oriented by structural protein components (fig. S6).

Putative location of the 5′-exon

We sought to locate the spliced 5′-exon in the structure, which should be present at a location that is close to Loop I of U5 snRNA. However, the cryogenic EM (cryo-EM) sample contains a mixture of different spliceosomal complexes (19), which is predicted to considerably weaken the EM density for the 5′-exon. Close examination of the EM density of the spliceosome reveals a surface channel that goes into the active site (Fig. 6A). Weak EM density was indeed present close to the nucleotides U50-U51-U52 in Loop I

of U5 snRNA, and its appearance is consistent with a few stacked nucleotides (Fig. 6B). Considering the degenerate sequences of the 5′-exon, the weak EM density is significant and allows putative modeling of four contiguous nucleotides representing the 5′-exon. Such a 5′-exon can be comfortably placed through the surface channel (Fig. 6C) into the vicinity of the active site, with the 3′ end of the 5′-exon within 5 Å of the catalytic Mg^{2+} ions (Fig. 6D). This putative channel for the 5′-exon is located in the middle of the Central Body, surrounded by N-terminal sequences from Spp42 and a helix-loop-helix motif from Cwf19 (Fig. 6C). Consistent with this analysis, this portion of the Spp42 surface is highly enriched by positively charged amino acids (Fig. 6E).

Comparison with the group IIB self-splicing intron

The catalytic center of the spliceosome closely resembles that of the group IIB self-splicing
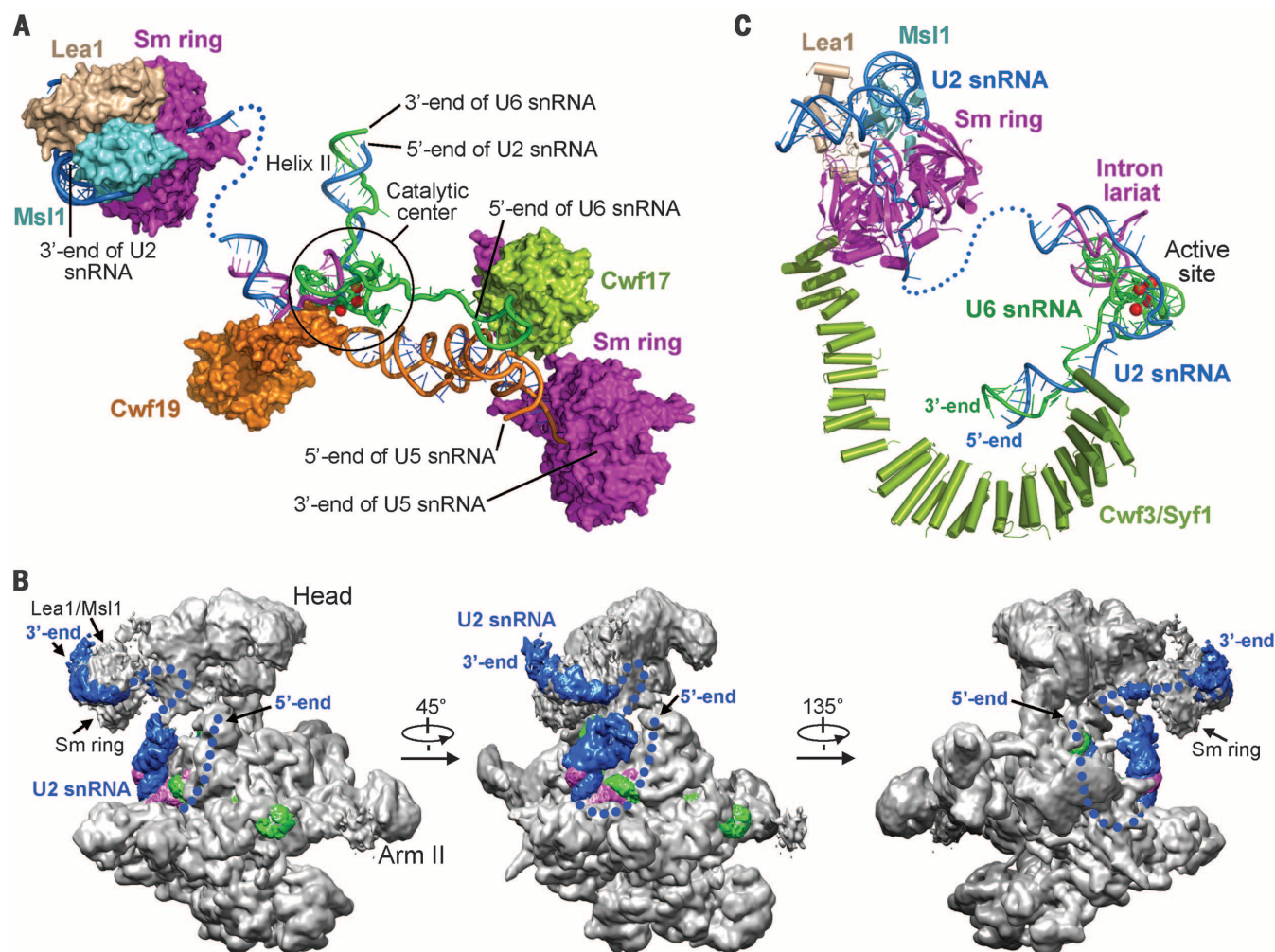
Fig. 5. Placement of RNA molecules by the protein components. (A) An overall view on the placement of three snRNAs in the spliceosome. Most of the protein components are omitted so as to highlight the characteristic organization of snRNAs. The ends of snRNAs are anchored away from the catalytic center, and their reactive pieces are placed into the catalytic center through protein-directed routes. (**B**) A surface view of the spliceosome so as to highlight the positioning of U2 snRNA. The 3′ end of U2 snRNA is anchored by Lea1/Msl1 in Arm I, whereas its 5′ end pairs up with the 3′ end of U6 snRNA at the tip of the Central Body. The intervening portion of the U2 snRNA sequences are continuously bound and directed by protein components, some of which remain to be identified owing to their flexibility. (**C**) An illustration of the placement of U2 snRNA.

intron (Fig. 7, A to C) (27–29). The ISL of U6 snRNA in the spliceosome corresponds to Domain V of the group IIB intron *P.li.LSUI2* from the brown algae *Pycnocoma littoralis* (29), and the Mg^{2+}-coordinating U68 in the spliceosome is replaced by the nucleotide A574 in *P.li.LSUI2*. The base-pairing interactions between the BPS of the intron lariat and U2 snRNA in the spliceosome are similar to those in Domain VI of the self-splicing intron, with the bulged branch adenine nucleotide in BPS corresponding to A615 in *P.li.LSUI2*. The catalytic triad A47-G48-C49 in the spliceosome is replaced by A551-G552-C553 in the group IIB intron. Formation of the triplex in the spliceosome also closely resembles that in the self-splicing intron (Fig. 7, B and C). The catalytically active Mg^{2+} ions are also similarly coordinated, by U68 in U6 snRNA and A574 in *P.li.LSUI2*. Both the positioning of the catalytic metal ions and the

catalytic triad are conserved, indicating a common evolutionary origin between these two ribozymes. In addition to the observed striking similarities in catalytic mechanism between the spliceosome and group IIB introns, the key protein component Spp42 (Prp8 in *S. cerevisiae*) contains an RT-like domain, whereas many group II introns depend on an RT for folding and activity (30).

Discussion

Splicing of pre-mRNA is an exceptionally dynamic and complex process. All five snRNPs are assembled in the spliceosomal B complex. Through the actions of the ATPases Prp28 (U5-100K in human) and Brr2, U1 and U4 snRNP are dissociated, forming an activated spliceosome [the activated B complex (B^{act})] (21, 23–26, 31). Then, the helicase Cdc28 (Prp2 in *S. cerevisiae*, hPrp2/HDX16 in human) dissociates the SF3a/b

complex from U2 snRNP, allowing BPS to participate in the Step I reaction in the catalytically competent spliceosome (B* complex) (32, 33). The Step I reaction is greatly facilitated by the presence of Cwf16 (Yju2 in *S. cerevisiae*, CCDC96 in human) and Cwf25 (cwc25 in *S. cerevisiae*, CWC25 in human), which juxtapose 5′SS and BPS. The catalytic step I spliceosome (C complex) is formed after the Step I reaction (34). Conformational rearrangement, induced by the ATPase Prp16, primes the 5′-exon and 3′SS for the initiation of the second step splicing (35–37). With the help of the splicing factors Slu7, Cdc40 (Prp17 in *S. cerevisiae*), Prp18, and the ATPase Prp22, the Step II reaction is completed, forming the post-catalytic spliceosome (P complex) (38–45). We speculate that the central components of the spliceosomal catalytic center—ISL of U6 snRNA, Helix I of the U2/U6 duplex, and Loop I of U5 snRNA—maintain a
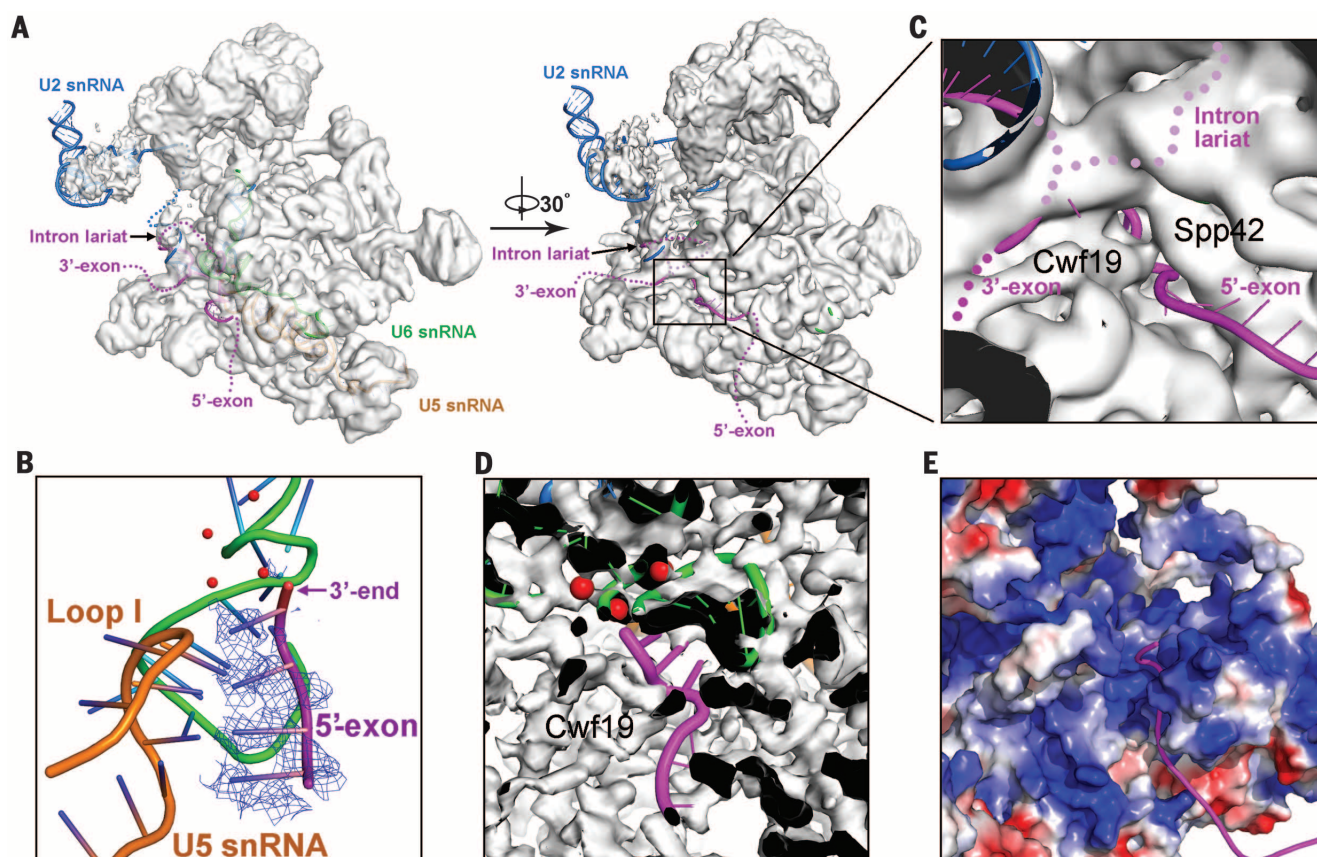
Fig. 6. The 5′-exon is likely located in a surface channel close to the active site. (**A**) An overall view on the potential position of 5′-exon in the spliceosome. Two views of the EM density of the entire spliceosome are shown, with the left displayed as a semitransparent surface. The 5′-exon has been modeled into the structure. (**B**) Weak EM density is found close to Loop I of U5 snRNA. This weak density, thought to belong to 5′-exon, allows putative model-ing of four contiguous RNA nucleotides. (**C**) The modeled 5′-exon can reach the active site through a surface channel. This channel is formed by Spp42 and Cwf19. (**D**) The modeled 5′-exon is located close to the catalytic Mg^{2+} ions. (**E**) The surface channel is highly enriched by positively charged amino acids. This feature is consistent with the suggestion that the channel is likely used to hold the 5′-exon.

generally similar conformation in the B^{act}, B*, C, and P complexes (fig. S7). In response to the different stages of the splicing reaction, the relative positions of 5′SS, BPS, 3′SS, and their associating U2 and U6 snRNA sequences may undergo concerted changes. In the B^{act} complex, the BPS and 5′SS are physically occluded from approaching each other (fig. S7), presum-ably by the presence of the SF3a/b complex. In the B* complex, the BPS and 5′SS are placed close to each other but can only proceed to the Step I reaction with the help of Cwf16 and Cwf25. In the C complex, the 5′-exon is poised for catalysis, but the 3′-exon needs to be brought into close proximity through the actions of Step II splicing factors. Last, in the P complex the 5′- and 3′-exons are ligated together and may only weakly associate with Loop I of U5 snRNA (fig. S7). Our model predicts a generally similar overall architecture among the four function-ally distinct spliceosomal complexes B^{act}, B*, C, and P. We further speculate that the splicing stage-specific factors and enzymes are recruited onto the generally similar spliceosomal com-plex to facilitate distinct stages of the splicing reaction.

Our structural analysis corroborates a large body of experimental observations. A U2/U6 three-way junction is formed at the core of the RNA network in the purified yeast spliceosome (Figs. 2 and 3), which was first proposed by Guthrie and colleagues in 1992 (46). Since then, extensive research effort has been directed at the structure and mechanism of this three-way junction. Involvement of the invariant triad AGC in the catalytic triplex has been confirmed with rescue experiments in which growth de-fects caused by triad mutation were suppressed by compensatory mutations in the predicted base-triple partners (6, 19, 46, 47). The U6 ISL, speci-fied by the bulged uridine nucleotide (U68 in S. pombe), adopts an unusual secondary structure and is indispensable for both steps of the splicing reaction (48, 49). Considering the invariant nu-cleotides in the catalytic center and the conserved catalytic mechanism, the human spliceosome should also contain the U2/U6 three-way junc-tion, rather than the proposed four-way junction (12). The observed structural features also sup-port the two-metal mechanism of pre-mRNA splicing and confirm the importance of the bulged uridine nucleotide in Mg^{2+} coordination

(2, 50). The observed U2/U6 three-way junction in our cryo-EM structure of *S. pombe* spliceo-some differs in a major way from the solution structure of an isolated U2/U6 snRNA complex from *S. cerevisiae* (51). In addition, the confor-mation of U6 snRNA in our structure is substan-tially different from that in the crystal structure of the core U6 snRNP (fig. S8) (47). Last, our structural analysis also confirms the detailed predictions of the RNA network in the spliceo-some (52).

Structural determination of the yeast spliceo-some at 3.6 Å resolution represents a major step forward for mechanistic understanding of the spliceosomal function. Spliceosome is a protein-controlled ribozyme. The RNA-based catalytic center is assembled on the scaffold of Spp42 and U5 snRNP. The ends of the snRNA are anchored away from the catalytic center, and the inter-vening sequences between the snRNA ends and the catalytic center are directed by both struc-tural protein components and RNP remodeling enzymes. Such a design likely optimizes the possibilities of regulation on the catalytic center and the splicing reaction. The collective action of the numerous protein components serves to
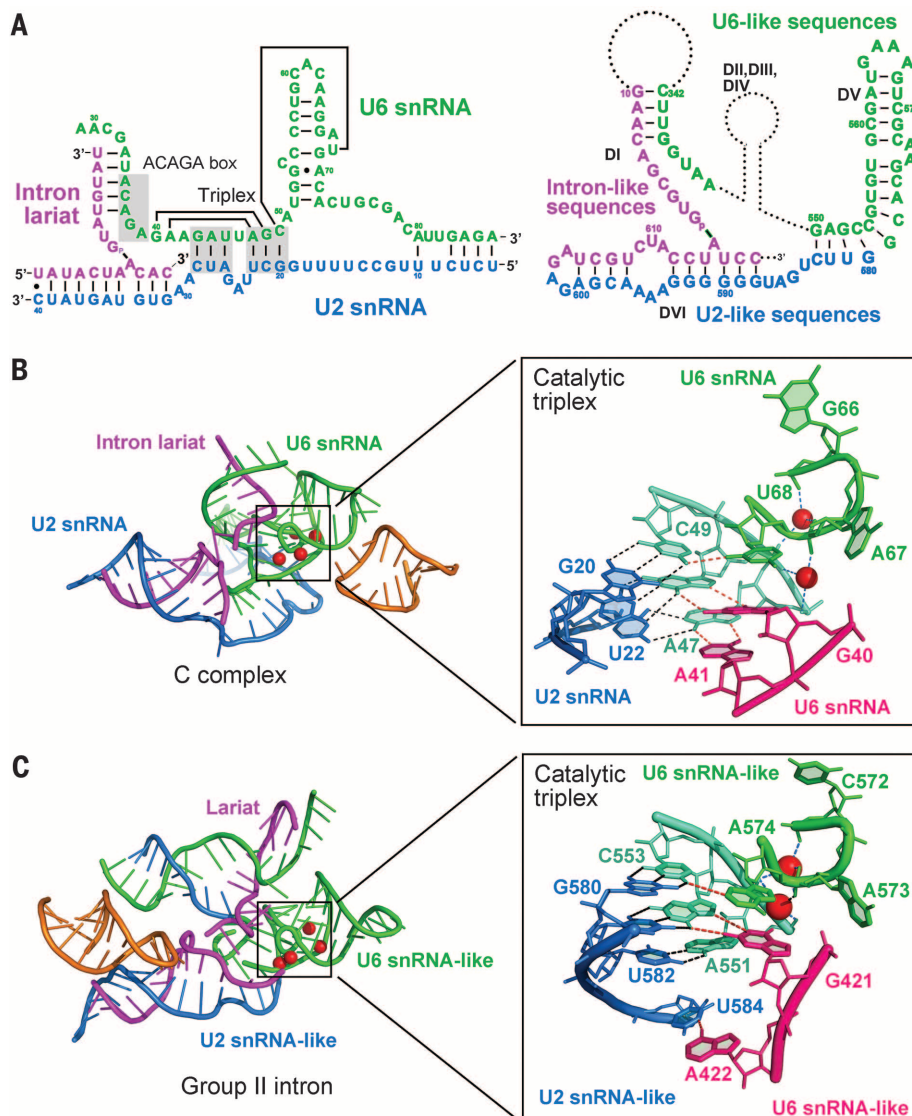
Fig. 7. Comparison of the catalytic centers between the spliceosome and the self-splicing group IIB intron. (**A**) Comparison of the secondary structural elements in the catalytic centers of the spliceosome and the self-splicing group IIB intron *P.li.LSUI2* from the brown algae *P. littoralis*. (**B**) Structure of the catalytic center of the spliceosome, with a close-up view on the catalytic triplex. Three bases from A41, G40, and U68 of U6 snRNA form non–Watson-Crick pairs with bases A47, G48, and C49, respectively. (**C**) Structure of the catalytic center of the self-splicing group IIB intron, with a close-up view on the catalytic triplex. A574 of the self-splicing intron corresponds to U68 in U6 snRNA, both playing a major role in Mg^{2+} coordination. Comparison between the spliceosome and the self-splicing group IIB intron was performed in PyMol (*48*).

deliver the critical pieces—5′SS, BPS, 3′SS, and 5′-exon—into the close proximity of the catalytic Mg^{2+} ions for catalysis.

REFERENCES AND NOTES

1. M. C. Wahl, C. L. Will, R. Lührmann, *Cell* **136**, 701–718 (2009).
2. S. M. Fica *et al.*, *Nature* **503**, 229–234 (2013).
3. M. J. Moore, C. C. Query, P. A. Sharp, in *The RNA World* (Cold Spring Harbor Monograph Archive, Cold Spring Harbor, NY, 1993).
4. T. A. Steitz, J. A. Steitz, *Proc. Natl. Acad. Sci. U.S.A.* **90**, 6498–6502 (1993).
5. P. M. Gordon, E. J. Sontheimer, J. A. Piccirilli, *RNA* **6**, 199–205 (2000).
6. S. M. Fica, M. A. Mefford, J. A. Piccirilli, J. P. Staley, *Nat. Struct. Mol. Biol.* **21**, 464–471 (2014).
7. E. J. Sontheimer, S. Sun, J. A. Piccirilli, *Nature* **388**, 801–805 (1997).
8. N. Toor, A. R. Robart, J. Christianson, S. Zimmerly, *Nucleic Acids Res.* **34**, 6461–6471 (2006).
9. A. M. Lambowitz, S. Zimmerly, *Cold Spring Harb. Perspect. Biol.* **3**, a003616 (2011).
10. S. Valadkhan, J. L. Manley, *Nature* **413**, 701–707 (2001).
11. D. G. Sashital, G. Cornilescu, C. J. McManus, D. A. Brow, S. E. Butcher, *Nat. Struct. Mol. Biol.* **11**, 1237–1242 (2004).
12. J. S. Sun, J. L. Manley, *Genes Dev.* **9**, 843–854 (1995).
13. S. Valadkhan, J. L. Manley, *RNA* **9**, 892–904 (2003).
14. L. Liu, C. C. Query, M. M. Konarska, *Nat. Struct. Mol. Biol.* **14**, 519–526 (2007).
15. R. J. Grainger, J. D. Beggs, *RNA* **11**, 533–557 (2005).
16. J. G. Umen, C. Guthrie, *Genetics* **143**, 723–739 (1996).
17. C. A. Collins, C. Guthrie, *Genes Dev.* **13**, 1970–1982 (1999).
18. W. P. Galej, T. H. Nguyen, A. J. Newman, K. Nagai, *Curr. Opin. Struct. Biol.* **25**, 57–66 (2014).
19. C. Yan *et al.*, *Science* **349**, 1182–1191 (2015).
20. C. L. Will, R. Lührmann, *Biol. Chem.* **386**, 713–724 (2005).
21. O. Cordin, D. Hahn, J. D. Beggs, *Curr. Opin. Cell Biol.* **24**, 431–438 (2012).
22. P. L. Raghunathan, C. Guthrie, *Curr. Biol.* **8**, 847–855 (1998).
23. D. Hahn, J. D. Beggs, *Biochem. Soc. Trans.* **38**, 1105–1109 (2010).
24. C. Maeder, A. K. Kutach, C. Guthrie, *Nat. Struct. Mol. Biol.* **16**, 42–48 (2009).
25. V. Pena *et al.*, *Mol. Cell* **35**, 454–466 (2009).
26. L. Zhang *et al.*, *Nat. Struct. Mol. Biol.* **16**, 731–739 (2009).
27. P. A. Sharp, *Cell* **42**, 397–400 (1985).
28. T. R. Cech, *Cell* **44**, 207–210 (1986).
29. A. R. Robart, R. T. Chan, J. K. Peters, K. R. Rajashankar, N. Toor, *Nature* **514**, 193–197 (2014).
30. S. Zimmerly, C. Semper, *Mob. DNA* **6**, 7 (2015).
31. J. Y. Chen *et al.*, *Mol. Cell* **7**, 227–232 (2001).
32. S. H. Kim, R. J. Lin, *Mol. Cell. Biol.* **16**, 6810–6819 (1996).
33. S. H. Kim, J. Smith, A. Claude, R. J. Lin, *EMBO J.* **11**, 2319–2326 (1992).
34. Y. F. Chiu *et al.*, *Mol. Cell. Biol.* **29**, 5671–5678 (2009).
35. B. Schwer, C. Guthrie, *Nature* **349**, 494–499 (1991).
36. B. Schwer, C. Guthrie, *EMBO J.* **11**, 5033–5039 (1992).
37. S. M. Burgess, C. Guthrie, *Cell* **73**, 1377–1391 (1993).
38. D. Bacíková, D. S. Horowitz, *RNA* **8**, 1280–1293 (2002).
39. A. Aronova, D. Bacíková, L. B. Crotti, D. S. Horowitz, B. Schwer, *RNA* **13**, 1437–1444 (2007).
40. L. B. Crotti, D. Bacíková, D. S. Horowitz, *Genes Dev.* **21**, 1204–1216 (2007).
41. M. Company, J. Arenas, J. Abelson, *Nature* **349**, 487–493 (1991).
42. R. M. Mayas, H. Maita, J. P. Staley, *Nat. Struct. Mol. Biol.* **13**, 482–490 (2006).
43. B. Schwer, *Mol. Cell* **30**, 743–754 (2008).
44. B. Schwer, C. H. Gross, *EMBO J.* **17**, 2086–2094 (1998).
45. J. D. Wagner, E. Jankowsky, M. Company, A. M. Pyle, J. N. Abelson, *EMBO J.* **17**, 2926–2937 (1998).
46. H. D. Madhani, C. Guthrie, *Cell* **71**, 803–817 (1992).
47. E. J. Montemayor *et al.*, *Nat. Struct. Mol. Biol.* **21**, 544–551 (2014).
48. W. L. DeLano, The PyMOL Molecular Graphics System; available at www.pymol.org (2002).
49. E. F. Pettersen *et al.*, *J. Comput. Chem.* **25**, 1605–1612 (2004).
50. S. L. Yean, G. Wuenschell, J. Termini, R. J. Lin, *Nature* **408**, 881–884 (2000).
51. J. E. Burke, D. G. Sashital, X. Zuo, Y. X. Wang, S. E. Butcher, *RNA* **18**, 673–683 (2012).
52. M. Anokhina *et al.*, *EMBO J.* **32**, 2804–2818 (2013).

REPORTS

MESOSCOPIC PHYSICS

Coherent manipulation of Andreev states in superconducting atomic contacts

C. Janvier,[1] L. Tosi,[1,2] L. Bretheau,[1]* Ç. Ö. Girit,[1]† M. Stern,[1] P. Bertet,[1] P. Joyez,[1] D. Vion,[1] D. Esteve,[1] M. F. Goffman,[1] H. Pothier,[1] C. Urbina[1]‡

Coherent control of quantum states has been demonstrated in a variety of superconducting devices. In all of these devices, the variables that are manipulated are collective electromagnetic degrees of freedom: charge, superconducting phase, or flux. Here we demonstrate the coherent manipulation of a quantum system based on Andreev bound states, which are microscopic quasi-particle states inherent to superconducting weak links. Using a circuit quantum electrodynamics setup, we performed single-shot readout of this Andreev qubit. We determined its excited-state lifetime and coherence time to be in the microsecond range. Quantum jumps and parity switchings were observed in continuous measurements. In addition to having possible quantum information applications, such Andreev qubits are a test-bed for the physics of single elementary excitations in superconductors.

The ground state of a uniform superconductor is a many-body coherent state. Microscopic excitations of this superconducting condensate—which can be created, for example, by the absorption of photons with high-enough energy—are delocalized and incoherent because they have energies in a continuum of states. Localized states arise in situations where the superconducting gap Δ or the superconducting phase undergo strong spatial variations: examples include Shiba states around magnetic impurities (1) and Andreev states in vortices (2) or in weak links between two superconductors (3). Because they have discrete energies within the gap, Andreev states are expected to be amenable to coherent manipulation (4–8). In the simplest weak link, a single conduction channel that is shorter than the superconducting coherence length ξ, there are only two Andreev levels $\pm E_A(\tau/\delta) = \pm\Delta\sqrt{1 - \tau\sin^2(\delta/2)}$, which are governed by the transmission probability τ of electrons through the channel and the phase difference δ between the two superconducting condensates (3). Despite the absence of actual barriers, quasi-particles (bogoliubons) occupying these Andreev levels are localized over a distance $\sim\xi$ around the weak link by the gradient of the superconducting phase, and the system can be considered an Andreev quantum dot (5, 6). Figure 1 shows the energies $E_{g,o,e}(\delta)$ of the different states of this dot. In the spin-singlet ground state $|g\rangle$, only the negative-energy Andreev level is occupied and $E_g = -E_A$. If a single quasi-particle is added, the dot reaches a spin-degenerate odd-parity state $|o\rangle$ with $E_o = 0$ (9–12). Adding a second quasi-particle of opposite spin to the dot in state $|o\rangle$ brings it to a spin-singlet even-parity excited state $|e\rangle$ with $E_e = +E_A$ (13, 14). The $|e\rangle$ state can also be reached directly from $|g\rangle$ by absorption of a photon of energy $2E_A$. In this work, we demonstrate experimentally the ma-

nipulation of coherent superpositions of states $|g\rangle$ and $|e\rangle$, even if parasitic transitions to $|o\rangle$ are also observed.

Atomic-size contacts are suitable systems to address the Andreev physics because they accommodate a small number of short conduction channels (15). We create them using the microfabricated break-junction technique (16). Figure 2 presents the sample used in the experiment. An aluminum loop with a narrow suspended constriction (Fig. 2C) is fabricated on a polyimide flexible substrate mounted on a bending mechanism cooled down to ~30 mK (17). The substrate is first bent until the bridge breaks. Subsequent fine-tuning of the bending allows creating different atomic contacts and adjusting the transmission probability of their channels. The magnetic flux ϕ threading the loop controls the phase drop $\delta = 2\pi\phi/\phi_0$ (ϕ_0, flux quantum) across the contact and, thus, also controls the Andreev transition frequency $f_A(\tau,\delta) = 2E_A/h$ (h, Planck's constant). To excite and probe the Andreev dot, the loop is inductively coupled to a niobium quarter-wavelength microwave resonator (17) (Fig. 2B) in a circuit quantum electrodynamics architecture (18, 19). The resonator is probed by reflectometry at a frequency f_0 close to its bare resonance frequency $f_R \simeq 10.134$ GHz. The actual resonator frequency is different for each one of the three Andreev dot states: In the odd state, the resonance frequency is unaltered, whereas the two even states lead to opposite shifts around f_R (20). The Andreev transition $|g\rangle\rightarrow|e\rangle$ is driven by a second tone of frequency f_1. Details of the setup are shown in figs. S1 and S2 (20).

Here we present data obtained on a representative atomic contact containing only one high-transmission channel. Data from other contacts are shown in figs. S6 to S8. First, we performed pulsed two-tone spectroscopy by applying a 13-μs driving pulse of variable frequency, immediately followed by a 1-μs-long measurement pulse ($f_0 \simeq 10.1337$ GHz) probing the resonator with an

[1]Quantronics Group, Service de Physique de l'État Condensé, CNRS UMR 3680, IRAMIS, CEA-Saclay, 91191 Gif-sur-Yvette, France. [2]Centro Atómico Bariloche and Instituto Balseiro, Comisión Nacional de Energía Atómica, 8400 Bariloche, Argentina.
*Present address: Department of Physics, Massachusetts Institute of Technology, Cambridge, MA 02215, USA. †Present address: USR 3573, CNRS, Collège de France, 11 Place Marcelin Berthelot, 75005 Paris, France. ‡Corresponding author. E-mail: cristian.urbina@cea.fr

Fig. 1. Single-channel Andreev quantum dot. (**A**) Energy levels: Two discrete Andreev bound levels detach symmetrically from the upper and lower continua of states (light gray regions for $|E| > \Delta$). Photons of energy $2E_A$ can induce transitions between the two Andreev levels (magenta arrows). (**B**) Occupation of Andreev levels in the four possible quantum states of the Andreev dot. Only the lower Andreev level is occupied in the ground state $|g\rangle$ (blue box). In the excited state $|e\rangle$ (red box), only the upper Andreev bound level is occupied. In the doubly degenerate odd state $|o\rangle$, both Andreev levels are either occupied or empty. (**C**) Energy of the four Andreev dot states for a channel of transmission probability $\tau = 0.98$, as a function of the phase difference δ across the weak link.

amplitude corresponding to an average number of photons in the resonator $\bar{n} \simeq 30$ (Fig. 3A). Apart from the signal at $f_1 \simeq f_0$, the spectrum displays a resonance corresponding to the Andreev transition. The spectrum is periodic in flux, with period ϕ_0, which allowed us to calibrate the value of δ across the contact (fig. S3). Fits of the measured lines for different contacts with the analytical form of $f_A(\tau, \delta)$ provide the transmission probability τ of highly transmitting channels with up to five significant digits, as well as the superconducting gap $\Delta/h = 44.3$ GHz of the aluminum electrodes.

The coupling between the resonator and the Andreev dot is evident from the avoided crossing between the two modes observed in single-tone continuous-wave spectroscopy (Fig. 3B). Fitting the data with the predictions of a Jaynes-Cummings model (19, 20) yields $g/2\pi = 74$ MHz (g, coupling strength) at the two degeneracy points where $f_A = f_R$. Notably, the resonance of the bare resonator is also visible for all values of the phase, signaling that on the time scale of the measurement the Andreev dot is frequently in the odd state $|o\rangle$ (10, 12, 21).

Figure 3C shows the density plots of the reflected signal quadratures (I and Q) corresponding to sequences of 8000 measurement pulses taken at $\delta = \pi$, without (Fig. 3C, left panel) and with (right panel) a π driving pulse applied just before each measurement pulse. The results gather in three separate clouds of points, demonstrating that a single measurement pulse allows resolution of the dot state. The normalized number of points in each cloud is a direct measurement of the populations of the three states.

The two panels of Fig. 3C show the population transfer between the two even states induced by the driving pulse. Continuous measurement of the state of the Andreev dot in the absence of drive reveals the quantum jumps (22) between the two even states and the changes of parity that correspond to the trapping and untrapping of quasi-particles in the dot (Fig. 3D). The analysis (23) of this real-time trace yields a parity-switching rate of ~50 kHz (20).

The coherent manipulation at $\delta = \pi$ of the two-level system formed by $|g\rangle$ and $|e\rangle$ is illustrated in Fig. 4. Figure 4A shows the Rabi oscillations between $|g\rangle$ and $|e\rangle$ obtained by varying the duration of a driving pulse at frequency $f_1 = f_A(\tau, \pi)$ (movie S1). Figure 4B shows how the populations of $|g\rangle$ and $|e\rangle$ change when the driving-pulse frequency f_1 is swept across the Andreev frequency
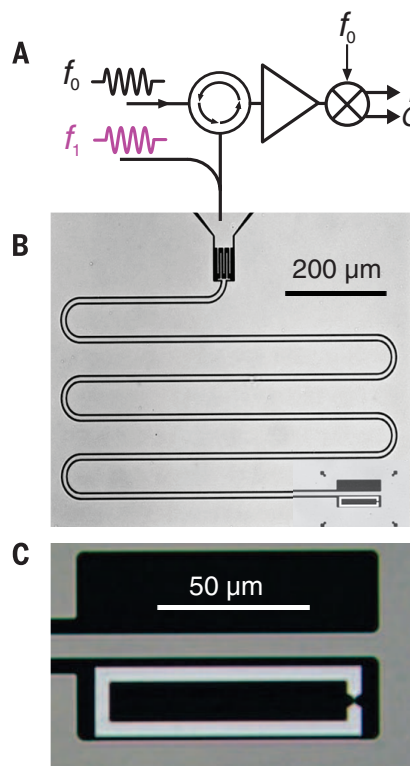
Fig. 2. Measurement setup of a superconducting atomic contact in a microwave resonator.
(**A**) Simplified two-tone microwave setup. The measurement (frequency f_0) and drive (frequency f_1) signals are coupled to the resonator through the same port. After amplification, the reflected signal at f_0 is homodyne-detected by an IQ mixer, and its two quadratures (I and Q) are digitized. (**B**) Optical micrograph of the quarter-wavelength niobium coplanar meander resonator with an interdigitated capacitor $C \simeq 3$ fF at the coupling port. At the shorted end, an aluminum loop is inductively coupled to the resonator field. The resonator has resonance frequency $f_R \simeq 10.134$ GHz, with a total quality factor $Q = 2200$, close to critical coupling (see fig. S4). (**C**) Detailed view of the aluminum loop. Upon bending the substrate, the loop breaks at the narrow constriction to create an atomic contact.
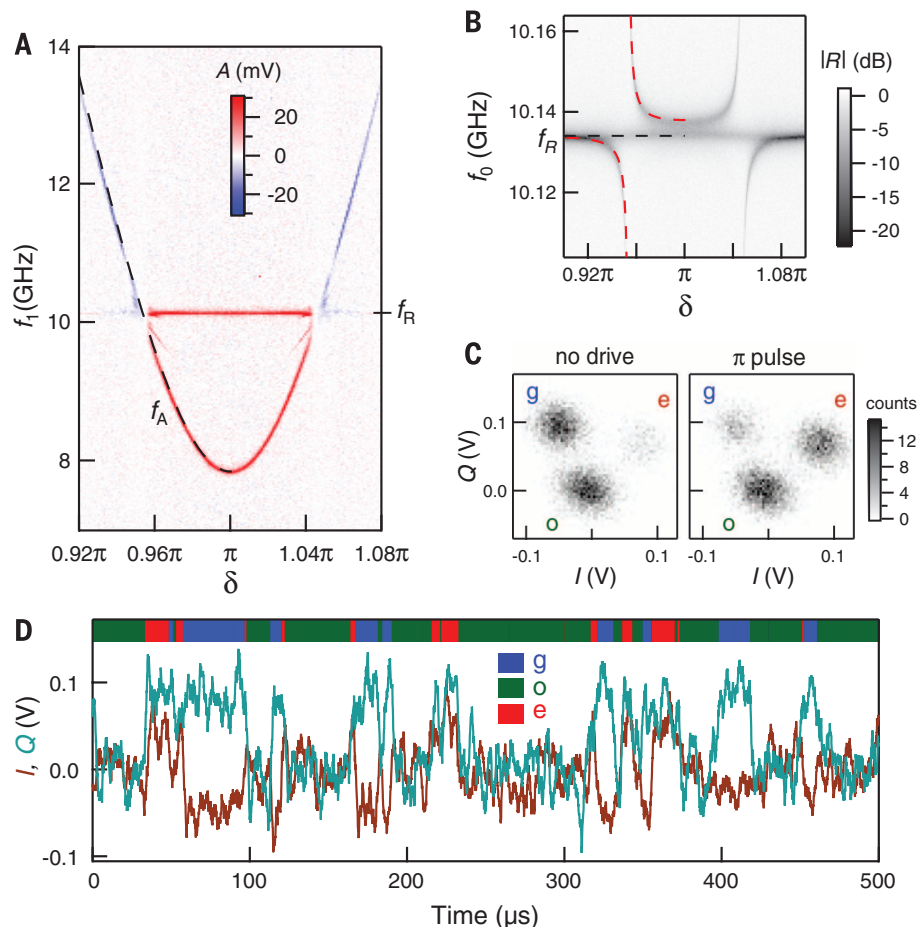
Fig. 3. Spectroscopy and quantum jumps. (**A**) Pulsed two-tone spectroscopy: color-coded amplitude A of one quadrature of reflected signal as a function of δ and f_1. The dashed black line shows the theoretical fit of Andreev transition frequency $f_A = 2E_A/h$ with $\tau = 0.99217$. A parasitic line, corresponding to a two-photon process $[2f_1 = f_R + f_A(\tau, \delta)]$, is visible just below 10 GHz. (**B**) Single-tone continuous-wave spectroscopy using a vector network analyzer (average number of photons in the resonator $\bar{n} \simeq 0.1$): resonator reflection amplitude $|R|$ as a function of δ and f_0. Red dashed curves correspond to fits of the anticrossings (20). Data aligned with the black dashed line correspond to the Andreev dot in state $|o\rangle$. (**C**) Density plots of I and Q quadratures at $\delta = \pi$ illustrate single-shot resolution of the quantum state of the dot. (Left) No drive at f_1. (Right) π pulse swapping the populations of $|g\rangle$ and $|e\rangle$. (**D**) Continuous measurement at $\delta = \pi$, with $\bar{n} \simeq 100$ and no driving signal. The brown (or cyan) time trace corresponds to the I (or Q) quadrature. The color (blue, green, or red) of the horizontal bar represents an estimate of the state (g, o, or e, respectively) found using a hidden Markov model toolbox (23).

$f_A(\tau,\pi)$. After a π pulse, the populations relax exponentially back to equilibrium with a relaxation time $T_1(\delta = \pi) \simeq 4$ μs (Fig. 4D). The Gaussian decay of detuned Ramsey fringes (Fig. 4F) provides a measurement of the coherence time $T_2^*(\delta = \pi) \simeq 38$ ns. This short coherence time is mainly due to low-frequency (i.e., lower-than-megahertz) fluctuations of the Andreev energy $E_A(\tau,\delta)$, as shown by the much longer decay time $T_2(\delta = \pi) \simeq 565$ ns $\gg T_2^*$ of a Hahn echo (Fig. 4G). Measurements at $\delta = \pi$ on other contacts with the same sample, with transmissions corresponding to a minimal Andreev frequency 3 GHz $< f_A(\tau,\pi) < 8$ GHz, give T_1 mostly around 4 μs (up to 8.5 μs), T_2^* around 40 ns (up to 180 ns), and T_2 around 1 μs (up to 1.8 μs), but no clear dependence of the characteristic times on τ is observed (figs. S7 and S8).

Figure 4E shows the measured relaxation rate $\Gamma_1 = 1/T_1$ as a function of the phase δ. The expected Purcell relaxation rate arising from the dissipative impedance seen by the atomic contact (light blue line in Fig. 4E) matches the experimental results only close to the degeneracy points where $f_A = f_R$ (vertical dotted lines) but is about five times smaller at $\delta = \pi$. On the basis of existing models, we estimate that relaxation rates due to quasi-particles (24–28) and phonons (7, 8, 21) are negligible. Empirically, we fit the data at $\delta = \pi$ by considering an additional phase-independent relaxation mechanism, which remains to be identified.

The linewidth of the spectroscopy line, which is a measure of the decoherence rate, shows a minimum at $\delta = \pi$ (Fig. 4C). The Gaussian decay of the Ramsey oscillations points to 1/f transmission fluctuations as the main source of decoherence at $\delta = \pi$, where the system is insensitive to flux noise to first order (28). Fluctuations of τ can arise from vibrations in the mechanical setup and from motion of atoms close to the contact. Figure 4C also shows the linewidths calculated, assuming 1/f transmission noise and both white and 1/f flux noise (20). The amplitude of the 1/f transmission noise, 2.5×10^{-6} Hz$^{-1/2}$ at 1 Hz, was adjusted to fit the measurement at $\delta = \pi$. The amplitudes of the white and 1/f flux noise were then obtained from a best fit of the linewidth phase dependence. The extracted 1/f noise amplitude (5 μϕ_0 Hz$^{-1/2}$ at 1 Hz) is a typical value for superconducting devices and has a negligible effect to second order (29). The source of the apparent white flux noise (48 nϕ_0 Hz$^{-1/2}$) has not yet been identified.

The Andreev quantum dot has been proposed as a new kind of superconducting qubit (5, 6), which differs markedly from existing ones (30). In qubits based on charge, flux, or phase (30), the states encoding quantum information correspond to collective electromagnetic modes, whereas in Andreev qubits they correspond to microscopic degrees of freedom of the superconducting condensate. Our results are a proof of concept of this new type of qubit. Further work is needed to fully understand the sources of decoherence and to couple several qubits in multichannel contacts (5, 8). With its parity sensitivity, the Andreev
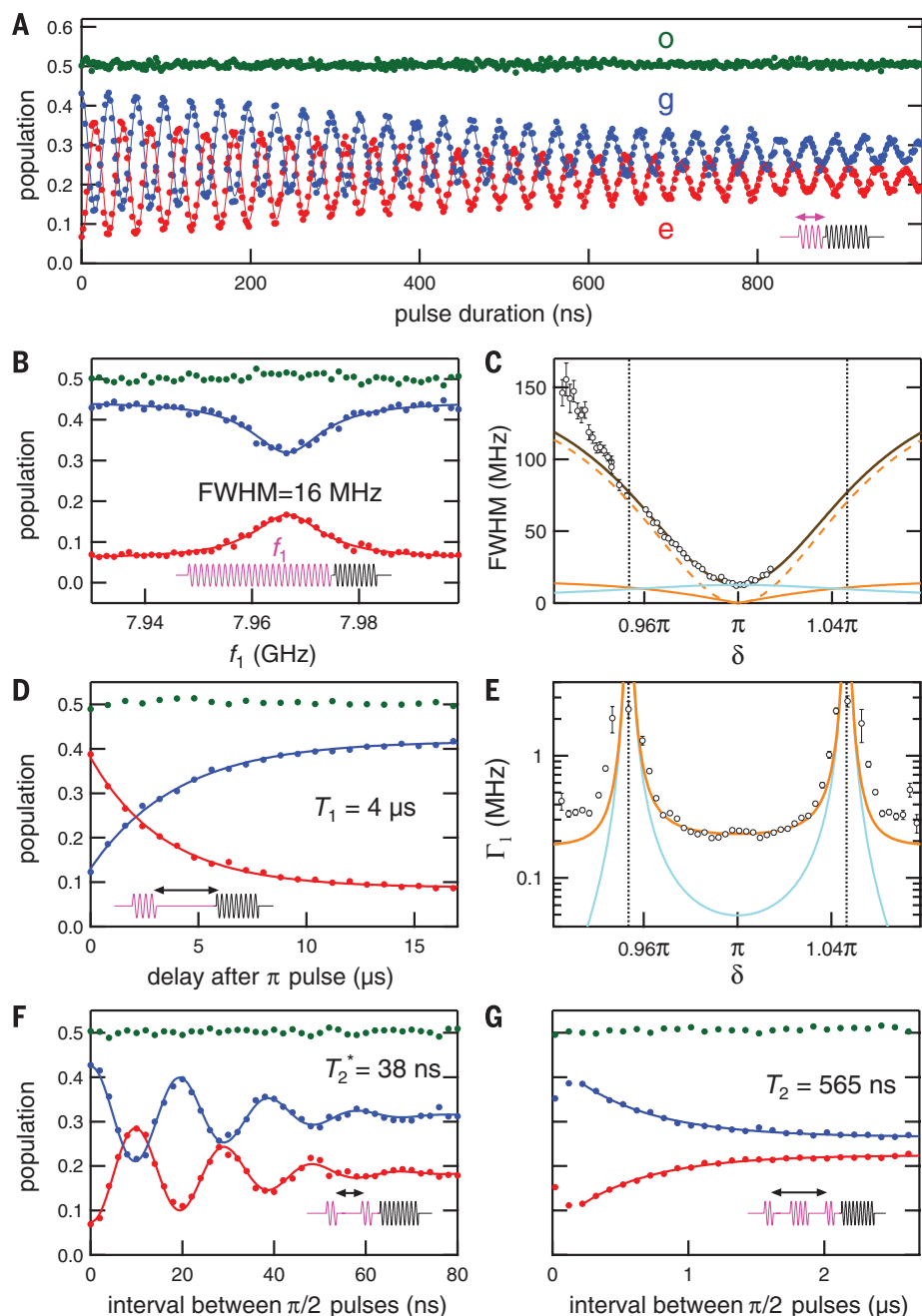
Fig. 4. Coherent manipulation of Andreev quantum dot states at δ = π. Colored dots show measured populations: ground (blue), excited (red), and odd (green) states. Lines indicate theoretical fits. Sketches of pulse sequences for each type of measurement are shown in each panel (magenta, drive; black, measurement). (**A**) Rabi oscillations: populations as a function of the driving-pulse duration. (**B**) Spectroscopy: populations as a function of frequency f_1 of the saturating drive pulse. FWHM, full width at half maximum. (**C**) Phase dependence of the linewidth (FWHM) of the spectral line. Circles correspond to the result of a Lorentzian fit of the experimental resonances (20). The brown curve is the best fit to the data, including the contributions of 1/f transmission noise (light blue line) and both 1/f (orange line) and white flux noise (orange dashed line). (**D**) Relaxation of populations after a π driving pulse. (**E**) Phase dependence of relaxation rate $\Gamma_1 = 1/T_1$. Circles represent experimental data. The orange curve is the sum of the expected Purcell rate (light blue line) and an empirical phase-independent rate (180 kHz). In (C) and (E), vertical dotted lines indicate degeneracy points $f_A = f_R$. Error bars on circles denote uncertainties of the fits. (**F**) Ramsey fringes: populations as a function of delay between the two π/2 pulses detuned at $f_1 = f_A(\tau,\pi) + 51$ MHz. (**G**) Hahn echo: populations as a function of delay between the two π/2 pulses with a π pulse in between.

quantum dot is also a powerful tool to investigate quasi-particle–related limitations on the performance of superconducting qubits (*28, 31, 32*) and detectors (*33*). Furthermore, our experimental strategy could be used to explore hybrid superconducting devices in the regime where Andreev states evolve into Majorana states (*34–36*).

REFERENCES AND NOTES

1. K. J. Franke, G. Schulze, J. I. Pascual, *Science* **332**, 940–944 (2011).
2. C. Caroli, P. G. de Gennes, J. Matricon, *Phys. Lett.* **9**, 307–309 (1964).
3. C. W. J. Beenakker, H. van Houten, *Phys. Rev. Lett.* **66**, 3056–3059 (1991).
4. M. A. Despósito, A. Levy Yeyati, *Phys. Rev. B* **64**, 140511(R) (2001).
5. A. Zazunov, V. S. Shumeiko, E. N. Bratus', J. Lantz, G. Wendin, *Phys. Rev. Lett.* **90**, 087003 (2003).
6. N. M. Chtchelkatchev, Yu. V. Nazarov, *Phys. Rev. Lett.* **90**, 226806 (2003).
7. A. Zazunov, V. S. Shumeiko, G. Wendin, E. N. Bratus', *Phys. Rev. B* **71**, 214505 (2005).
8. C. Padurariu, Yu. V. Nazarov, *Europhys. Lett.* **100**, 57006 (2012).
9. J.-D. Pillet *et al.*, *Nat. Phys.* **6**, 965–969 (2010).
10. M. Zgirski *et al.*, *Phys. Rev. Lett.* **106**, 257003 (2011).
11. E. M. Levenson-Falk, F. Kos, R. Vijay, L. Glazman, I. Siddiqi, *Phys. Rev. Lett.* **112**, 047002 (2014).
12. A. Zazunov, A. Brunetti, A. Levy Yeyati, R. Egger, *Phys. Rev. B* **90**, 104508 (2014).
13. L. Bretheau, Ç. Ö. Girit, H. Pothier, D. Esteve, C. Urbina, *Nature* **499**, 312–315 (2013).
14. L. Bretheau, Ç. Ö. Girit, C. Urbina, D. Esteve, H. Pothier, *Phys. Rev. X* **3**, 041034 (2013).
15. E. Scheer, P. Joyez, D. Esteve, C. Urbina, M. H. Devoret, *Phys. Rev. Lett.* **78**, 3535–3538 (1997).
16. J. M. van Ruitenbeek *et al.*, *Rev. Sci. Instrum.* **67**, 108 (1996).
17. C. Janvier *et al.*, *J. Phys. Condens. Matter* **26**, 474208 (2014).
18. A. Wallraff *et al.*, *Nature* **431**, 162–167 (2004).
19. G. Romero, I. Lizuain, V. S. Shumeiko, E. Solano, F. S. Bergeret, *Phys. Rev. B* **85**, 180506 (2012).
20. Materials and methods are available as supplementary materials on *Science* Online.
21. D. G. Olivares *et al.*, *Phys. Rev. B* **89**, 104504 (2014).
22. R. Vijay, D. H. Slichter, I. Siddiqi, *Phys. Rev. Lett.* **106**, 110502 (2011).
23. M. Greenfield, D. S. Pavlichin, H. Mabuchi, D. Herschlag, *PLOS ONE* **7**, e30024 (2012).
24. J. M. Martinis, M. Ansmann, J. Aumentado, *Phys. Rev. Lett.* **103**, 097002 (2009).
25. G. Catelani, R. J. Schoelkopf, M. H. Devoret, L. I. Glazman, *Phys. Rev. B* **84**, 064517 (2011).
26. F. Kos, S. E. Nigg, L. I. Glazman, *Phys. Rev. B* **87**, 174521 (2013).
27. I. M. Pop *et al.*, *Nature* **508**, 369–372 (2014).
28. C. Wang *et al.*, *Nat. Commun.* **5**, 5836 (2014).
29. Y. Makhlin, A. Shnirman, *Phys. Rev. Lett.* **92**, 178301 (2004).
30. J. Clarke, F. K. Wilhelm, *Nature* **453**, 1031–1042 (2008).
31. U. Vool *et al.*, *Phys. Rev. Lett.* **113**, 247001 (2014).
32. D. Ristè *et al.*, *Nat. Commun.* **4**, 1913 (2013).
33. P. J. de Visser *et al.*, *Phys. Rev. Lett.* **106**, 167004 (2011).
34. W. Chang, V. E. Manucharyan, T. S. Jespersen, J. Nygård, C. M. Marcus, *Phys. Rev. Lett.* **110**, 217005 (2013).
35. V. Mourik *et al.*, *Science* **336**, 1003–1007 (2012).
36. D. Chevallier, P. Simon, C. Bena, *Phys. Rev. B* **88**, 165401 (2013).

CRITICAL PHENOMENA

Critical behavior at a dynamic vortex insulator-to-metal transition

Nicola Poccia,[1,2] Tatyana I. Baturina,[3,4,5] Francesco Coneri,[1] Cor G. Molenaar,[1] X. Renshaw Wang,[1] Ginestra Bianconi,[6] Alexander Brinkman,[1] Hans Hilgenkamp,[1] Alexander A. Golubov,[1,7] Valerii M. Vinokur[5]*

An array of superconducting islands placed on a normal metal film offers a tunable realization of nanopatterned superconductivity. This system enables investigation of the nature of competing vortex states and phase transitions between them. A square array creates the eggcrate potential in which magnetic field–induced vortices are frozen into a vortex insulator. We observed a vortex insulator–vortex metal transition driven by the applied electric current and determined critical exponents that coincided with those for thermodynamic liquid-gas transition. Our findings offer a comprehensive description of dynamic critical behavior and establish a deep connection between equilibrium and nonequilibrium phase transitions.

C ritical behaviors near phase transitions can be classified into universality classes determined only by a few properties characterizing the system, such as space dimensionality, range of interaction, and symmetry (*1, 2*). A paradigmatic concept of universality brought deep understanding of equilibrium critical phenomena [see, e.g., (*3*) and references therein]. Phase transitions and criticality far from equilibrium are less well understood. The experimental evidence for universality of nonequilibrium phase transitions is still scarce, calling for intensified experimental efforts.

Superconducting vortices offer a unique tunable laboratory for studying classical critical dynamics. To that end, we prepared an array of superconducting islands where vortices are pinned between the islands in the areas of weaker proximity-induced superconductivity—that is, at the energy dimples of an eggcrate potential (*4*). If thermal fluctuations are not strong enough to overcome the combined localizing action of mutual repulsion and pinning, vortices form the so-called vortex Mott insulating state at commensurate

[1]MESA+ Institute for Nanotechnology, University of Twente, 7500 AE Enschede, Netherlands. [2]Rome International Center for Materials Science Superstripes (RICMASS), Via dei Sabelli 119A, 00185 Roma, Italy. [3]A. V. Rzhanov Institute of Semiconductor Physics, Siberian Branch of the Russian Academy of Sciences, Novosibirsk 630090, Russia. [4]Novosibirsk State University, Novosibirsk 630090, Russia. [5]Materials Science Division, Argonne National Laboratory, Argonne, IL 60637, USA. [6]School of Mathematical Sciences, Queen Mary University of London, London E1 4NS, UK. [7]Moscow Institute of Physics and Technology, Dolgoprudnyi, Moscow District, Russia.
*Corresponding author. E-mail: vinokur@anl.gov

fields corresponding to an integer number of vortices per pinning site (*5*). The predicted vortex Mott state seen in experiments on antidot arrays in superconducting films (*6, 7*) was conclusively confirmed in (*8*). In our experiment, performed in a classical regime, varying the magnetic field provides precise control over the vortex density and tunes the ratio of the vortex repulsion to the mobility, enabling the observation of a vortex insulator-to-metal transition.

Each of our samples consists of a 40-nm Au layer, patterned as a four-point setup in a van der Pauw configuration for transport measurements, on a Si/SiO$_2$ substrate (*9*). The Au pattern is overlaid with a square array of superconducting niobium (Nb) islands 45 nm thick. An array contains 90,000 Nb islands placed with a period a = 267 nm. The diameter of an island is 220 ± 3 nm and the island separation is 47 ± 3 nm. Shown in Fig. 1, A to D, are scanning electron microscopy (SEM), atomic force microscopy (AFM), and optical images of a sample and the height profile along one of the principal axes of the array. The superconducting transition temperature of the array, determined as the midpoint of the temperature resistance curve in the upper inset in Fig. 1A, is T_c = 7.3 K, which is 2 K lower than that of bulk Nb (T_{c0} = 9.3 K). This implies that the array is a strongly coupled network of superconducting islands (*10–12*). The parameters of our array ensure that the intersite barriers are high enough to provide pinning sufficient for formation of the vortex Mott insulator state and that vortex motion is thermally activated.

The measurements are carried out in a shielded cryostat at temperature T = 1.4 K. Figure 2A shows
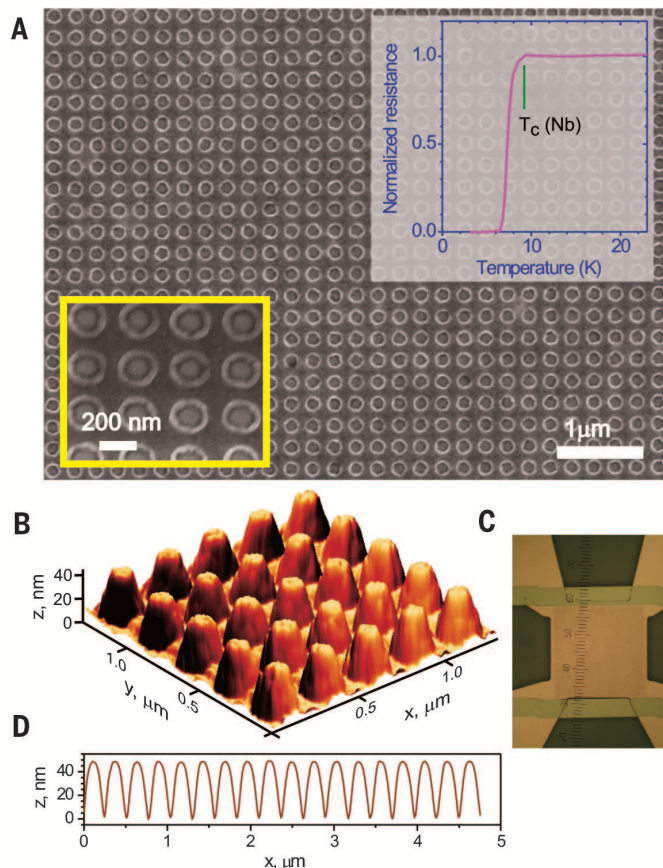
color plots of the differential resistance, dV/dI, as a function of the applied current and the magnetic field in units of frustration parameter $f = B/B_0$,

where $B_0 = \Phi_0/a^2 = 28.6$ mT, and $\Phi_0 = \pi\hbar/e$ is the magnetic flux quantum. Figure 2B displays representative isocurrent cuts as dV/dI versus B.

At modest currents, the data reveal a wealth of dips in dV/dI at integer frustrations, namely at $f = 1, 2,$ and 3 (corresponding to integer numbers of flux quanta per elemental square of an array), as well as a fine structure of fractional dips at $f = \frac{1}{3}, \frac{1}{2}, \frac{2}{3}, \frac{4}{3}, \frac{3}{2}, \ldots$. These minima reflect the modulation of the ground-state energy E_g due to formation of periodic vortex patterns in a magnetic field (Fig. 2, C and D). The energy spectrum of the fractional vortex Mott insulator shown in Fig. 2C is the Hofstadter butterfly spectrum of the Harper equation (13). The dips in the resistance and singularities in magnetization at commensurate frustrations were observed in numerous experiments [see (14) and references therein].

Our key observation is a reversal of the minima in dV/dI into maxima at rational f upon increasing the current bias. Scaling analysis (see below) shows that this is a direct manifestation of the existence of the vortex Mott insulator and its transition into a metallic state. Reversals at commensurate fields $f_c = \frac{1}{3}, \frac{1}{2}, \frac{2}{3}, 1, \ldots$ are most pronounced at integer and half-integer frustration factors (Fig. 2B). The insulating behavior appears as a tendency to downward divergence of the dV/dI traces on approach to f_c. Upon the vortex Mott insulator-to-metal transition with the increasing current, an upward divergence of dV/dI traces marks the metallic-like dV/dI behavior near f_c. Figure 3 shows the plots of dV/dI versus B in the vicinity of $f_c = \frac{1}{2}, 1, 2$. Similar minima-to-maxima flips were observed in regular superconducting systems of different geometries (15, 16). However, the mechanism of current-stimulated depinning proposed in (15, 16) would lead to disappearance of the dips in the resistance $R = V/I$ responsible for the dissipation, and not only in dV/dI. This is not the case in our

Fig. 1. Experimental setup.

Fig. 1. Experimental setup. (**A**) SEM image of the square array of Nb islands on Au. The inset at lower left is a magnified image of the array. The inset at upper right shows the temperature dependence of the resistance near the superconducting transition T_c of bulk Nb (marked by the vertical bar). (**B**) 1.4 μm × 1.4 μm AFM topography of the superconductor islands on the metallic template of the same sample. (**C**) Optical image of the Au template with four contacts (yellow), Nb bus bars (light green), and the array of 300 × 300 Nb islands barely visible as a red square shadow on a Si/SiO$_2$ substrate (dark green). (**D**) Height profile along the principal axis of the array.

Fig. 2. Vortex Mott insulator-to-metal transition. (**A**) Color plots of dV/dI versus current and magnetic field. The color scale indicates dV/dI values in ohms. (**B**) Representative dV/dI versus $f = B/B_0$ curves at different bias currents. At low current bias (blue, orange, and yellow), dV/dI minima at $f = \frac{1}{3}, \frac{1}{2}, \frac{2}{3}, 1, \frac{4}{3}, \frac{3}{2}, \frac{5}{3}, 2, \frac{7}{3}, \frac{5}{2}, \frac{8}{3},$ and 3 indicate formation of a vortex Mott insulator. Increasing current reverses minima into maxima (red

and violet). Reversals manifesting the insulator-to-metal transition are highlighted by vertical arrows. (**C**) Ground-state energy E_g versus f obtained from the Harper equation (14, 23). (**D**) Vortex configurations at rational frustrations $f = 0, \frac{1}{3}, \frac{1}{2}, \frac{2}{3},$ and 1. Periodic arrays of vortices (yellow circles) are superimposed on the SEM subimages of the square array of Nb islands.

experiment (see fig. S1). The resistance exhibits pronounced dips indicating strong pinning at rational f even at the currents where dV/dI shows profound maxima. Hence, the dip-to-maxima flips cannot be explained as vortex depinning.

Shown in the upper row of Fig. 3 are detailed plots of dV/dI versus B in the vicinity of $f_c = \frac{1}{2}$, 1, 2. There are separatrices, $I_0^\pm$, highlighted by dots in Fig. 3, A to C, dividing insulating-like and metallic-like curves. We identify $I_0^\pm$ as critical currents at which the dynamic vortex Mott transition occurs, and find them from the condition $d(dV/dI)/df|_{f=f_c^\pm} = 0$. For $I > I_0^+$ the dV/dI traces display minima, marked by strokes in Fig. 3, A to C. That I_0^- and I_0^+ are different implies that in the current intervals $I \in (\min\{I_0^-, I_0^+\}, \max\{I_0^-, I_0^+\})$ at commensurate values f, vortex Mott insulating and metallic phases coexist (17).

Now we turn to the proximity of the vortex insulator-to-metal transition critical point, (I_0, f_c). We conjecture mapping of the variables describing the critical behavior of the static electronic Mott transition to those of the dynamic vortex Mott transition (9): $|U - U_c| \rightarrow b = |f_c - f|$, $|T - T_c| \rightarrow |I - I_0|$, and the critical point $(T_c, U_c) \rightarrow (I_0, f_c)$,

yielding critical scaling $|I - I_0| \propto |b|^\varepsilon$. To demonstrate the critical behavior, we scale dV/dI data into the universal form

$$\frac{dV(f, I)}{dI} - \left[\frac{dV(f, I)}{dI}\right]_{I = I_0} = F_\pm\left(\frac{|I - I_0^\pm|}{|b|^\varepsilon}\right) \quad (1)$$

where ε is an adjustable parameter. The best fit of the data near $f_c = \frac{1}{2}$ is achieved at $\varepsilon = \frac{1}{2}$ (Fig. 3D). The same procedure for the left and right sides of $f_c = 1$ and 2 gives rise to $\varepsilon = \frac{2}{3}$ (Fig. 3, E and F). Double-logarithmic plots in the vicinity of the above values of f_c display a power-law functional form of $F_\pm(x) \propto x^\mu$, as shown in the lower panels of Fig. 3, D to F. For $f_c = \frac{1}{2}$, we find $\mu = 1 \pm 0.03$. For both $f_c = 1$ and $f_c = 2$, we find $\mu = 1.2 \pm 0.03$ for all four plots. This universal scaling behavior of dV/dI experimentally establishes the existence of the vortex Mott insulator and the dynamic vortex insulator-to-metal transition in superconducting networks.

To gain insight into the observed scaling behaviors, we focus on $f_c = 1$. At $I \ll I_0$, thermally activated dynamics of vortices is governed by motion of large vortex bundles and occurs via a creep

mechanism without breaking the vortex lattice integrity, resulting in $V \propto \exp(-I_0/I)$ (18). General creep considerations (19) suggest that at some threshold current less than the depinning current, the elastic continuity of the vortex system breaks down and vortex dynamics occurs via the plastic gliding of dislocations. The latter is equivalent to phase slips of the superconducting order parameter resulting in the linear ohmic response (i.e., the metallic behavior). Identifying this plastic threshold current with I_0 leads to the notion that the vortex metal is a phase whose dynamics is controlled by phase slips. Very near the threshold, $I \rightarrow I_0$, thermally activated dynamics are governed by activation over a small parabolic barrier whose height scales as $[1 - (I/I_0)]^{3/2}$, giving rise to

$$V \propto \frac{1}{1 + \exp\{\text{const}[1 - (I/I_0)]^{3/2}\}} \quad (2)$$

(20). Thus, the characteristic energy controlling the response of the vortex system near the vortex insulator-to-metal transition scales as $|I - I_0|^{3/2}$, which explains the origin of the experimentally observed scaling $|b| \propto |I - I_0|^{3/2}$
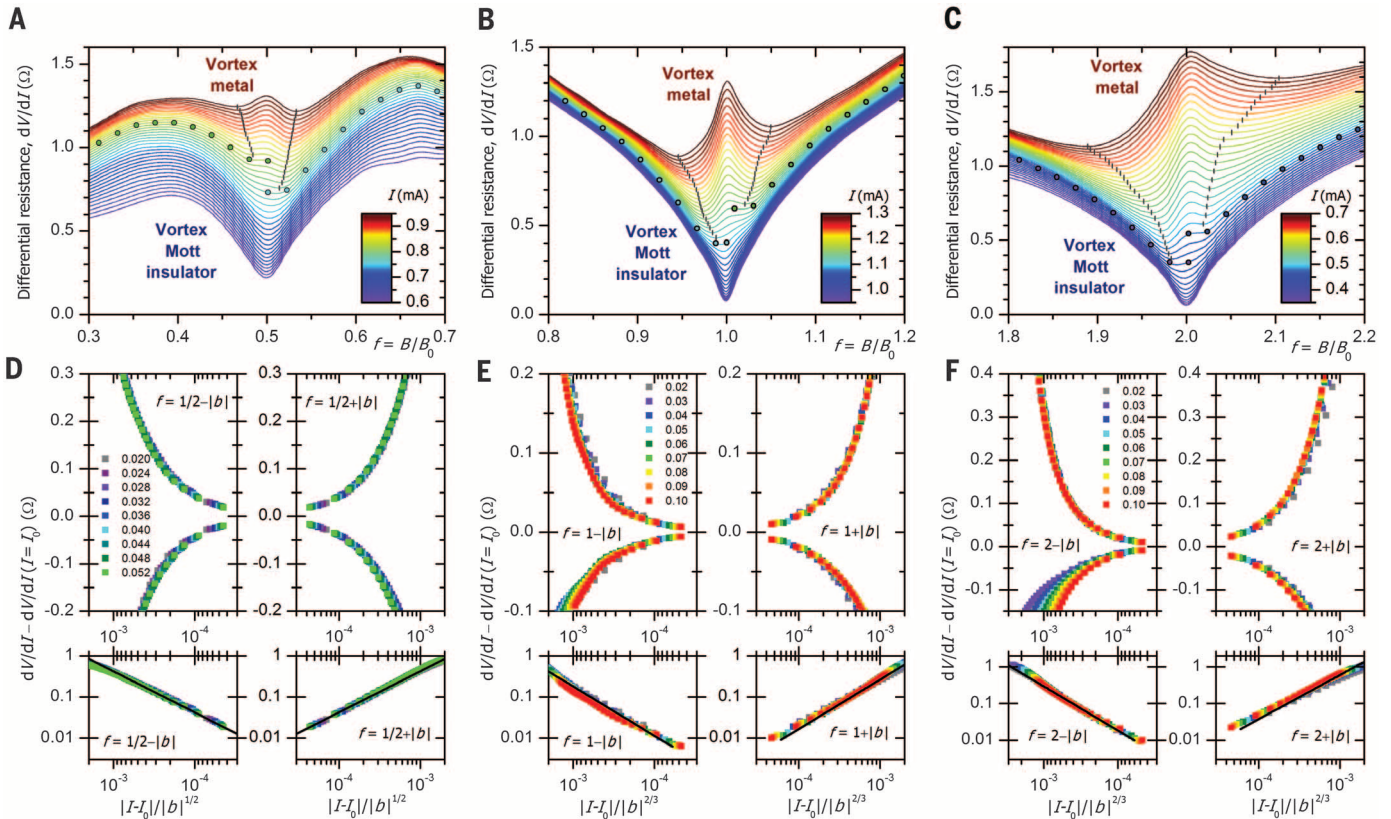
Fig. 3. Scaling at the dynamic vortex Mott insulator-to-metal transition. (A to C) dV/dI versus f in the vicinity of $f_c = \frac{1}{2}$, 1, and 2, respectively. Each panel contains 36 traces in 0.01-mA steps. Colors reflect magnitudes of the current. The dots mark $(dV/dI)(I = I_0)$ values separating insulating-like and metallic-like behaviors. The separatrix traces are chosen so that dV/dI values start to turn upward on approach to f_c at $I > I_0$, dV/dI maintains a downward trend near f_c at $I < I_0$, and $d(dV/dI)/df|_{f = f_c} = 0$ at $I = I_0$. In the metallic regions, dV/dI minima marked with strokes enclose the critical regions around f_c. The traces are not symmetric with respect to f_c, so I_0^- and I_0^+ are different: (A) $I_0^- = 0.83$ mA, $I_0^+ = 0.78$ mA;

(B) $I_0^- = 1.10$ mA, $I_0^+ = 1.14$ mA; (C) $I_0^- = 0.45$ mA, $I_0^+ = 0.48$ mA. **(D to F)** Scaling of the same data after subtracting the corresponding separatrix, $dV/dI - (dV/dI)(I = I_0)$ with respect to variable $|I - I_0|/|b|^{(\delta-1)/\delta}$ with $b = f - f_c$ and $\delta = 2$ for $f_c = \frac{1}{2}$ (D) and $\varepsilon = \frac{2}{3}$ for $f_c = 1$ and $f_c = 2$ [(E) and (F)]. Subpanels at left and right show scaling plots in the $f_c - |b|$ and $f_c + |b|$ vicinities of the critical frustration parameters, respectively; the colors refer to different $|b|$ values. Upper panels use the linear scales of $dV/dI - (dV/dI)(I = I_0)$; lower panels use logarithmic scales. The scales are the same for each f_c pairwise for the left and right subpanels. The black lines in the lower panels correspond to powers $\mu = 1$ for $f_c = \frac{1}{2}$, and to $\mu = 1.2 \pm 0.03$ for $f_c = 1$ and 2.

for integer frustrations. Notably, the observed value of $\varepsilon = {}^2/_3$ for the integer dynamic transition coincides with the corresponding mean-field value for the temperature- and pressure-driven thermodynamic electronic Mott transition (21) belonging in the class of the liquid-gas transition of classical systems (1, 21, 22). The universal scaling properties of the current- and magnetic field–dependent dynamical resistivity experimentally demonstrate that a vortex Mott insulator undergoes a phase transition resembling a liquid-to-gas transition at the nonequilibrium critical end point. The critical exponent at $f_c = {}^1/_2$ is $\varepsilon = {}^1/_2$, indicating that fractional vortex Mott transitions belong in different universality classes.

REFERENCES AND NOTES

1. L. P. Kadanoff *et al.*, *Rev. Mod. Phys.* **39**, 395–431 (1967).
2. M. E. Fisher, *Rev. Mod. Phys.* **46**, 597–616 (1974).
3. M. Henkel, H. Hinrichsen, S. Lübeck, *Non-Equilibrium Phase Transitions* (Springer, New York, 2008).
4. R. S. Newrock, C. J. Lobb, U. Geigenmüller, M. Octavio, *Solid State Phys.* **54**, 263–512 (1999).
5. D. R. Nelson, V. M. Vinokur, *Phys. Rev. B* **48**, 13060–13097 (1993).
6. M. Baert, V. V. Metlushko, R. Jonckheere, V. V. Moshchalkov, Y. Bruynseraede, *Phys. Rev. Lett.* **74**, 3269–3272 (1995).
7. K. Harada *et al.*, *Science* **274**, 1167–1170 (1996).
8. S. Goldberg *et al.*, *Phys. Rev. B* **79**, 064523 (2009).
9. See supplementary materials on *Science* Online.
10. M. Tinkham, D. W. Abraham, C. J. Lobb, *Phys. Rev. B* **28**, 6578–6581 (1983).
11. T. I. Baturina, Yu. A. Tsaplin, A. E. Plotnikov, M. R. Baklanov, *JETP Lett.* **81**, 10–14 (2005).
12. S. Eley, S. Gopalakrishnan, P. M. Goldbart, N. Mason, *Nat. Phys.* **8**, 59–62 (2012).
13. D. R. Hofstadter, *Phys. Rev. B* **14**, 2239–2249 (1976).
14. T. I. Baturina *et al.*, *Europhys. Lett.* **93**, 47002 (2011).
15. S. P. Benz, M. S. Rzchowski, M. Tinkham, C. J. Lobb, *Phys. Rev. B* **42**, 6165–6171 (1990).
16. Z. Jiang, D. A. Dikin, V. Chandrasekhar, V. V. Metlushko, V. V. Moshchalkov, *Appl. Phys. Lett.* **84**, 5371–5373 (2004).
17. M. J. Rozenberg, R. Chitra, G. Kotliar, *Phys. Rev. Lett.* **83**, 3498–3501 (1999).
18. G. Blatter, M. V. Feigel'man, V. B. Geshkenbein, A. I. Larkin, V. M. Vinokur, *Rev. Mod. Phys.* **66**, 1125–1388 (1994).
19. J. Kierfeld, H. Nordborg, V. M. Vinokur, *Phys. Rev. Lett.* **85**, 4948–4951 (2000).
20. L. D. Landau, E. M. Lifshitz, *Quantum Mechanics* (Elsevier, Oxford, 1977).
21. P. Limelette *et al.*, *Science* **302**, 89–92 (2003).
22. G. Kotliar, E. Lange, M. J. Rozenberg, *Phys. Rev. Lett.* **84**, 5180–5183 (2000).
23. P. G. Harper, *Proc. Phys. Soc. A* **68**, 874–878 (1955).

QUANTUM MECHANICS

A self-interfering clock as a "which path" witness

Yair Margalit, Zhifan Zhou, Shimon Machluf,* Daniel Rohrlich, Yonathan Japha, Ron Folman†

In Einstein's general theory of relativity, time depends locally on gravity; in standard quantum theory, time is global—all clocks "tick" uniformly. We demonstrate a new tool for investigating time in the overlap of these two theories: a self-interfering clock, comprising two atomic spin states. We prepare the clock in a spatial superposition of quantum wave packets, which evolve coherently along two paths into a stable interference pattern. If we make the clock wave packets "tick" at different rates, to simulate a gravitational time lag, the clock time along each path yields "which path" information, degrading the pattern's visibility. In contrast, in standard interferometry, time cannot yield "which path" information. This proof-of-principle experiment may have implications for the study of time and general relativity and their impact on fundamental effects such as decoherence and the emergence of a classical world.

Two-slit interferometry of quanta, such as photons and electrons, figured prominently in the Bohr-Einstein debates on the consistency of quantum theory (1, 2). A fundamental principle emerging from those debates—intimately related to the uncertainty principle—is that "which path" information about the quanta passing through slits blocks their interference. At the climax of the debates, Einstein claimed that a clock, emitting a photon at a precise time while being weighed on a spring scale to measure the change in its mass-energy, could evade the uncertainty principle. Yet Bohr showed that the clock's gravitational redshift induces enough uncertainty in the emission time to satisfy the uncertainty principle. Inspired by the subtle role that time may play, we have now sent a clock through a spatial interferometer. Our proof-of-principle experiment introduces clock interferometry as a new tool for studying the interplay of general relativity (3) and quantum mechanics (4).

Time in standard quantum mechanics is a global parameter, which cannot differ between paths. Hence, in standard interferometry (5) a difference in height between two paths merely affects their relative phase, shifting their interference pattern without degrading its visibility. In contrast, general relativity predicts that a clock must "tick" slower along the lower path; thus if the paths of a clock through an interferometer have different heights, a time differential between the paths will yield "which path" information and degrade the visibility of the interference pattern (6). Consequently, whereas standard interferometry may probe general relativity (7–9), clock interferometry probes the interplay of general relativity and quantum mechanics. For example, loss of visibility because of a proper time lag would be evidence that gravitational effects contribute to decoherence and the emergence of a classical world (10).

Although our interferometer is of a new type, it is worthwhile noting decades of progress in matter-wave interferometry (11). Specifically, we note experiments in which neutron spins have been rotated in a magnetic field (12, 13) and experiments in which different paths were labeled (14). For completeness, we also note recent work on the so-called Compton clock interferometer (15) and the debates that ensued [(16, 17) and references therein].

In our experiment, atomic clocks—atoms in superpositions of internal states—pass through an atomic matter-wave interferometer. We demonstrate that the visibility of interference patterns produced by thousands of self-interfering clocks [atoms in a Bose-Einstein condensate (BEC)] depends on the (simulated) proper time differential between the recombined wave packets of each clock. We simulated the time differential or lag by artificially making one clock wave packet "tick" faster than the other. Although our clock is not accurate enough to be sensitive to special- or general-relativistic effects, it is able to demonstrate that a differential time reading affects the visibility of a clock self-interference pattern (6); specifically, the visibility equals the scalar product of the interfering clock states.

In principle, any system evolving with a well-defined period can be a clock. We used a quantum two-level system: a ^{87}Rb atom in a superposition of two Zeeman sublevels, the $m_F = 1$ and $m_F = 2$ sublevels of the $F = 2$ hyperfine state.

The general scheme of the clock interferometer is shown in Fig. 1 (18). To prepare the clock in a superposition of two different locations, we made use of the previously demonstrated Stern-Gerlach type matter-wave interferometer on an atom chip (19), creating a coherent spatial superposition of a ^{87}Rb BEC (~10^4 atoms) 90 μm below the chip surface. Initially, after the application of a field gradient beam splitter (FGBS) and a stopping pulse that zeroes the relative velocity of

Department of Physics, Ben-Gurion University of the Negev, Beer-Sheva 84105, Israel.
*Present address: Van der Waals-Zeeman Institute, University of Amsterdam, Science Park 904, 1090 GL Amsterdam, Netherlands.
†Corresponding author. E-mail: folman@bgu.ac.il

the two atomic wave packets, the wave packets are in the same internal atomic state ($|F, m_F\rangle = |2, 2\rangle \equiv |2\rangle$) as well as in the same external momentum state. A radio-frequency (RF) $\pi/2$ pulse (Rabi frequency Ω_R and duration T_R) tuned to the transition from $|2\rangle$ to $|1\rangle \equiv |2, 1\rangle$ forms the clock by transferring the atoms from the $|2\rangle$ state to the internal superposition state $(|1\rangle + |2\rangle)/\sqrt{2}$.

The pulse is applied under a strong homogeneous magnetic field in order to push the transition to $|2, 0\rangle$ out of resonance via the nonlinear Zeeman effect, thus forming a pure two-level system (18).

In order to examine the coherence of the clock spatial superposition, we let the two clock wave packets freely expand and overlap to create spatial interference fringes (Fig. 2A). Because two BEC wave packets are always expected to yield fringes when they overlap, many experimental cycles are required in order to prove phase stability or, in other words, coherent splitting of the clock. In the averaged picture of 100 single shots taken continuously over a period of ~2 hours (Fig. 2B), the contrast falls by a mere 2% relative to the mean of the single-shot visibility, demonstrating a stable phase. The narrow phase distribution in the data (18) reveals that the clock splitting is coherent (meaning the clock was in a superposition of two locations).

We now show that clock time is indeed a "which path" witness. For a single-internal-state interferometer, a phase difference will not change the visibility of the fringes. In contrast, the relative rotation between the two clock wave packets is expected to influence the interferometric visibility. In the extreme case, when the two clock states are orthogonal—for example, one in the state $(|1\rangle + |2\rangle)/\sqrt{2}$ and the other in the state $(|1\rangle - |2\rangle)/\sqrt{2}$—the visibility of the clock self-interference should drop to zero. We applied a magnetic gradient pulse [inducing a "tick" rate difference $\Delta\omega$ (18)] of duration T_G so as to induce a relative angle of rotation between the two clock wave packets (Fig. 1). When the relative rotation angle is π, we observed in a single shot that the visibility of the interference pattern drops to zero (Fig. 2C). Again, this is unlike standard interferometers in which a phase difference does not suppress visibility, which this is contrary to standard split-BEC interference experiments in
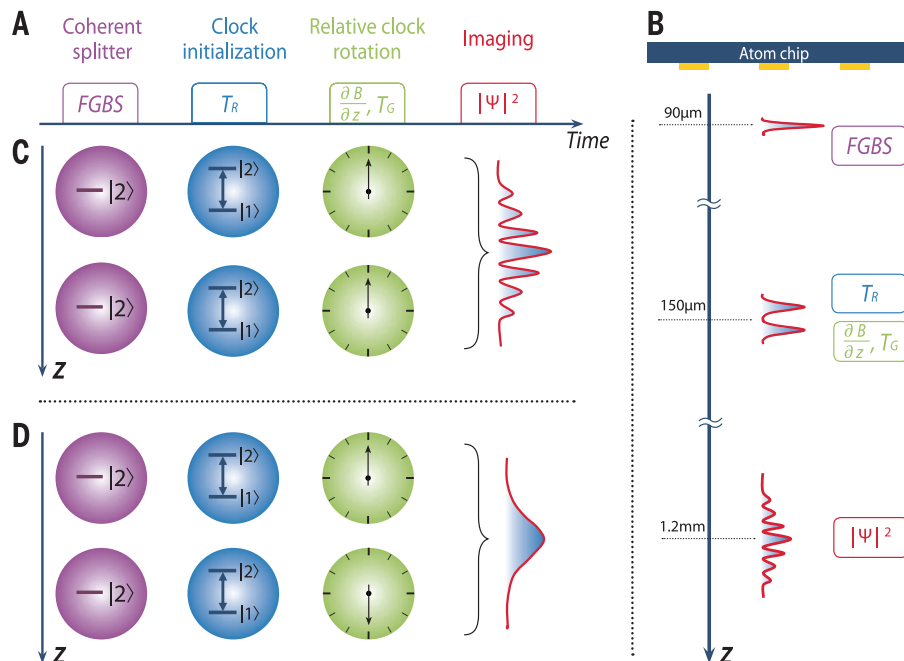
Fig. 1. Experimental sequence of the clock interferometer. (**A**) Detailed sequence (not to scale). After a coherent spatial splitting by the FGBS and a stopping pulse, the system consists of two wave packets in the $|2\rangle$ state (separated along the z axis, the direction of gravity) with zero relative velocity (19). The clock is then initialized with a RF pulse of length T_R, after which the relative "tick" rate of the two clock wave packets may be changed by applying a magnetic field gradient $\partial B/\partial z$ of duration T_G. Last, before an image is taken (in the xz plane) the wave packets are allowed to expand and overlap. (**B**) The same sequence as in (A) presented in space (in the yz plane). The chip wires are parallel to x, and the imaging beam is parallel to y. (**C**) Evolution in time, synchronized with (A). Each clock wave packet shows as a one-handed clock, in which the hand corresponds to a vector in the equatorial plane of the Bloch sphere. When the clock reading (the position of the clock hand) in the two clock wave packets is the same, fringe visibility is high. (**D**) When the clock reading is opposite (orthogonal), it becomes a "which path" witness, and there is no interference pattern.

Fig. 2. Clock interference. (**A**) A single experimental shot of a clock interfering with itself (z axis values are relative to the chip surface). As $T_G = 0$, the clock rate is approximately the same in the two wave packets, and interference is visible. As can be seen from Fig. 3, a constant differential rotation of the clocks, ϕ_0, exists even for $T_G = 0$ [because of a residual magnetic gradient in our chamber (18)]. This somewhat reduces the

visibility. (**B**) To prove the coherence of the clock spatial splitting, an average of 100 consecutive shots such as that in (A) is presented, with only a 2% drop in visibility (18). (**C**) To prove that clock time acts as a "which path" witness, we present a single shot in which the differential rotation angle $\phi_0 + \Delta\omega T_G$ equals π. (**D**) Similar to (B), but where indistinguishability is restored by $\phi_0 + \Delta\omega T_G = 2\pi$ (visibility is $47 \pm 1\%$, down from a single-shot average of $51 \pm 2\%$). The fits are a simple combination of a sine with a Gaussian envelope (19). The vertical position as well as the vertical extent of the clouds is explained in (18). Throughout this work, all data samples are from consecutive measurements without any post-selection or post-correction.
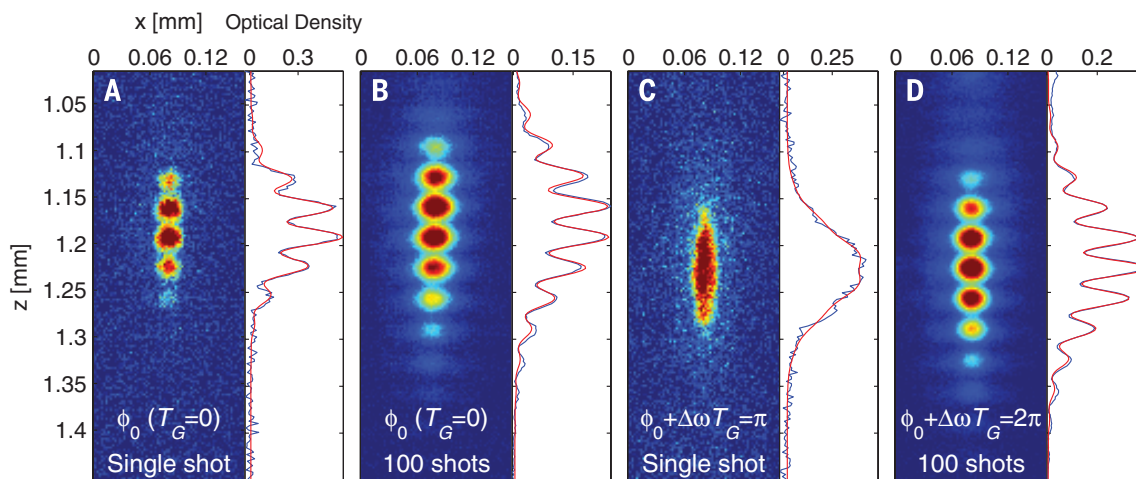
which a single shot always exhibits substantial visibility. A revival of the single-shot visibility is seen when the differential rotation angle is taken to be 2π (where we again present an average of 100 shots to confirm coherence) (Fig. 2D).

To obtain a more general view of the effect, we studied the dependence of the interference pattern visibility on the differential rotation angle between the two clock wave packets over the range 0 to 4π, by varying T_G to alternate between clock indistinguishability and orthogonality (Fig. 3). The blue data in Fig. 3 present the clock interference pattern visibility, clearly showing os-

cillations [consistent with the expected period (18)]. Comparing the latter oscillations with the visibility of a single-internal-state "no clock" interference ($\Omega_R T_R = 0$) (Fig. 3, red data) confirms that the oscillations are due to the existence of a clock. The single-internal-state interference data also confirm that the overall drop in visibility is not due to the formation of the clock. This upper bound is due to the magnetic gradient pulse causing imperfect overlap between the two wave packets (18). A lower bound on the visibility is due to the spatial separation of the $|1\rangle$ and $|2\rangle$ wave packets (gradual breakup of the clock), again due

to the magnetic gradient (18), which results in an increase of the visibility as expected from two independent single-state interferometers.

The essence of the clock is that it consists of a superposition of two levels, $|1\rangle$ and $|2\rangle$. In Fig. 3, we chose to work with an equal population of the $|1\rangle$ and $|2\rangle$ states upon clock initialization to create a proper clock, thus maximizing the visibility's dependence on the differential rotation. To further prove that it is the clock reading that is responsible for the observed oscillations of visibility, we modulated the very formation of the clock by varying the clock-initiating RF pulse (T_R) so that the system preparation alternates between a proper clock and no clock at all (Fig. 4). Specifically, varying T_R changes the population ratio of the two components of the clock. When the differential rotation of the two clock wave packets ($\Delta\omega T_G$) is set to π (orthogonal clocks), as shown by the blue data in Fig. 4A, the interferometer visibility oscillates as a function of the ratio of the clock states' initial population. This is so because when $\Omega_R T_R$ equals multiples of π, only one of the clock states is populated, and the system is actually not a clock. In this case, we have a standard interferometer; "clock orthogonality" and clock time as a "which path" witness do not exist irrespective of the fact that $\Delta\omega T_G = \pi$, and consequently, full visibility is obtained. When a proper clock is formed (equal initial populations), clock time is an effective witness, and the visibility drops. In contrast, when $\Delta\omega T_G = 2\pi$ (Fig. 4A, red data), the interferometer visibility is always high because the two wave packets are not orthogonal whether they are clocks or states with a definite m_F.

Our realization of clock interferometry demonstrates a way to probe the interplay between quantum mechanics and general relativity. In this context, some even suggest that wave-function collapse may be due to gravity (20–22). It remains to be seen whether clock interferometers can provide new insight regarding such mechanisms as well. In addition, because time is considered by some a parameter that is still far from being fully understood (23), such an interferometer may shed new light on a variety of related fundamental questions.

Fig. 3. Varying the orthogonality of the two clock wave packets. To study the properties of clock time as a "which path" witness, we measure visibility while continuously varying the relative rotation of the two clock wave packets (blue). Each data point is an average of the single-shot visibility obtained in several experimental cycles, and the error bars are the variance in this subsample. A fit returns an oscillation constant of $\Delta\omega = 0.166 \pm 0.003$ rad/μs, which is

consistent with an independent estimate (18). As inferred from the single-internal-state "no clock" interferometer (red line), the oscillations are due to the existence of a clock. The upper and lower bounds are explained in the text.
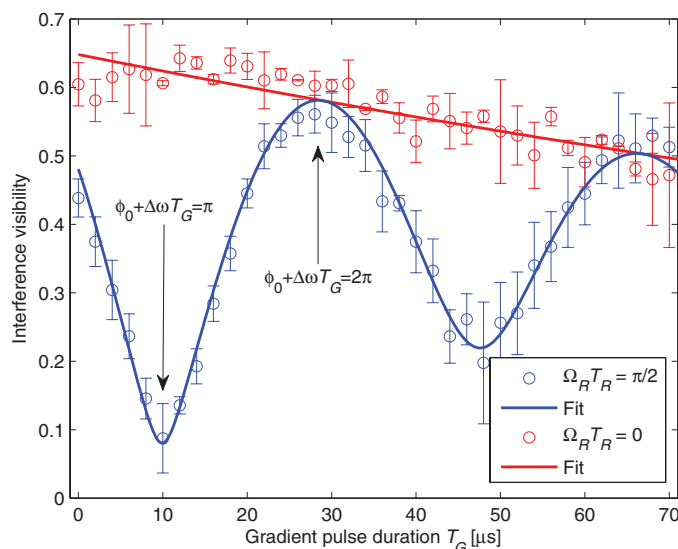
Fig. 4. Varying the preparation of the clock. To further prove that it is the clock reading that is responsible for the observed oscillations in visibility, we modulate the very formation of the clock by varying T_R, so that the system preparation alternates between a proper clock and no clock at all. (**A**) When the imprinted relative rotation between the two clock wave packets is π, whether a proper clock is formed or not has a dramatic effect (blue). In con-

trast, when the relative rotation is 2π, whether a proper clock is formed or not has no effect (red). The error bars are the standard deviation of several data points. (**B**) The oscillation period appearing in (A) is as expected from an independent measurement of the Rabi oscillations induced by T_R when the rest of the RF sequence has been eliminated (18).

REFERENCES AND NOTES

1. N. Bohr, in *Albert Einstein: Philosopher–Scientist*, P. A. Schilpp, Ed. (Tudor, New York, 1951), pp. 201–41.
2. Y. Aharonov, D. Rohrlich, *Quantum Paradoxes: Quantum Theory for the Perplexed* (Wiley-VCH, Weinheim, Germany, 2005), section 2.4.
3. M. Moerchen, R. Coontz, *Science* **347**, 1083 (2015).
4. I. Georgescu, *Nat. Phys.* **10**, 253 (2014).
5. R. Colella, A. W. Overhauser, S. A. Werner, *Phys. Rev. Lett.* **34**, 1472–1474 (1975).
6. M. Zych, F. Costa, I. Pikovski, Č. Brukner, *Nat. Commun.* **2**, 505 (2011).
7. S. Dimopoulos, P. W. Graham, J. M. Hogan, M. A. Kasevich, *Phys. Rev. Lett.* **98**, 111102 (2007).
8. H. Müntinga et al., *Phys. Rev. Lett.* **110**, 093602 (2013).
9. C. C. N. Kuhn et al., *New J. Phys.* **16**, 073035 (2014).
10. I. Pikovski, M. Zych, F. Costa, Č. Brukner, *Nat. Phys.* (2015).
11. A. D. Cronin, J. Schmiedmayer, D. E. Pritchard, *Rev. Mod. Phys.* **81**, 1051–1129 (2009).
12. H. Rauch et al., *Phys. Lett. A* **54**, 425–427 (1975).

13. H. Rauch, S. A. Werner, *Neutron Interferometry: Lessons in Experimental Quantum Mechanics* (Calderon Press, Oxford, UK, 2000).
14. S. Dürr, T. Nonn, G. Rempe, *Nature* **395**, 33–37 (1998).
15. S.-Y. Lan *et al.*, *Science* **339**, 554–557 (2013).
16. W. P. Schleich, D. M. Greenberger, E. M. Rasel, *Phys. Rev. Lett.* **110**, 010401 (2013).
17. S. Peil, C. R. Ekstrom, *Phys. Rev. A* **89**, 014101 (2014).
18. Materials and methods are available as supplementary materials on *Science* Online.
19. S. Machluf, Y. Japha, R. Folman, *Nat. Commun.* **4**, 2424 (2013).
20. R. Penrose, *The Emperor's New Mind: Concerning Computers, Minds, and the Laws of Physics* (Oxford Univ. Press, New York, 1989), chap. 6.
21. L. Diósi, *J. Phys. Conf. Ser.* **442**, 012001 (2013).
22. A. Bassi, K. Lochan, S. Satin, T. P. Singh, H. Ulbricht, *Rev. Mod. Phys.* **85**, 471–527 (2013).
23. Lee Smolin, *Time Reborn* (Mariner Books, Wilmington, MA, 2014).

ELECTROCHEMISTRY

Covalent organic frameworks comprising cobalt porphyrins for catalytic CO_2 reduction in water

Song Lin,[1,2]* Christian S. Diercks,[1,3]* Yue-Biao Zhang,[1,3,4]* Nikolay Kornienko,[1] Eva M. Nichols,[1,2] Yingbo Zhao,[1] Aubrey R. Paris,[1] Dohyung Kim,[5] Peidong Yang,[1,3,5,6] Omar M. Yaghi,[1,3,6,7]† Christopher J. Chang[1,2,8,9]†

Conversion of carbon dioxide (CO_2) to carbon monoxide (CO) and other value-added carbon products is an important challenge for clean energy research. Here we report modular optimization of covalent organic frameworks (COFs), in which the building units are cobalt porphyrin catalysts linked by organic struts through imine bonds, to prepare a catalytic material for aqueous electrochemical reduction of CO_2 to CO. The catalysts exhibit high Faradaic efficiency (90%) and turnover numbers (up to 290,000, with initial turnover frequency of 9400 hour^{-1}) at pH 7 with an overpotential of −0.55 volts, equivalent to a 26-fold improvement in activity compared with the molecular cobalt complex, with no degradation over 24 hours. X-ray absorption data reveal the influence of the COF environment on the electronic structure of the catalytic cobalt centers.

Global energy demands and climate change underpin broad interest in the sustainable reductive transformation of carbon dioxide (CO_2) to value-added carbon products such as carbon monoxide (CO) (*1*, *2*). Electrolytic approaches benefit from using water as the reaction medium, as it is a cheap, abundant, and environmentally benign solvent that facilitates proton and electron transfer (*3*, *4*). However, the competitive and often kinetically favored off-pathway reduction of water itself to hydrogen must be avoided. In this context, molecular catalysts for electrochemical CO_2 conversions can be systematically tuned to achieve high activity and selectivity over proton reduction (*5–13*), but they typically require organic media to achieve optimal selectivity and/or stability, often to maximize solubility and minimize water- or proton-induced catalyst degradation and/or hydrogen production. In contrast, heterogeneous catalysts are often stable in water, but optimizing their activity through structural changes at a molecular level remains a substantial challenge (*14–19*). Against this backdrop, we sought to investigate crystalline porous frameworks—specifically, covalent organic frameworks (COFs) (*20–22*)—as tunable materials for electrocatalysis. We reasoned that such materials could potentially combine advantages of both molecular and heterogeneous catalysts: (i) Construction with molecular building blocks would enable precise manipulation of the spatial arrangement of catalytic centers within the predetermined COF structure (*23*); (ii) the frameworks could be expanded and functionalized without changing the underlying topology of the structure (*24*, *25*); and (iii) the conserved pore environment around the active sites within the COF could be tuned electronically and sterically (*26*) while providing ready access for the substrate (*27–32*) (Fig. 1). Moreover, these crystalline porous frameworks offer the possibility to perform multivariate synthesis, in which topologically identical and yet functionally modified building blocks can be introduced into the structure. This approach can potentially give rise to materials with emergent properties that are greater than the sum of the individual molecular parts, because one can predictably prepare a topologically ordered framework yet introduce heterogeneity in the number and ratio of functionalities by the choice of building blocks (*33*). Here we show that incorporation of catalytic cobalt porphyrin (*34*) units into COFs, along with multivariate synthesis of frameworks bearing catalytic cobalt and structural copper units, gives highly active, stable, and selective catalysts for electrochemical reduction of carbon dioxide to carbon monoxide in water. A member of the COF series that we studied exhibits a 26-fold increase in activity compared with the parent molecular precursor and, in many respects, outperforms state-of-the-art molecular and solid-state catalysts, with broad opportunities for further improvement through modular synthesis using appropriate combinations of building units. X-ray absorption measurements reveal that the COF framework can directly influence the electronic structure of the catalytic cobalt centers, in a manner akin to redox noninnocent ligand behavior observed in molecular systems (*35*), thereby contributing to the observed gains in reaction selectivity and activity beyond the steric effects of surface area and site isolation.

We focused our initial electrocatalysis studies on COFs, as we sought to exploit the charge-carrier mobility of these materials derived from π conjugation and π-π stacking (*22*, *36–38*), as well as the stability from reticular assembly with strong covalent bonds. We synthesized a model framework (COF-366-Co) by the imine condensation of 5,10,15,20-tetrakis(4-aminophenyl)porphinato]cobalt [Co(TAP)] with 1,4-benzenedicarboxaldehyde (BDA) (Fig. 1). The porous COF material was evacuated by activation with supercritical carbon dioxide and heating to 100°C for 18 hours. The retention of cobalt in the coordinating porphyrin units within the framework was confirmed by elemental analysis (supplementary materials section S1.1), thermogravimetric analysis (fig. S1), and

[1]Department of Chemistry, University of California, Berkeley, CA 94720, USA. [2]Chemical Sciences Division, Lawrence Berkeley National Laboratory, Berkeley, CA 94720, USA. [3]Materials Sciences Division, Lawrence Berkeley National Laboratory, Berkeley, CA 94720, USA. [4]School of Physical Science and Technology, ShanghaiTech University, Shanghai, 201210, China. [5]Department of Materials Science and Engineering, University of California, Berkeley, CA 94720, USA. [6]Kavli Energy Nanoscience Institute, Berkeley, CA 94720, USA. [7]King Fahd University of Petroleum and Minerals, Dhahran 34464, Saudi Arabia. [8]Howard Hughes Medical Institute, University of California, Berkeley, CA 94720, USA. [9]Department of Molecular and Cell Biology, University of California, Berkeley, CA 94720, USA.
*These authors contributed equally to this work. †Corresponding author. E-mail: yaghi@berkeley.edu (O.M.Y.); chrischang@berkeley.edu (C.J.C.)

solid-state ultraviolet-visible (UV-Vis) spectroscopy (fig. S3). The formation of the imine linkages in the COF was confirmed by attenuated total reflectance–Fourier transform infrared spectroscopy, which showed the characteristic imine stretching vibration band at 1621 cm^{-1}, as well as the absence of the aldehyde stretching vibration band at 1684 cm^{-1} (fig. S10). The morphologies of the activated COF samples were examined by scanning electron microscopy (SEM), which showed aggregation of only one kind of crystallite of rectangular rod-shaped morphology (~50 nm in length) (Fig. 2A). Powder x-ray diffraction (PXRD) patterns (Fig. 2B) showed intense peaks in the expected low-angle range, with no residual peaks characteristic of the starting materials. To elucidate the constitution of the framework, we used Materials Studio 7.0 to build a structural model (Fig. 1) in an orthorhombic *Cmmm* space group to allow the lattice distortion from regular square nets. Pawley refinements of the PXRD patterns were carried out for full profile fitting against the proposed models, resulting in a good agreement factor (weighted-profile *R* factor R_{wp} = 2.59% and unweighted-profile *R* factor R_p = 1.38% after convergence) and reasonable profile differences. These refinements revealed one-dimensional (1D) channels, 21 Å in width, running along the *c* axis, with a distance of 4.4 Å between the stacking 2D sheets. The porosity and specific surface area were

determined using nitrogen adsorption isotherms at 77 K (Fig. 2C). The Brunauer-Emmett-Teller (BET) surface area was determined to be 1360 m^2/g. Density functional theory (DFT) fitting of the adsorption branches showed relatively narrow pore size distributions (10 to 18 Å), in agreement with that of the proposed model.

For electrochemical experiments, the activated microcrystalline COF powders were deposited on porous, conductive carbon fabric. Cyclic voltammetry (CV) measurements on COF-366-Co were conducted in pH 7 aqueous phosphate buffer (Fig. 3A). Under a nitrogen atmosphere, the voltammogram trace shows a departure from the electrode background at about –0.45 V versus a reversible hydrogen electrode (RHE). A broad reduction wave, which was assigned to the Co(II)/Co(I) redox couple, is also apparent at about –0.67 V. The surface concentration of electrochemically active cobalt porphyrin sites was measured by integration of the reduction wave to be 1×10^{-8} mol/cm^2, corresponding to activity at 4% of the cobalt porphyrin sites in the material. The observed continuous current increase at potentials more negative than –0.67 V likely arises from Co(I)-catalyzed proton reduction activity (*39*). After the solution was saturated with carbon dioxide, a substantial current enhancement was observed [catalytic current/noncatalytic current ratio (i_{cat}/i_p) = 1.8 at –0.67 V] (*40*), with a catalytic onset potential at –0.42 V,

indicating a prominent catalytic effect of COF-366-Co on the reduction of carbon dioxide in neutral aqueous solution. In contrast, the carbon fabric electrode alone showed minimal current enhancement under a carbon dioxide or nitrogen atmosphere (fig. S56).

In controlled potential electrolyses performed in carbon dioxide–saturated aqueous bicarbonate buffer (pH = 7.3) under applied potentials between –0.57 and –0.97 V (versus RHE), carbon monoxide was observed as the major reduction product (Fig. 3B), with no other detectable carbon-based products. At –0.67 V, which represents an overpotential of –0.55 V, the catalyst displayed optimal performance (figs. S63 and S64). More positive potentials led to sluggish carbon dioxide reactivity, whereas more negative potentials promoted off-pathway water reduction. At –0.67 V, COF-366-Co promoted carbon monoxide evolution at an initial current density of 5 mA per milligram of catalyst (~80 mA per milligram of cobalt), with high selectivity over competing proton reduction [Faradaic efficiency for carbon monoxide (FE$_{CO}$) = 90%]. Catalytic cobalt porphyrin centers in the COF showed greater than 10% enhancement in carbon dioxide to proton selectivity over the molecular cobalt porphyrin unit alone (Fig. 3B). The catalytic activity of the COF could be maintained for 24 hours, accumulating more than 36 ml of carbon monoxide [standard
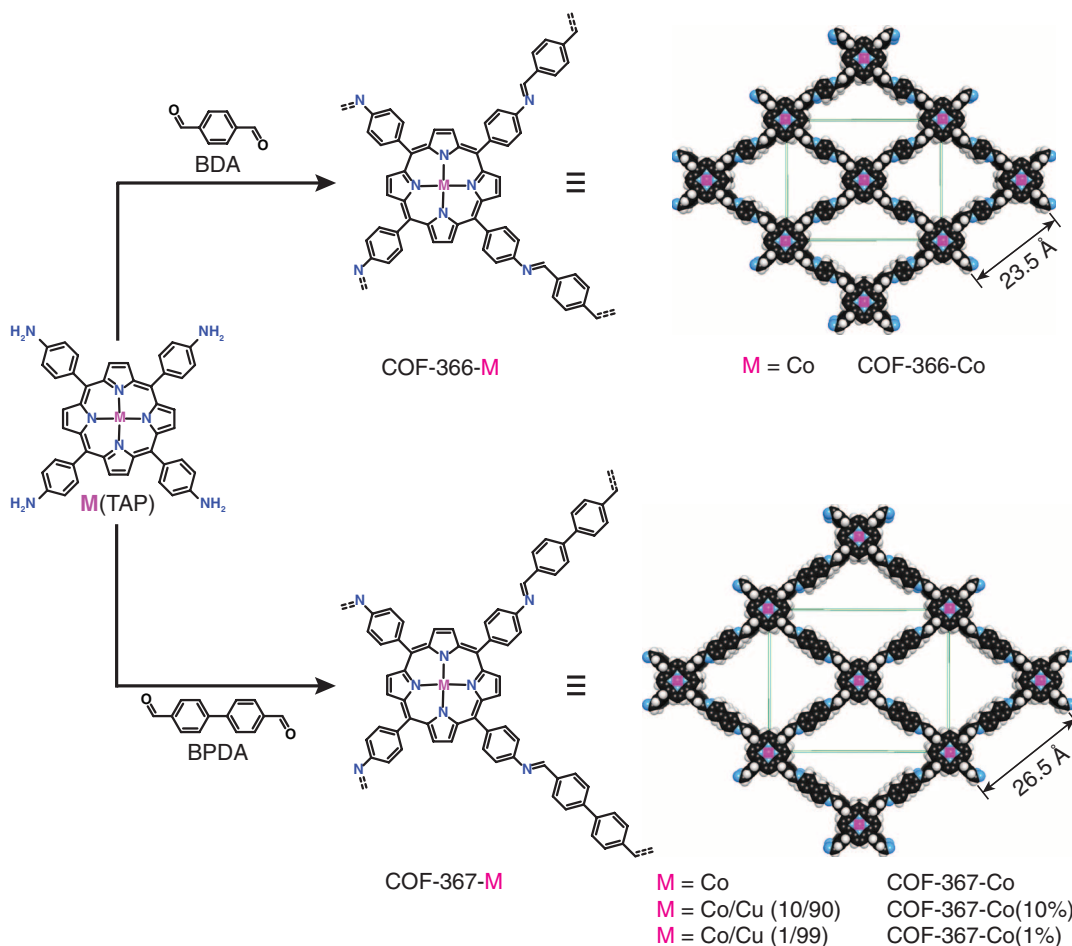
Fig. 1. Design and synthesis of metalloporphyrin-derived 2D covalent organic frameworks. The space-filling structural models of COF-366-M and COF-367-M were obtained using Materials Studio 7.0 and refined with experimental PXRD data.

temperature and pressure (STP), equivalent to 1.6 mmol] per milligram of COF. This corresponds to a turnover number (TON) of 1352 [TON per electroactive cobalt based on the measurements described above ($TON_{EA} \approx 34{,}000$)], with an initial turnover frequency (TOF) of 98 hour^{-1} [TOF per electroactive cobalt ($TOF_{EA} \approx 2500$)]. This result represents a substantial improvement over the molecular Co(TAP), which showed an initial TOF of 36 hour^{-1} ($TOF_{EA} \approx 360$) and a TON of 794 ($TON_{EA} \approx 8300$) after 24 hours of reaction [surface coverage of electroactive sites on a Co(TAP)–modified electrode constitutes ~10% of the total cobalt]. PXRD (fig. S73) and SEM (fig. S74) measurements on the COF catalyst after electrolysis showed neither marked changes in crystallinity and microscopic morphology nor evidence of cobalt nanoparticle formation. By incorporating this molecular unit into a COF scaffold, the resulting hybrid catalyst could be recovered from the electrolysis mixture and reused at least five times without decrease in activity and selectivity (table S8). Control experiments with COFs containing either free-base or copper-metallated porphyrin units, a physical mixture of independently synthesized cobalt nanoparticles (fig. S75) and COF, and Co_3O_4 and related cobalt salts that could be formed as impurities during COF synthesis did not produce appreciable carbon dioxide reduction (fig. S76).

To optimize this carbon dioxide catalyst platform by a modular reticular approach, we prepared the expanded COF-367-Co analog using biphenyl-4,4'-dicarboxaldehyde (BPDA) as the strut in place of BDA (Fig. 1). We reasoned that a larger pore size would allow for higher capacity of carbon dioxide adsorption inside the framework, as well as higher electrochemical and chemical accessibility of the catalytic cobalt porphyrin active sites. COF-367-Co was obtained as a dark purple powder comprising rectangular rod-shaped crystallite aggregates (~100 nm in length) (Fig. 2D). The structural model based on PXRD data and DFT fitting indicated that the constitution and topology of COF-367-Co is analogous to that of COF-366-Co, with the former showing an increased channel width (24 Å) and interlayer distance (4.8 Å) (Fig. 2E). The BET surface area was determined by nitrogen adsorption isotherm (Fig. 2F) as 1470 m^2/g, and pore size distribution is consistent with the model (12 to 23 Å). Cyclic voltammetry studies with COF-367-Co on a carbon fabric electrode in bicarbonate buffer indicated that this extended organic framework exhibits an improved surface concentration (2×10^{-9} mol/cm^2) of electroactive cobalt porphyrin sites over COF-366-Co, which corresponds to accessibility of 8% of the cobalt sites in the bulk material. When the solution was saturated with CO_2, a catalytic current was evident with an onset potential at –0.40 V and a 2.2-fold enhancement at –0.67 V, indicating a prominent effect of COF-367-Co in the catalysis of CO_2 reduction at these potentials (Fig. 3A). As predicted, electrolysis under the same conditions described above revealed that this expanded COF displays improved catalytic efficiency as compared with COF-366-Co. At an applied potential of –0.67 V, COF-367-Co produced more than 100 ml of carbon monoxide (STP, equivalent to 4.5 mmol) per milligram of COF during a 24-hour period (TON = 3901, $TON_{EA} \approx 48{,}000$), with high Faradaic efficiency (91%). The increased TON_{EA} over COF-366-Co indicated that lattice expansion allowed for more efficient exposure of the electroactive sites to the reactants.

In addition to framework expansion, we also sought to optimize catalyst performance by introducing building-block heterogeneity through a multivariate strategy (33), as we hypothesized that not all electroactive cobalt porphyrin sites in the material fully participated in electrocatalysis, owing to the low aqueous solubility of carbon dioxide. Specifically, we reasoned that using isostructural metalloporphyrin units that are catalytically inactive for carbon dioxide reduction (fig. S76) to dilute electroactive cobalt porphyrin active sites within the extended lattice could increase the proportion of the active sites exposed to the reactant and thereby improve the turnover frequency on a per-cobalt basis. Copper porphyrin was chosen for this study, as the corresponding COF-367-Cu had the highest surface area among all analogous COF-367-M (M = Ni, Zn, H$_2$) synthesized. The resulting bimetallic COF-367 derivatives, termed COF-367-Co(10%) and COF-367-Co(1%), were prepared; the numbers in the parentheses indicate the proportion of cobalt in all metal sites (Fig. 1). Inductively coupled plasma
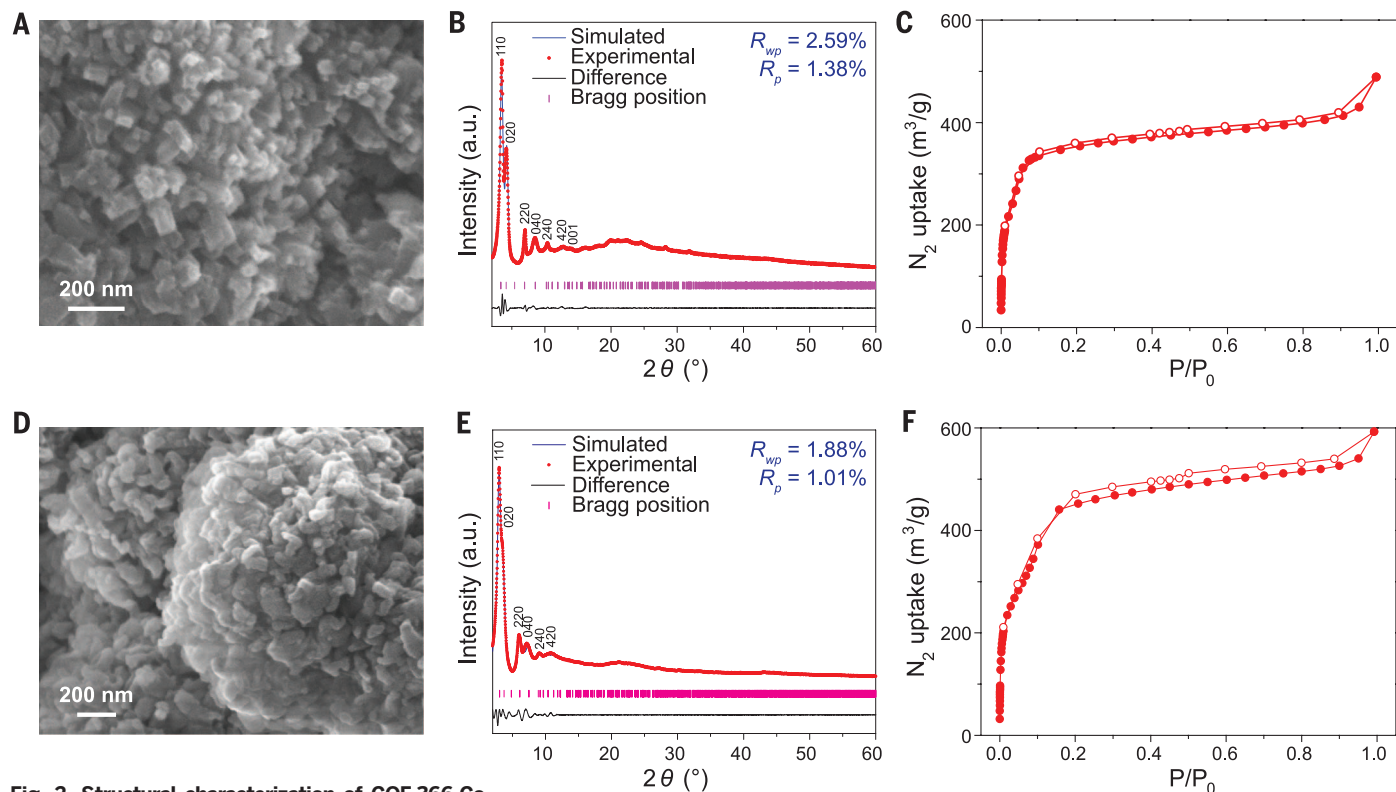
Fig. 2. Structural characterization of COF-366-Co and COF-367-Co. (**A**) SEM image of COF-366-Co. (**B**) Experimental (red line) and simulated (blue line) PXRD patterns of COF-366-Co. a.u., arbitrary units. (**C**) Nitrogen adsorption isotherm for COF-366-Co. P, pressure of the system; P$_0$, saturation pressure. (**D**) SEM image of COF-367-Co. (**E**) Experimental (red line) and simulated (blue line) PXRD patterns of COF-367-Co. (**F**) Nitrogen adsorption isotherm for COF-367-Co.

(ICP) analyses confirmed that the final chemical composition of the COFs obtained reflected the initial ratio of the two metalloporphyrin starting materials that we used (supplementary materials section S1.1). The TOF per electroactive cobalt site for carbon monoxide production in these multivariate Co/Cu COF-367 catalysts showed a substantial improvement with each 10-fold dilution of cobalt loading. The average

TOF per active cobalt for the first 4 hours of reaction was measured as follows: COF-367-Co, 165 hour^{-1} (TOF$_{EA}$ ≈ 1900); COF-367-Co(10%), 360 hour^{-1} (TOF$_{EA}$ ≈ 4400); and COF-367-Co(1%), 764 hour^{-1} (TOF$_{EA}$ ≈ 9400) (Fig. 3C). The TOF$_{EA}$ values were roughly estimated, assuming that all three frameworks had comparable percentages of electroactive sites (8%). Although the low cobalt concentration in COF-367-Co(10%) and

COF-367-Co(1%) hampered the accurate determination of the surface concentration of electrochemically accessible cobalt sites by CV, the bimetallic frameworks had nearly identical pore sizes, interlayer distances, and surface areas to the parent COF-367-Co on the basis of PXRD and nitrogen adsorption measurements (figs. S25 and S32 to S43), which suggests that such an assumption may be valid. Owing to the moderate
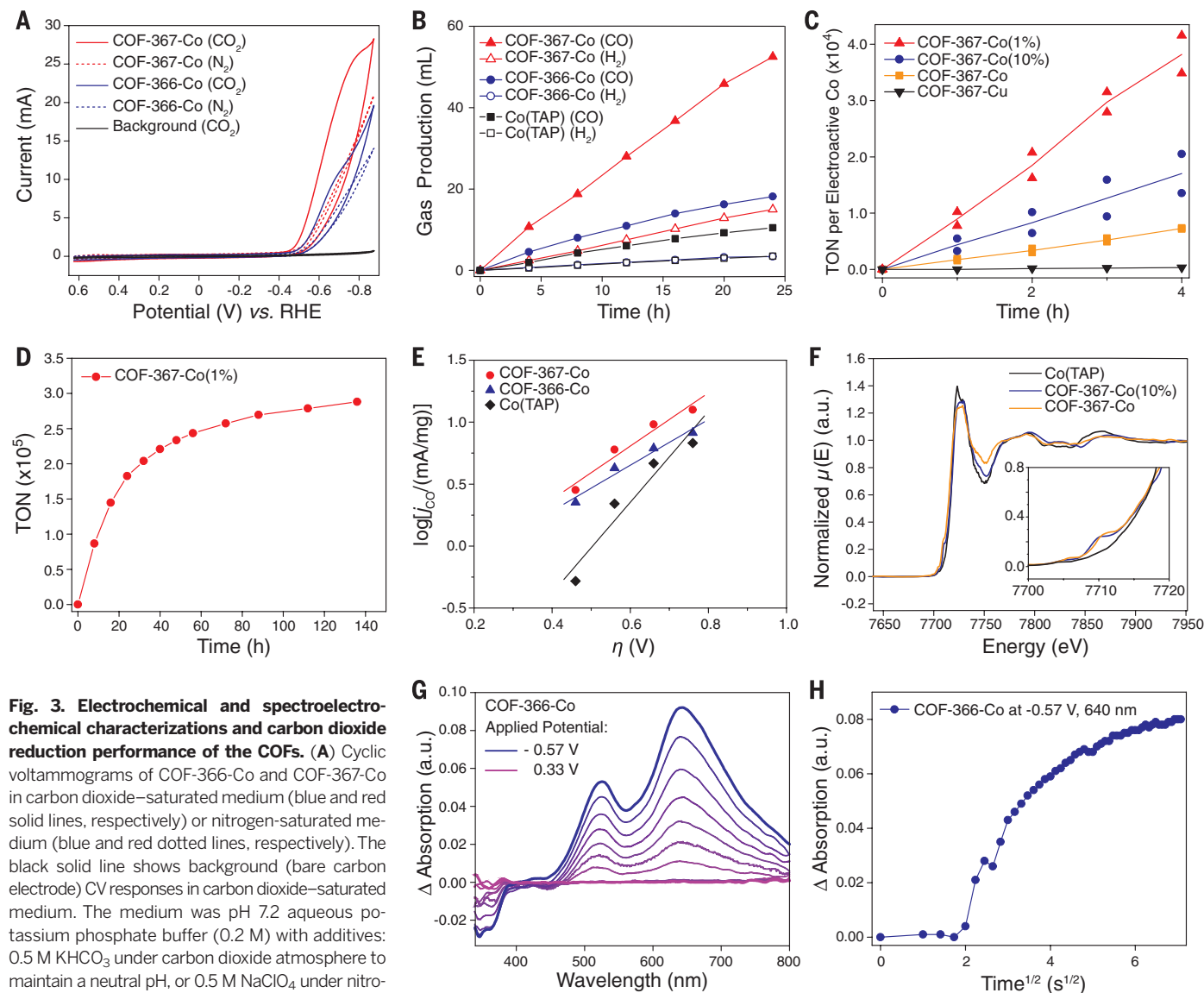
Fig. 3. Electrochemical and spectroelectrochemical characterizations and carbon dioxide reduction performance of the COFs. (**A**) Cyclic voltammograms of COF-366-Co and COF-367-Co in carbon dioxide–saturated medium (blue and red solid lines, respectively) or nitrogen-saturated medium (blue and red dotted lines, respectively). The black solid line shows background (bare carbon electrode) CV responses in carbon dioxide–saturated medium. The medium was pH 7.2 aqueous potassium phosphate buffer (0.2 M) with additives: 0.5 M KHCO$_3$ under carbon dioxide atmosphere to maintain a neutral pH, or 0.5 M NaClO$_4$ under nitrogen atmosphere to match the ionic strength. (**B**) Long-term bulk electrolyses at −0.67 V (versus RHE), showing the volume of carbon monoxide produced by COF-367-Co (red solid triangles), COF-366-Co (blue solid circles), or Co(TAP) (black solid squares) and the volume of hydrogen produced by COF-367-Co (red open triangles), COF-366-Co (blue open circles), or Co(TAP) (black open squares). (**C**) Bulk electrolyses of bimetallic COFs at −0.67 V (versus RHE), showing TON of carbon monoxide production by COF-367-Co(1%) (red solid triangles), COF-367-Co(10%) (blue solid circles), COF-367-Co (orange solid squares), or COF-367-Cu (purple solid inverted triangle; TON with respect to the amount of copper porphyrin). Two separate experimental runs were conducted for each time point, with the line showing the average of the measurements. (**D**) Long-term bulk electrolysis of COF-367-Co(1%) at −0.67 V (versus RHE). (**E**) Tafel plots of electrolysis using COF-367-Co (red solid circles), COF-366-Co (blue solid triangles), or Co(TAP) (black solid

diamonds), showing only the linear, low–current density regime where the reaction rate is not limited by mass transport. (**F**) X-ray absorption spectra of COF-367-Co (orange line), COF-367-Co(10%) (blue line), and Co(TAP) (black line). The inset shows the pre-edge regime of the same spectra. (**G**) Spectroelectrochemical data using in situ UV-Vis, showing the steady-state relative absorbance at different applied potentials (0.23 to −0.57 V versus RHE) with reference to that at 0.33 V. (**H**) Time dependence of the relative UV-Vis absorbance at 640-nm wavelength at −0.57 V, with respect to the steady-state UV-Vis absorbance at 640 nm at 0.33 V. Potential is applied at 4 s. Linear regression yielded the apparent diffusion coefficient (D_{app}) according to a modified Cottrell equation:

$$\Delta Absorption = \frac{2A_{max}D_{app}^{1/2}t^{1/2}}{d\pi^{1/2}}$$

(fig. S81) (47). Here, A_{max} is the maximum absorption of the thin films at 640 nm, d is the overall thickness of the thin films, and t is time.

proton reduction ability of the copper porphyrin sites in the hybrid organic framework, the TOF increased as the Co/Cu ratio decreased, at the expense of Faradaic efficiency for carbon monoxide production [FE_{CO} = 70% for COF-367-Co(10%) and 40% for COF-367-Co(1%)]. In a long-term electrolysis experiment (Fig. 3D), COF-367-Co (1%) displayed a TON of > 24,000 (TON_{EA} ≈ 296,000), which indicates that it is one of the most efficient electrochemical carbon dioxide reduction catalysts reported to date (3, 4). The observed activity enhancements for the bimetallic COFs are due to their multivariate nature; indeed, the analogous physical mixture of COF-367-Co and COF-367-Cu in a 1:9 ratio produced far less carbon dioxide reduction activity compared with COF-367-Co(10%) (table S17).

In addition to challenges posed by the low aqueous solubility and limited diffusion of CO_2 within the COF, only a small portion (4 to 8%) of the cobalt centers in the COF material deposited in this manner proved to be electroactive, presumably because of the limited electrochemical contact between the COF powder and the electrode (41). As such, we explored the possibility of growing COF directly onto the surface of an electrode substrate in the form of oriented thin films (42–44). Layers of COF sheets could be successfully synthesized directly on glassy carbon, fluorine-doped tin oxide (FTO), and silicon oxide. Grazing-incidence wide-angle x-ray scattering (GIWAXS) patterns showed the formation of highly crystalline COF thin films (figs. S48 to S51) (45). With the use of ICP, the concentration of COF on the substrate surface was determined to be 1.3×10^{-5} mmol Co per square centimeter, corresponding to a thickness of ~350 nm, which is consistent with images obtained by cross-sectional SEM (figs. S54 and S55). The charge transport through the COF-366-Co thin films was characterized using spectroelectrochemistry. Under an applied potential more negative than –0.37 V in nitrogen- or carbon dioxide–saturated pH 7 aqueous buffer, the UV-Vis spectrum of the FTO-supported COF underwent changes attributable to Co(II)/Co(I) reduction (Fig. 3G and figs. S78 to S82). Using the steady-state spectroscopic response to the reduction potentials in combination with the Nernst equation, the redox potential ($E_{1/2}$) could be estimated to be more negative than –0.52 V (fig. S83), in agreement with the CV measurements ($E_{1/2}$ ≈ –0.67 V) (46). The time-dependence of the UV-Vis response of a COF-coated FTO electrode to an applied potential of -0.57 V was studied in a CO_2-saturated $KHCO_3$ solution (Fig. 3G), and a fit of the data to a modified Cottrell equation afforded an apparent diffusion coefficient of 2×10^{-12} cm^2/s (fig. S81), a value substantially higher than that obtained with analogous metal-organic framework (MOF) thin films bearing cobalt porphyrin units (47). Using the silicon oxide–hosted sample, we measured the direct current conductivity of COF-366-Co to be ~10^{-6} S/cm, which is also higher than that of the MOF (figs. S84 and S85). In addition to a presumably increased portion of electroactive cobalt sites, the favorable charge-transport properties led to a higher cata-

lytic efficiency. Under the same electrolysis conditions, COF-366-Co thin films on glassy carbon exhibited a TOF of 665 hour^{-1}, a value seven times as high as that of the same material deposited on a carbon fabric, with a high current density of 45 mA/mg and a Faradaic efficiency of 86%.

Electrokinetics experiments indicated that covalently linking cobalt porphyrin active sites within a COF influences the mechanistic pathways for carbon dioxide reduction. For the systems employing COF-366-Co, COF-367-Co, and COF-367-Co(10%), Tafel plots of the logarithm of current density [$\log(j_{CO})$] versus the overpotential (η) display comparable slopes between 470 and 550 mV/dec (where 1 dec is one order of magnitude) in the linear, lower–current density regime (–0.57 to –0.87 V). This result differs considerably from what is observed for the molecular Co(TAP) analog (270 mV/dec) (Fig. 3E and figs. S65 to S68). This difference suggests that, when embedded in a structurally and electronically extended framework, cobalt porphyrin catalyzes carbon dioxide reduction by a different mechanism than that which pertains with the simple molecular analog. In addition, both the COF and Co(TAP) catalysts showed a first-order rate dependence on the partial pressure of carbon dioxide (fig. S87) and no rate dependence on the pH (figs. S88 and S89), indicating that the rate-limiting chemical step involves the participation of one molecule of carbon dioxide and no proton.

Finally, we applied x-ray absorption spectroscopy (XAS) as a probe to evaluate how the surrounding COF influenced the electronic structures of incorporated catalytic cobalt porphyrin units and, in turn, the associated carbon dioxide reduction mechanism (48, 49). Comparison of the cobalt K-edge XAS spectra of Co(TAP), COF-367-Co, and COF-367-Co(10%) (Fig. 3F) reveals a similar line size, shape, and position, consistent with a formal Co(II) oxidation state for all samples. When a reduction potential (–0.67 V) was applied to COF-367-Co under a carbon dioxide atmosphere, the K-edge revealed a line-shape change consistent with the partial reduction of Co(II) to Co(I) (fig. S96). The two COF catalysts also exhibited an additional pre-edge feature not present in the molecular Co(TAP) analog (Fig. 3F, inset); this difference shows that the COF environment could directly modulate the electronic properties of molecular centers coupled into the extended lattice (50, 51). This feature, unique to the COFs, was also observed when the catalysts were subjected to open-circuit or electrolysis (–0.67 V) potentials in a bicarbonate buffer (figs. S92 to S95). The communication between the metal and COF lattice could furnish a cobalt center with a more delocalized electronic structure, a network-solid analog to noninnocent ligand behavior in molecular systems (35).

Incorporating tunable molecular units within an extended COF thus gives rise to electrocatalysts that display advantageous features of both molecular and heterogeneous systems and promote carbon dioxide reduction to carbon monoxide with exceptionally high activity and selectivity compared with existing systems (table S21). We

anticipate that these hybrid molecular-material platforms will be applicable to a broad range of catalytic applications, particularly those that require sustainable electrical and/or solar input and aqueous compatibility.

REFERENCES AND NOTES

1. N. S. Lewis, D. G. Nocera, *Proc. Natl. Acad. Sci. U.S.A.* **103**, 15729–15735 (2006).
2. H. B. Gray, *Nat. Chem.* **1**, 7 (2009).
3. C. Costentin, M. Robert, J.-M. Savéant, *Chem. Soc. Rev.* **42**, 2423–2436 (2013).
4. B. Kumar et al., *Annu. Rev. Phys. Chem.* **63**, 541–569 (2012).
5. A. M. Appel et al., *Chem. Rev.* **113**, 6621–6658 (2013).
6. B. Fisher, R. Eisenberg, *J. Am. Chem. Soc.* **102**, 7361–7363 (1980).
7. J. Hawecker, J.-M. Lehn, R. Ziessel, *J. Chem. Soc. Chem. Commun.* **1984**, 328–330 (1984).
8. M. Beley, J. P. Collin, R. Ruppert, J. P. Sauvage, *J. Am. Chem. Soc.* **108**, 7461–7467 (1986).
9. E. B. Cole et al., *J. Am. Chem. Soc.* **132**, 11539–11551 (2010).
10. M. Bourrez, F. Molton, S. Chardon-Noblat, A. Deronzier, *Angew. Chem. Int. Ed.* **50**, 9903–9906 (2011).
11. J. Schneider et al., *Energy Environ. Sci.* **5**, 9502–9510 (2012).
12. V. S. Thoi, N. Kornienko, C. G. Margarit, P. Yang, C. J. Chang, *J. Am. Chem. Soc.* **135**, 14413–14424 (2013).
13. P. Kang, T. J. Meyer, M. Brookhart, *Chem. Sci.* **4**, 3497–3502 (2013).
14. B. A. Rosen et al., *Science* **334**, 643–644 (2011).
15. K. P. Kuhl, E. R. Cave, D. N. Abram, T. F. Jaramillo, *Energy Environ. Sci.* **5**, 7050–7059 (2012).
16. C. W. Li, M. W. Kanan, *J. Am. Chem. Soc.* **134**, 7231–7234 (2012).
17. W. Zhu et al., *J. Am. Chem. Soc.* **135**, 16833–16836 (2013).
18. D. Kim, J. Resasco, Y. Yu, A. M. Asiri, P. Yang, *Nat. Commun.* **5**, 4948 (2014).
19. S. Zhang, P. Kang, T. J. Meyer, *J. Am. Chem. Soc.* **136**, 1734–1737 (2014).
20. A. P. Côté et al., *Science* **310**, 1166–1170 (2005).
21. E. L. Spitler, W. R. Dichtel, *Nat. Chem.* **2**, 672–677 (2010).
22. S. Wan et al., *Chem. Mater.* **23**, 4094–4097 (2011).
23. H. M. El-Kaderi et al., *Science* **316**, 268–272 (2007).
24. E. L. Spitler et al., *Angew. Chem. Int. Ed.* **51**, 2623–2627 (2012).
25. W. Lu et al., *Chem. Soc. Rev.* **43**, 5561–5593 (2014).
26. D. N. Bunck, W. R. Dichtel, *Angew. Chem. Int. Ed.* **51**, 1885–1889 (2012).
27. L. Ma, J. M. Falkowski, C. Abney, W. Lin, *Nat. Chem.* **2**, 838–846 (2010).
28. J. Lee et al., *Chem. Soc. Rev.* **38**, 1450–1459 (2009).
29. J. Park, D. Feng, H.-C. Zhou, *J. Am. Chem. Soc.* **137**, 1663–1672 (2015).
30. D. J. Xiao et al., *Nat. Chem.* **6**, 590–595 (2014).
31. C. Wang, Z. Xie, K. E. deKrafft, W. Lin, *J. Am. Chem. Soc.* **133**, 13445–13454 (2011).
32. S. Pullen, H. Fei, A. Orthaber, S. M. Cohen, S. Ott, *J. Am. Chem. Soc.* **135**, 16997–17003 (2013).
33. H. Deng et al., *Science* **327**, 846–850 (2010).
34. D. Behar et al., *J. Phys. Chem. A* **102**, 2870–2877 (1998).
35. R. Eisenberg, H. B. Gray, *Inorg. Chem.* **50**, 9741–9751 (2011).
36. G. H. V. Bertrand, V. K. Michaelis, T. C. Ong, R. G. Griffin, M. Dincă, *Proc. Natl. Acad. Sci. U.S.A.* **110**, 4923–4928 (2013).
37. J. Guo et al., *Nat. Commun.* **4**, 2736 (2013).
38. M. Calik et al., *J. Am. Chem. Soc.* **136**, 17802–17807 (2014).
39. In pH 7.2 phosphate buffer, electrolyses at potentials equal to or more negative than –0.67 V resulted in moderate hydrogen evolution reactivity. However, this activity was largely suppressed when the solution was saturated with carbon dioxide (see below).
40. The intrinsic i_{cat}/i_p value was likely higher, as under carbon dioxide atmosphere, the current resulting from proton reduction was inhibited.
41. C. R. DeBlase et al., *ACS Nano* **9**, 3178–3183 (2015).
42. J. W. Colson et al., *Science* **332**, 228–231 (2011).
43. D. D. Medina et al., *ACS Nano* **8**, 4042–4052 (2014).
44. X.-H. Liu et al., *J. Am. Chem. Soc.* **135**, 10470–10474 (2013).
45. The COF-coated glassy carbon showed an ill-defined GIWAXS pattern due to high background scattering (figs. S52 and S53). Because the synthetic conditions were identical to those used with FTO and silicon oxide, we assumed that the COF grown on glassy carbon also formed a crystalline thin film.
46. $E_{1/2}$ could not be accurately measured with this method, owing to decomposition of FTO at potentials more negative than –0.57 V.
47. S. R. Ahrenholtz, C. C. Epley, A. J. Morris, *J. Am. Chem. Soc.* **136**, 2464–2472 (2014).
48. A. A. Peterson, J. K. Nørskov, *J. Phys. Chem. Lett.* **3**, 251–258 (2012).

49. N. Kornienko *et al.*, *J. Am. Chem. Soc.* **137**, 7448–7455 (2015).
50. F. de Groot, G. Vankó, P. Glatzel, *J. Phys. Condens. Matter* **21**, 104207 (2009).
51. J. Yano *et al.*, *Science* **314**, 821–825 (2006).

GEOPHYSICS

Stress orientations in subduction zones and the strength of subduction megathrust faults

Jeanne L. Hardebeck

Subduction zone megathrust faults produce most of the world's largest earthquakes. Although the physical properties of these faults are difficult to observe directly, their frictional strength can be estimated indirectly by constraining the orientations of the stresses that act on them. A global investigation of stress orientations in subduction zones finds that the maximum compressive stress axis plunges systematically trenchward, consistently making an angle of 45° to 60° with respect to the subduction megathrust fault. These angles indicate that the megathrust fault is not substantially weaker than its surroundings. Together with several other lines of evidence, this implies that subduction zone megathrusts are weak faults in a low-stress environment. The deforming outer accretionary wedge may decouple the stress state along the megathrust from the constraints of the free surface.

S ubduction zones pose a considerable hazard as the main source of great earthquakes (magnitude ≥8). Relative to other fault types, subduction zone megathrust faults may also have unique physical properties, due to the sediments and fluids that are entrained by the subducting oceanic plate (*1*). The presence of fluids, particularly at high fluid pressures, can weaken faults substantially (*2*). Direct evidence suggests that subduction zone megathrust faults slip with low frictional resistance near Earth's surface (*3*). The strength of these faults at seismogenic depths is less clear, as they can only be studied indirectly.

The orientation of a fault with respect to the stress field can be an indicator of the fault's strength. Faults optimally oriented for frictional failure make an angle of ~30° to the maximum compressive stress axis, σ_1. Nonoptimally oriented faults can also be active, but faults with typical frictional strength should not slip at a high angle to σ_1 (≥60°) (*4*). Faults operating at a high angle to σ_1 must be very weak compared to the surrounding material to slip at relatively low applied shear stress. Similarly, faults ori-

ented at a very low angle to σ_1 (<10°) must also be weak.

The traction at Earth's surface is zero, requiring an Andersonian stress state in which one principal stress axis is vertical (*5*). Most crustal faulting is consistent with an Andersonian stress state (*6*). The very shallow dip (~10°) of the upper portion of many subduction zone megathrusts (*7*) suggests that, if these faults exist within an Andersonian stress state, they operate at a high angle to one principal stress axis (and at a low angle to the other two) and are therefore frictionally weak. However, observations from some subduction zone locations indicate that the stress in these locations is not Andersonian (*8*–*11*).

I systematically investigate the stress orientations in subduction zones worldwide, to determine whether the stress state is generally non-Andersonian and whether megathrust faults are well-oriented for failure. I compile the moment tensors (*12*, *13*) of earthquakes located within 20 km of the subduction zone interface (*7*) to represent the megathrust region, and more shallow events to represent the upper plate. I stack the events for each subduction zone to invert for stress orientation (*14*) as a one-dimensional function of subduction interface depth. For the several subduction zones

near Japan, there are enough moment tensors to invert for the two-dimensional spatially varying stress field as well.

The stress state in the subduction zones near Japan is generally not Andersonian. The σ_1 axis in most megathrust regions plunges systematically trenchward (opposite the direction of subduction zone dip), generally plunging between 10° and 50° (Fig. 1A). A similar plunge of the σ_1 axis is observed within the upper plate above the Japan Trench, Kuril Trench, and Nankai Trough (Fig. 1G), whereas back-arc extension (near-vertical σ_1) dominates above the Ryukyu and Izu-Bonin trenches.

Comparing the plunge of the σ_1 axis in the megathrust region to the dip of the subduction interface (*7*) gives the angle of σ_1 to the megathrust fault (Fig. 1B). For the Kuril, Japan, and Izu-Bonin trenches, the σ_1 axis is typically at an angle of 20° to 50° to the fault. For the Ryukyu Trench, the σ_1 axis makes somewhat larger angles of 30° to 80° to the fault. In the Nankai Trough, σ_1 is oriented at 10° to 30° to the fault in the upper 20 km, while at deeper depths, the σ_1 axis is near-vertical. The plunge of the σ_1 axis is stable with depth (Fig. 1C), except in the Nankai Trough (Fig. 1D), and the subduction megathrust is generally well oriented for failure from the near-surface to at least 60 km depth (Fig. 1E). The stacked Kuril, Japan, and Izu-Bonin trenches (the subducting Pacific plate) show a megathrust fault that is optimally oriented for failure, at ~30° to σ_1, over the full depth range. The megathrust at the Ryukyu Trench is generally well oriented for failure at <60° down to 30 km depth, and is marginally oriented at ~60° from 30 km to 60 km depth. The exception is the Nankai Trough (Fig. 1F), which is well oriented at ~20° to σ_1 only in the upper 20 km. Below 30 km, the megathrust is not oriented for reverse faulting within the error bounds. This suggests that 30 km is the downward limit of coupling between the subducting and overriding plates.

For all global subduction zones studied, for almost all depths, the σ_1 axis plunges systematically trenchward, with plunge generally between 10° and 50° (Fig. 2A). The plunge tends to decrease with depth, while the subduction zone dip increases (*7*), so that the angle of σ_1 to the subduction interface is remarkably stable with depth (Fig. 2B). This angle is also remarkably similar across subduction zones, most falling within the range 45° to 60°.

The Japan and South American subduction zones are anomalous in being more optimally

U.S. Geological Survey, Menlo Park, CA, USA.
E-mail: jhardebeck@usgs.gov

oriented at 20° to 40°, as is the Nankai Trough in the upper 20 km. The Marianas Trench, similar to the Ryukyu Trench, is at a somewhat high angle at 20 to 40 km depth, although in both cases angles of <60° are within the error bounds. The Mexico Trench is the only case in which the megathrust is unambiguously at high angle, although only below 40 km, implying that this megathrust may be unusually weak at depth. These few anomalous stress orientations are not correlated with the age of the subducting plate (15) or the trench sediment thickness

(16). The subduction zones at low angle (Japan, Nankai, South America) all exhibit strong seismic coupling (17). However, subduction zones at moderate to high angles exhibit a wide range of seismic coupling, so there is no clear correlation.

The most-vertical principal stress axis, σ_V, must be vertical at Earth's surface. However, the systematic plunge of the σ_1 axis implies that σ_V is generally not vertical. I invert for stress orientation the earthquakes near the main Japanese islands, separated into megathrust and upper plate regions and binned by hypocentral

depth (14), to investigate whether σ_V becomes closer to vertical near the free surface. I include the aftershock sequence of the 2011 Tohoku earthquake, which contains many shallow events in the megathrust region. The aftershocks must be inverted separately because of the impact of the Tohoku earthquake on the local stress field (8, 9) and on the distribution of earthquakes in the upper plate (18). The megathrust zone shows no rotation of σ_V toward vertical at shallower depths near the trench, either before or after the Tohoku earthquake (Fig. 3, A and B). The upper
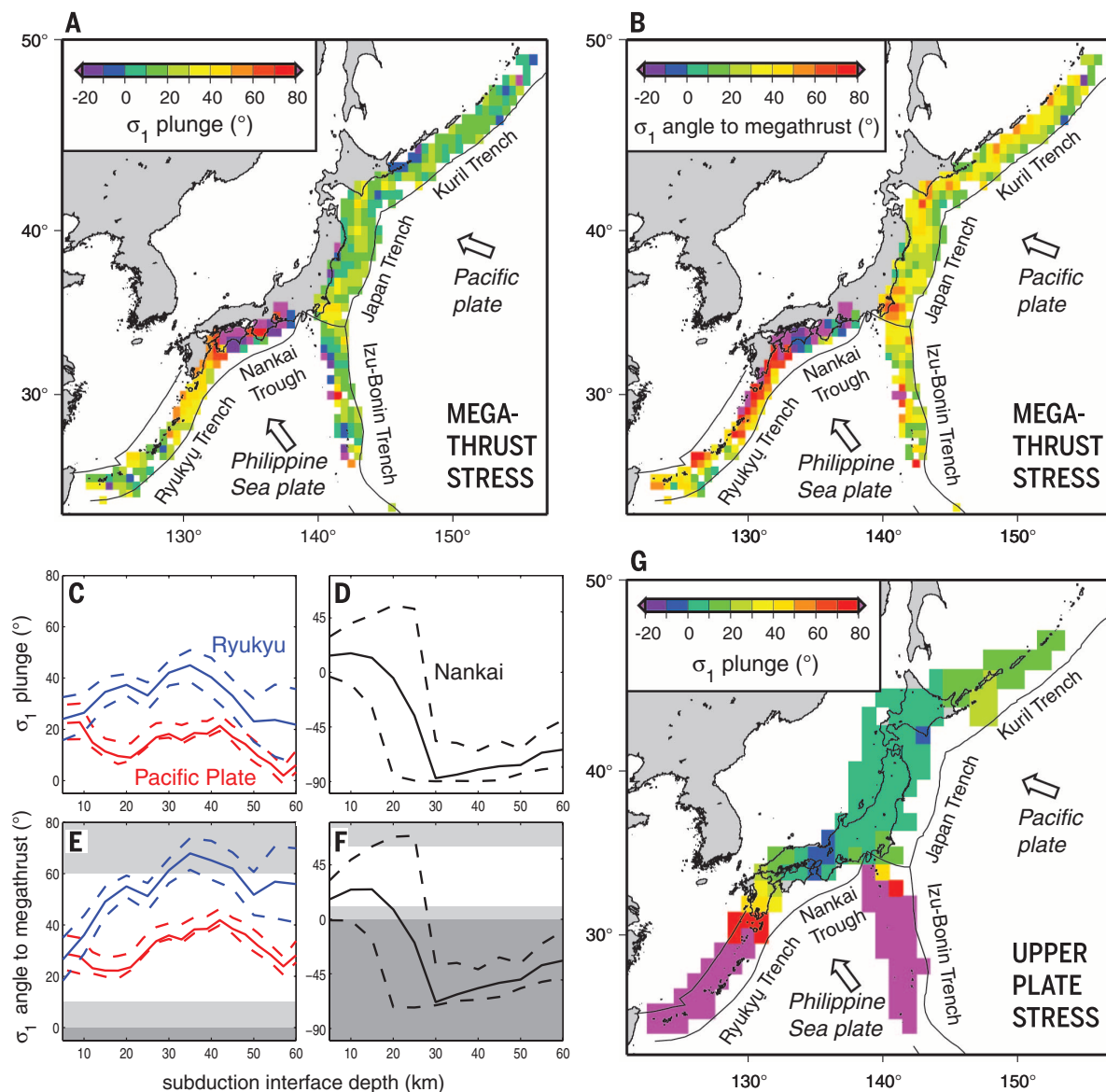
Fig. 1. Orientation of the maximum compressive stress axis, σ_1, for subduction zones near Japan. (**A**) Spatial distribution of the plunge of σ_1 near the megathrust, positive if σ_1 plunges trenchward (i.e., opposite to the direction of subduction zone dip). (**B**) Spatial distribution of the angle of σ_1 to the subduction zone interface, positive to drive reverse slip. (**C**) The plunge of σ_1 near the megathrust as a function of subduction zone depth, shown separately for the subducting Pacific Plate (Kuril, Japan, and Izu-Bonin trenches) and the Ryukyu Trench. Dashed lines indicate 95% confidence range. (**D**) The plunge of

σ_1 near the megathrust for the Nankai Trough. (**E**) The angle of σ_1 to the subduction zone interface, as a function of subduction zone depth, for the subducting Pacific Plate and the Ryukyu Trench. Dashed lines indicate 95% confidence range. Light shading indicates high or low angles implying a poorly oriented fault; dark shading indicates angles inconsistent with reverse slip. (**F**) The angle of σ_1 to the subduction zone interface for the Nankai Trough. Shading as in (E). (**G**) Spatial distribution of the plunge of σ_1 in the upper plate, positive if σ_1 plunges trenchward.

plate, however, demonstrates a clear rotation of σ_V toward vertical with decreasing depth, over the whole depth range considered (Fig. 3, C and D). The upper plate appears to see the free surface at depth, but the megathrust zone does not. The difference may be due to the deforming outer accretionary wedge (19). The outer wedge permanently deforms in response to the applied stresses, including any difference in traction between the free surface and the base of the wedge, which may decouple the stress along the megathrust at greater depths from the constraints of the free surface.

The angle of σ_1 to the subduction interface indicates the frictional strength of the megathrust fault. The observed optimal to moderate angles imply that the megathrust frictional strength is similar to that of its surroundings. These angles are inconsistent with models of a relatively weak megathrust in a strong crust (20). The observed stability of the angle of σ_1 to the subduction interface suggests that the coefficient of friction of the megathrust is similar in most subduction zones worldwide and does not vary substantially from the near-surface to at least 60 km depth. The strength of a fault can be estimated from the angle of σ_1 to the fault, using a Mohr circle construction (21), if assumptions are made about the strength of the surrounding material. If the region around the megathrust is assumed to be strong and critically stressed (all other faults have a typical friction coefficient of $\mu = 0.6$, and pore pressure is hydrostatic), the megathrust coefficient of friction is implied to be $\mu = 0.35$ to 0.6. If pore pressure is elevated only within the megathrust fault zone, the required megathrust pore pressure would be 0.3 to 0.6 of lithostatic pressure.

Several lines of evidence suggest that the megathrust is weaker than the above assumptions imply. A coefficient of friction of $\mu = 0.08$ is estimated from the heat flow observed at shallow depths after the 2011 Tohoku earthquake (3), and the coefficient of friction inferred from heat flow for subduction zones worldwide is generally $\mu < 0.1$ (22). Seismological imaging of fluids in subduction zones implies nearly lithostatic pore pressure at greater depths (23, 24). Rotations of the stress field due to large subduction zone earthquakes imply low deviatoric stress levels (8, 9). A more likely model, therefore, is that the entire region is at low deviatoric stress. In this model, all faults, including the megathrust, are weak and support only low shear stress. A similar model has been proposed for the San Andreas continental transform plate boundary (25), despite the very different tectonic setting.

If the entire subduction zone region is at low strength, this implies that high fluid pressures or low friction coefficients are pervasive. We rule out a model of a broad area of high fluid pressure as seismic observations limit them to a narrow plate interface (26). Therefore, other active faults in the subduction zone region must be weakened as a result of narrow zones of high fluid pressure or low friction coefficient. The
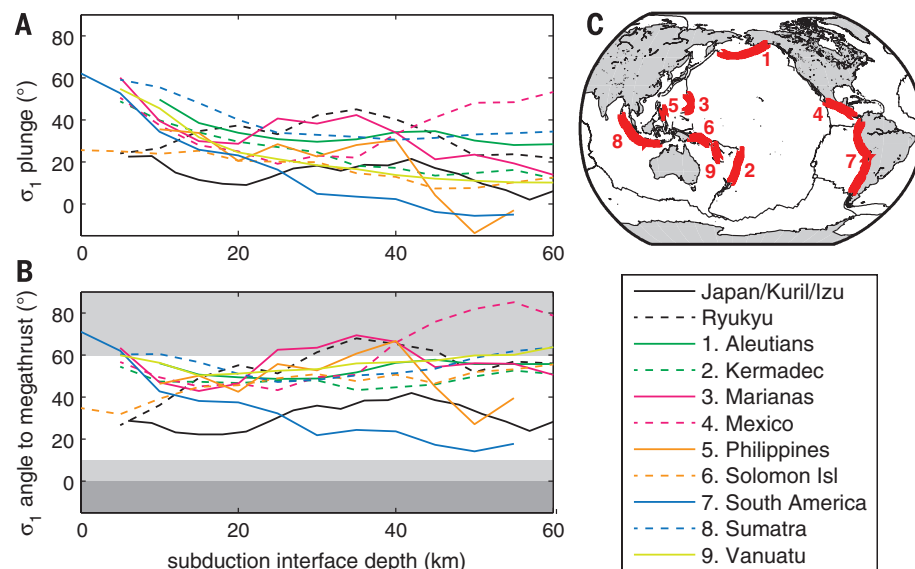
Fig. 2. Orientation of the maximum compressive stress axis, σ_1, as a function of depth for subduction zones worldwide. (**A**) The plunge of σ_1 near the megathrust, positive if σ_1 plunges trenchward, as a function of subduction zone depth. Line colors and styles correspond to subduction zones as shown in the key; results from Japan are reproduced in black. The 95% confidence (not shown) is on average ±8°. (**B**) The angle of σ_1 to the subduction zone interface as a function of subduction zone depth. Light shading indicates high or low angles implying a poorly oriented fault; dark shading indicates angles inconsistent with reverse slip. (**C**) Map with the subduction zones used indicated in red, excluding Japan. Numbers correspond to those in the key.
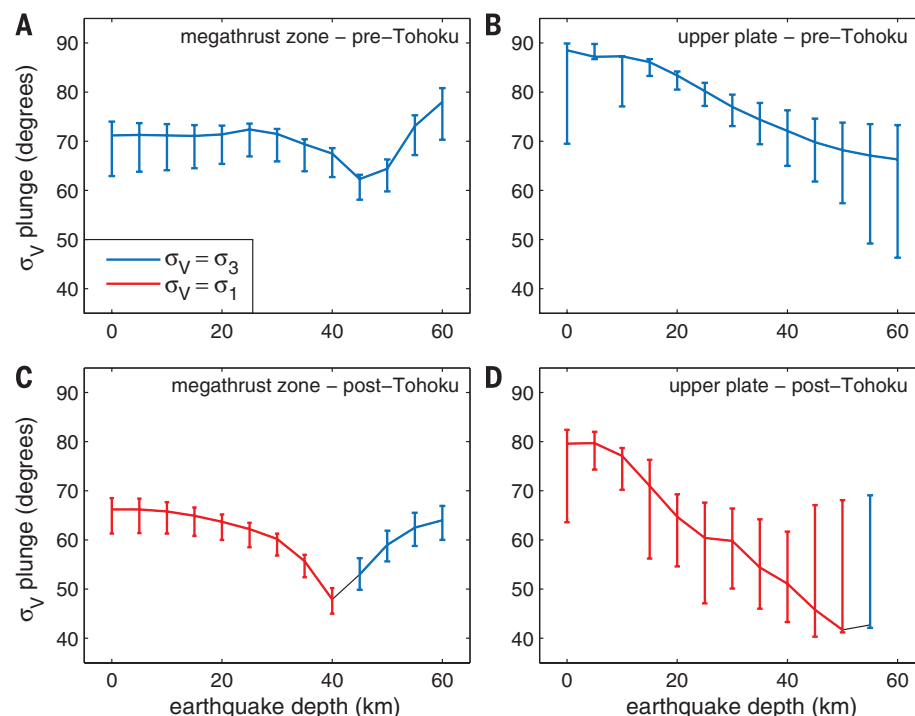
Fig. 3. Orientation of the most-vertical principal stress axis, σ_V, for the main islands of Japan as a function of earthquake hypocentral depth. Error bars indicate 95% confidence range. Color indicates which stress axis is most vertical. Depth is relative to sea level. (**A**) The plunge of σ_V in the Japan Trench megathrust region prior to the 2011 M9 Tohoku earthquake. (**B**) The plunge of σ_V in the upper plate of the main islands of Japan prior to the Tohoku earthquake. (**C**) The plunge of σ_V in the Japan Trench megathrust region for the 3 months following the Tohoku earthquake. (**D**) The plunge of σ_V in the upper plate of the main islands of Japan for the 3 months following the Tohoku earthquake.

stability of the observed stress orientations with depth implies that there are no large down-dip changes in the relative strengths of the mega-thrust and other faults, despite substantial changes in temperature and pressure. This suggests that all faults in the subduction zone region have similar physical mechanisms controlling their strength.

REFERENCES AND NOTES

1. S. A. Peacock, *Science* **248**, 329–337 (1990).
2. R. H. Sibson, *Tectonophysics* **600**, 142–152 (2013).
3. P. M. Fulton *et al.*, *Science* **342**, 1214–1217 (2013).
4. R. H. Sibson, *J. Struct. Geol.* **7**, 751–754 (1985).
5. E. M. Anderson, *The Dynamics of Faulting and Dyke Formation with Application to Britain* (Oliver & Boyd, Edinburgh, 1951).
6. B. Célérier, *Rev. Geophys.* **46**, RG4001 (2008).
7. G. P. Hayes, D. J. Wald, R. L. Johnson, *J. Geophys. Res.* **117**, B01302 (2012).
8. A. Hasegawa, K. Yoshida, T. Okada, *Earth Planets Space* **63**, 703–707 (2011).
9. J. L. Hardebeck, *Geophys. Res. Lett.* **39**, L21313 (2012).
10. S. Ghimire, Y. Tanioka, *Tectonophysics* **51**, 1–13 (2011).
11. M. Pardo, D. Comte, T. Monfret, *J. S. Am. Earth Sci.* **15**, 11–22 (2002).
12. A. Kubo, E. Fukuyama, H. Kawai, K. Nonomura, *Tectonophysics* **356**, 23–48 (2002).
13. G. Ekström, M. Nettles, A. M. Dziewonski, *Phys. Earth Planet. Inter.* **200–201**, 1–9 (2012).
14. See supplementary materials on *Science* Online.
15. P. Molnar, T. Atwater, *Earth Planet. Sci. Lett.* **41**, 330–340 (1978).
16. A. Heuret, C. P. Conrad, F. Funiciello, S. Lallemand, L. Sandri, *Geophys. Res. Lett.* **39**, L05304 (2012).
17. C. H. Scholz, J. Campos, *J. Geophys. Res.* **117**, B05310 (2012).
18. S. Toda, R. S. Stein, J. Lin, *Geophys. Res. Lett.* **38**, L00G03 (2011).
19. K. Wang, Y. Hu, *J. Geophys. Res.* **111**, B06410 (2006).
20. M. E. Magee, M. D. Zoback, *Geology* **21**, 809–812 (1993).
21. R. J. Twiss, E. M. Moores, *Structural Geology* (Freeman, New York, ed. 2, 2007).
22. X. Gao, K. Wang, *Science* **345**, 1038–1041 (2014).
23. S. Husen, E. Kissling, *Geology* **29**, 847–850 (2001).
24. P. Audet, M. G. Bostock, N. I. Christensen, S. M. Peacock, *Nature* **457**, 76–78 (2009).
25. J. L. Hardebeck, A. J. Michael, *J. Geophys. Res.* **109**, B11303 (2004).
26. D. Eberhart-Phillips, M. Reyners, *Geophys. Res. Lett.* **26**, 2565–2568 (1999).

SUPPLEMENTARY MATERIALS

www.sciencemag.org/content/349/6253/1213/suppl/DC1
Materials and Methods
Figs. S1 and S2
References (*27*, *28*)

14 May 2015; accepted 15 July 2015
10.1126/science.aac5625

Tuning of fast-spiking interneuron properties by an activity-dependent transcriptional switch

Nathalie Dehorter,[1,2] Gabriele Ciceri,[2]* Giorgia Bartolini,[1,2] Lynette Lim,[1,2] Isabel del Pino,[1,2]† Oscar Marín[1,2]‡

The function of neural circuits depends on the generation of specific classes of neurons. Neural identity is typically established near the time when neurons exit the cell cycle to become postmitotic cells, and it is generally accepted that, once the identity of a neuron has been established, its fate is maintained throughout life. Here, we show that network activity dynamically modulates the properties of fast-spiking (FS) interneurons through the postmitotic expression of the transcriptional regulator Er81. In the adult cortex, Er81 protein levels define a spectrum of FS basket cells with different properties, whose relative proportions are, however, continuously adjusted in response to neuronal activity. Our findings therefore suggest that interneuron properties are malleable in the adult cortex, at least to a certain extent.

F ast-spiking (FS), parvalbumin-expressing (PV⁺) basket cells make up the most abundant population of GABAergic interneurons in the cerebral cortex. Although they probably represent no more than 5% of the total neuronal population, they contribute to feedback and feedforward inhibition and are critically involved in the generation of network oscillations that are crucial for sensory perception, cognition, and behavior (*1–5*). In addition, FS PV⁺ basket cells play a prominent role in the regulation of plasticity and learning (*6–9*). Although it is likely that different classes of FS PV⁺ interneurons exist, the molecular mechanisms regulating their properties remain largely unknown (*10*).

We previously found that neurons generated in the medial ganglionic eminence (MGE) express the transcription factor Etv1/Er81 (*11*). Because PV⁺ interneurons derive from the MGE (*10*), we investigated whether Er81 is expressed in this population of interneurons. Although Er81 expression in the neocortex has been ascribed only to layer V pyramidal cells (*12*), we observed that this transcription factor is also expressed in scattered cells throughout the neocortex of postnatal mice (Fig. 1A). In layer II-III, where Er81⁺ expressing cells are particularly abundant, the majority of these cells are PV⁺ interneurons (fig. S1). Conversely, over 60% of PV⁺ interneurons in layer II-III contain detectable levels of Er81 protein (Fig. 1B).

[1]MRC Centre for Developmental Neurobiology, Medical Research Council, New Hunt's House, Guy's Campus, King's College London, London SE1 1UL, UK. [2]Instituto de Neurociencias, Consejo Superior de Investigaciones Científicas and Universidad Miguel Hernández, 03550 Sant Joan d'Alacant, Spain.
*Present address: Sloan-Kettering Institute for Cancer Research, 1275 York Avenue, New York, NY 10065, USA. †Present address: Neurocentre Magendie, 146 rue Léo Saignat, 33076 Bordeaux cedex, France. ‡Corresponding author. E-mail: oscar.marin@kcl.ac.uk

Because PV⁺ interneurons in superficial layers of the cortex are heterogeneous (*13*), we wondered whether Er81 expression defines the properties of FS interneurons. We thus performed whole-cell recordings in acute slices through the primary somatosensory cortex of *PV-Cre;RCE* mice, in which PV⁺ interneurons express an enhanced form of green fluorescent protein (GFP). We confirmed the identity of FS PV⁺ interneurons on the basis of well-described features of their action potentials (*14*). Different classes of PV⁺ FS interneurons have distinctive features in their pattern of discharge. For example, some classes of PV⁺ interneurons display a prominent delay to the first spike near spike threshold potential, whereas others do not (*15*, *16*). The majority of PV⁺ interneurons in layer II-III had a delayed firing pattern and expressed Er81 (n = 22/33 cells) (Fig. 1, C and E). By contrast, PV⁺ interneurons with very short latency or purely nondelayed firing consistently lacked detectable levels of Er81 protein (n = 11/33 cells) (Fig. 1, D and E). Thus, although the basic membrane properties of these cells are similar (fig. S2A), Er81 expression clearly segregates two classes of PV⁺ interneurons on the basis of their physiological parameters at near-threshold potential (Fig. 1, E to H). The correlation between Er81 expression and firing pattern seems universal among FS interneurons in the telencephalon. Chandelier cells, an important class of FS interneurons that exhibit nondelayed firing (*17*) (fig. S3), and the large majority of PV⁺ FS cells in layer IV, which also display nondelayed features, both lack Er81 expression (fig. S4, A to D). By contrast, PV⁺ interneurons in the striatum displayed a delayed firing pattern and contain Er81 (fig. S4, E to H).

To extend our observations, we analyzed the connectivity of FS interneurons in layer II-III of the somatosensory cortex. Recordings of miniature excitatory and inhibitory postsynaptic

currents (mEPSCs and mIPSCs, respectively) revealed that Er81+ FS interneurons receive significantly more excitatory synapses and far fewer inhibitory contacts than Er81− FS interneurons (Fig. 1, I to N, and fig. S2, B to G).

To determine whether Er81 plays an instructive role in the specification of delay-type FS interneurons, we specifically deleted *Er81* from the embryonic MGE by breeding *Lhx6-Cre* mice (*18*) with mice carrying loxP-flanked (F) *Er81* alleles (*19*). We observed no differences in the density and laminar distribution of PV+ interneurons in the cerebral cortex of control and *Lhx6-Cre;Er81^{F/F};RCE* mice at postnatal day 30 (P30) (Fig. 2A and fig. S5A), which indicated that Er81 is not required for the migration and early specification of FS interneurons. However, most FS interneurons in *Er81* conditional mutants displayed a dramatic reduction in the mean latency to the first spike, hyperpolarization of the threshold potential for spike, and a lower rheobase than control FS interneurons (Fig. 2B and fig. S5, B to D).

To assess whether Er81 function is also necessary for the maintenance of delay-type FS interneurons in the mature cortex, we generated conditional *Er81* mutant mice using *PV-Cre* mice, which only achieve effective recombination in the cortex in young adult mice (*20*). As in *Lhx6-Cre;Er81^{F/F};RCE* mice, we did not observe differences in the density or distribution of PV+ interneurons in the cortex of *PV-Cre;Er81^{F/F};RCE* mice compared with controls at P60 (Fig. 2C and fig. S6A). However, the postnatal elimination of *Er81* also caused a prominent decrease in the mean latency to the first spike in FS interneurons from the cortex of *PV-Cre;Er81^{F/F};RCE* mice (Fig. 2D and fig. S6, B to D). Because background conductance inputs may influence the relative delay in firing of the first spike, we analyzed this parameter while blocking synaptic activity. We did not observe changes in the mean latency to the first spike at threshold potential in *Er81* mutant interneurons with or without synaptic blockers (69.7 ± 19.1 ms and 60.5 ± 16.7 ms, respectively; $n = 5$, Student's t test, $P = 0.6$), which ruled out non–cell autonomous effects on these parameters.

The ability of some FS interneurons to exhibit a prominent delay of the first spike near spike threshold potential is thought to serve as an important gating mechanism of inhibitory function that is mediated by Kv1.1-containing potassium channels localized to the axon initial segment (*21*). Er81 could therefore control delayed firing in FS interneurons by regulating the expression of Kv1.1 channels. We found a prominent decrease in Kv1.1 protein levels in cortical lysates obtained from *PV-Cre;Er81^{F/F};RCE* mice compared with controls (Fig. 2E). To confirm that Er81 transcriptionally controls the expression of Kv1.1 in PV+ interneurons, we isolated these cells from the cortex of control and *PV-Cre;Er81^{F/F};RCE* mice using fluorescence-activated cell sorting (FACS) and carried out quantitative polymerase chain reaction (PCR) analyses. We found significantly lower *Kv1.1 mRNA* levels in mutant FS interneurons than in controls (Fig. 2F). Finally, we identified ETS binding sequences upstream of the transcriptional initiation site of *Kv1.1* and demonstrated specific binding of Er81 using chromatin immunoprecipitation (ChIP) analysis in cortical lysates (Fig. 2G). Although this later experiment lacks cellular resolution, the results are consistent with the notion that Er81 regulates the intrinsic neural excitability of delay-type FS interneurons, at least in part by controlling the expression of Kv1.1 channels.

Our initial observation that delay-type and nondelay-type FS interneurons receive, on average, different number of excitatory synapses (Fig. 1, H to K) prompted us to examine the connectivity of cortical PV+ interneurons in conditional *Er81* mutants. To this end, we first measured synaptic activity on FS interneurons in acute slices obtained from control and conditional *Lhx6-Cre;Er81^{F/F};RCE* mice. We found a significant decrease in the frequency and amplitude of mEPSCs in mutant FS interneurons compared with control cells (Fig. 3, A to E), which suggests that loss of Er81 during development changes the inputs received by these cells. To test whether the late removal of Er81 has the same effect, we recorded synaptic activity from FS interneurons
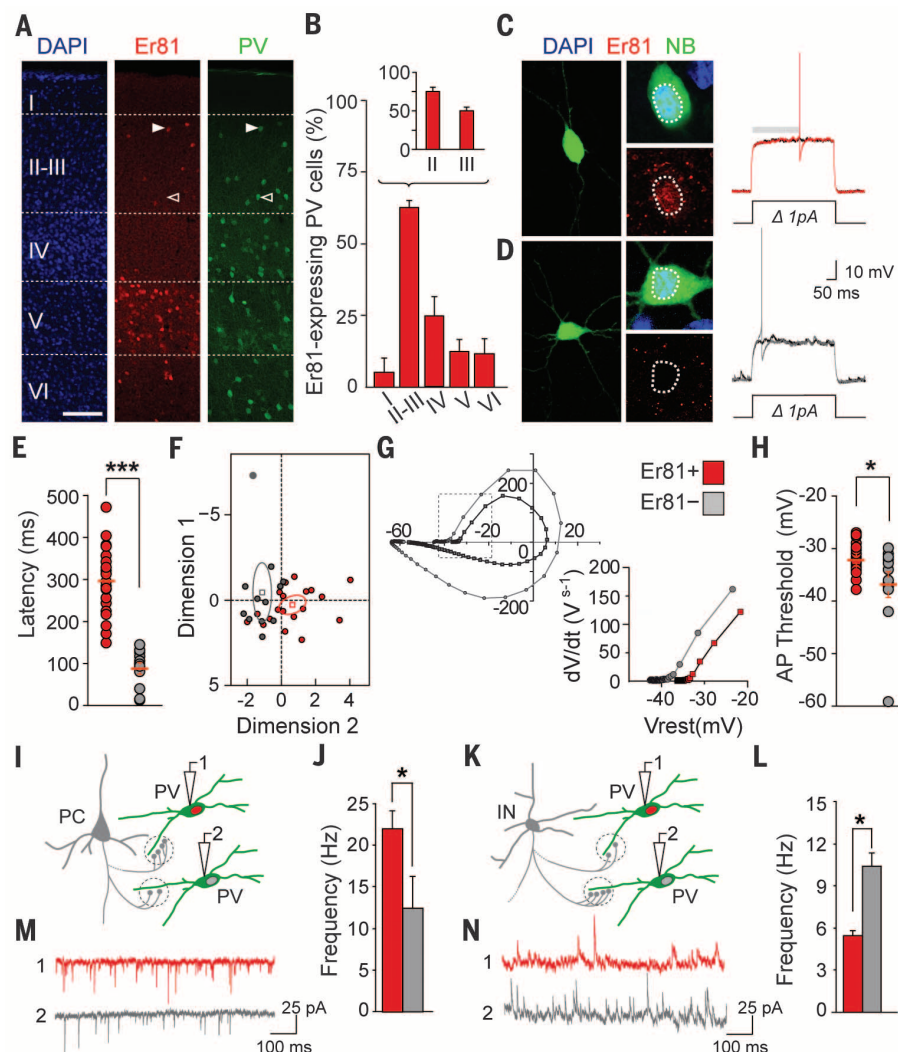
Fig. 1. Er81 expression distinguishes PV+ basket cell *n* subtypes. (A) Er81 protein expression in the somatosensory cortex. **(B)** PV+/Er81+ interneurons are particularly abundant in cortical layer II-III, with a superficial to deep gradient within this layer ($n = 11$ P25 mice). **(C** and **D)** Representative traces of firing at near threshold potential for Er81+ (red) and Er81− (gray) PV+ interneurons. NB, Neurobiotin. **(E)** Mean latency to the first spike ($n = 22$ and 9 cells, respectively; $P < 0.001$). **(F)** Individual factor maps from principal component analysis performed on recorded cells reveals a significant segregation between Er81+ and Er81− PV+ interneurons. **(G)** Phase plane plots for Er81+ and Er81− PV+ interneurons. **(H)** Threshold potential for spike is significantly different between Er81+ and Er81− PV+ interneurons ($n = 21$ and 11 cells, respectively; $P < 0.05$). **(I** and **K)** Schematic of mEPSCs and mIPSCs recordings in PV+ interneurons. PC, pyramidal cell; PV, PV+ interneuron; IN, Interneuron. **(M** and **N)** Representative traces. **(J** and **L)** Measurements of mEPSC ($n = 15$ and 6 cells, respectively; $P < 0.05$) and mIPSC ($n = 7$ and 4 cells, respectively; $P < 0.05$) frequencies in PV+ interneurons. Scale bars, 100 μm (A) and 10 μm (C) and (D). Graphs represent means ± SEM.

in control and *PV-Cre;Er81*^{F/F}*;RCE* mice. We found a significant decrease in the frequency of mEPSCs on mutant FS interneurons compared with controls, indicative of a reduced number of excitatory synapses, but no changes in their amplitude (Fig. 3, A to E). We also found that the density of vesicular glutamate transporter type 1 (VGlut1⁺) terminals contacting the soma of FS interneurons lacking Er81 is also reduced compared with

Fig. 2. Er81 regulates intrinsic properties of PV⁺ interneurons and Kv1.1 expression. (A) Normal distribution of PV⁺ interneurons in P30 layer II-III after embryonic genetic deletion of *Er81*. **(B)** Latency to the first spike and threshold potential for spike are significantly reduced in *Lhx6-Cre;Er81* conditional mutants (*n* = 20 and 18 cells, respectively; *P* < 0.05 for both values). **(C)** Normal distribution of PV⁺ interneurons in P60 layer II-III after postnatal genetic deletion of *Er81*. **(D)** Latency to the first spike and threshold potential for spike is significantly reduced in *PV-Cre;Er81* conditional mutants (*n* = 29 and 20 cells, respectively; *P* < 0.001 and *P* < 0.05, respectively). **(E)** Representative immunoblots (left) and quantification (right) of Kv1.1 protein in the cortex of control and conditional mutant mice (*n* = 5, *P* < 0.01). **(F)** Kv1.1 mRNA levels in PV⁺ interneurons isolated through FACS in control and conditional mutant mice (*n* = 4, *P* < 0.01). **(G)** ChIP assays on cortical tissue showing Er81 binding to Kv1.1 promoter regions (*n* = 3; *P* < 0.05 for site 2). Scale bar, 100 μm (A) and (C). Graphs represent means ± SEM.
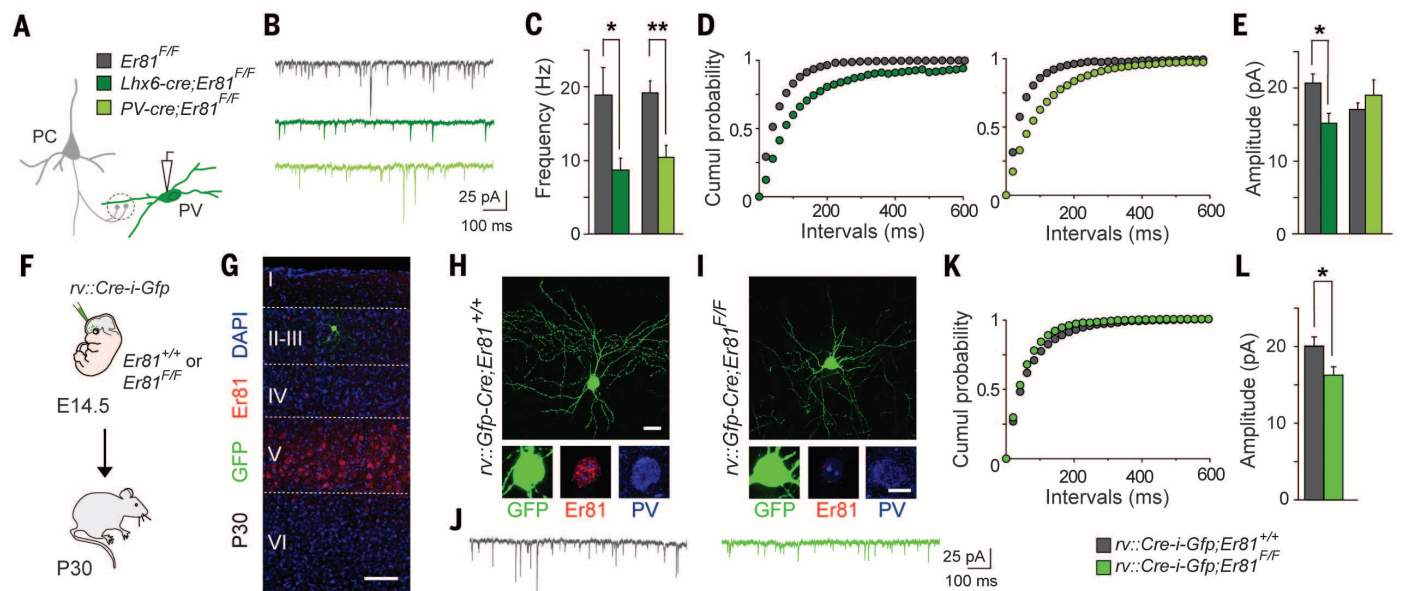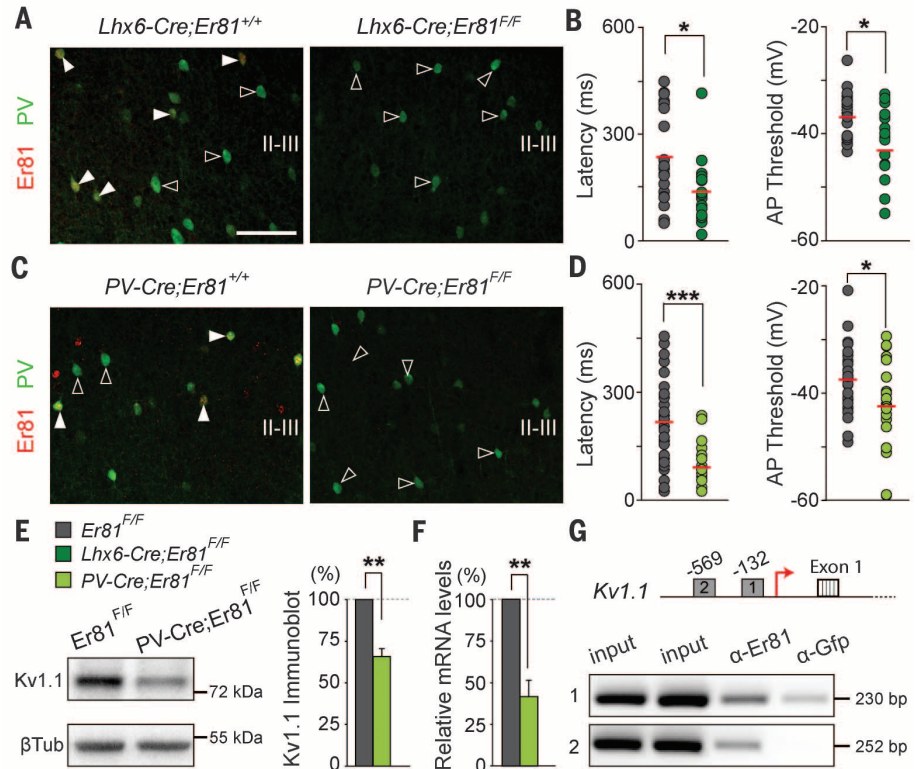
Fig. 3. Reduced excitatory inputs onto PV interneurons in conditional *Er81* mutants. (A) Schematic of mEPSCs recordings in PV⁺ interneurons. **(B)** Representative traces. **(C and D)** Measurement and cumulative plot of mEPSC frequencies in *Lhx6-Cre;Er81*^{F/F} (*n* = 11 and 9 cells, respectively; *P* < 0.05) and *PV-Cre;Er81*^{F/F} (*n* = 17 and 10 cells, respectively; *P* < 0.01) mutants. **(E)** Measurement of mEPSC amplitudes in *Lhx6-Cre;Er81*^{F/F} (*n* = 11 and 9 cells, respectively; *P* < 0.05) and *PV-Cre;Er81*^{F/F} mutants (*n* = 17 and 10 cells, respectively; *P* = 0.06). **(F)** Experimental design for the labeling of sparse control and *Er81* mutant MGE-derived interneurons. **(G)** Labeled interneurons are sparsely distributed throughout the cerebral cortex at very low density. **(H and I)** Representative images of layer II-III PV⁺ interneurons after viral infection in the MGE. **(J)** Representative traces of mEPSCs from control and *Er81* mutant interneurons. **(K)** Cumulative plot of mEPSCs frequencies (*n* = 10 and 11 cells, respectively; *P* = 0.45). **(L)** Measurement of mEPSCs amplitudes (*n* = 10 and 11 cells, respectively; *P* < 0.05). Scale bars, 10 μm and 5 μm (G) and (H) and 100 μm (I). Graphs represent means ± SEM.

controls (fig. S7, A and B), whereas the probability of release of these terminals is comparable for controls and mutants (fig. S7C). By contrast, recordings of mIPSCs from FS interneurons revealed a strong increase in their frequency without changes in amplitude in *PV-Cre;Er81^{F/F};RCE* mice compared with controls (fig. S8, A to D). This increase likely reveals an increase in the number of presynaptic inhibitory contacts received by FS interneurons in the absence of Er81, because no changes were observed in γ-aminobutyric acid (GABA) release probability (fig. S8E).

The observed changes in the inputs received by FS interneurons in *Er81* conditional mutants

have two possible explanations. One possibility is that Er81 directly regulates the connectivity of delay-type FS interneurons, as has been suggested for primary sensory neurons (*22*). Alternatively, the changes observed in conditional *Er81* mutants may reflect homeostatic adaptations in response to the loss of delay-type FS interneurons from cortical networks. To distinguish between these two possibilities, we ablated *Er81* from sparse cortical FS interneurons in each mouse. We used ultrasound imaging to inject low-titer retroviruses encoding *Cre* and *Gfp* into the MGE of wild-type and *Er81^{F/F}* embryos on embryonic day 14.5 (E14.5)

(Fig. 3F), when FS interneurons are being generated. These experiments labeled very few interneurons that migrate to layer II-III in both genotypes and that lack Er81 expression only in *Er81^{F/F}* mice (Fig. 3, G to I). We then performed whole-cell recordings from layer II GFP⁺ cells in P30 acute slices obtained from these mice. We found an almost complete loss of delay-type FS interneurons in the absence of Er81, as evidenced by a prominent reduction in the mean latency to the first spike and the levels of Kv1.1 expression in FS interneurons lacking Er81 compared with control cells (fig. S9, A to E). In contrast to these changes in intrinsic properties, we did not find
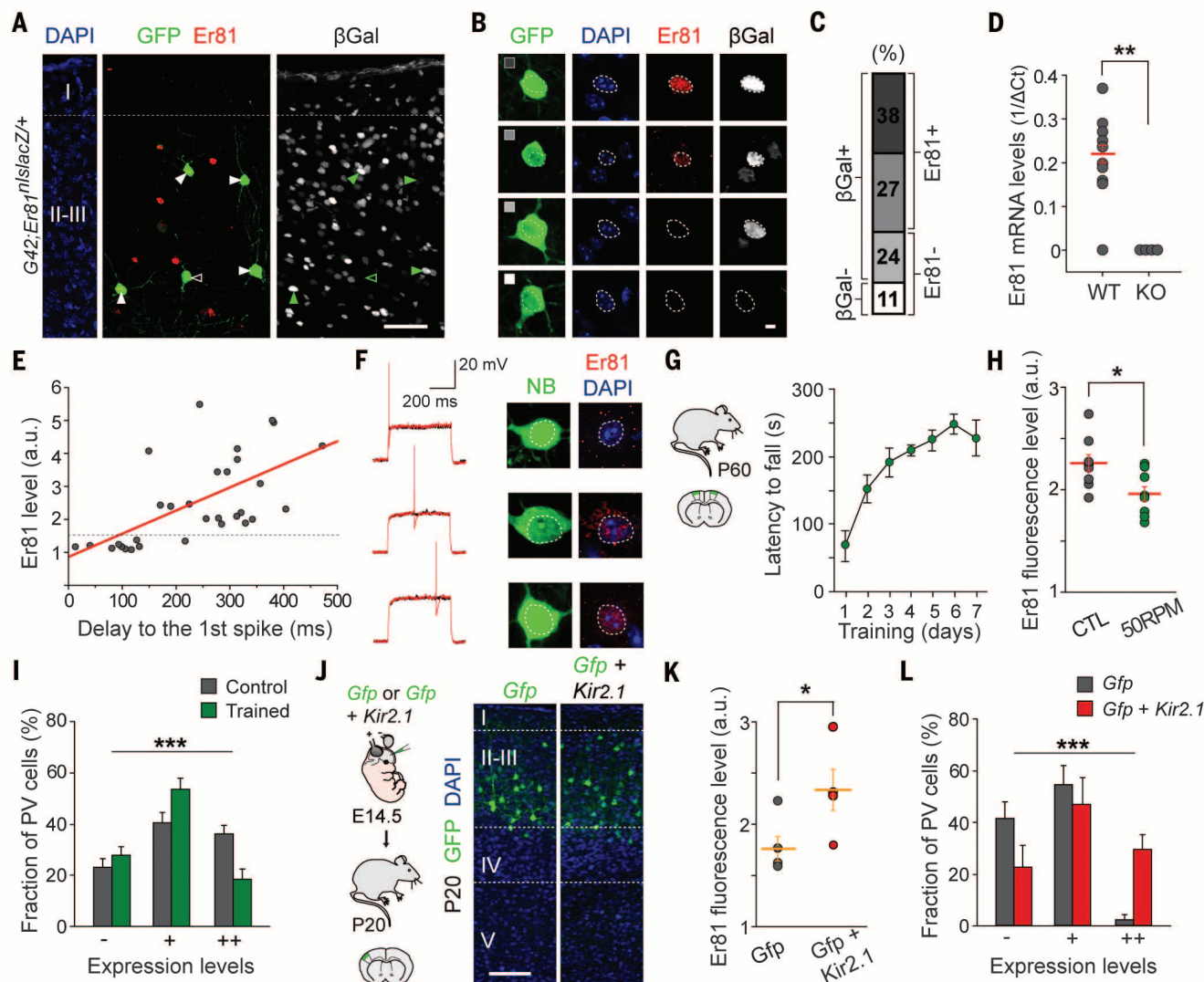
Fig. 4. Activity-dependent changes in Er81 expression. (**A**) Expression of Er81 and beta-galactosidase (βGal) in layer II-III PV⁺ interneurons. (**B** and **C**) Representative examples and relative proportion of four groups of layer II-III PV⁺ interneurons based on Er81 and βGal expression. (**D**) Most PV⁺ interneurons contain significant Er81 mRNA levels. (**E**) Scatter plot of Er81 expression and latency to the first spike. Line, linear regression fit (R^2) = 0.63 ($P < 0.0001$). (**F**) Representative traces of recorded PV⁺ interneurons illustrating the positive correlation between delayed firing and Er81 expression. (**G**) Learning curve (RotaRod performance) for motor task. (**H**) Er81 fluorescence intensity levels in PV⁺ interneurons from control and trained animals ($n = 8$; $P < 0.05$). (**I**) Dis-

tribution of Er81 fluorescence intensities in layer II PV⁺ interneurons from control and trained mice ($n = 8$; $P < 0.001$). Cells were grouped into three main classes on the basis of their levels of fluorescence intensity for nuclear Er81, < 1.3 times background levels (−), 1.3 to 1.6 times background (+), and > 1.6 times background levels (++). (**J**) Experimental design and distribution of electroporated pyramidal cells in layer II-III. (**K**) Mean Er81 fluorescence intensity in PV⁺ interneurons from control and *Kir2.1*-electroporated mice ($n = 4$; $P < 0.01$). (**L**) Distribution of Er81 fluorescence intensities in layer III PV⁺ interneurons from control and *Kir2.1*-electroporated mice ($n = 4$; $P < 0.001$), groups as in (I). Scale bars, 50 μm (A), 5 μm (B), and 100 μm (J). Graphs represent means ± SEM.

differences in the frequency of mEPSCs (Fig. 3, J to L) or the density of VGlut1+ terminals contacting the soma of FS interneurons lacking Er81 compared with controls cells (fig. S9, F and G).

Our results demonstrate that Er81 generates cell diversity within FS basket cells in the mouse cortex. Because Er81 function is also required for the maintenance of delay-type FS interneurons in the adult cortex (as revealed by the analysis of *PV-Cre;Er81^{F/F};RCE* mice), we next wondered when Er81 expression begins to distinguish both populations of interneurons. We used mice in which *nLacZ* have been inserted in the coding region of *Er81* (*Er81^{nlsLacZ/+}*) (22) and analyzed the fraction of FS interneurons expressing β-galactosidase in layer II-III of the somatosensory cortex. The large majority of layer II-III PV+ interneurons contained β-galactosidase in the adult cortex, including many cells with undetectable levels of nuclear Er81 protein (Fig. 4, A to C). This surprising result suggests that almost all FS interneurons transcribe *Er81* mRNA. Alternatively, because β-galactosidase is known to perdure long after being synthesized (23), this result may indicate that the majority of FS interneurons may have transcribed *Er81* at some point during development. To distinguish between these two possibilities, we performed whole-cell patch-clamp recordings in PV+ interneurons from layers II-III of the adult somatosensory cortex and subsequently collected the cytoplasm for single-cell reverse transcriptase PCR of *Er81*. Compared with *Er81* mutant interneurons (used to calibrate background), nearly all FS basket cells in the adult layer II-III of the somatosensory cortex contained substantial and comparable levels of *Er81* mRNA (10 out of 11 cells) (Fig. 4D), which suggests that the expression of Er81 in these interneurons is regulated posttranscriptionally. In addition, we found a direct correlation between the levels of nuclear Er81 protein and the latency to the first spike at near-threshold potential in FS interneurons (Fig. 4, E and F).

These observations prompted us to investigate whether the relative proportion of delay-type and nondelay-type FS interneurons remains constant in the adult cortex. Er81 transcription and activity is modulated by activity-dependent changes in intracellular calcium (24, 25), which raises the possibility that the complement of layer II-III FS interneuron subtypes might be adjusted in response to variations in network activity (26, 27). To test this hypothesis, we pharmacologically modified network activity levels in acute cortical slices. KCl or kainate rapidly decreased the relative proportion of layer II-III Er81+ FS interneurons within 2 hours (fig. S10, A and B). This reduction in Er81+ interneurons was associated with a parallel decrease in the mean latency to the first spike (fig. S10C). By contrast, pharmacological reduction of network activity with the L-type calcium channel blocker Nifedipine led to a significant rise in the proportion of Er81+ FS interneurons and a concomitant increase in the mean latency to the first spike of these cells (fig. S10, D to F).

To characterize the activity-dependent regulation of Er81 expression in more physiological conditions, we trained mice in a motor-learning paradigm and analyzed the levels of Er81 expression in layer II of the motor cortex (Fig. 4G). Motor learning significantly decreased the proportion of Er81+ FS interneurons compared with controls, because of a shift in Er81 levels toward lower intensity values (Fig. 4, H and I). To decrease the overall levels of activity in layer II-III pyramidal cells, we introduced the inward-rectifier potassium ion channel Kir2.1 in their cortical progenitor cells by means of in utero electroporation (28, 29) and examined the levels of Er81 protein in layer III of the somatosensory cortex in adult mice (Fig. 4J). We found a prominent increase in the proportion of Er81+ FS interneurons compared with controls, due to a change in Er81 levels toward higher-intensity values (Fig. 4, K and L). It was interesting that we did not observe comparable changes in other layers of the cortex, which suggests that this type of cellular plasticity mediated by Er81 might be limited to cortical layer II-III (fig. S11).

Our findings provide a mechanistic explanation for the activity-dependent regulation of interneuron properties through the transcriptional control of neuronal excitability and the modulation of synaptic inputs. Er81 has been previously shown to regulate the terminal differentiation of dopaminergic neurons and cerebellar granule cells (30, 31). In the cortex, Er81 shapes information processing by modulating the intrinsic properties of FS interneurons through the regulation of the Kv1.1 channel subunit, the expression of which is necessary for delayed firing (21). Other factors are likely involved in this process, because loss of Er81 does not completely transform fast-spiking interneurons into nondelayed cells. Kv1.1 function is also regulated by ErbB4 (32), a tyrosine kinase receptor that is highly expressed in the postsynaptic density of glutamatergic synapses contacting FS basket cells (33). This delineates a possible pathway through which synaptic activity may control Er81 expression to modulate the intrinsic properties of FS basket cells.

Our results also support the notion that activity-dependent mechanisms play a prominent role in the specification of neuronal properties (34, 35). However, in contrast to the classical view in which the "specification" typically refers to the process by which cells achieve and maintain a stable fate independent of environment, our results suggest that layer II-III fast spiking basket cells may not exist as distinct classes of interneurons, but rather as a continuum of interneurons with "tunable" characteristics that adapt to the changing environment. The observation that cortical circuits reversibly adapt to changing levels of activity by tuning the efficacy of delayed firing within the population of FS basket cells suggests a novel mechanism of network plasticity, and reinforces the notion that interneuron function is ultimately context dependent (5).

Recent work has linked different configurations of FS basket cells, as revealed by distinct

levels of PV expression, with learning and memory (7). Our analysis of *Er81* conditional mutant mice indicate that drastic imbalances in network configuration are accompanied by population-driven changes in structural synaptic plasticity, through which FS basket cells may lose their ability to filter out relatively weak, asynchronous stimulus.

REFERENCES AND NOTES

1. J. A. Cardin et al., Nature 459, 663–667 (2009).
2. V. S. Sohal, F. Zhang, O. Yizhar, K. Deisseroth, Nature 459, 698–702 (2009).
3. O. Yizhar et al., Nature 477, 171–178 (2011).
4. J. Courtin et al., Nature 505, 92–96 (2014).
5. H. Hu, J. Gan, P. Jonas, Science 345, 1255263 (2014).
6. Y. Yazaki-Sugiyama, S. Kang, H. Câteau, T. Fukai, T. K. Hensch, Nature 462, 218–221 (2009).
7. F. Donato, S. B. Rompani, P. Caroni, Nature 504, 272–276 (2013).
8. S. J. Kuhlman et al., Nature 501, 543–546 (2013).
9. S. B. Wolff et al., Nature 509, 453–458 (2014).
10. C. P. Wonders, S. A. Anderson, Nat. Rev. Neurosci. 7, 687–696 (2006).
11. N. Flames et al., J. Neurosci. 27, 9682–9695 (2007).
12. R. F. Hevner et al., Dev. Neurosci. 25, 139–151 (2003).
13. G. A. Ascoli et al., Nat. Rev. Neurosci. 9, 557–568 (2008).
14. B. Rudy, C. J. McBain, Trends Neurosci. 24, 517–526 (2001).
15. A. Gupta, Y. Wang, H. Markram, Science 287, 273–278 (2000).
16. J. Helm, G. Akgul, L. P. Wollmuth, J. Neurophysiol. 109, 1600–1613 (2013).
17. A. Woodruff, Q. Xu, S. A. Anderson, R. Yuste, Front. Neural Circuits 3, 15 (2009).
18. M. Fogarty et al., J. Neurosci. 27, 10935–10946 (2007).
19. T. D. Patel et al., Neuron 38, 403–416 (2003).
20. S. Hippenmeyer et al., PLOS Biol. 3, e159 (2005).
21. E. M. Goldberg et al., Neuron 58, 387–400 (2008).
22. S. Arber, D. R. Ladle, J. H. Lin, E. Frank, T. M. Jessell, Cell 101, 485–498 (2000).
23. M. I. Arnone, I. J. Dmochowski, C. Gache, Methods Cell Biol. 74, 621–652 (2004).
24. J. W. Cave et al., J. Neurosci. 30, 4717–4724 (2010).
25. H. Abe, M. Okazawa, S. Nakanishi, Proc. Natl. Acad. Sci. U.S.A. 108, 12497–12502 (2011).
26. P. Li, M. M. Huntsman, Neuroscience 265, 60–71 (2014).
27. E. Campanac et al., Neuron 77, 712–722 (2013).
28. L. Cancedda, H. Fiumelli, K. Chen, M. M. Poo, J. Neurosci. 27, 5224–5235 (2007).
29. M. Xue, B. V. Atallah, M. Scanziani, Nature 511, 596–600 (2014).
30. N. Flames, O. Hobert, Nature 458, 885–889 (2009).
31. H. Abe, M. Okazawa, S. Nakanishi, Proc. Natl. Acad. Sci. U.S.A. 109, 8734–8739 (2012).
32. K.-X. Li et al., Nat. Neurosci. 15, 267–273 (2012).
33. P. Fazzari et al., Nature 464, 1376–1380 (2010).
34. L. N. Borodinsky et al., Nature 429, 523–530 (2004).
35. I. Spiegel et al., Cell 157, 1216–1229 (2014).

SUPPLEMENTARY MATERIALS

www.sciencemag.org/content/349/6253/1216/suppl/DC1
Materials and Methods
Figs. S1 to S13
References (36–42)

15 April 2015; accepted 6 August 2015
10.1126/science.aab3415

GLOBAL CARBON CYCLE

The reinvigoration of the Southern Ocean carbon sink

Peter Landschützer,[1]* Nicolas Gruber,[1,2] F. Alexander Haumann,[1,2]
Christian Rödenbeck,[3] Dorothee C. E. Bakker,[4] Steven van Heuven,[5]† Mario Hoppema,[5]
Nicolas Metzl,[6] Colm Sweeney,[7,8] Taro Takahashi,[9]
Bronte Tilbrook,[10] Rik Wanninkhof[11]

Several studies have suggested that the carbon sink in the Southern Ocean—the ocean's strongest region for the uptake of anthropogenic CO_2—has weakened in recent decades. We demonstrated, on the basis of multidecadal analyses of surface ocean CO_2 observations, that this weakening trend stopped around 2002, and by 2012 the Southern Ocean had regained its expected strength based on the growth of atmospheric CO_2. All three Southern Ocean sectors have contributed to this reinvigoration of the carbon sink, yet differences in the processes between sectors exist, related to a tendency toward a zonally more asymmetric atmospheric circulation. The large decadal variations in the Southern Ocean carbon sink suggest a rather dynamic ocean carbon cycle that varies more in time than previously recognized.

Simulations with ocean biogeochemical models have suggested a stagnation or even a reduction of the Southern Ocean carbon sink from the 1980s to the early 2000s (1–3), a result that has been supported by inversion studies (1) based on atmospheric CO_2 data. Such a stagnation has wide-reaching implications for climate, because the Southern Ocean south of 35°S accounts for about 40% of the global oceanic uptake of anthropogenic CO_2 (4–6), thereby removing a disproportionally large share of anthropogenic CO_2 from the atmosphere. The trend toward a saturation of the Southern Ocean carbon sink has been attributed mainly to the intensification and poleward shift of the westerly winds associated with a trend toward a more positive state of the Southern Annular Mode (1, 2). The resulting enhanced upwelling of deep waters with high concentrations of dissolved inorganic carbon (DIC) drove an anomalously strong flux of natural CO_2 out of the surface ocean, counteracting the increase in the oceanic uptake of anthropogenic CO_2 (2).

Several studies based on observations of the surface partial pressure of CO_2 (pCO_2) (7–9) corroborated these model-based trends in the Southern Ocean carbon sink, but all of them used the observations without any interpolation. Given the sparsity and spatial heterogeneity of these surface ocean observations (8), the conclusions drawn in these studies regarding the trends turn out to be rather sensitive to the chosen method of trend calculation (9) and the beginning and end year of analysis (10). Nevertheless, these studies tended to support a weakening sink trend up to the mid-2000s. One of these studies (9) also pointed out that the trend may have reversed in recent years, a finding corroborated by the analysis of pCO_2 observations along a single meridional transect south of Tasmania (11).

To address the sparse data coverage, we used a neural network technique (12) to interpolate the pCO_2 observations in time and space. We then evaluated the results using (i) a complementary pCO_2 observation–based product based on the interpolation by a data-driven mixed-layer scheme (13) and (ii) an atmospheric CO_2 inverse estimate (14). Both surface ocean–based methods were extended for this study to produce multidecadal distributions of the surface ocean pCO_2 field (15–17). The air-sea CO_2 flux variations were then computed with the use of a standard bulk parameterization (supplementary text 1.4). Although each of these estimates faces limits due to the available information, their combination allows us to gain confidence in the inferred features.

The two surface ocean data–based air-sea CO_2 flux products confirm that the Southern Ocean carbon sink (south of 35°S) weakened through much of the 1990s, in agreement with the model-based studies and the atmospheric inversions (1, 2), but they reveal that it has strengthened substantially since about 2002, increasing by more than ~0.6 Pg of C year^{-1} (Fig. 1) to a vigorous uptake of ~1.2 Pg of C year^{-1} in 2011. This increase has returned the Southern Ocean sink to levels expected from the increase in atmospheric CO_2 (5), computed from an ocean biogeochemistry model forced with just the increase in atmospheric CO_2 (18). The increase in the Southern Ocean carbon uptake since 2002 is responsible for roughly half of the global trend in the ocean carbon sink over this period (15), highlighting the importance of the Southern Ocean in moderating the growth of atmospheric CO_2.

Both surface ocean observation–based methods rely on the to-date largest sea surface pCO_2 observation database [Surface Ocean CO_2 Atlas (SOCAT) version 2] (19), which contains more than 2.6 million observations in the Southern Ocean south of 35°S. The neural network technique (12, 15) interpolates these observations

[1]Environmental Physics, Institute of Biogeochemistry and Pollutant Dynamics, ETH Zürich, Zürich, Switzerland. [2]Center for Climate Systems Modeling, C2SM, ETH Zürich, Zürich, Switzerland. [3]Max Planck Institute for Biogeochemistry, Jena, Germany. [4]Centre for Ocean and Atmospheric Sciences, School of Environmental Sciences, University of East Anglia, Norwich, UK. [5]Alfred Wegener Institute Helmholtz Centre for Polar and Marine Research, Bremerhaven, Germany. [6]Sorbonne Universités (UPMC, Univ Paris 06)-CNRS-IRD-MNHN, LOCEAN/IPSL Laboratory, 4 place Jussieu, F-75005 Paris, France. [7]Cooperative Institute for Research in Environmental Science, University of Colorado, Boulder, CO 80309, USA. [8]National Oceanic and Atmospheric Administration (NOAA) Earth System Research Laboratory, Boulder, CO, USA. [9]Lamont-Doherty Earth Observatory of Columbia University, Palisades, NY, USA. [10]Commonwealth Scientific and Industrial Research Organisation and Antarctic Climate and Ecosystems Co-operative Research Centre, Hobart, Australia. [11]Atlantic Oceanographic and Meteorological Laboratory of NOAA, Miami, FL, USA.
*Corresponding author. E-mail: peter.landschutzer@usys.ethz.ch †Present address: Department of Marine Geology and Chemical Oceanography, Royal Netherlands Institute for Sea Research (NIOZ), Texel, Netherlands.

Fig. 1. Evolution of the Southern Ocean carbon sink anomaly south of 35°S. The lines show the integrated air-sea CO_2 flux derived from two complementary surface ocean pCO_2 interpolation methods [a two-step neural network technique (15) and a mixed-layer scheme (17)] as well as the integrated flux from an atmospheric inversion based on measurements of atmospheric CO_2 (14). These estimates are compared with the expected uptake based on the growth of atmospheric CO_2 alone, based on a simulation with the ocean component of the Community Climate System Model (CCSM3) (18). All data are plotted as anomalies by subtracting the 1980s mean flux from each method. Negative values indicate anomalous uptake by the ocean.

to a 1° × 1° global grid at a monthly resolution for the period from 1982 through 2011, resulting in a multidecadal reconstruction of the global ocean carbon sink. The method relies on nonlinear but robust relations between the limited pCO$_2$ observations and the properties that are measured more frequently, such as sea surface temperature, sea surface salinity, satellite measurements of chlorophyll a, and mixed-layer depth (supplementary text 1.2). The mixed-layer scheme (13, 17) (version oc_v1.2), in contrast, does not regress pCO$_2$ variations to physical, chemical, or biological driver data but directly assimilates the available pCO$_2$ observations into a mass budget of the mixed layer at a resolution of 4° × 5° in space and daily in time. This method also uses several ancillary observations to parameterize the air-sea CO$_2$ exchange, solubility, and carbon chemistry but does not use them to interpolate the pCO$_2$ to regions without observations. Instead, it interpolates the pCO$_2$ data directly.

Extensive validation of the neural network–based estimate using independent observations reveals that the method is able to map the sparse pCO$_2$ data with little bias (with mean differences between SOCAT observations and neural network estimates of generally less than 2 μatm; table S1) in space and time. Both methods agree well regarding the sign and the magnitude of the decadal trends within the two decades from 1992 through 2001 and 2002 through 2011 (Fig. 1 and table S2), when the majority of surface ocean pCO$_2$ observations were made (fig. S3).

However, given the methodological differences in the data treatment in data-sparse regions (interpolation versus regression), there is less agreement regarding higher-frequency variability such as the year-to-year variations in the sink strength. This lower agreement is a result of the weaker signal-to-noise ratio of the pCO$_2$ data in the interannual frequency band. Under such conditions, the direct interpolation scheme of the mixed-layer method tends to extrapolate high-frequency noise present in the observations to the data-sparse regions, probably generating overly strong variations there. In contrast, the neural network scheme suppresses the high-frequency noise by being constrained by the ancillary observations, resulting in a possible underestimation of the year-to-year variability in the data-sparse regions. In contrast, the relatively strong pCO$_2$ signals that underlie the decadal changes in the Southern Ocean are distinctly captured by the two methods, resulting in very similar decadal trends.

The changes in the Southern Ocean carbon sink are almost entirely driven by changes in the air-sea difference of pCO$_2$; i.e., ΔpCO$_2$ = pCO$_2^{sea}$ − pCO$_2^{atm}$ (pCO$_2^{atm}$ = atmospheric pCO$_2$), because the direct effect of changes in the wind and temperature on the gas transfer coefficient is small (fig. S8). The spatial pattern of the trends in ΔpCO$_2$ from the neural network method reveals for both decades a very uniform trend pattern across the entire Southern Ocean, with the strongest ΔpCO$_2$ trends at high latitudes (Fig. 2, A and B). The spatial trends for the mixed-layer scheme are similar, although at coarser resolu-

tion and with somewhat more zonal variations, part of which may be spurious because of missing data constraints there, reflecting the more variance-producing nature of this method in data-sparse regions (fig. S6). From 1992 through 2001, the trend in ΔpCO$_2$ was strongly positive, driven by the surface ocean pCO$_2$ increasing at nearly twice the rate of pCO$_2^{atm}$ around Antarctica. In contrast, from 2002 onward, the growth of surface ocean pCO$_2$ nearly stalled, strongly increasing the degree of surface ocean undersaturation, which ultimately drove the increasing uptake of atmospheric CO$_2$.

We tested the robustness of this result on the basis that such strong decadal changes in the CO$_2$

uptake across most of the Southern Ocean should leave an imprint on atmospheric CO$_2$, taking advantage of the lack of land regions with substantial CO$_2$ fluxes south of 35°S. Specifically, we used an atmospheric inversion method (14) to infer the air-sea CO$_2$ fluxes that are optimally consistent with the atmospheric CO$_2$ data, while taking into consideration atmospheric transport and mixing. The setup of the employed version s85_v3.7 uses the atmospheric winds from the ERA-Interim reanalysis (20). The evolution of the Southern Ocean carbon sink from this inversion of atmospheric CO$_2$ data also supports our postulated larger–than-expected increase in the strength of the Southern Ocean carbon
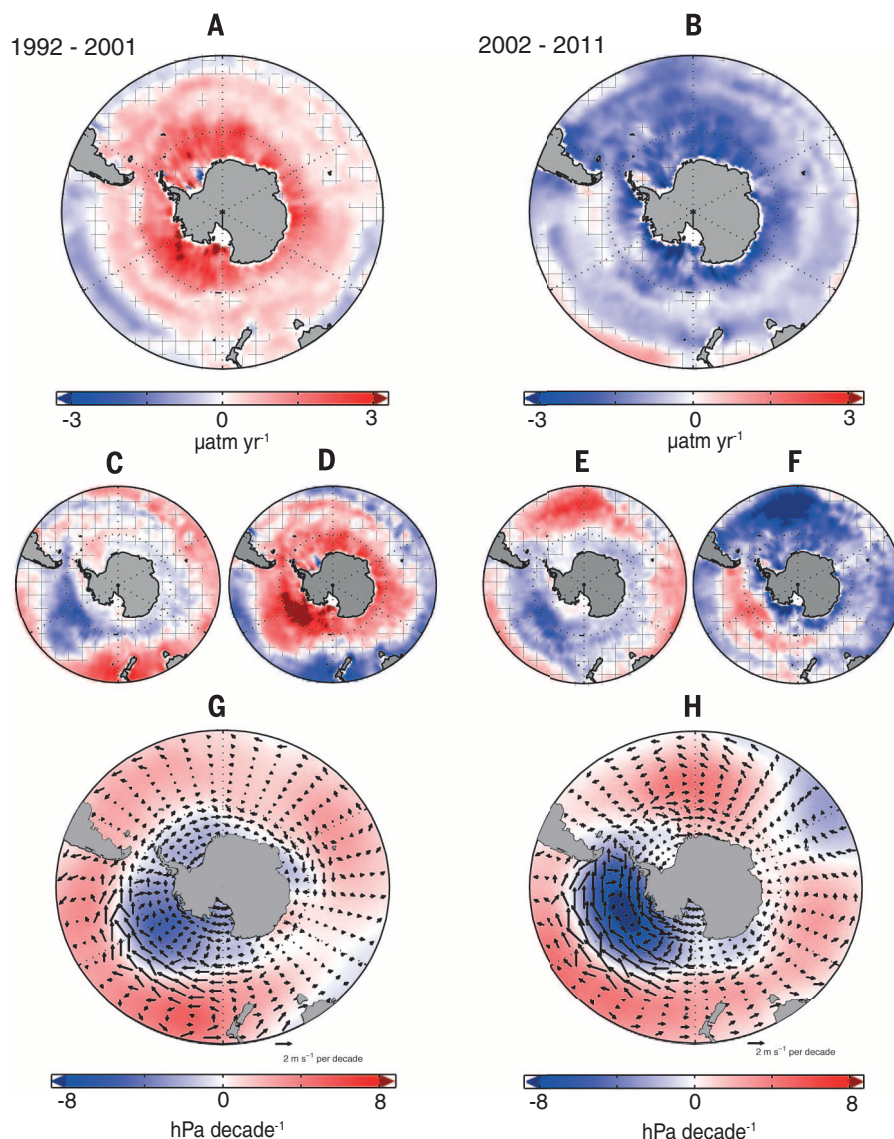
Fig. 2. Trends in ΔpCO$_2$ based on the neural network output and its two components for the two analysis decades: 1992 through 2001 and 2002 through 2011. (**A**) Linear trend in ΔpCO$_2$ for the 1990s. (**B**) As (A) but for the 2000s. Linear trend in (**C**) thermal pCO$_2$ and (**D**) nonthermal ΔpCO$_2$ for the 1990s. (**E**) and (**F**), as (C) and (D) but for the 2000s. Positive (red) ΔpCO$_2$ trends indicate a faster increase of pCO$_2$ in the surface ocean than in the atmosphere (i.e., a decreasing sink) and vice versa for positive (blue) trends. Hatched areas indicate where the linear trends are outside the 5% significance level ($P \geq$ 0.05). (**G**) and (**H**) illustrate decadal trends of sea level pressure (shading) and 10-m wind (vectors) from 1992 through 2001 (G) and 2002 through 2011 (H) based on data from the ERA-Interim reanalysis (20).

sink within the past decade (Fig. 1), even though it shows much less of a weakening during the 1990s. Thus, two complementary pCO_2 database estimates, as well as an atmospheric CO_2 inversion, confirm that the Southern Ocean carbon sink has experienced a significant strengthening since the early 2000s.

This reinvigoration after the early 2000s cannot be a simple reversal of the Southern Annular Mode–driven wind trend that has been suggested to cause the weakening of the Southern Ocean carbon sink over the past decades (1, 2), because the ERA-Interim reanalysis winds (20) do not show such a signal (Fig. 2, G and H). Instead, the atmospheric circulation became more zonally asymmetric with a wavenumber two pattern, reminiscent of the lower-frequency pattern of variability of the Antarctic Circumpolar Wave (21). But how can this zonally asymmetric forcing result in a relatively zonally uniform response of the surface ocean pCO_2?

Insight into the drivers is gained by separating the ΔpCO_2 trend pattern into a component driven by changes in sea surface temperature [the thermal trend (Fig. 2, C and E)] and one driven by changes in the DIC and/or alkalinity [the nonthermal trend (Fig. 2, D and F)] (22). For both analysis periods, the trends in the thermal and nonthermal components are generally opposed for any given location, which is in line with previous studies (22–24). The thermal component shows a sink increase in both decades in the Pacific sector, where the advection of cold air from Antarctica and sea-ice changes led to a persistent surface cooling trend (25). In the lower latitudes of the

Atlantic and Indian sectors, we find a reduced thermally driven uptake in the 2000s due to surface ocean warming, which is probably related to the more asymmetric atmospheric circulation that caused a reduced northward Ekman transport (fig. S11) of cold polar waters in these regions.

In the nonthermal component, we find more distinct differences between the two periods. Between 1992 and 2001, the nonthermal component increased the oceanic pCO_2 over most of the Southern Ocean (Fig. 2D), in particular in the high latitudes and in the Pacific sector. The estimated changes in Ekman pumping velocity [estimated from ERA-Interim winds (20), fig. S11] support the hypothesis that wind changes led to an increased surface divergence and an associated upwelling of DIC-rich waters into all sectors of the high-latitude Southern Ocean (2) in the first period. During the subsequent period, the nonthermal component primarily reduced the oceanic pCO_2 in the Atlantic and Indian sectors and over the Antarctic shelf (Fig. 2F). In contrast, this component continued to increase pCO_2 in most of the Pacific sector, although at a much weaker rate than in the 1990s. This much weaker DIC- and/or alkalinity-induced increase in pCO_2 in the Pacific sector could no longer compensate for the thermal trend, so that the negative trend in the total pCO_2 in this region for the period after 2001 is dominated by the thermal trend. In contrast, in the Atlantic and Indian sectors and over the Antarctic shelf, the negative nonthermal trend dominates the thermal changes. Thus, overall, the temperature-dominated pCO_2 trend in the Pacific sector and the DIC/alkalinity–driven trend in the

other regions have worked in tandem to prevent pCO_2 from increasing across the entire Southern Ocean since the early 2000s. Over the same period, atmospheric CO_2 continued to rise strongly, resulting in a substantial increase in the undersaturation of the surface ocean with regard to atmospheric CO_2, hence driving a strong increase in the flux of CO_2 into the entire Southern Ocean.

We interpret this zonal asymmetry of thermally and DIC/alkalinity–driven changes to be primarily the result of an increased asymmetry in the Southern Hemisphere atmospheric circulation in the years since 2001 (Fig. 3). Specifically, the conditions became more cyclonically dominant in the Pacific sector, and more anti-cyclonically dominant in the Atlantic and parts of the Indian sector (Fig. 2H). As a result of the associated increase in the meridional wind components, more cold air was advected from the Antarctic continent over the Pacific sector, and more warm air was advected from subtropical latitudes over the Atlantic and part of the Indian sectors. Together with the changes in northward Ekman transport (fig. S11), this provides an explanation for the strengthened asymmetry in the sea surface temperature trends, which underlie the thermal trends in Fig. 2E.

A strengthening of the carbon sink in the Pacific sector, combined with the further intensification of the winds (Fig. 2H) during the 2000s, provide a paradox at first sight, because the increased upwelling in the Pacific sector should have increased the surface DIC content further. A possible explanation is that the recent stabilization of the surface waters (26) counteracted
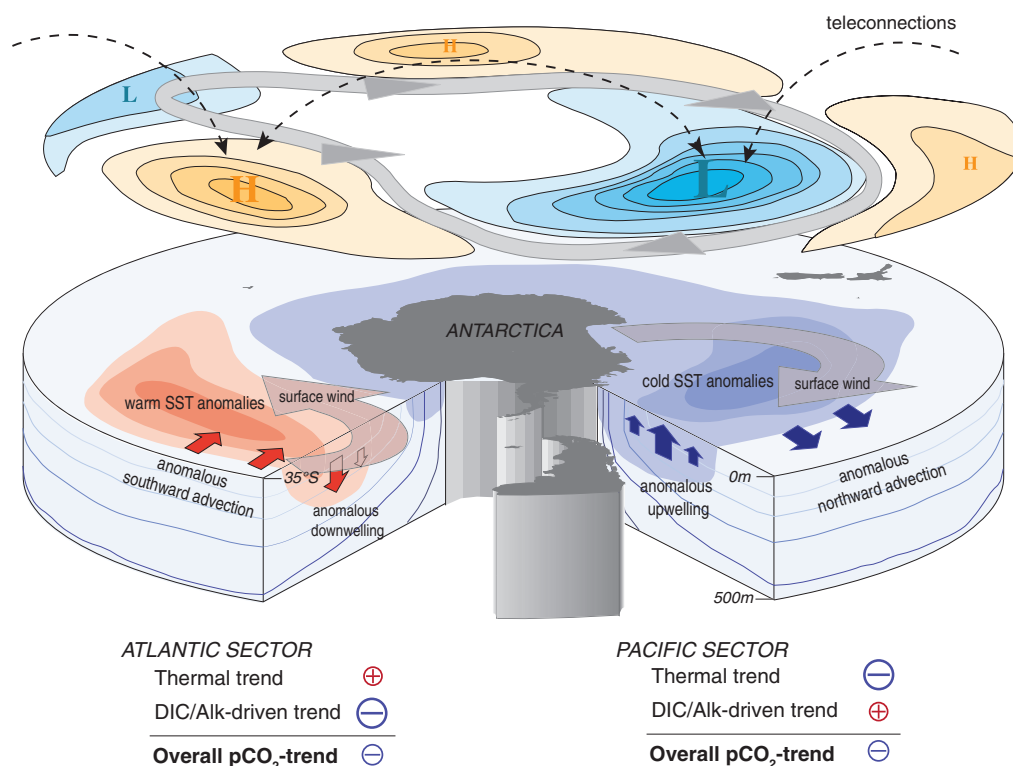
Fig. 3. Schematic of the processes governing the changes in the ΔpCO_2 trends in the Southern Ocean since 2001. The trend toward a zonally more asymmetric distribution of the atmospheric pressure systems in the past decade led to stronger meridional winds bringing either colder air (Pacific sector) or warmer air (Atlantic sector) to the open Southern Ocean, causing strong cooling of the sea surface in the Pacific sector and warming in the Atlantic sector. The changes in wind also affected the oceanic circulation pattern, with the net effect being an increase in the DIC/alkalinity–driven pCO_2 component in the Pacific sector and a decrease of this component in the Atlantic sector (i.e., opposing the effect of sea surface temperature on pCO_2). In the Pacific sector, the effect of the cooling trend on pCO_2 prevails, whereas in the Atlantic sector, the effect of circulation/mixing on DIC/alkalinity prevails, also causing a lowering trend in pCO_2. Thus, owing to the interaction between temperature and circulation changes, the zonally asymmetric forcing caused a zonally relatively symmetric response of the ocean carbon sink.

teleconnections

ANTARCTICA

warm SST anomalies   surface wind

cold SST anomalies   surface wind

anomalous southward advection

anomalous downwelling

anomalous upwelling

anomalous northward advection

35°S

0m

500m

ATLANTIC SECTOR
Thermal trend $\oplus$
DIC/Alk-driven trend $\ominus$
Overall pCO₂-trend $\ominus$

PACIFIC SECTOR
Thermal trend $\ominus$
DIC/Alk-driven trend $\oplus$
Overall pCO₂-trend $\ominus$

the wind-induced upwelling. In the Pacific sector and in coastal regions, strong surface freshening (26, 27) might have caused most of this stabilization, whereas in the lower latitudes of the Atlantic and Indian sectors, warming stabilized the surface waters. The reduction in northward Ekman transport to the lower-latitude Atlantic and Indian sectors during the 2000s (fig. S11), which is probably the result of the zonally more asymmetric atmospheric circulation, also reduced the northward advection of high-latitude waters, lowering the DIC content and/or increasing the alkalinity at the surface.

The trend toward a zonally more asymmetric atmospheric circulation may be related to longterm variations of the tropical sea surface temperature; i.e., to the more prevalent La Niña conditions in the Pacific since the early 2000s (28) and the more positive phase of the Atlantic Multidecadal Oscillation over recent decades (29). Alternatively, it may be driven by a zonally asymmetric response of the Southern Hemisphere near-surface circulation to the anthropogenic forcing (25).

Our results indicate that Earth's most important sink for anthropogenic CO_2 (5, 6) is more variable than previously suggested and that it responds quite sensitively to physical climate variability. This also suggests that should current climate trends reverse in the near future, the Southern Ocean might lose its recently regained uptake strength, leading to a faster accumulation of CO_2 in the atmosphere and consequently an acceleration of the rate of global warming.

REFERENCES AND NOTES

1. C. Le Quéré et al., Science 316, 1735–1738 (2007).
2. N. S. Lovenduski, N. Gruber, Global Biochem. Cyc. 22, GB3016 (2008).
3. A. Lenton et al., Biogeosciences 10, 4037–4054 (2013).
4. C. L. Sabine et al., Science 305, 367–371 (2004).
5. S. E. Mikaloff Fletcher et al., Global Biogeochem. Cycles 20, GB2002 (2006).
6. T. L. Frölicher et al., J. Clim. 28, 862–886 (2015).
7. N. Metzl, Deep Sea Res. Part II Top. Stud. Oceanogr. 56, 607–619 (2009).
8. T. Takahashi et al., Oceanography 25, 26–37 (2012).
9. A. R. Fay, G. A. McKinley, N. S. Lovenduski, Geophys. Res. Lett. 41, 6833–6840 (2014).
10. N. S. Lovenduski, A. R. Fay, G. A. McKinley, Global Biogeochem. Cyc. 29, 416–426 (2015).
11. L. Xue, L. Gao, W.-J. Cai, W. Yu, M. Wei, Geophys. Res. Lett. 42, 3973–3979 (2015).
12. P. Landschützer et al., Biogeosciences 10, 7793–7815 (2013).
13. C. Rödenbeck et al., Ocean Science 9, 193 (2013).
14. C. Rödenbeck, S. Houweling, M. Gloor, M. Heimann, Atmos. Chem. Phys. 3, 1919–1964 (2003).
15. P. Landschützer, N. Gruber, D. C. E. Bakker, U. Schuster, Global Biogeochem. Cyc. 28, 927–949 (2014).
16. P. Landschützer, N. Gruber, D. C. E. Bakker, A 30 Years Observation-Based Global Monthly Gridded Sea Surface pCO2 Product from 1982 Through 2011 (Carbon Dioxide Information Analysis Center, Oak Ridge National Laboratory, U.S. Department of Energy, Oak Ridge, TN, 2015).
17. C. Rödenbeck et al., Biogeosciences 11, 4599–4613 (2014).
18. H. D. Graven, N. Gruber, R. Key, S. Khatiwala, X. Giraud, J. Geophys. Res. 117, C10005 (2012).
19. D. C. E. Bakker et al., Earth System Sci. Data 6, 69–90 (2014).
20. D. P. Dee et al., Q. J. R. Meteorol. Soc. 137, 553–597 (2011).
21. A. F. Carril, A. Navarra, Geophys. Res. Lett. 28, 4623–4626 (2001).
22. T. Takahashi et al., Deep Sea Res. Part II Top. Stud. Oceanogr. 49, 1601–1622 (2002).
23. N. Gruber et al., Global Biogeochem. Cycles 23, GB1005 (2009).
24. J. D. Majkut, J. L. Sarmiento, K. B. Rodgers, Global Biogeochem. Cycles 28, 335–351 (2014).
25. F. A. Haumann, D. Notz, H. Schmidt, Geophys. Res. Lett. 41, 8429–8437 (2014).
26. C. De Lavergne, J. B. Palter, E. D. Galbraith, R. Bernardello, I. Marinov, Nat. Clim. Change 4, 278–282 (2014).
27. S. S. Jacobs, C. F. Giulivi, J. Clim. 23, 4508–4524 (2010).
28. Q. Ding, E. J. Steig, D. S. Battisti, M. Küttel, Nat. Geosci. 4, 398–403 (2011).
29. X. Li, D. M. Holland, E. P. Gerber, C. Yoo, Nature 505, 538–542 (2014).

PLANT SCIENCE

Six enzymes from mayapple that complete the biosynthetic pathway to the etoposide aglycone

Warren Lau and Elizabeth S. Sattely*

Podophyllotoxin is the natural product precursor of the chemotherapeutic etoposide, yet only part of its biosynthetic pathway is known. We used transcriptome mining in *Podophyllum hexandrum* (mayapple) to identify biosynthetic genes in the podophyllotoxin pathway. We selected 29 candidate genes to combinatorially express in *Nicotiana benthamiana* (tobacco) and identified six pathway enzymes, including an oxoglutarate-dependent dioxygenase that closes the core cyclohexane ring of the aryltetralin scaffold. By coexpressing 10 genes in tobacco—these 6 plus 4 previously discovered—we reconstitute the pathway to (−)-4′-desmethylepipodophyllotoxin (the etoposide aglycone), a naturally occurring lignan that is the immediate precursor of etoposide and, unlike podophyllotoxin, a potent topoisomerase inhibitor. Our results enable production of the etoposide aglycone in tobacco and circumvent the need for cultivation of mayapple and semisynthetic epimerization and demethylation of podophyllotoxin.

Although numerous clinically used drugs derive from plant natural products, little is known about their biosynthetic genes, which prevents access to engineered hosts for their production (1). Very few complete pathways exist, and only three—artemisinic acid (2), the benzylisoquinoline alkaloids (3, 4), and the monoterpenoid indole alkaloids (5, 6)—have been transferred to a heterologous host for current or future industrial production. Knowledge of plant pathways is especially stark in comparison with the >700 bacterial and fungal biosynthetic pathways that have been characterized (7).

Podophyllotoxin, a lignan from mayapple, is the natural product precursor to the topoisomerase inhibitor etoposide (8–10), which is used in dozens of chemotherapy regimens for a variety of malignancies. Although etoposide is on the World Health

Department of Chemical Engineering, Stanford University, Stanford, CA 94305, USA.
*Corresponding author. E-mail: sattely@stanford.edu

Organization's list of essential medicines, production requires isolation of (–)-podophyllotoxin from the medicinal plant *Podophyllum* (*11*). Subsequent semisynthetic steps to produce etoposide are required for topoisomerase inhibitory activity not present in podophyllotoxin. A complete biosynthetic route would enable more facile access to etoposide and natural and unnatural derivatives that are difficult to produce synthetically (*12*). Early steps of podophyllotoxin biosynthesis (*13–16*) involve the unusual enantio- and site-selective dimerization of coniferyl alcohol to form (+)-pinoresinol and provide a starting point for identifying additional biosynthetic genes (Fig. 1). However, biosynthetic gene discovery in *Podophyllum* is a challenge, because the plant grows slowly, the genome is large [~16 Gb (*17*)] and unsequenced, and methods for constructing mutants are laborious (*18*).

We used *Agrobacterium*-mediated transient expression in *N. benthamiana* to test candidate genes for the podophyllotoxin pathway for two reasons. First, this versatile plant host would likely produce correctly folded, active proteins from a variety of enzyme superfamilies without optimization. Second, we wanted to rapidly and combinatorially express candidate enzymes without knowing the order of steps or identities of metabolic intermediates and without additional cloning. Combinatorial expression can be accomplished by coinfiltrating multiple *Agrobacterium* strains—each harboring a different expression construct—and analyzing the resulting plant tissue extracts by using untargeted metabolomics to identify products.

In our initial approach to produce the pathway intermediate (–)-pluviatolide in *N. benthamiana* leaves, we coexpressed three of the four known podophyllotoxin biosynthetic enzymes: pinoresinol-lariciresinol reductase (PLR), secoisolariciresinol dehydrogenase (SDH), and CYP719A23 [dirigent protein (DIR) was not required]. Although we observed low levels of (–)-pluviatolide in the re-

sulting leaf extracts, the amount was insufficient for detecting downstream intermediates produced when coexpressing candidate enzymes (fig. S1). No pluviatolide was detected in control experiments when only green fluorescent protein (GFP) is expressed. To enhance (–)-pluviatolide production *in planta*, we infiltrated leaves expressing CYP719A23 with (–)-matairesinol (isolated from *Forsythia × intermedia*) 5 days after *Agrobacterium* infiltration. After 1 day, (–)-pluviatolide concentrations were ~75 times those in leaves expressing PLR, SDH, and CYP719A23, without substrate infiltration (fig. S2), which provided sufficient (–)-pluviatolide to enable candidate enzyme screening.

To select candidate enzymes for conversion of (–)-pluviatolide to the next pathway intermediate, we mined the publicly available *P. hexandrum* RNA-sequencing (RNA-Seq) data set from the Medicinal Plants Consortium. We noted that all known podophyllotoxin genes were highly expressed in rhizome, stem, and leaf tissues, and we selected candidate genes with similar expression profiles (fig. S3). As the order of steps in the pathway was not known, we chose four putative *O*-methyltransferases (*OMT1–4*), 12 cytochromes P450 (*CYP*), and a 2-oxoglutarate/Fe(II)-dependent dioxygenase (*2-ODD*). We infiltrated (–)-matairesinol into leaves each coexpressing CYP719A23 and a single candidate enzyme. Liquid chromatography–mass spectrometry (LC-MS) analysis revealed the consumption of (–)-pluviatolide in tobacco leaves coexpressing just one of the candidates, OMT3 (fig. S4). By computationally comparing untargeted metabolomics data from tissue extracts, we identified two compound mass signals unique to CYP719A23 + OMT3 samples relative to CYP719A23 alone: One corresponds to (–)-5′-desmethoxy-yatein (fig. S5); the other, with much lower ion abundance, likely derives from the double methylation of (–)-matairesinol (fig. S6). Expression of OMT3 alone, followed by infiltration of (–)-matairesinol, results in greater amounts of the doubly methylated product, which suggests that this enzyme

can accept multiple substrates. We recombinantly expressed OMT3 in *Escherichia coli* and measured its kinetic parameters for (–)-pluviatolide methylation [apparent Michaelis constant (K_m) = 1.4 µM and enzymatic rate (k_{cat}) = 0.72 s^{-1}] (fig. S7). OMT3 accepts (–)-matairesinol and (–)-arctigenin with much lower efficiency and cannot turn over (+)-pinoresinol; these data suggest that OMT3 catalyzes methylation of pluviatolide to generate (–)-5′-desmethoxy-yatein as the next step in the pathway.

We next coexpressed individual candidate CYP and 2-ODD enzymes with CYP719A23 and OMT3; however, we did not observe consumption of (–)-5′-desmethoxy-yatein in leaf extracts, which suggested that our set of candidate genes was incomplete. We reasoned that additional transcriptome data from *P. hexandrum* tissue samples with differential expression of pathway genes could aid candidate selection.

The expression of known (–)-podophyllotoxin biosynthetic genes is up-regulated in *P. hexandrum* leaves after wounding (*19*) (Fig. 2A and fig. S8). LC-MS analysis of metabolites in wounded leaves (removed from the stem to eliminate the possibility of metabolite transport) revealed that both (–)-yatein and (–)-deoxypodophyllotoxin [proposed precursors to (–)-podophyllotoxin (*20*, *21*)] accumulate and reach a maximum level 12 to 24 hours after wounding (fig. S9). Consistent with previous reports (*16*), we did not detect (–)-podophyllotoxin or its glucoside in leaf tissues.

We took advantage of the pathway's inducibility and performed RNA-Seq on triplicate *P. hexandrum* leaf samples, 0, 3, 9, and 12 hours after wounding, from a single plant with the strongest metabolite response. We assembled a leaf transcriptome, determined expression levels, and used predicted enzyme activities required for the missing pathway steps to mine the data for gene sequences encoding *OMTs*, *CYPs*, *2-ODDs*, and polyphenol oxidases (*PPOs*). A computational analysis based on expression profile similarity with
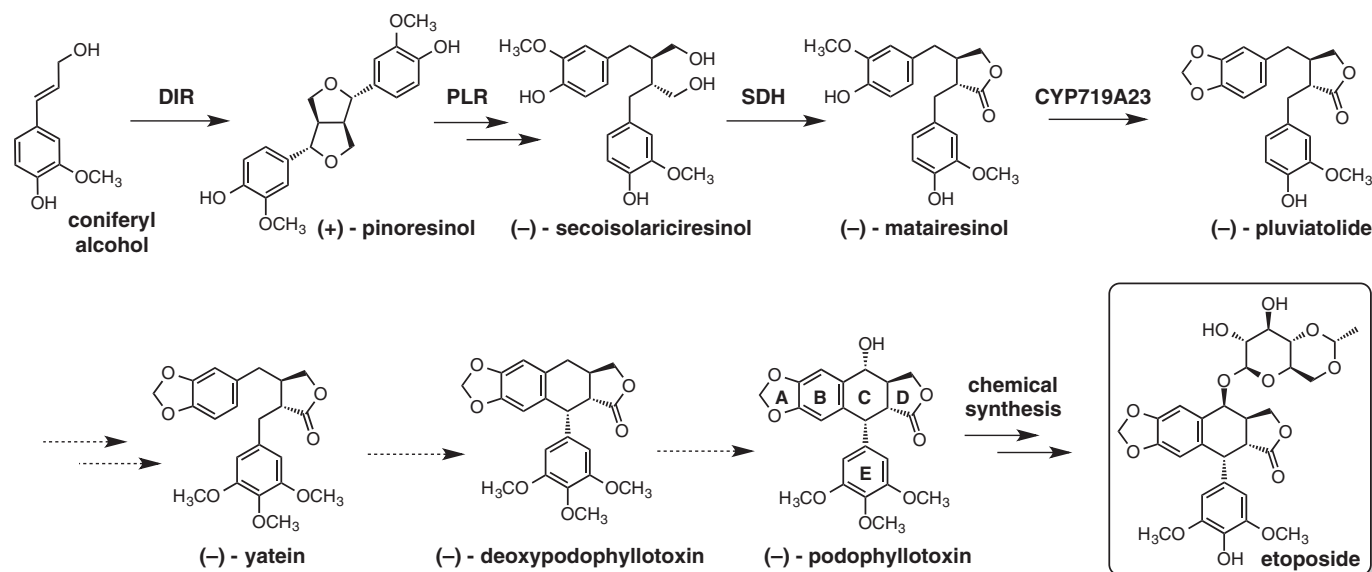
Fig. 1. Biosynthetic pathway of (–)-podophyllotoxin in *P. hexandrum*. Uncharacterized steps are indicated by dashed lines.
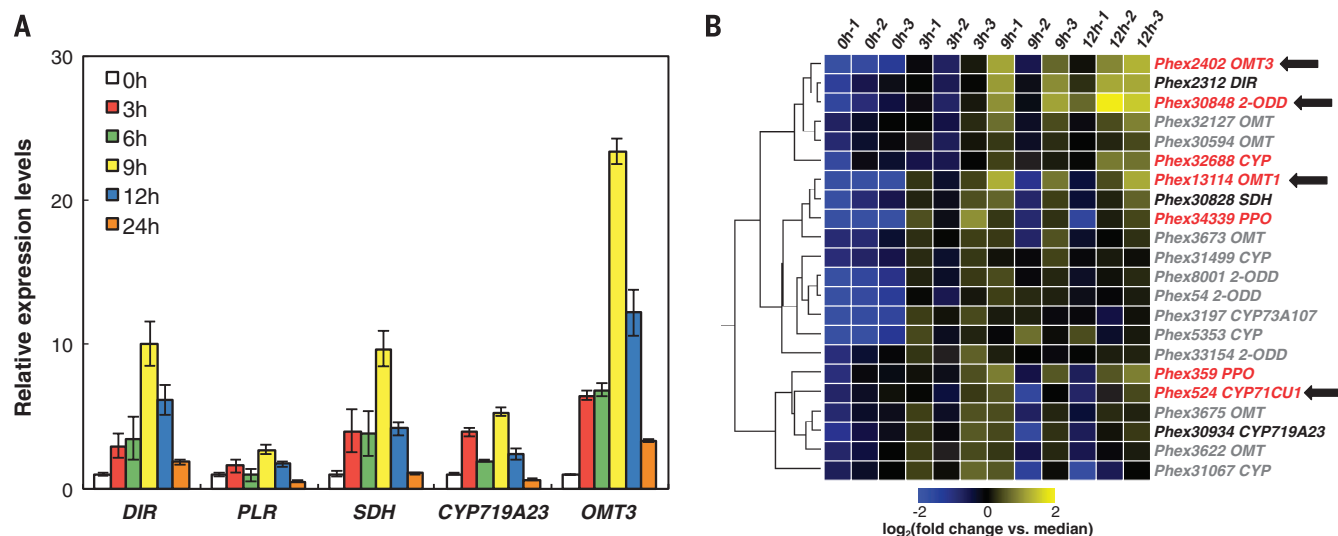
Fig. 2. Expression analysis to identify candidate genes. (**A**) qRT-PCR analysis of podophyllotoxin biosynthetic genes after *P. hexandrum* leaf wounding (at $t = 0$ hour). Relative expression levels were normalized to $t = 0$ hour. Data are average values (three technical replicates) ± one SD. (**B**) Hierarchical clustering of RNA-Seq expression data after filtering by enzyme family and expression level. Heat map depicts the expression levels from a single node from the resulting cluster. Color key: Known biosynthetic genes (black), candidate genes (red), genes identified in this report (red with black arrows).

known pathway genes *DIR* and *CYP719A23* and overall expression level yielded seven candidate pathway genes: *Phex30848* (*2-ODD*); *Phex32688* (*CYP*); *Phex13114* (*OMT1*, previously tested); *Phex359* (*PPO*); *Phex34339* (*PPO*); *Phex524* (*CYP71CU1*); and *Phex15199* (*CYP*) (fig. S10 to S12). Hierarchical clustering analysis of 336 expressed genes, selected by filtering all data (34,384 total genes; see table S1) by enzyme family, revealed a single clade of 91 genes; further filtering by expression level condensed this clade to 22 genes containing six of these seven candidates, three of four known pathway genes, and *OMT3* (Fig. 2B).

We individually coexpressed six of these seven candidate enzymes (the putative hydroxylases) with CYP719A23 and OMT3 in tobacco leaves to test for a (–)-5′-desmethoxy-yatein hydroxylase. We infiltrated leaves with (–)-matairesinol 4 days after infiltration and harvested a day later for LC-MS analysis. In samples coexpressing Phex524 (CYP71CU1), we observed turnover of (–)-5′-desmethoxy-yatein (Fig. 3). A comparison of the leaf metabolomes revealed two CYP71CU1-dependent compound mass signals that correspond to the calculated m/z of (–)-5′-desmethyl-yatein [assignment supported by tandem mass spectrometry (MS/MS)] (fig. S13). The earlier eluting mass signal is likely an in-source fragmentation ion originating from a glycosylated derivative of (–)-5′-desmethyl-yatein produced by endogenous tobacco enzymes. Thus, CYP71CU1 likely catalyzes the next pathway step as part of E-ring functionalization.

To complete the biosynthesis of (–)-yatein, a proposed intermediate in the podophyllotoxin pathway (*21*), we tested Phex13114 (OMT1) for the ability to methylate (–)-5′-desmethyl-yatein. We infiltrated (–)-matairesinol into tobacco leaves expressing OMT1 in combination with CYP719A23, OMT3, and CYP71CU1. (–)-5′-Desmethyl-yatein could not be detected in leaf extracts in which

OMT1 had been coexpressed (Fig. 3 and fig. S14); instead, we detected the accumulation of (–)-yatein. Thus, OMT1 likely converts (–)-5′-desmethylyatein to (–)-yatein as the seventh step in the pathway.

The remainder of the pathway involves closing the central six-membered ring in the aryltetralin scaffold and oxidative tailoring. In our initial screen (coexpression with CYP719A23 and OMT3), we observed substantial consumption of (–)-5′-desmethoxy-yatein in samples coexpressing Phex30848 (2-ODD). Computational comparison of leaf metabolomes revealed a new 2-ODD–dependent compound mass signal that corresponds to 5′-desmethoxy-deoxypodophyllotoxin bearing the required aryltetralin scaffold (assignment supported by MS/MS analysis) (fig. S14). We hypothesize that the reaction mechanism involves activation of the 7′ carbon by hydroxylation, followed by dehydration and carbon-carbon bond formation via a quinone methide intermediate (fig. S16).

Prior feeding studies (*21*) and our *P. hexandrum* wounding metabolomics data suggest that (–)-yatein is the native substrate for ring closure. Therefore, we tested whether 2-ODD could also catalyze the conversion of (–)-yatein to (–)-deoxypodophyllotoxin *in planta*. We expressed 2-ODD in tobacco leaves along with CYP719A23, OMT3, CYP71CU1, and OMT1. Four days after *Agrobacterium* infiltration, we infiltrated leaves with (–)-matairesinol and, a day later, harvested them for LC-MS analysis. We observed that (–)-yatein was consumed in a 2-ODD–dependent fashion, and a computational comparison of metabolite extracts confirmed the accumulation of (–)-deoxypodophyllotoxin in tobacco leaves coexpressing 2-ODD (Fig. 3 and fig. S17). Thus 2-ODD catalyzes oxidative ring closure to establish the core of the aryltetralin scaffold.

We sought to confirm the activities of these enzymes by biochemical analysis. We isolated

microsomes enriched with Phex524 (CYP71CU1) after expression in *Saccharomyces cerevisiae WAT11*, and purified Phex13114 (OMT1) and Phex30848 (2-ODD) with C-terminal hexahistidine tags after expression in *E. coli*. As expected, incubation of (–)-5′-desmethoxy-yatein with CYP71CU1 and the reduced form of nicotinamide adenine dinucleotide phosphate (NADPH) gave the hydroxylated product, (–)-5′-desmethyl-yatein; incubation with CYP71CU1 and OMT1, and with the cofactors, NADPH and *S*-adenosylmethionine, gave (–)-yatein (fig. S18). Incubation of 2-ODD with (–)-yatein as the substrate in the presence of 2-oxoglutarate and Fe^{2+} yielded (–)-deoxypodophyllotoxin. All enzymes showed little to no activity on similar substrates under identical assay conditions. These data confirm the enzyme activities and order of reactions for the pathway through (–)-deoxypodophyllotoxin (Fig. 3 and fig. S19).

To identify the enzyme involved in what we hypothesized to be the final step of (–)-podophyllotoxin biosynthesis, the hydroxylation of (–)-deoxypodophyllotoxin, we returned to the publicly available transcriptome data to identify *CYPs* predominantly and highly expressed in *P. hexandrum* rhizomes, the tissue in which (–)-podophyllotoxin is primarily produced. We identified six *CYP* candidates that matched our criterion (fig. S20). We screened the candidates in tobacco by individual coexpression with the five (–)-deoxypodophyllotoxin biosynthetic genes, starting from CYP719A23 and infiltration of (–)-matairesinol. By a comparative metabolomic analysis, we observed consumption of (–)-deoxypodophyllotoxin in leaves coexpressing the candidate enzyme, Ph14372 (CYP71BE54), but—contrary to our expectation—no (–)-podophyllotoxin was detected (Fig. 3). Instead, we observed CYP71BE54-dependent accumulation of two compound mass signals with predicted molecular formulas and MS/MS data that correlate to
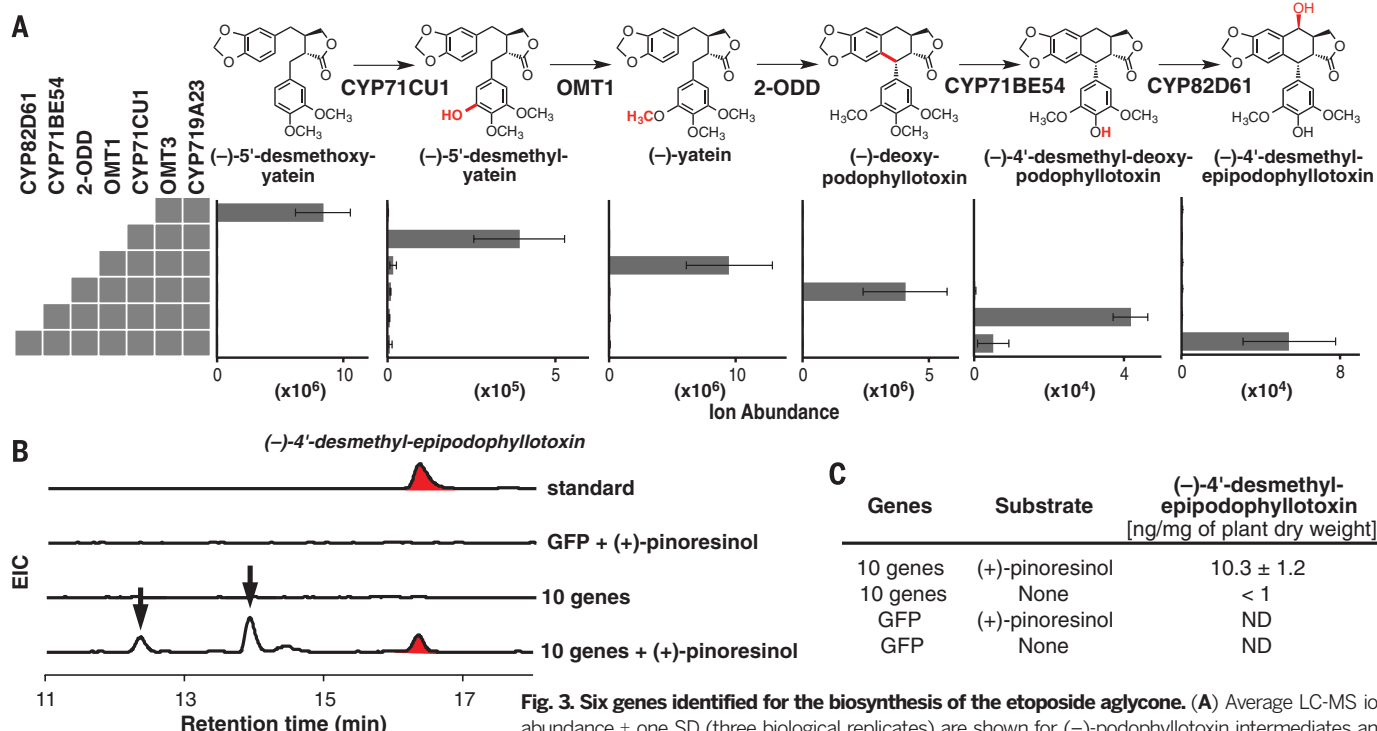
Fig. 3. Six genes identified for the biosynthesis of the etoposide aglycone. (**A**) Average LC-MS ion abundance ± one SD (three biological replicates) are shown for (−)-podophyllotoxin intermediates and derivatives produced in tobacco after expression of indicated enzymes and (−)-matairesinol infiltration. (**B**) Extracted ion chromatograms (EIC) for the etoposide aglycone, (−)-4′-desmethylepipodophyllotoxin (m/z = 401) in tobacco leaves expressing GFP or DIR, PLR, SDH, CYP719A23, and the six genes identified in this report with and without the infiltration of (+)-pinoresinol. Arrows indicate glycosylated derivatives of (−)-4′-desmethylepipodophyllotoxin. (**C**) Average amounts of (−)-4′-desmethylepipodophyllotoxin detected in tobacco ± one SD (three biological replicates).

compounds derived from the demethylation of (−)-deoxypodophyllotoxin, formally (−)-4′-desmethyl-deoxypodophyllotoxin (fig. S21). The earlier eluting mass signal is likely derived from a glycosylated derivative. The observed activity of CYP71BE54 implies that the demethylated lignans found in *P. hexandrum* (22–24) are a result of enzymatic demethylation rather than the failure of OMT3 to methylate a portion of the lignan flux. Consistent with this view, CYP71CU1-enriched microsomes cannot accept (−)-pluviatolide as a substrate, which indicates a need for fully methylated substrate earlier in the pathway. Despite poor expression in yeast, isolated CYP71BE54 microsomes accepted (−)-deoxypodophyllotoxin as a substrate but not other similar molecules (fig. S22).

Upon screening an additional candidate P450, *Ph35407* (*CYP82D61*), we also observed consumption of (−)-deoxypodophyllotoxin. However, we did not detect formation of (−)-podophyllotoxin; instead, we observed accumulation of its epimer, (−)-epipodophyllotoxin (fig. S23). To confirm the activity of CYP82D61 in the context of the late pathway enzymes, we infiltrated (−)-matairesinol into tobacco leaves expressing CYP71BE54, CYP82D61, and the five (−)-deoxypodophyllotoxin biosynthetic genes starting from CYP719A23. Comparative metabolomics demonstrated the accumulation of (−)-4′-desmethylepipodophyllotoxin, along with two other earlier eluting compound mass signals that are likely derived from glycosylated (−)-4′-desmethylepipodophyllotoxin derivatives (Fig. 3 and fig. S24). (−)-4′-Desmethylepipodophyllotoxin is the direct precursor to etoposide, which cur-

rently is made by chemical modification of podophyllotoxin. Potent topoisomerase activity of etoposide was discovered by serendipitous derivatization of trace amounts of (−)-4′-desmethyl-epipodophyllotoxin glucoside, present in *P. hexandrum* rhizome extracts (8).

Having discovered six enzymes that complete the pathway to (−)-4′-desmethylepipodophyllotoxin, we then sought to reconstitute the pathway in *N. benthamiana* from (+)-pinoresinol. We expressed DIR, PLR, SDH, CYP719A23, and the six enzymes that we identified in tobacco leaves and subsequently infiltrated 100 μM (+)-pinoresinol, yielding 10.3 ng of (−)-4′-desmethylepipodophyllotoxin per mg of plant dry weight. The total amount produced is likely even higher, as some of the product is derivatized by tobacco enzymes and could not be quantified. Less than 1 ng of product per mg of plant dry weight was obtained without infiltration of (+)-pinoresinol, which suggested that native production of this intermediate in tobacco is limiting (Fig. 3, B and C). We also produced (−)-deoxypodophyllotoxin and (−)-epipodophyllotoxin starting from (+)-pinoresinol in *N. benthamiana* by omitting CYP71BE54 and CYP82D61, and CYP71BE54, respectively (figs. S25 and S26); pathway intermediates do not accumulate in either case (fig. S27). The yield of (−)-deoxypodophyllotoxin in tobacco (~90 ng/mg dry weight) is more than one-third of the yield from wound-induced leaves of *Podophyllum*.

Thus, the etoposide aglycone, (−)-4′-desmethyl-epipodophyllotoxin, can be produced in *N. benthamiana*, which circumvents the current

need for mayapple cultivation and subsequent semisynthetic epimerization and demethylation (fig. S28). By coupling transcriptome mining with combinatorial expression of candidate enzymes in tobacco, we identified six biosynthetic enzymes, including a 2-ODD that catalyzes the novel C-C bond-forming step for stereoselective cyclization to close the aryltetralin scaffold and a late-stage P450 to unmask the E-ring phenol. A similar approach could be used to engineer synthetic pathways that produce podophyllotoxin derivatives with improved bioactive properties.

REFERENCES AND NOTES

1. V. De Luca, V. Salim, S. M. Atsumi, F. Yu, *Science* **336**, 1658–1661 (2012).
2. C. J. Paddon *et al.*, *Nature* **496**, 528–532 (2013).
3. K. Thodey, S. Galanie, C. D. Smolke, *Nat. Chem. Biol.* **10**, 837–844 (2014).
4. W. C. DeLoache *et al.*, *Nat. Chem. Biol.* **11**, 465–471 (2015).
5. S. Brown, M. Clastre, V. Courdavault, S. E. O'Connor, *Proc. Natl. Acad. Sci. U.S.A.* **112**, 3205–3210 (2015).
6. Y. Qu *et al.*, *Proc. Natl. Acad. Sci. U.S.A.* **112**, 6224–6229 (2015).
7. P. Cimermancic *et al.*, *Cell* **158**, 412–421 (2014).
8. H. F. Stähelin, A. von Wartburg, *Cancer Res.* **51**, 5–15 (1991).
9. C. Canel, R. M. Moraes, F. E. Dayan, D. Ferreira, *Phytochemistry* **54**, 115–120 (2000).
10. M. Gordaliza, P. A. García, J. M. Miguel del Corral, M. A. Castro, M. A. Gómez-Zurita, *Toxicon* **44**, 441–459 (2004).
11. H. Lata, C. S. Mizuno, R. M. Moraes, in *Protocols for in Vitro Cultures and Secondary Metabolite Analysis of Aromatic and Medicinal Plants* (Springer, 2009), pp. 387–402.
12. A. Kamal, S. M. Ali Hussaini, A. Rahim, S. Riyaz, Podophyllotoxin derivatives: A patent review (2012–2014). *Expert Opin. Ther. Patents* 10.1517/13543776.2015.1051727 (2015).
13. A. T. Dinkova-Kostova *et al.*, *J. Biol. Chem.* **271**, 29473–29482 (1996).
14. L. B. Davin *et al.*, *Science* **275**, 362–367 (1997).

15. Z.-Q. Xia, M. A. Costa, H. C. Pélissier, L. B. Davin, N. G. Lewis, *J. Biol. Chem.* **276**, 12614–12623 (2001).
16. J. V. Marques *et al.*, *J. Biol. Chem.* **288**, 466–479 (2013).
17. A. Nag, S. Chanda, R. Subramani, *J. Cell Plant Sci.* **2**, 19–23 (2011).
18. M. Rajesh *et al.*, *Plant Cell Tissue Organ Cult.* **114**, 71–82 (2013).
19. D. P. Wankhede, D. K. Biswas, S. Rajkumar, A. K. Sinha, *Protoplasma* **250**, 1239–1249 (2013).
20. W. M. Kamil, P. M. Dewick, *Phytochemistry* **25**, 2089–2092 (1986).
21. W. M. Kamil, P. M. Dewick, *Phytochemistry* **25**, 2093–2102 (1986).
22. A. J. Broomhead, M. M. A. Rahman, P. M. Dewick, D. E. Jackson, J. A. Lucas, *Phytochemistry* **30**, 1489–1492 (1991).
23. D. E. Jackson, P. M. Dewick, *Phytochemistry* **23**, 1147–1152 (1984).
24. D. E. Jackson, P. M. Dewick, *Phytochemistry* **23**, 1037–1042 (1984).

ANTIVIRAL IMMUNITY

Viruses transfer the antiviral second messenger cGAMP between cells

A. Bridgeman,[1] J. Maelfait,[1] T. Davenne,[1] T. Partridge,[2] Y. Peng,[1] A. Mayer,[1] T. Dong,[1] V. Kaever,[3] P. Borrow,[2] J. Rehwinkel[1]*

Cyclic GMP–AMP synthase (cGAS) detects cytosolic DNA during virus infection and induces an antiviral state. cGAS signals by synthesis of a second messenger, cyclic GMP-AMP (cGAMP), which activates stimulator of interferon genes (STING). We show that cGAMP is incorporated into viral particles, including lentivirus and herpesvirus virions, when these are produced in cGAS-expressing cells. Virions transferred cGAMP to newly infected cells and triggered a STING-dependent antiviral program. These effects were independent of exosomes and viral nucleic acids. Our results reveal a way by which a signal for innate immunity is transferred between cells, potentially accelerating and broadening antiviral responses. Moreover, infection of dendritic cells with cGAMP-loaded lentiviruses enhanced their activation. Loading viral vectors with cGAMP therefore holds promise for vaccine development.

Type I interferons (IFNs) play pivotal roles in the immune response to virus infection (*1*). IFN expression is induced by signaling pathways activated by sensors of virus presence, including cytosolic DNA sensors (*2*, *3*). Cyclic GMP–AMP synthase (cGAS) is a cytosolic DNA sensor that signals by catalyzing the synthesis of a second messenger, cyclic GMP-AMP (cGAMP) (*4*, *5*). cGAMP binds to and activates stimulator of interferon genes (STING) (*5*, *6*), which plays a central role in cytosolic DNA sensing by relaying signals from DNA sensors to transcription factors driving *IFN* gene transcription (*3*, *7*).

DNA viruses and retroviruses trigger cGAS-dependent IFN responses in infected cells (*8–15*). This is thought to involve sensing by cGAS of viral DNA, leading to *IFN* gene transcription in the same cell where DNA detection occurred or in neighboring cells connected by gap junctions

[1]Medical Research Council Human Immunology Unit, Medical Research Council Weatherall Institute of Molecular Medicine, Radcliffe Department of Medicine, University of Oxford, Oxford OX3 9DS, UK. [2]Nuffield Department of Medicine, University of Oxford, Oxford OX3 7FZ, UK. [3]Research Core Unit Metabolomics, Institute of Pharmacology, Hannover Medical School, Carl-Neuberg-Strasse 1, D-30625 Hannover, Germany.
*Corresponding author. E-mail: jan.rehwinkel@imm.ox.ac.uk

(*16*). However, it is conceivable that IFN induction upon virus infection could also occur independently of cGAS if the infecting virus were to incorporate and transfer the cGAMP second messenger. For example, human immunodeficiency virus 1 (HIV-1) particles incorporate host molecules such as APOBEC3G (*17*). Given this precedent, we hypothesized that cGAMP can be packaged into virions and elicits an IFN response in newly infected cells independently of cGAS expression by the latter, allowing for potentiation of innate antiviral immunity.

To test this idea, we produced HIV-1–based lentiviral vectors by plasmid transfection in 293T cells, a human cell line that does not express cGAS (*4*). Virus particles were pseudotyped with vesicular stomatitis virus glycoprotein (VSV-G), and viral genome contained enhanced green fluorescent protein (EGFP) in the *Env* open reading frame. These viruses, henceforth referred to as HIV-1-GFP, are replication incompetent due to the lack of functional *Env*. Some 293T cells were cotransfected with expression constructs for either wild-type mouse cGAS (m-cGAS) or catalytically inactive m-cGAS-G198A/S199A (m-cGAS-AA) (*4*). Titrated virus stocks were then used to infect fresh human embryonic kidney 293 (HEK293) cells, which express endogenous

STING (*7*, *18*) and induce IFN in response to cGAMP (fig. S1, A to D). HIV-1-GFP collected from cGAS-expressing cells triggered induction of an *IFN*β promoter reporter, whereas viruses produced in the absence of exogenous cGAS or in the presence of mutant cGAS did not (Fig. 1A). Next, we analyzed IFN secretion by transferring supernatants from infected cells to a reporter cell line (HEK293-ISRE-luc), in which firefly luciferase expression is driven by interferon-stimulated response elements (ISREs) (fig. S1E). Only virus stocks produced in wild-type cGAS-expressing cells triggered IFN secretion (fig. S1F). Moreover, infected cells induced *IFI44* and *IFIT1* mRNAs specifically when cGAS was present in virus producer cells, further demonstrating induction of interferon-stimulated genes (ISGs) (fig. S1G). We made similar observations when infecting the myeloid cell line THP1 (fig. S2). Next, we infected primary mouse bone marrow–derived macrophages (BMDMs). IFN and ISGs were induced in BMDMs that had been infected with HIV-1-GFP produced in cGAS-reconstituted 293T cells (Fig. 1, B and C). STING-deficient BMDMs did not induce IFN and ISGs in response to the same virus preparations, although retinoic acid–inducible gene I (RIG-I)–dependent IFN production triggered by Sendai virus (SeV) was normal (Fig. 1, B and C). The increased IFN production triggered by HIV-1–GFP was functionally relevant, because infection with HIV-1-GFP produced in the presence of cGAS conferred a STING-dependent antiviral state against subsequent challenge with encephalomyocarditis virus (EMCV) or herpes simplex virus 1 (HSV-1) (Fig. 1D).

To exclude the possibility that transfer of plasmid DNA or of a soluble factor accounts for IFN production by freshly infected cells, we treated virus preparations with deoxyribonuclease or pelleted virions by centrifugation. Neither treatment affected the ability of HIV-1-GFP produced in cGAS-expressing cells to induce IFN (fig. S3, A and B). The IFN response in target cells was independent of reverse transcription and integration, as shown by pharmacological inhibition with nevirapine and raltegravir, respectively (fig. S3C). Virus-like particles lacking the viral RNA genome induced IFN in target cells when collected from cGAS-expressing producer cells (fig. S3D). These observations demonstrate that neither the viral genome nor its reverse transcription products account for IFN

Fig. 1. HIV-1-GFP produced in cGAS-reconstituted 293T cells induces IFN. (**A**) HEK293 cells were transfected with p125-F-Luc (*IFN*β promoter reporter) and pRL-TK. After 6 to 8 hours, cells were infected [multiplicity of infection (MOI) = 1] with HIV-1–GFP from producer cells expressing cGAS as indicated. F-Luc activity was analyzed after 24 hours and normalized to R-Luc. m-cGAS-AA is a catalytically inactive mutant (*N* = 2 biological replicates, average and individual values are shown). (**B**) BMDMs of the indicated genotypes were infected with HIV-1-GFP (MOI = 5) or SeV (wedges: MOI=1, 0.5, 0.1). Supernatant was tested after 24 hours for mIFNα by enzyme-linked immunosorbent assay (ELISA) (n.d.: not detectable; dashed line: lower limit of detection; *N* = 2 biological replicates, average and individual values are shown). (**C**) BMDMs were infected as in (B) and the indicated mRNAs were quantified relative to *GAPDH* mRNA by reverse transcription–quantitative polymerase chain reaction (RT-QPCR) (*N* = 4 replicates; error bars indicate SD, and significance was determined by analysis of variance (ANOVA); ****$P < 0.0001$; ***$P < 0.001$; **$P < 0.01$. (**D**) Lung fibroblasts were treated with IFN-A/D or infected with HIV-1-GFP (MOI = 2). Cells were then infected with EMCV or HSV-1 (wedges: fourfold dilutions starting at MOI = 4 or MOI = 64, respectively). After 24 hours, cells were stained with crystal violet. Data are representative of three or more independent experiments.

induction in this setting. Substitution of VSV-G with thogotovirus glycoprotein did not diminish the IFN-inducing property of virus stocks from cGAS-expressing cells, showing that these effects are not related to VSV-G pseudotyping (fig. S3E) (*19*).

HIV-1-GFP stocks are likely to contain exosomes and other enveloped vesicles such as apoptotic bodies. Treatment of cGAS-reconstituted producer cells with the exosome inhibitor GW4869 (*20*) or the caspase inhibitor Ac-DEVD-CHO during virus preparation did not affect IFN induction by HIV-1-GFP (Fig. 2A). Reduced amounts of the exosome marker syntenin (*21*) in virus preparations and diminished cleavage of caspase 3 in virus producer cells confirmed the efficacy of these compounds (Fig. 2B). We then separated virions from exosomes and other extracellular vesicles by density gradient centrifugation (*22*) and found that the fraction containing most of the viral p24 protein and of VSV-G was also the most potent fraction

inducing IFN (Fig. 2C). Next, we transfected 293T cells with cGAS plasmid alone and prepared mock "virus" stocks. These preparations did not induce detectable amounts of IFN (Fig. 2D), suggesting that vesicles constitutively shed by cells do not account for IFN induction. Moreover, overexpression of tetherin, which inhibits virion release (*23*), diminished IFN induction (Fig. 2E). Together, these observations show that most of the IFN-inducing activity is associated with virions.

Next, we prepared small-molecule extracts from HIV-1-GFP, which we then added to PMA (phorbol 12-myristate 13-acetate)–differentiated THP1 cells that were mildly permeabilized with digitonin (fig. S4). HIV-1-GFP extracts collected from wild-type cGAS-reconstituted producer cells induced IFN secretion, whereas HIV-1-GFP extracts collected from catalytically inactive m-cGAS-AA–reconstituted producer cells failed to induce IFN secretion (Fig. 3A). Preincubation of extracts with snake venom phosphodiesterase I

(SVPDE), which cleaves cGAMP (*24*), abrogated this effect (Fig. 3B). To further test whether cGAMP is present in lentiviral particles, we transfected virus producer cells with biotin-labeled cGAMP. Biotin-cGAMP was detectable in virus preparations (Fig. 3C). Next, we quantified the amount of cGAMP present in HIV-1-GFP preparations using mass spectrometry. cGAMP was detectable only in extracts from virus produced in cGAS-expressing cells (Fig. 3D). Based on a calibration curve and the efficiency of extraction (fig. S5), we found that 2.50×10^{-17} mol of cGAMP were present in virus stocks per infectious unit (Fig. 3D). A similar estimate was obtained from the data in Fig. 3A.

These results show that cGAMP can be packaged into HIV-1-GFP and induces IFN via STING in newly infected cells. Similarly, we found that an HIV-2–based, replication-deficient lentivirus produced in cGAS-expressing cells induced IFN secretion in HEK293 cells (fig. S6). To further

Fig. 2. IFN induction triggered by HIV-1-GFP from cGAS-expressing cells is mediated by virions. (**A**, **C** to **E**) HEK293 cells were infected for 24 hours and then washed; after an additional 48 hours, secreted IFN was analyzed by bioassay. (**A**) HIV-1-GFP was produced in cells reconstituted with m-cGAS that were also treated with 20 μM GW4869 or 60 μM Ac-DEVD-CHO, or were left untreated (control). Fresh cells were infected with pelleted virus (wedges: 10-fold dilutions; $N = 3$ biological replicates). Differences between groups were not statistically significant (ANOVA). (**B**) Pelleted viruses from (A) (top) or whole-cell extracts (bottom) from virus producer cells were tested by Western blot. FL: full length; CL: cleaved caspase 3. (**C**) HIV-1-GFP from cGAS-expressing cells was loaded onto density gradients. Wedges indicate increasing iodixanol concentration in 12 collected fractions. Twenty and 2 μl of each fraction and of the input were tested. p24 concentrations were determined by ELISA (bottom left) and p24 and VSV-G were analyzed by Western blot (bottom right). (**D**) 293T cells were transfected as indicated to produce mock "virus" stocks (wedges: 10-fold dilutions; $N = 3$ biological replicates). (**E**) Vpu-deficient lentivectors produced in cells expressing cGAS and either wild-type or mutant tetherin were tested. The fraction of infected cells was determined by flow cytometry (right). $N = 3$ biological replicates. Error bars are ±SD, and significance was determined by ANOVA (A and D) or unpaired t test (E) (****$P < 0.0001$; *$P < 0.05$). Data are representative of two (C) or three (A, B, D, and E) independent experiments.

Fig. 3. Small-molecule extracts from HIV-1-GFP generated in cGAS-reconstituted producer cells induce IFN and contain cGAMP. (**A**) Extracts from viruses produced in the absence of cGAS or in the presence of wild-type (m-cGAS) or mutant cGAS (m-cGAS-AA) were added to digitonin permeabilized THP1 cells. IFN in THP1 supernatants was assessed by bioassay. Gray wedges represent a 1:2 dilution series starting with extract from 10^7 infectious units. As controls, synthetic 2'3'-cGAMP was either directly added to THP1 cells (gray bars) or was spiked into medium and then included in the extraction procedure (orange bars). Black wedges represent a 1:3 dilution series starting with 50 ng of 2'3'-cGAMP. Extraction efficiency (fig. S5B) was taken into account to estimate the amount of cGAMP per infectious unit (dotted line). (**B**) Extract from 10^7 infectious units of HIV-1-GFP produced in the presence of cGAS was incubated with or without SVPDE for 1 hour and then added to digitonin-permeabilized THP1 cells. IFN in THP1 supernatants was assessed by bioassay. Wedges represent a 1:3 dilution series. (**C**) HIV-1-GFP produced in the absence or presence of cGAS or in biotin-cGAMP–transfected cells was probed by dot blot for biotin (left). The stripped membrane was reprobed for p24 (right). Wedges represent a 1:10 dilution series starting with $2 × 10^6$ infectious units. (**D**) cGAMP concentration in samples from (A) was analyzed by mass spectrometry. n.d., not detectable. Data are representative of two (B) or three (A, C, D) independent experiments.

explore the relevance of our findings, we extended our study from replication-deficient, VSV-G–pseudotyped lentiviruses to fully infectious HIV-1 bearing a native CXCR4-tropic envelope glycoprotein. Human monocyte–derived dendritic cells (hMDDCs) infected with HIV-1 that had been produced in 293T cells reconstituted with wild-type cGAS induced the expression of IFN and of CD86, encoded by an ISG (Fig. 4A and figs. S7 to S9). Density gradient centrifugation demonstrated that most of the CD86-inducing activity fractionated together with infectious virus particles (Fig. 4B). Next, we prepared extracts and found that these induced IFN secretion by THP1 cells (Fig. 4C). Mass spec-

trometry confirmed that cGAMP was specifically present in extracts from HIV-1 stocks from cGAS-expressing cells (Fig. 4D). These results show that cGAMP is not only incorporated into VSV-G–pseudotyped lentivectors but can also be incorporated into fully infectious HIV-1. However, these experiments relied on overexpression of cGAS in virus producer cells. We therefore asked whether triggering of endogenous cGAS during virus infection results in the packaging of cGAMP into progeny virus particles. We used mouse cytomegalovirus (MCMV), an enveloped DNA virus, for these experiments (fig. S10) because this virus induces STING-dependent IFN responses (25). We propagated MCMV in primary

mouse embryonic fibroblasts (MEFs). Extracts from MCMV stocks collected from wild-type cells contained an activity that induced IFN secretion and ISG expression in THP1 cells, whereas extracts from virus from cGAS-deficient cells did not (Fig. 4, E and F). Mass spectrometry confirmed the presence of cGAMP in MCMV stocks from wild-type cells (Fig. 4G). Similarly, virus produced in $Sting^{-/-}$ cells contained cGAMP, whereas no cGAMP was detectable in virus preparations from $cGas^{-/-}$ cells (Fig. 4G). Consistent with this observation, MCMV produced in cGAS-sufficient MEFs induced IFNα secretion by $cGas^{-/-}$ BMDMs upon infection, but failed to do so in $Sting^{-/-}$ cells (Fig. 4H). In contrast, the response to MCMV
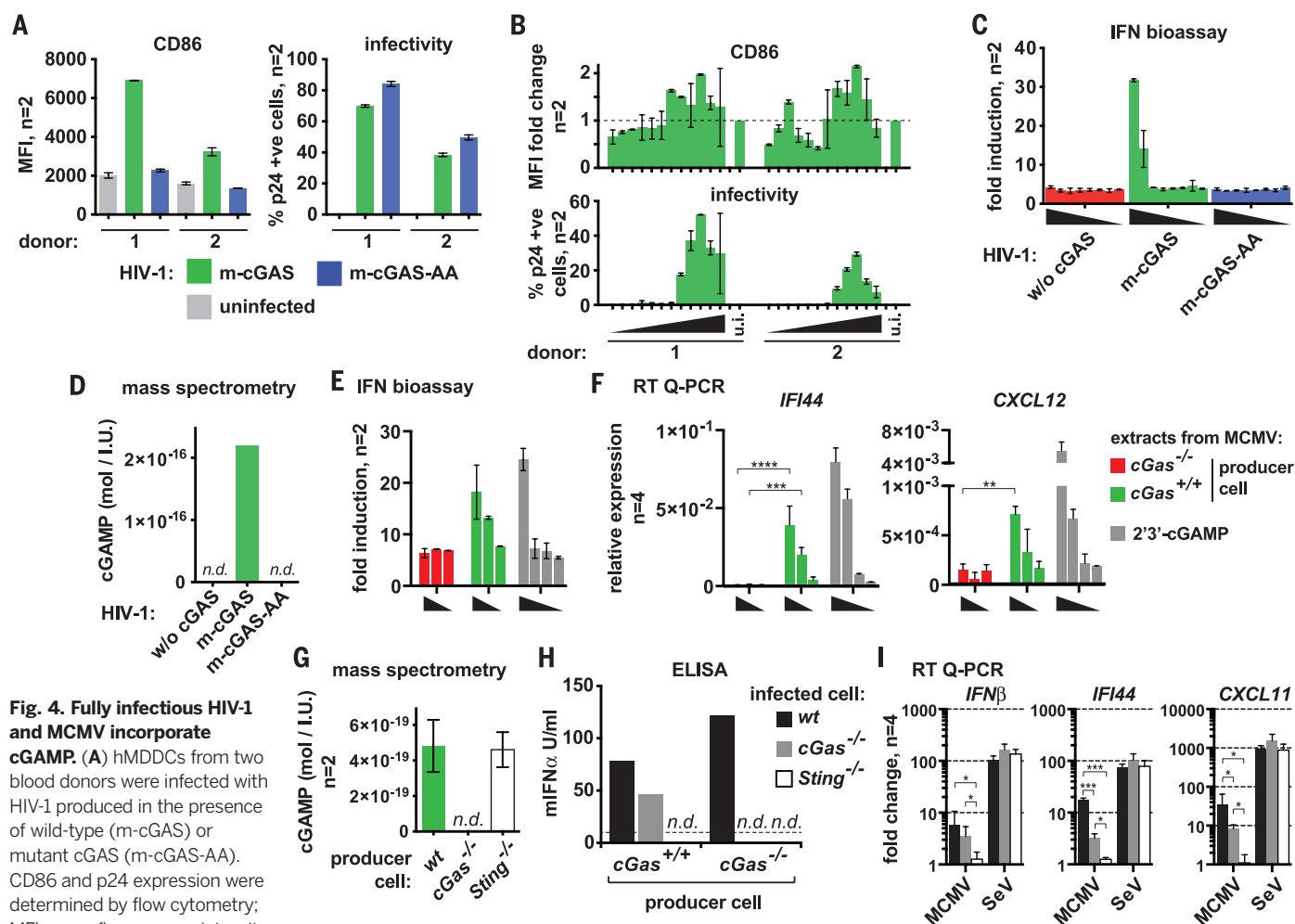
Fig. 4. Fully infectious HIV-1 and MCMV incorporate cGAMP. (A) hMDDCs from two blood donors were infected with HIV-1 produced in the presence of wild-type (m-cGAS) or mutant cGAS (m-cGAS-AA). CD86 and p24 expression were determined by flow cytometry; MFI: mean fluorescence intensity (N = 2 infections per donor; average and individual values are shown). (B) HIV-1 produced in the presence of wild-type cGAS was fractionated on density gradients and analyzed as in (A). CD86 MFI in uninfected (u.i.) cells was set to 1 (N = 2 infections per donor; average and individual values are shown). (C) Extracts from HIV-1 were tested as in Fig. 3A. wedges: threefold dilutions (N = 2 biological replicates; average and individual values are shown). (D) 2'3'-cGAMP concentration in samples from (C) was analyzed by mass spectrometry. n.d., not detectable. (E and F) MCMV was propagated in primary MEFs of the indicated genotypes. Virus extracts or 2'3'-cGAMP was added to permeabilized THP1 cells. Secreted IFN was assessed by bioassay [(E), N = 2 biological replicates; average and individual values are shown] and the indicated mRNAs were quantified by RT-QPCR relative to GAPDH mRNA [(F), N = 4 replicates]. Wedges represent a 1:3 dilution series starting with extract from 250,000 in-

fectious units or 0.0686 ng of cGAMP. (G) cGAMP concentrations in MCMV extracts were analyzed by mass spectrometry. n.d., not detectable. Data were pooled from two independent experiments. Average and individual values are shown. (H) BMDMs of the indicated genotypes were infected with MCMV (MOI = 7) from $cGas^{+/+}$ or $cGas^{-/-}$ MEFs, and supernatant mIFNα was analyzed by ELISA after 20 hours (n.d., not detectable; dashed line: lower limit of detection). (I) BMDMs as in (H) were infected with MCMV (MOI = 1) from $cGas^{+/+}$ MEFs for 20 hours. The indicated mRNAs were quantified by RT-QPCR relative to GAPDH mRNA, and fold changes compared to mock infected cells were calculated (N = 4 replicates). SeV was used as a control (MOI = 0.5). In (F) and (I), error bars indicate SD, and significance was determined by ANOVA (****P < 0.0001; ***P < 0.001; **P < 0.01; *P < 0.05). Data are representative of three (A) or two (B to F, I) independent experiments.

from cGAS-deficient producer cells required both cGAS and STING. Furthermore, *IFN*β, ISG, and chemokine mRNA up-regulation after infection with MCMV from wild-type producer cells was partially cGAS-independent but fully STING-dependent (Fig. 4I). Taken together, these results demonstrate that cGAMP produced by endogenous cGAS is incorporated into MCMV particles, which contributes to IFN induction in newly infected cells in a cGAS-independent but STING-dependent manner.

Incorporation of cGAMP into virions may broaden the spectrum of cells that initiate an IFN response. For example, HIV-1 reverse transcription, which is inhibited in some cells by SAMHD1 (*26*), is not required for virus sensing via cGAMP transfer. This Trojan horse mechanism may also accelerate the IFN response. We speculate that cGAMP packaging had been overlooked in previous studies owing to virus production in cGAS-negative cell lines such as 293T. Whether the incorporation of cGAMP into virus particles is a selective process or is based on diffusion remains to be determined. It is likely that a lipid envelope is required to encompass cGAMP in virus particles. Indeed, nonenveloped adenovirus produced in cGAS-reconstituted cells did not induce IFN in newly infected cells (fig. S11). In our experimental settings, cGAMP was primarily transferred by virions; however, these data do not exclude a role of extracellular vesicles such as exosomes in shuttling cGAMP between cells in other models (for example, sterile inflammation). Although it remains unclear whether HIV virions produced during natural infection contain appreciable amounts of cGAMP, our observations have important translational implications. cGAMP delivery via lentiviral vectors results in heightened activation of DCs (figs. S8, S9, and S12). This could be harnessed in vaccination settings in which viral vectors codeliver to DCs cyclic dinucleotides as innate stimuli, as well as viral antigens. Moreover, IFN induction by oncolytic viruses has been reported to enhance tumor killing (*27*) and may be achieved by cGAMP loading. In sum, we have identified a mechanism by which a signal for innate immunity is transferred between cells.

REFERENCES AND NOTES

1. C. E. Samuel, *Clin. Microbiol. Rev.* **14**, 778–809 (2001).
2. A. Pichlmair, C. Reis e Sousa, *Immunity* **27**, 370–383 (2007).
3. S. R. Paludan, A. G. Bowie, *Immunity* **38**, 870–880 (2013).
4. L. Sun, J. Wu, F. Du, X. Chen, Z. J. Chen, *Science* **339**, 786–791 (2013).
5. J. Wu et al., *Science* **339**, 826–830 (2013).
6. P. Gao et al., *Cell* **154**, 748–762 (2013).
7. H. Ishikawa, G. N. Barber, *Nature* **455**, 674–678 (2008).
8. D. Gao et al., *Science* **341**, 903–906 (2013).
9. M. R. Jakobsen et al., *Proc. Natl. Acad. Sci. U.S.A.* **110**, E4571–E4580 (2013).
10. X. Lahaye et al., *Immunity* **39**, 1132–1142 (2013).
11. J. Rasaiyaah et al., *Nature* **503**, 402–405 (2013).
12. P. Dai et al., *PLOS Pathog.* **10**, e1003989 (2014).
13. J. W. Schoggins et al., *Nature* **505**, 691–695 (2014).
14. E. Lam, S. Stein, E. Falck-Pedersen, *J. Virol.* **88**, 974–981 (2014).
15. X.-D. Li et al., *Science* **341**, 1390–1394 (2013).
16. A. Ablasser et al., *Nature* **503**, 530–534 (2013).
17. M. H. Malim, *Philos. Trans. R. Soc. Lond. B Biol. Sci.* **364**, 675–687 (2009).
18. D. L. Burdette et al., *Nature* **478**, 515–518 (2011).
19. A. Pichlmair et al., *J. Virol.* **81**, 539–547 (2007).
20. J. Li et al., *Nat. Immunol.* **14**, 793–803 (2013).
21. M. F. Baietti et al., *Nat. Cell Biol.* **14**, 677–685 (2012).
22. M. Dettenhofer, X. F. Yu, *J. Virol.* **73**, 1460–1467 (1999).
23. S. J. D. Neil, *Curr. Top. Microbiol. Immunol.* **371**, 67–104 (2013).
24. A. Ablasser et al., *Nature* **498**, 380–384 (2013).
25. C. Sun et al., *J. Immunol.* **194**, 1819–1831 (2015).
26. N. Laguette, M. Benkirane, *Trends Immunol.* **33**, 26–33 (2012).
27. L.-C. S. Wang et al., *Mol. Ther.* **20**, 736–748 (2012).

ANTIVIRAL IMMUNITY

Transmission of innate immune signaling by packaging of cGAMP in viral particles

Matteo Gentili,[1] Joanna Kowal,[1]* Mercedes Tkach,[1]* Takeshi Satoh,[1] Xavier Lahaye,[1] Cécile Conrad,[1] Marilyn Boyron,[2] Bérangère Lombard,[3] Sylvère Durand,[4] Guido Kroemer,[4] Damarys Loew,[3] Marc Dalod,[2] Clotilde Théry,[1,5] Nicolas Manel[1,5,6]†

Infected cells detect viruses through a variety of receptors that initiate cell-intrinsic innate defense responses. Cyclic guanosine monophosphate (GMP)–adenosine monophosphate (AMP) synthase (cGAS) is a cytosolic sensor for many DNA viruses and HIV-1. In response to cytosolic viral DNA, cGAS synthesizes the second messenger 2'3'-cyclic GMP-AMP (cGAMP), which activates antiviral signaling pathways. We show that in cells producing virus, cGAS-synthesized cGAMP can be packaged in viral particles and extracellular vesicles. Viral particles efficiently delivered cGAMP to target cells. cGAMP transfer by viral particles to dendritic cells activated innate immunity and antiviral defenses. Finally, we show that cell-free murine cytomegalovirus and Modified Vaccinia Ankara virus contained cGAMP. Thus, transfer of cGAMP by viruses may represent a defense mechanism to propagate immune responses to uninfected target cells.

To protect multicellular organisms against viruses, it is vital that infected cells trigger antiviral defense responses that can be rapidly transmitted to noninfected cells. Cells are equipped with cytosolic viral sensors that recognize viral infection and induce innate immune responses (*1*). The resulting innate immune responses can restrain the pathogen, repair the host, and shape an adaptive immune response (*2*). Cyclic guanosine monophosphate (GMP)–adenosine monophosphate (AMP) synthase (cGAS) is a cytosolic DNA sensor that synthesizes 2'3'-cyclic GMP-AMP (cGAMP), a second messenger that binds to the STING protein and activates a type I interferon (IFN) response (*3–5*). cGAS is essential to induce an antiviral response against several DNA viruses, as well as HIV (*6–8*).

Dendritic cells (DCs) link innate sensing of pathogens to induction of adaptive immune responses. In DCs, the cGAS-cGAMP pathway also activates the expression of cytokines and co-stimulatory molecules for T cell activation, similar to adjuvants (*7*, *9*). In human DCs, HIV-1 normally evades sensing by cGAS, suggesting a crucial

¹INSERM U932, Immunity and Cancer Unit, Institut Curie, Paris, France. ²Centre d'Immunologie de Marseille-Luminy, Aix Marseille Université UM2, INSERM U1104, CNRS UMR7280, 13288 Marseille, France. ³Laboratoire de Spectrométrie de Masse Protéomique, Institut Curie, Paris, France. ⁴Metabolomics and Cell Biology Platforms, Gustave Roussy Comprehensive Cancer Institute, 94805 Villejuif, France. ⁵Labex Dendritic Cell Biology (DCBIOL), Paris, France. ⁶Labex Vaccine Research Institute (VRI), Paris, France.
*These authors contributed equally to this work. †Corresponding author. E-mail: nicolas.manel@curie.fr
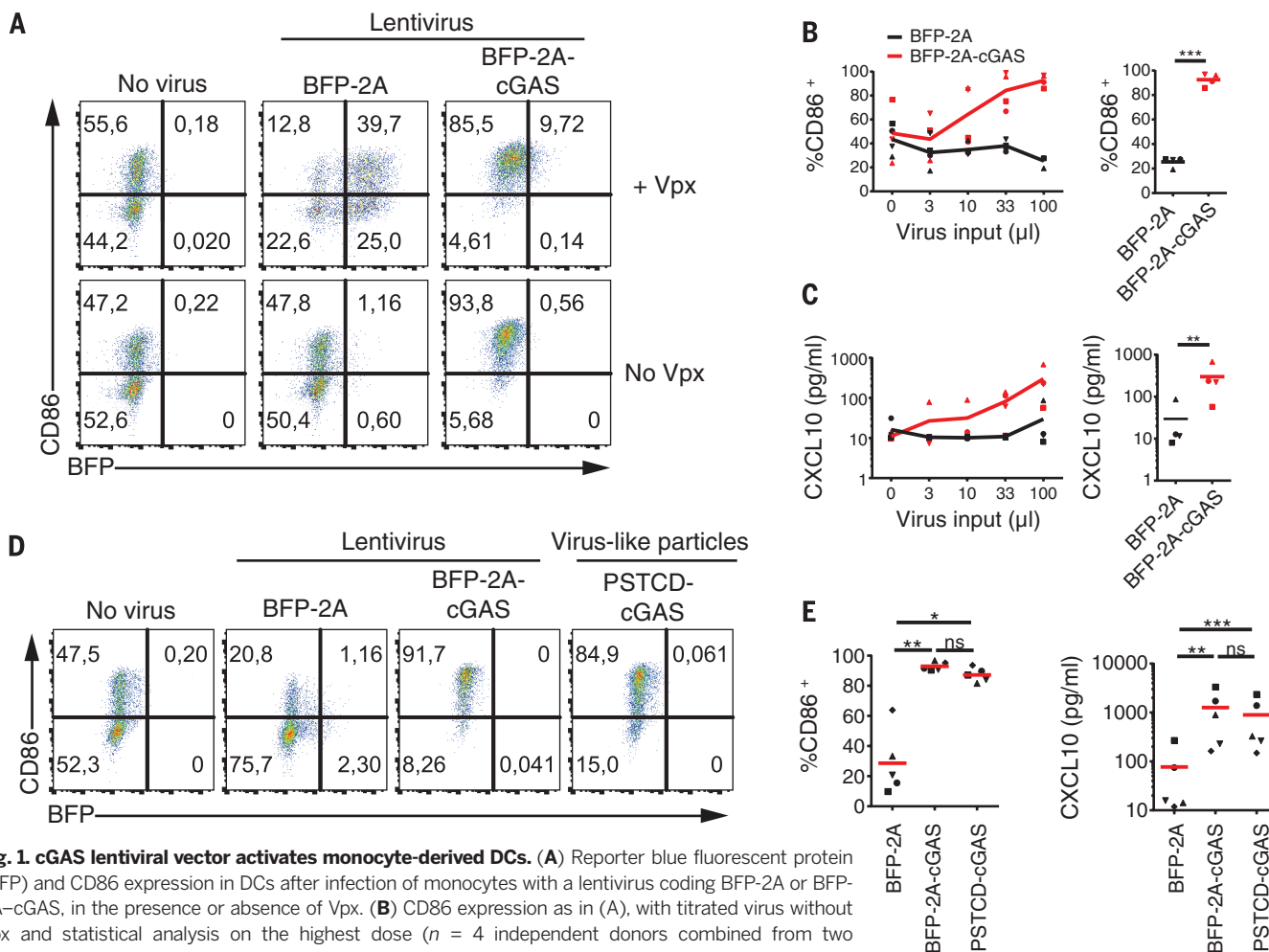
Fig. 1. cGAS lentiviral vector activates monocyte-derived DCs. (**A**) Reporter blue fluorescent protein (BFP) and CD86 expression in DCs after infection of monocytes with a lentivirus coding BFP-2A or BFP-2A–cGAS, in the presence or absence of Vpx. (**B**) CD86 expression as in (A), with titrated virus without Vpx and statistical analysis on the highest dose ($n = 4$ independent donors combined from two experiments, paired t test; ***$P < 0.001$). Bars indicate average. (**C**) CXCL10 production as in (A), with titrated virus without Vpx and statistical analysis on the highest dose ($n = 4$ independent donors combined from two experiments, paired t test on log-transformed data; **$P < 0.01$). (**D**) BFP and CD86 expression in DCs after infection of monocytes with a lentivirus coding BFP-2A or BFP-2A–cGAS or with VLPs produced in the presence of a nonlentiviral plasmid encoding for cGAS (PSTCD-cGAS). (**E**) CD86 expression and CXCL10 production as in (D) [$n = 5$ independent donors combined from three experiments, one-way analysis of variance (ANOVA) with post-hoc Tukey test for CD86 expression analysis, one-way ANOVA with post-hoc Tukey test on log-transformed data for CXCL10; ***$P < 0.001$, **$P < 0.01$, *$P < 0.05$, ns = not significant]. Symbols reflect individual donors.

role for this pathway in host–HIV-1 interactions (6, 10).

To study cGAS function, we sought to manipulate its expression in human monocyte–derived DCs. We generated a lentivector expressing cGAS and infected monocytes before differentiating them into DCs (see supplementary materials and methods). At day 4, DCs exposed to the cGAS virus expressed CD86 and were activated, despite low transduction efficiency (Fig. 1A). In contrast, infection with a control lentivector efficiently transduced DCs but did not change basal activation of the cells (Fig. 1A). This observation confirmed that lentivectors themselves do not activate DCs (10) and suggested that an activating innate immune signal was associated with infection with a cGAS-expressing lentivector.

Efficient lentivector transduction of DCs requires the protein Vpx that alleviates the restriction to HIV infection imposed by SAMHD1 (11–13). Omitting Vpx prevented efficient transduction, but DC activation by the cGAS lentivirus was maintained

(Fig. 1, A and B), suggesting that cGAS expression in the target cells was not required. Type I IFN–inducible cytokine CXCL10 was also produced by DCs (Fig. 1C). The resulting DCs were fully differentiated as positive for DC-SIGN and negative for CD14 (fig. S1A). The cGAS lentivector also activated DCs that were fully differentiated before infection (fig. S1, B and C). To exclude a low level of cGAS vector transduction, we produced HIV-1 virus-like particles (VLPs) lacking the lentiviral genome, and we coexpressed cGAS from a nonlentiviral plasmid (fig. S1D). The VLP-containing supernatant from cGAS-expressing cells activated DCs (Fig. 1, D and E), indicating transmission of an innate signal.

To determine the nature of this signal, we fractionated viral supernatants over a 10-kD filter. Activity was depleted from the filtrate and maintained in the retentate (fig. S2, A and B). We performed differential ultracentrifugation (14) to separate extracellular vesicles (EVs) released by cells (15) from soluble factors. Cell debris and large apoptotic bodies pellet first (2000 g), fol-

lowed by medium-sized vesicles (10,000 g), and finally small EVs, including exosomes (100,000 g) (16, 17). The activity corresponded to the fraction that contained Gag, regardless of the presence of the exosome-associated proteins CD63, CD9, and CD81 and cytosolic syntenin-1 (Fig. 2A and fig. S2, C and D). This finding suggested that viral particles can transmit the innate signal.

Next, we examined which components were required. Activity was abrogated when Glu^{225}→Ala^{225} (E225A) and Asp^{227}→Ala^{227} (D227A) mutations were introduced to the cGAS catalytic active site (18) (Fig. 2, B and C). VLPs are produced by expressing the viral proteins Gag and Pol and the fusogenic viral envelope protein VSV-G (vesicular stomatitis virus glycoprotein). Omitting expression of Gag and Pol, VSV-G, or all three proteins decreased induction of CD86 and CXCL10 in DCs (Fig. 2, B and C, and fig. S3A). The absence of VSV-G led to a strong decrease in DC activation (Fig. 2, B and C, and fig. S3A), indicating that fusogenic viral protein–containing extracellular material is the major DC-activating factor. We
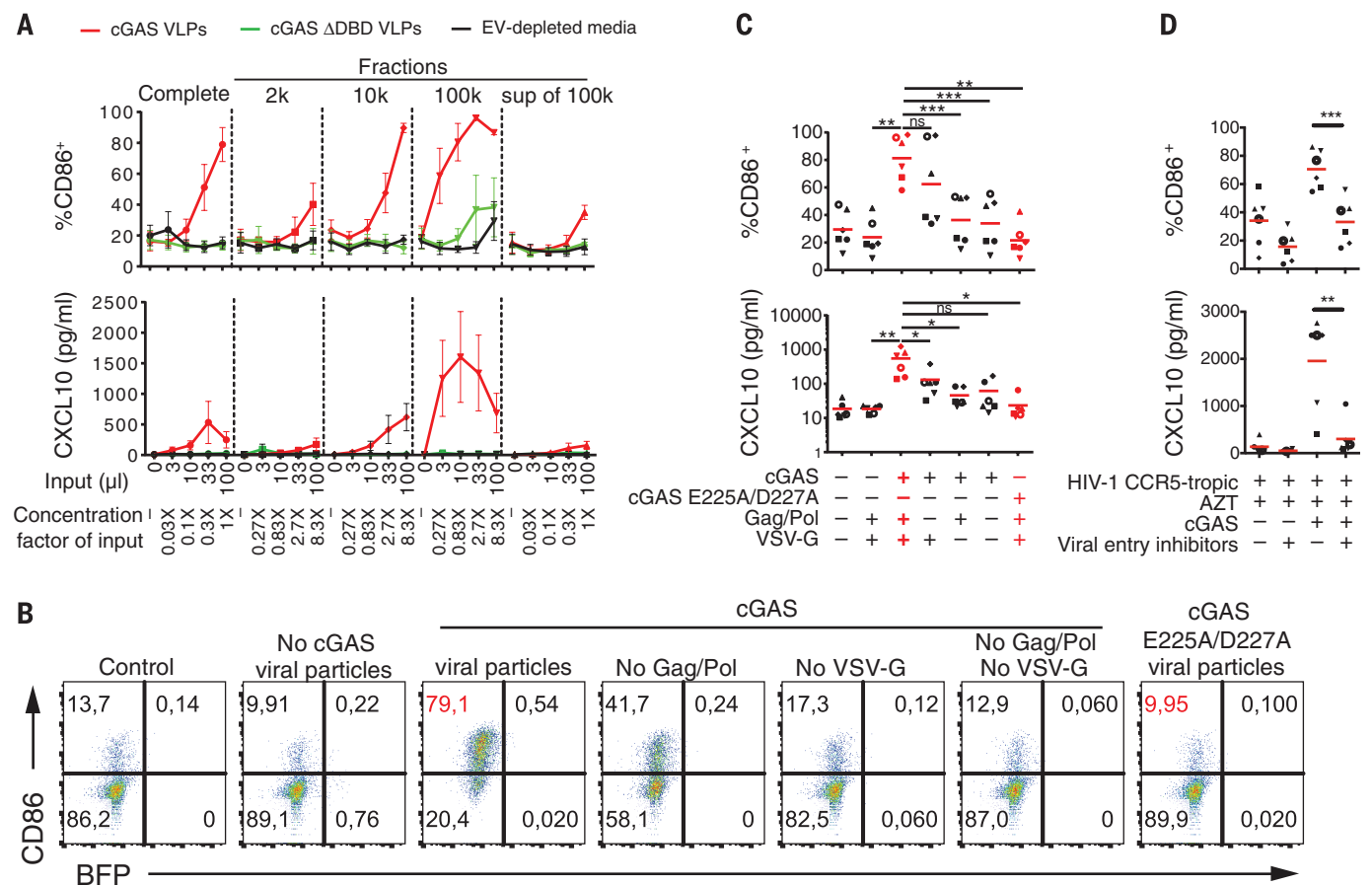
Fig. 2. HIV-1 particles transfer an innate signal initiated by cGAS. (**A**) CD86 expression and CXCL10 production in DCs after dose-response infections of monocytes with differentially fractionated supernatants containing VLPs produced from 293FT expressing WT cGAS or an inactive cGAS mutant lacking the DNA binding domain (ΔDBD). The volume of each fraction used for infection and the corresponding concentration factor compared to the initial supernatant are indicated (n = 3 independent donors combined from two experiments; mean and SEM plotted). (**B**) BFP and CD86 expression in DCs after exposure of monocytes to cell-free supernatants of cells transfected with combinations of plasmids expressing Gag, Pol, and VSV-G together with plasmids encoding cGAS, cGAS E225A and D227A, or control. (**C**) Analysis of CD86 expression and CXCL10 production as in (B) (n = 6 independent donors combined from three experiments; one-way ANOVA with post-hoc Tukey test for CD86 expression, one-way ANOVA with post-hoc Tukey test on log transformed data for CXCL10 production; ***P < 0.001, **P < 0.01, *P < 0.05, ns = not significant). (**D**) CD86 expression and CXCL10 production in DCs after infection of monocytes with CCR5-tropic HIV-1 viral particles produced in presence or absence of cGAS and HIV-1 entry inhibitors. Azidothymidine (AZT) was added to inhibit HIV-1 cDNA synthesis in the target cells (n = 6 independent donors combined from three experiments; one-way ANOVA with post-hoc Tukey test for CD86 expression, one-way ANOVA with post-hoc Tukey test on log transformed data for CXCL10 production; ***P < 0.001, **P < 0.01). Symbols reflect individual donors.

next examined the effect of tetherin expression, an inhibitor of viral particle release (*19*). Tetherin inhibited viral particle release and significantly decreased transfer of the innate signal (fig. S3, B to D). To rule out the possibility that transmission of the innate signal was unique to VSV-G, which can lead to production of tubulovesicular structures (*20*), we produced VLPs carrying the influenza virus envelope proteins H1N1 and H5N1 instead of VSV-G. When produced in the presence of cGAS, the VLPs activated DCs (fig. S4, A and E). VSV-G–pseudotyped gammaretroviral murine leukemia virus particles and HIV-1 particles expressing the wild-type (WT) CCR5-tropic envelope protein BaL also transmitted the innate signal (fig. S4, B to E). Incubation of target cells with HIV-1 entry inhibitors disrupted transfer of the innate signal without impairing the response to transfected cGAMP (Fig. 2D and fig. S4F). These data demonstrate that fusogenic viral particles trans-

fer the innate signal from cGAS-expressing cells to DCs.

We could not detect cGAS protein in the pelleted supernatants (fig. S1D and fig. S2C). We hypothesized that cGAMP, a small molecule (mass = 675 daltons) produced in the cytosol, could be packaged in the viral particles and EVs because these structures contain cytosol from the producing cells (*16*).

If cGAMP was transferred by viral particles, the latter should activate a type I IFN response in a STING-dependent but cGAS-independent manner. We transfected an IFN reporter construct with or without a STING plasmid in 293FT cells that lack detectable cGAS expression (fig. S1D), and we validated the assay by transfected synthetic cGAMP or a cGAS expression plasmid (Fig. 3A). VLPs produced from cGAS-expressing cells activated the reporter only in the presence of STING (Fig. 3A and fig. S5A). Supernatants

from cGAS-expressing cells that did not produce VLPs were much less effective (Fig. 3A and fig. S5A). To further demonstrate that cGAMP was present in the viral particles, we used a bioassay based on permeabilized THP-1 cells (a monocytic cell line) and an IFN reporter cell line (*21, 22*) (Fig. 3B). We extracted small molecules from virus-producing cells and pelleted VLPs. cGAMP activity was detected in cells transfected with cGAS but not in control cells. cGAMP activity was also detected in the pelleted VLPs and was lost when we introduced the cGAS E225A and D227A mutations (Fig. 3B). To confirm the presence of cGAMP in viral particles, we quantified the amount of cGAMP in the fractionated supernatants of cells expressing cGAS with or without viral particles. Expression of viral particles increased the quantity of pelleted cGAMP, whereas levels of the exosomal protein syntenin-1 were not affected (fig. S5, B to E). We also confirmed the

Fig. 3. Viral particles package and transfer cGAMP. (**A**) 293FT cells transfected with a luciferase reporter plasmid under control of the IFN-β promoter with or without a STING coding plasmid. The cells were stimulated with titrated amounts of supernatants from cells producing viral particles in the presence (cGAS viral particles) or absence (control viral particles) of murine cGAS and supernatants from cells expressing murine cGAS (cGAS no Gag/Pol no VSV-G), stimulated with synthetic cGAMP using lipofectamine, or transfected with a plasmid coding for cGAS (cGAS transfection) (n = 3 independent experiments; one-way ANOVA with post-hoc Tukey test on log-transformed data; ****P < 0.0001. Graph shows average ± SEM). The dilution factor of the wedges is threefold per bar. (**B**) cGAMP quantification in extracts coming from 293FT transfected cells and pelleted viral particles. 293FT cells were transfected with a lentiviral packaging plasmid in the presence of cGAS alone or catalytically inactive cGAS with E225A and D227A mutations. Type I IFN activity was measured after permeabilized PMA-differentiated THP-1 cells were exposed to synthetic 2'3'-cGAMP (left) or the benzonase-resistant extracts (right) (n = 3 independent experiments, except n = 2 for empty control. Graph shows average ± SEM). The dilution factor of the wedges is threefold per bar. (**C**) Liquid chromatography–tandem mass spectrometry analysis was used to identify cGAMP in extracts of pelleted cell-free EVs from cells producing VLPs in the presence of cGAS. (Top) Extracted ion chromatogram (XIC) of synthetic cGAMP [mass/charge ratio (m/z) = 675.05 to 675.15], full mass spectrum (MS1) at 12.6 min, and tandem mass spectrum (MS2) cumulated (12.6 to 12.9 min) after fragmentation of the precursor ion (m/z = 675.1) shown in the MS1 scan. (Bottom) XIC of cGAS viral particle extract (m/z = 675.05 to 675.15), full mass spectrum (MS1) at 12.6 min, and tandem mass spectrum (MS2) cumulated (12.6 to 12.8 min) after fragmentation of the precursor ion (m/z = 675.1) shown in the MS1 scan (with subtracted MS2 scan at 12.57 and 12.82 min). Arrows indicate the m/z values specific to cGAMP.

Fig. 4. cGAMP is packaged in enveloped viruses produced by infection, and its transfer by viral particles induces an antiviral response in target cells. (**A**) Detection of cGAMP in extracts of MVA–green fluorescent protein (GFP) [4 × 10^6 plaque-forming units (pfu)] and mCMV (2.7 × 10^4 pfu). XICs were measured by ultrahigh-performance liquid chromatography coupled with triple quadrupole mass spectrometry in multiple-reaction monitoring mode of the target ion with m/z = 476.1. Gray traces show the blank before the sample. Red dashed lines indicate the retention time of cGAMP. A representative analysis is shown, and additional replicates are shown in fig. S8. (**B**) Outline of the experiment in (C). (**C**) Monocytes were infected with the indicated supernatants or treated with type I IFN. The resulting DCs were infected with a dose-response of HSV-1 encoding GFP. GFP expression was analyzed after 24 hours (n = 4 independent donors combined from two experiments; one-way ANOVA with post-hoc Tukey test; ***P < 0.001, ns = not significant). Symbols reflect individual donors. MOI, multiplicity of infection.

presence of cGAMP by performing mass spectrometry analysis on the extract of pelleted viral particles, using synthetic cGAMP for reference (Fig. 3C).

Next, we sought to determine whether transfer of cGAMP by viral particles would occur at a natural level of cGAS expression. HeLa cells express the cGAS protein and produced cGAMP after DNA stimulation in a cGAS-dependent manner (fig. S6, A and B). We pelleted the supernatants of unstimulated HeLa, DNA-stimulated HeLa, or HeLa transfected with VLPs coding plasmids that also provide a DNA stimulus. cGAMP was detected in the supernatants of all DNA-stimulated HeLa cells, consistent with its packaging in both EVs and viral particles (fig. S6C). However, although HeLa-derived VLPs induced CXCL10 production in phorbol 12-myristate 13-acetate (PMA)–treated THP-1 cells, EVs from control HeLa or DNA-stimulated HeLa cells did not (fig. S6D). To ascertain whether cGAMP was transferred, we tested the supernatants in the luciferase reporter assay. HeLa-derived VLPs, but not EVs from DNA-stimulated HeLa, activated the reporter in a STING-dependent manner (fig. S6, E and F). Overall, these data demonstrate that viral particles and EVs package cGAMP produced by endogenous cGAS, but only viral particles can efficiently transfer the second messenger cGAMP.

Transfected DNA provides a strong stimulation for cGAS. We sought to test whether HIV-1 infection itself, which generates cDNA after reverse transcription, would lead to sufficient cGAMP production for packaging in virus progeny. Upon infection of HeLa cells, cGAMP accumulation was observed in the cells and inhibited by reverse transcriptase inhibitors, indicating that cGAMP was produced in response to the infection (fig. S7, A and B). cGAMP was also detected in the supernatants of both transfected and infected cells (fig. S7, C to E). Thus, when HIV-1 infection activates cGAS, cGAMP is incorporated in the extracellular material containing the viral progeny. Additionally, we examined the presence of cGAMP in two DNA viruses: murine cytomegalovirus (mCMV), a member of the herpesviridae family of which herpes simplex virus (HSV) was shown to stimulate cGAS (4), and Modified Vaccinia Ankara virus (MVA), an attenuated poxvirus that requires cGAS for sensing by murine DCs (23). MVA and mCMV were produced by infection of cGAS-expressing cells (table S1). We found that cGAMP was present in the extracts of sucrose-purified stocks of both viruses (Fig. 4A and fig. S8, A and B).

Finally, we tested whether eliciting cGAMP transfer to DCs by HIV-1 particles could induce a functional antiviral response. We exposed monocytes to cGAMP-containing VLPs, control VLPs, or supernatants from cGAS-expressing cells and challenged them with a replication-competent HSV-1 (24) and a replication-defective vaccinia strain (Fig. 4B and fig. S8C). IFN treatment was used as a positive control (Fig. 4C and fig. S8D). cGAMP-containing VLPs, but not control VLPs or supernatants from cGAS-expressing cells, conferred protection against viral infections (Fig. 4C and fig. S8D). Collectively, our results provide evidence that cGAMP can be transferred between cells by virtue of packaging within viral particles, defining a mechanism of innate immune signal transmission (fig. S9).

The spread of innate responses is generally attributed to the production of cytokines, including IFNs. Effectors such as APOBEC3G can be packaged into viral particles and EVs (25–27), but they do not signal in the target cells. cGAMP can diffuse between physically connected cells via gap junctions (28). Viral transfer of cGAMP does not require a direct contact between the cells, which may allow distant transmission of an innate signaling molecule within the organism or between hosts. This process could maximize the rapid induction of effector responses in target cells and bystander uninfected cells through local IFN production. Similarly, immunostimulatory cyclic dinucleotides naturally produced by bacteria can be delivered into the target cell (3).

Our results establish that HIV-1 may generate a cGAMP-containing progeny in cells that express cGAS. However, HIV-1 escapes cytosolic innate sensing by cGAS and thus is unlikely to contain cGAMP upon natural infection (6, 10, 29, 30). Eliciting cGAMP transfer by HIV-1 leads to activation of antiviral defenses. This parallels antiviral restriction factors that are inactive against the WT virus (31). In contrast, we find that purified stocks of mCMV and MVA contain cGAMP. Thus, cGAMP packaging is likely relevant to a large number of viruses and vaccines that naturally stimulate cGAS. The contribution of virally packaged cGAMP as compared to other innate signals will probably vary according to the functionality of cGAS in target cells.

Our results indicate that cell-derived EVs that include exosomes can package cGAMP as well. EVs also package and transmit cellular RNA between cells (32, 33). However, transmission of cGAMP by cellular EVs is not efficient. Viral envelope proteins increase transmission, indicating that fusion of EVs from noninfected cells with target cells is limiting. Nonetheless, low-efficiency transmission of cGAMP by host EVs may contribute to the tonic IFN response (8, 34).

Packaging of cGAMP within viral particles can be interpreted as an immune tagging process, allowing infected cells to further signify progeny viruses as nonself, or danger, to alert subsequent target cells. We speculate that other signaling molecules are also packaged and disseminated by viral particles. Subverting viral particles with cGAMP constitutes an attractive approach for therapeutics and vaccines.

REFERENCES AND NOTES

1. D. Goubau, S. Deddouche, C. Reis e Sousa, *Immunity* **38**, 855–869 (2013).
2. R. Medzhitov, D. S. Schneider, M. P. Soares, *Science* **335**, 936–941 (2012).
3. D. L. Burdette et al., *Nature* **478**, 515–518 (2011).
4. L. Sun, J. Wu, F. Du, X. Chen, Z. J. Chen, *Science* **339**, 786–791 (2013).
5. J. Wu et al., *Science* **339**, 826–830 (2013).
6. X. Lahaye et al., *Immunity* **39**, 1132–1142 (2013).
7. X. D. Li et al., *Science* **341**, 1390–1394 (2013).
8. J. W. Schoggins et al., *Nature* **505**, 691–695 (2014).
9. J. J. Woodward, A. T. Iavarone, D. A. Portnoy, *Science* **328**, 1703–1705 (2010).
10. N. Manel et al., *Nature* **467**, 214–217 (2010).
11. C. Goujon et al., *Gene Ther.* **13**, 991–994 (2006).
12. N. Laguette et al., *Nature* **474**, 654–657 (2011).
13. K. Hrecka et al., *Nature* **474**, 658–661 (2011).
14. C. Théry, S. Amigorena, G. Raposo, A. Clayton, *Curr. Protoc. Cell Biol.* **3**, 3.22.1–3.22.29 (2006).
15. S. J. Gould, G. Raposo, *J. Extracell. Vesicles* **2**, 20389 (2013).
16. C. Théry, M. Ostrowski, E. Segura, *Nat. Rev. Immunol.* **9**, 581–593 (2009).
17. R. Crescitelli et al., *J. Extracell. Vesicles* **2**, 20677 (2013).
18. P. J. Kranzusch, A. S. Lee, J. M. Berger, J. A. Doudna, *Cell Reports* **3**, 1362–1368 (2013).
19. S. J. Neil, T. Zang, P. D. Bieniasz, *Nature* **451**, 425–430 (2008).
20. A. Pichlmair et al., *J. Virol.* **81**, 539–547 (2007).
21. A. Ablasser et al., *Nature* **498**, 380–384 (2013).
22. G. Uzé et al., *J. Mol. Biol.* **243**, 245–257 (1994).
23. P. Dai et al., *PLOS Pathog.* **10**, e1003989 (2014).
24. P. Desai, S. Person, *J. Virol.* **72**, 7563–7568 (1998).
25. R. S. Harris et al., *Cell* **113**, 803–809 (2003).
26. R. Mariani et al., *Cell* **114**, 21–31 (2003).
27. A. K. Khatua, H. E. Taylor, J. E. Hildreth, W. Popik, *J. Virol.* **83**, 512–521 (2009).
28. A. Ablasser et al., *Nature* **503**, 530–534 (2013).
29. D. Gao et al., *Science* **341**, 903–906 (2013).
30. J. Rasaiyaah et al., *Nature* **503**, 402–405 (2013).
31. M. H. Malim, P. D. Bieniasz, *Cold Spring Harbor Perspect. Med.* **2**, a006940 (2012).
32. H. Valadi et al., *Nat. Cell Biol.* **9**, 654–659 (2007).
33. M. Dreux et al., *Cell Host Microbe* **12**, 558–570 (2012).
34. D. J. Gough, N. L. Messina, C. J. Clarke, R. W. Johnstone, D. E. Levy, *Immunity* **36**, 166–174 (2012).

ACKNOWLEDGMENTS

SUPPLEMENTARY MATERIALS

www.sciencemag.org/content/349/6253/1232/[suppl]/DC1
Materials and Methods
Supplementary Text
Figs. S1 to S9
Table S1
References (35–46)

17 April 2015; accepted 22 July 2015
Published online 30 July 2015
10.1126/science.aab3628

CHROMOSOMES

The inner centromere–shugoshin network prevents chromosomal instability

Yuji Tanno,[1] Hiroaki Susumu,[1,2] Miyuki Kawamura,[1,2] Haruhiko Sugimura,[3] Takashi Honda,[1] Yoshinori Watanabe[1,2]*

Chromosomal instability (CIN) is a major trait of cancer cells and a potent driver of tumor progression. However, the molecular mechanisms underlying CIN still remain elusive. We found that a number of CIN+ cell lines have impairments in the integrity of the conserved inner centromere–shugoshin (ICS) network, which coordinates sister chromatid cohesion and kinetochore-microtubule attachment. These defects are caused mostly by the loss of histone H3 lysine 9 trimethylation at centromeres and sometimes by a reduction in chromatin-associated cohesin; both pathways separately sustain centromeric shugoshin stability. Artificial restoration of the ICS network suppresses chromosome segregation errors in a wide range of CIN+ cells, including RB- and BRCA1-deficient cells. Thus, dysfunction of the ICS network might be a key mechanism underlying CIN in human tumorigenesis.

Most cancer cells exhibit elevated chromosome mis-segregation, called whole-chromosomal instability, as well as structural changes in their chromosomes (e.g., translocations, deletions). These chromosome aberrations are believed to allow cells to rapidly acquire genetic changes that promote tumorigenesis (1). Several cellular defects, such as replication stress (2), multipolarity of the spindle (3), weak cohesion (4) and increased stability of kinetochore fibers (5), are proposed to be involved in CIN in cancer cells. Although merotely (the attachment of a single kinetochore to microtubules oriented toward opposite poles) might be a major cause of CIN (6, 7), the underlying molecular mechanisms remain elusive.

We assessed 17 cell lines, including tumor- and non–tumor-derived cell lines, for anaphase chromosome segregation errors, which were classified into two categories: (i) lagging chromosomes containing kinetochore signals, which reflect attachment defects, and (ii) acentric lagging chromosomes and chromosome bridges, which reflect structural defects (Fig. 1A). The ratio of attachment and structure defects in CIN cells deviates somewhat from earlier results, in part because CIN cells are not isogenic (7–9). Intriguingly, although widely used HeLa cell lines (HeLa-2 and HeLa-3) showed segregation errors, a variant HeLa cell line (HeLa-1) showed few errors in anaphase (Fig. 1A). On the basis of the frequency of segregation errors, we define cell lines that are error-prone as CIN+ and those that are error-free

as CIN−. Consistent with a previous observation (5), the majority of our CIN+ cell lines showed increased kinetochore-microtubule fibers as compared with CIN− cell lines (correlation coefficient $r = 0.40$) (Fig. 1B), whereas these lines have an intact spindle checkpoint (10) and show some correlation ($r = 0.28$) with spindle multipolarity (3) (fig. S1, A and B). Thus, our results favor the notion that microtubule attachment to kinetochores is abnormally stabilized in CIN+ cell lines (5, 6).

Because mutations affecting sister chromatid cohesion might also underlie CIN (4, 11), we examined centromeric cohesion in the same collection of cell lines. Sister chromatid cohesion at metaphase is largely normal in CIN+ cells (7). However, when cells were arrested at metaphase with the proteasome inhibitor MG132, most CIN+ cells exhibited premature sister chromatid separation to various extents, whereas CIN− cells largely retained cohesion (Fig. 1C and fig. S1C); these findings reveal that "cohesion fatigue" (12) is a cohesion defect closely related to CIN ($r = 0.54$). Together, our analyses indicate that stabilized kinetochore-microtubule attachment and decreased centromeric cohesion are shared traits of CIN+ cells, which suggests that these defects are caused by a common (but as yet unknown) abnormality in cancer cells.

Sister chromatid cohesion and kinetochore-microtubule attachment are regulated by shugoshin (SGO) and the Aurora B–containing chromosomal passenger complex (CPC), core components of the inner centromere–shugoshin (ICS) network (13–15). Therefore, we hypothesized that the ICS network might be impaired in CIN+ cells. Although humans have two shugoshin-like proteins (SGO1 and SGO2), SGO1 predominantly functions in both cohesin protection and CPC localization during mitosis (16, 17) (fig. S2A). In HCT116 (CIN−) cells, when centromeres come under tension in metaphase, kinetochore-associated BUB1 (a SGO1

recruiter) is pulled outward while a substantial amount of SGO1 remains at the inner centromere, together with the CPC (18) (Fig. 1D and fig. S2, B to D). In HeLa-2 (CIN+) cells, however, SGO1 largely disperses on aligned chromosomes with the effect of reducing the CPC from the inner centromere (Fig. 1D). Although a previous study suggested that CPC localization is reduced in two cancer cell lines, particularly on unaligned chromosomes (19), our analyses reveal that the reduction in the SGO1-CPC pool is pronounced on aligned chromosomes in HeLa-2 (CIN+) cells (Fig. 1D). We do not know the reason for this discrepancy; however, SGO1-CPC reduction on aligned chromosomes is a prevalent feature of our CIN+ cell lines (12 of 14 cell lines) (Fig. 1E and fig. S3). Further, our analyses (fig. S4) suggest a potential causal link between SGO1-CPC reduction and CIN. Because the activity of Aurora B kinase at the inner centromere is required to destabilize kinetochore microtubules (13, 14) (fig. S5), we reason that the dispersion of the CPC under tension leads to the stabilization of erroneous microtubule attachment, a cause of merotely (5–7).

To further explore the root cause of SGO1-CPC reduction, we focused on nine cell lines that show dominant attachment defects (fig. S6). Given that SGO1 interacts with the heterochromatin protein HP1α (20), we envisaged that HP1α might play an important role in anchoring SGO1-CPC to the inner centromere. Indeed, HP1α localizes to the inner centromere in CIN− cells, whereas it is dispersed during alignment in a number of CIN+ cells (Fig. 2A). The reduction of HP1α by RNA interference (RNAi) in HCT116 (CIN−) cells indeed caused SGO1-CPC dispersion on aligned chromosomes and the CIN phenotype (Fig. 2B and fig. S7). Notably, all these CIN+ cell lines were defective in trimethylated Lys[9] of histone H3 (H3K9me3) (Fig. 2C and fig. S8), which usually occupies centromeric chromatin and acts as a basis of HP1α binding in CIN− cells (21). Indeed, the chromodomain mutant (Val[22] → Met) of HP1α, whose binding affinity to methylated H3K9 is diminished (22), showed reduced localization at centromeres (fig. S9). We therefore reasoned that centromeric HP1α binds H3K9me3 and aids stabilization of the ICS network by tethering SGO1 to H3K9me3 (see below).

Because members of the KDM4 subfamily (demethylases of H3K9me3) are often overexpressed in cancer cells (23), we examined their expression in the CIN+ cell lines, and found an elevated expression of KDM4s in eight of nine CIN+ cell lines (fig. S10). HeLa-2 (CIN+) cells overexpressed KDM4C in comparison with HeLa-1 (CIN−) cells (fig. S10). Accordingly, the ectopic expression of KDM4C in HeLa-1 (CIN−) cells leads to a loss of H3K9me3 on the mitotic centromeres, resulting in a reduction of HP1α and SGO1-CPC on aligned chromosomes, which leads to CIN (fig. S11). These results argue for a causal link between centromeric H3K9me3 and CIN that is mediated by the ICS network.

Notably, three of nine CIN+ cell lines with defects in microtubule attachment showed a

[1]Laboratory of Chromosome Dynamics, Institute of Molecular and Cellular Biosciences, University of Tokyo, Yayoi, Tokyo 113-0032, Japan. [2]Department of Biological Sciences, Graduate School of Science, University of Tokyo, Yayoi, Tokyo 113-0032, Japan. [3]First Department of Pathology, Hamamatsu University School of Medicine, Hamamatsu, Shizuoka 431-3192, Japan.
*Corresponding author. E-mail: ywatanab@iam.u-tokyo.ac.jp

reduction in cohesin localization during G_2 phase (fig. S12A). Considering that cohesin interacts directly with SGO1 and that this interaction is required for the retention of SGO1 at the inner centromeres (24), we confirmed that partial depletion of RAD21 (cohesin subunit) by RNAi in HCT116 cells and the H4 neuroglioma cell line harboring an inactivating mutation of STAG2 (another cohesin subunit) produced a marked impairment of SGO1-CPC localization in aligned chromosomes and chromosome segregation errors at anaphase (fig. S13, A to E). Cohesin-defective cells, however, retained intact centromeric H3K9me3 (fig. S13F), which suggests

that cohesin and H3K9me3-HP1α are separate pathways acting to sustain the ICS network.

The foregoing results suggest that the stability of SGO1 at centromeres may be impaired in CIN$^+$ cells. We performed FRAP (fluorescence recovery after photobleaching) experiments in four cell lines expressing SGO1 fused to green fluorescent protein (GFP-SGO1). GFP-SGO1 proteins exhibited a shorter half-recovery time in CIN$^+$ cells relative to CIN$^-$ cells (Fig. 3, A and B), implying that SGO1 localization is destabilized in CIN$^+$ cells. Because SGO1 interacts directly with cohesin and HP1α through distinct domains (20, 24), we generated point mutations in the SGO1 protein—Thr^{346} →

Ala (T346A), Val^{453} → Glu (V453E), or both (TAVE)—that disrupt the specific interaction with cohesin or HP1α, respectively (20, 24). Although all mutant proteins fused with GFP were expressed equally in HeLa-1 (CIN$^-$) cells, the centromeric localization was moderately impaired for the SGO1-T346A and SGO1-V453E proteins and was mostly abolished in the SGO1-TAVE protein (Fig. 3C). Even in CIN$^-$ cells, mutant GFP-SGO1 proteins exhibited a shorter half-recovery time (Fig. 3D), implying that the interactions of SGO1 with cohesin or HP1α act independently but cooperatively to stabilize SGO1 at the inner centromeres (Fig. 3E). Therefore, although the cohesin and H3K9me3-
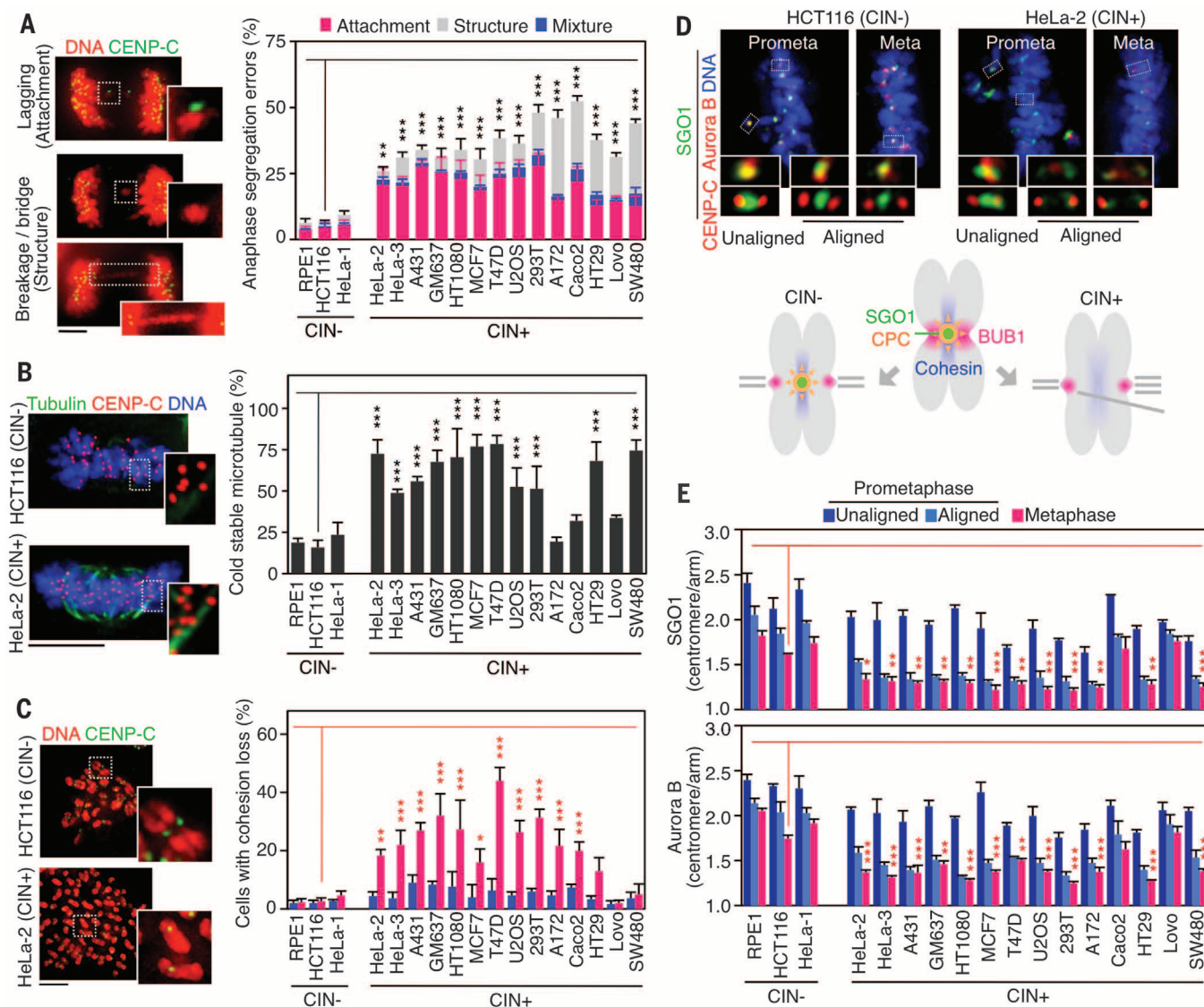
Fig. 1. The ICS network underlies CIN. (**A**) Left: A classification of anaphase chromosome segregation errors. Right: Percentage of anaphases showing chromosome segregation errors. (**B**) Cold-stable kinetochore microtubules in metaphase were quantified. (**C**) Cells showing >50% sister chromatid separation were counted after treatment with MG132 nocodazole. A total of 100 cells or microtubules were counted in each experiment; error bars, SD from three independent experiments. (**D**) The indicated cell lines were immunostained in prometaphase or metaphase. Kinetochore pairs on aligned or un-

aligned chromosomes are magnified. A schematic diagram shows SGO1-CPC (Aurora B) localization in CIN$^-$ and CIN$^+$ cells. (**E**) Quantification of SGO1 (top) and Aurora B (bottom) enrichment in the inner centromeres. The intensity of the signal at the inner centromere was divided by the intensity at the chromatin region; $n = 50$ centromeres. Error bars, SEM from three independent experiments. *$P < 0.05$, **$P < 0.01$, ***$P < 0.001$, one-way analysis of variance (ANOVA) with Bonferroni's multiple comparisons test relative to HCT116. Scale bars, 5 μm.
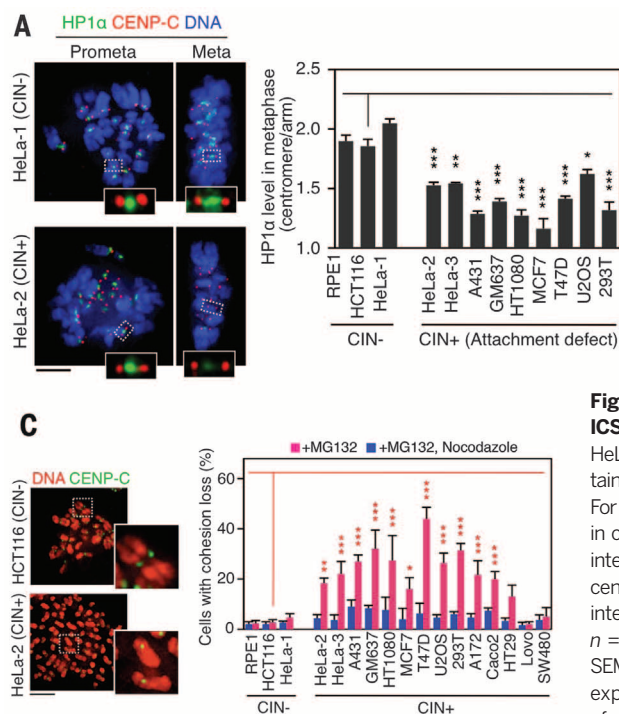
Fig. 2. HP1-H3K9me3 sustains the ICS network. (**A**) HeLa-1 (CIN⁻) and HeLa-2 (CIN⁺) cells were immunostained with the indicated antibodies. For quantification of HP1α enrichment in centromeres at metaphase, the intensity of the signal at the inner centromere was divided by the intensity on the chromatin region; n = 50 centromeres. Error bars, SEM from three independent experiments. (**B**) Percentage of anaphases showing attachment defects. Error bars, SD from three independent experiments. (**C**) Quantification of H3K9me3 enrichment in centromeres in nocodazole-arrested cells. The signal intensity at the centromere was divided by the intensity at the chromosome arm region; n = 50 centromeres. Error bars, SEM from three independent experiments. *$P < 0.05$, **$P < 0.01$, ***$P < 0.001$, one-way ANOVA with Bonferroni's multiple comparisons test relative to HCT116 [(A) and (C)] or t test (B). Scale bars, 5 μm.

HP1α pathways may regulate global chromatin functions such as transcriptional regulation (*25, 26*), our results argue that these pathways act to suppress CIN by stabilizing SGO1 at the centromeres. Further, we examined the ICS network in cells defective in two well-known tumor suppressor genes, RB or BRCA1, and found that they are required for the integrity of cohesin and/or H3K9me3 (figs. S12B and S14; also see below).

Our immunostaining assays (Fig. 2C and figs. S12 and S14F) indicate that CIN⁺ cells with predominant defects in kinetochore-microtubule attachment can be classified into three categories: (i) H3K9me3-defective, (ii) cohesin-defective, and (iii) doubly defective cells (Fig. 4). To examine whether the reduction of centromeric H3K9me3 and/or chromatin-associated cohesin in CIN⁺ cells is the cause of CIN, we sought to restore these defects by tethering H3K9 trimethyltransferase Suv39H1 to centromeres (CENP-B fusion; Suv39-CB) and/or by expressing a cohesin stabilizer, sororin (*27*) (Fig. 4A and fig. S15). Strikingly, the expression of Suv39-CB suppressed CIN in four of five H3K9me3-defective CIN⁺ cells but not in cohesin-defective RB-reduced HCT116 (CIN⁺) cells (Fig. 4, A and B). In contrast, the expression of sororin suppressed CIN in RB-reduced HCT116 (CIN⁺) cells but not in H3K9me3-defective CIN⁺ cells, validating the specificity of the assay. Finally, two of three CIN⁺ cell lines defective in both the H3K9me3 and cohesin pathways were suppressed for CIN by the expression of both Suv39-CB and sororin, but not either alone (Fig. 4, A and B). We confirmed that CIN suppression is in each case accompanied by the restoration of the ICS network (fig. S15).
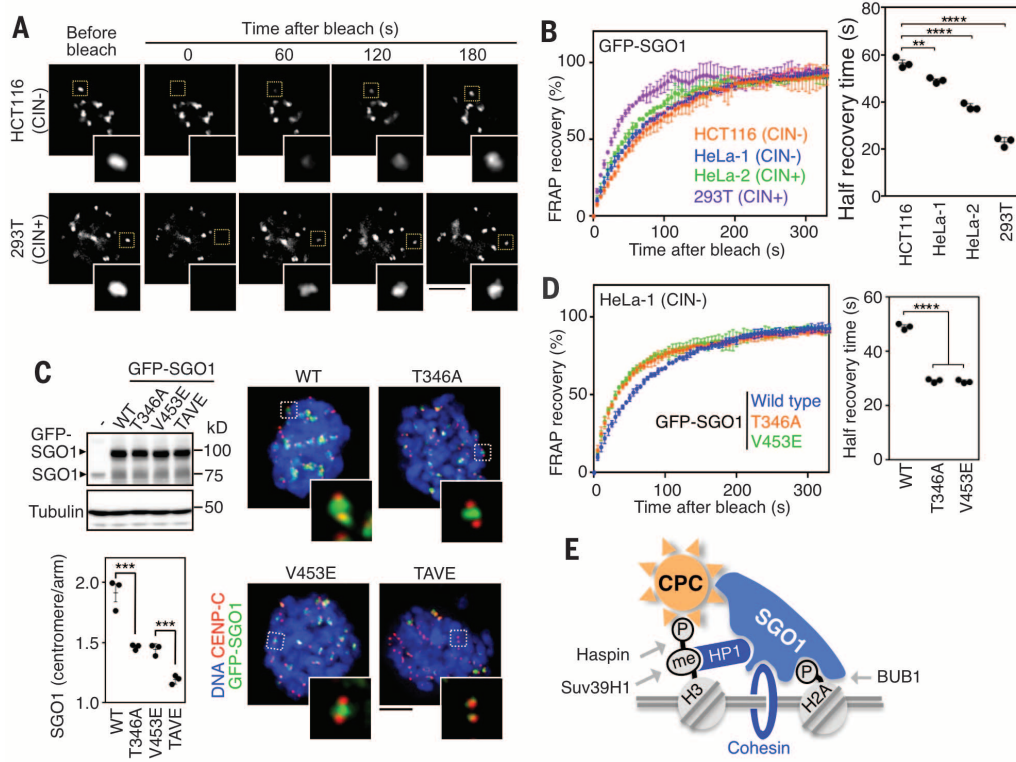
Fig. 3. HP1 and cohesin cooperate to sustain the ICS network. (**A**) Nocodazole-treated cells expressing GFP-SGO1 were examined by FRAP analysis. (**B**) Left: Recovery of the fluorescence signal intensity after photobleaching (t = 0) relative to the prebleached intensity (100%); n = 5 cells (HCT116, HeLa-2, 293T) or 10 cells (HeLa-1). Right: Half-recovery time. Error bars, SD from three independent experiments. (**C**) Nocodazole-treated HeLa-1 (CIN⁻) cells transiently expressing GFP-SGO1 and its mutants were examined by immunoblotting and immunostaining. The relative localization of SGO1 was examined; n = 50 centromeres. (**D**) Turnover of GFP-SGO1 in cells prepared as in (C) was examined by FRAP analysis; n = 10 cells. (**E**) A schematic illustration of the ICS network. Error bars, SEM from three independent experiments. **$P < 0.01$, ***$P < 0.001$, ****$P < 0.001$, one-way ANOVA with Bonferroni's multiple comparisons test. Scale bars, 5 μm.

A

(i) H3K9me3 defective

(ii) Cohesin defective

(iii) Doubly defective

B

Fig. 4. Promotion of H3K9me3 and cohesin association with chromatin suppress CIN. (**A**) The percentage of anaphases showing attachment defects was measured in the indicated cells expressing HA-Suv39H1-CENP-B and/or GFP-sororin. Error bars, SEM from three independent experiments. **P < 0.01, ***P < 0.001, one-way ANOVA with Bonferroni's multiple comparisons test relative to non-expressing cells. (**B**) Suppression of ICS network defects and CIN in various CIN+ cell lines with defects (−) in H3K9me3 and chromatin-associated cohesin. The solid box indicates the suppression.

In summary, both ICS network defects and mitotic segregation errors are rescued by restoring H3K9me3 and/or cohesin in seven of nine CIN+ cells, which suggests that these two pathways are important CIN-susceptible targets in human cells.

Our study reveals that impairment in the ICS network prevails among human CIN+ cell lines and acts as a key molecular mechanism to generate CIN. Although numerous cellular mutations may influence chromosome segregation, only mutations that moderately impair chromosome segregation will establish CIN+ cells, which divide but exhibit genomic instability. In fact, the depletion of a core component of the ICS network (BUB1, SGO1, or the CPC) from cells provokes serious mitotic defects that lead to lethal mitosis, whereas hypomorphic mutations in the ICS network components cause CIN in cultured human cells and promote tumorigenesis in mice (28, 29). Nonetheless, mutations in components of the ICS network (BUB1, SGO1, CPC) are rare in human cancer genomes (30), implying that the pathways regulating the ICS network, rather than its core components, might be genetically or epigenetically altered during tumorigenesis. Indeed, we detected an ICS network defect associated with chromosome segregation errors in a patient with non–small cell lung cancer (fig. S16). Future studies, including the inspection of a substantial number of clinical samples, will validate the potential linkage between ICS network defects and CIN in tumors.

REFERENCES AND NOTES

1. C. Lengauer, K. W. Kinzler, B. Vogelstein, *Nature* **396**, 643–649 (1998).
2. R. A. Burrell, N. McGranahan, J. Bartek, C. Swanton, *Nature* **501**, 338–345 (2013).
3. N. J. Ganem, S. A. Godinho, D. Pellman, *Nature* **460**, 278–282 (2009).
4. T. D. Barber et al., *Proc. Natl. Acad. Sci. U.S.A.* **105**, 3443–3448 (2008).
5. S. F. Bakhoum, G. Genovese, D. A. Compton, *Curr. Biol.* **19**, 1937–1942 (2009).
6. D. Cimini et al., *J. Cell Biol.* **153**, 517–527 (2001).
7. S. L. Thompson, D. A. Compton, *J. Cell Biol.* **180**, 665–672 (2008).
8. R. A. Burrell et al., *Nature* **494**, 492–496 (2013).
9. S. F. Bakhoum et al., *Curr. Biol.* **24**, R148–R149 (2014).
10. K. E. Gascoigne, S. S. Taylor, *Cancer Cell* **14**, 111–122 (2008).
11. D. A. Solomon et al., *Science* **333**, 1039–1043 (2011).
12. J. R. Daum et al., *Curr. Biol.* **21**, 1018–1024 (2011).
13. M. A. Lampson, I. M. Cheeseman, *Trends Cell Biol.* **21**, 133–140 (2011).
14. T. U. Tanaka, *EMBO J.* **29**, 4070–4082 (2010).
15. Y. Watanabe, *Nat. Rev. Mol. Cell Biol.* **13**, 370–382 (2012).
16. T. S. Kitajima et al., *Nature* **441**, 46–52 (2006).
17. Y. Tanno et al., *Genes Dev.* **24**, 2169–2179 (2010).
18. J. Lee et al., *Nat. Cell Biol.* **10**, 42–52 (2008).
19. K. J. Salimian et al., *Curr. Biol.* **21**, 1158–1165 (2011).
20. Y. Yamagishi, T. Sakuno, M. Shimura, Y. Watanabe, *Nature* **455**, 251–255 (2008).
21. T. Hirota, J. J. Lipp, B. H. Toh, J. M. Peters, *Nature* **438**, 1176–1180 (2005).
22. A. L. Nielsen et al., *Mol. Cell* **7**, 729–739 (2001).
23. P. A. Cloos et al., *Nature* **442**, 307–311 (2006).
24. H. Liu, L. Jia, H. Yu, *Curr. Biol.* **23**, 1927–1933 (2013).
25. J. M. Peters, A. Tedeschi, J. Schmitz, *Genes Dev.* **22**, 3089–3114 (2008).
26. M. L. Suvà, N. Riggi, B. E. Bernstein, *Science* **339**, 1567–1570 (2013).
27. T. Nishiyama et al., *Cell* **143**, 737–749 (2010).
28. K. Jeganathan, L. Malureanu, D. J. Baker, S. C. Abraham, J. M. van Deursen, *J. Cell Biol.* **179**, 255–267 (2007).
29. H. Y. Yamada et al., *Cell Cycle* **11**, 479–488 (2012).
30. M. S. Lawrence et al., *Nature* **505**, 495–501 (2014).

WESTERN ASSAYS MASS SPEC CROSSLINKING

Invest in Austria_

Why not turn science fiction into reality?

Jost Bernasch is Managing Director of the Virtual Vehicle Research Center at the Graz University of Technology. This internationally-leading research center works closely with well-known companies in the automotive and transport industry. Together with his team, Mr. Bernasch is conducting research on future mobility. He thanks Research Location Austria for the combined innovative strength of his highly trained employees. You can make more room for know-how from Austria at www.investinaustria.at

Room for Ideas_

RESEARCH LOCATION
AUSTRIA

Top-Down Proteomics:
Turning Protein Mass Spec Upside-Down

Between alternative transcription start sites, alternative splicing, and posttranslational modifications, a given gene may produce dozens of protein variants, each with a different biological activity. Teasing apart those structure-function relationships requires mapping specific variants to their associated biological functions, and the tool of the trade for doing so is mass spectrometry. But not just any mass spec will do. Researchers need a holistic view of protein structure, data that is lost with the popular "bottom-up" proteomics strategy. Powered by today's ultrahigh-resolution, high mass-accuracy mass specs, protein biochemists are increasingly turning bottom-up upside-down. Their new alternative: top-down proteomics. **By Jeffrey M. Perkel**

I f you want to know which of a gene's many variants, or "proteoforms," is responsible for a particular biological activity, you need a way to detect that isoform directly. That's easier said than done.

Proteoform analysis is fundamentally a two-part problem. The first part, protein identification, is a simple question of peptide sequencing: matching spectral peaks to a protein's amino acid sequence and thence to the gene that encoded it. This can be complicated if related proteins are present in a sample, because they share identical stretches of amino acid sequences, but in general is relatively straightforward.

Tougher by far is characterization. A given protein may exist in dozens of forms distinguished by just a few daltons, variants that differ in terms of messenger RNA (mRNA) splicing, post-translational proteolytic processing, and chemical modification. Take histones, for instance. Histone proteins can be heavily modified by methyl, acetyl, and phosphoryl groups, among others, at their N-termini, which in turn can impact chromatin

structure and gene expression. In 2009, **University of Pennsylvania** Presidential Associate Professor Benjamin Garcia (then at Princeton University) used a so-called middle-down strategy—in which relatively large protein fragments (bigger than tryptic peptides but smaller than intact proteins) are analyzed and sequenced in the mass spectrometer—and some clever chromatography to resolve and identify 70 proteoforms of human histone H4 and 200 of human histone H3.2.

It isn't clear that every one of those variants has a different biological activity, of course. But the only way to know is to accurately tally them and track their changes under different biological conditions. And therein lies the rub. In bottom-up proteomics, researchers digest their proteoforms to peptides, separate them via liquid chromatography, and deliver them to the mass spectrometer. But as it cleaves the peptide backbone, trypsin also destroys any chance researchers have of understanding how posttranslation modifications are linked. The enzyme can cleave the 15 kilodalton (kDA) histone H3.2 29 times, including more than a dozen sites in the critical N-terminal tail. Using a bottom-up strategy effectively destroys information on how those individual chemical modifications are related, meaning researchers may be able to see that given modifications are present, but are largely blind to their interplay and stoichiometry. They certainly wouldn't be able to determine if, say, two modifications were coincident or mutually exclusive.

In the top-down approach, the histone proteoforms are delivered to the mass spec intact and then sequenced by fragmentation inside the instrument, thereby retaining the critical linkage data. This is a more technically challenging strategy, in that intact proteins are harder to fractionate and fragment than peptides, and much harder to separate by liquid chromatography. Furthermore, it takes relatively high-end instrumentation to resolve such large molecules when they are so similar in size, and special software to do the analysis. Lysine trimethylation, for instance, increases protein mass by 42.0470 Da, while acetylation adds 42.0106 Da, a difference of just 0.0364 Da.

Still, top-down is on the upswing, says Neil Kelleher, the Glass Professor of Life Sciences at **Northwestern University**, founding member of the Consortium for Top Down Proteomics and a top-down evangelist. At the recent annual meeting of the American Society for Mass Spectrometry (ASMS), for example, top-down accounted for "10% to 15%" of the conference, Kelleher says. "A decade ago, it was around 0.1%, or very fringe."

Top of the line

One driver for the growth in top-down is the increasing availability of instrumentation capable of running the experiments. Given the need to distinguish proteins varying by only small chemical changes, top-down researchers typically use high-end, high-resolution instrumentation. Just a few years ago, that mostly meant top-of-the-line Fourier-transform ion-cyclotron resonance (FT-ICR) mass spectrometers, massive and complicated hardware offering **continued>**

ILLUSTRATION: © PETARG/SHUTTERSTOCK.COM
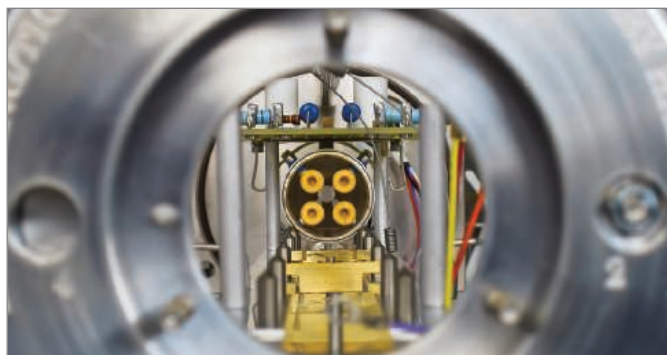
Flight tube of a triple-quadrupole mass spectrometer.

One driver for the growth in top-down is the increasing availability of instrumentation capable of running the experiments.

resolution values—and pricing—in the millions. Today, more affordable quadrupole-time-of-flight (qTOF) instruments, such as the **Waters** SYNAPT G2-Si, the **Bruker** maXis II, and the **Thermo Fisher Scientific** benchtop Orbitrap mass spectrometers, have made the technology more accessible.

Still, for some jobs, only an FT-ICR will do. And one of the world's most powerful such systems just went online at the **Pacific Northwest National Laboratory** (PNNL), in Washington state.

FT-ICR mass spectrometers derive their exquisite resolution from the massive cryo-cooled magnets that power them, and as magnetic field strength rises, so too does performance, says Ljiljana Paša-Tolić, lead scientist for mass spectrometry at PNNL's Environmental Molecular Sciences Laboratory user facility. Thus, with a more powerful magnet, "you can think about getting higher resolving power in the same acquisition time, or you can get equal resolving power in a shorter acquisition time."

The PNNL already has several FT-ICR instruments, including systems with 12 and 15 tesla (T) magnets. The new instrument, which went online in mid-March, clocks in at 21 T. With a linear ion trap (Thermo Scientific LTQ-Velos) on the front end and an **Agilent Technologies** magnet on the back, the instrument "occupies almost the whole room; it [weighs] about 24 tons," Paša-Tolić says. The magnet itself requires about 4,000 L of liquid helium to maintain its working temperature of 2.19 Kelvin. (A second 21 T instrument, employing a Bruker magnet, has been installed at the **National High Magnetic Field Laboratory** in Tallahassee, Florida.)

The PNNL instrument went online in mid-March, Paša-Tolić says, and preliminary data were presented at the recent ASMS conference. "We were able to demonstrate resolving power of about 8 million for 12-second transients, which is great," she says. That 12-second analysis time is too slow for the traditional LC-MS workflow, in which proteins flow straight from a liquid chromatography (LC) column into the mass spectrometer (MS), she notes. But even at a more LC-compatible rate, the instrument yields resolutions of about 1 million, she says, and further improvements are in the

works. "We have demonstrated a resolving power … an order of magnitude greater than what is attainable with currently available commercial technology."

Among other things, Paša-Tolić hopes to use the 21 T to break the size barrier that bedevils top-down research. Top-down researchers typically struggle to characterize proteins larger than about 50 kDa, though some have used the technique to tackle the posttranslational modifications of 150 kDa biotherapeutic antibodies. But with a more powerful magnet, it may be possible to routinely hit 100 kDa or more, Paša-Tolić says. Indeed, her lab already presented data at ASMS demonstrating "isotopically resolved" analysis of 70 kDa proteins (such as intact bovine serum albumin) at high spectral-acquisition rates.

Paša-Tolić now plans to direct the instrument at secreted fungal enzymes, especially those that degrade lignocellulose. These heavily glycosylated proteins, weighing between 50,000 and 100,000 Da, could advance biofuel development, and Paša-Tolić is developing new reverse-phase chromatography strategies to separate them. "It would be very beneficial to figure out how this pattern of glycosylation relates to function and stability and eventually glycoengineer these enzymes to be more stable and more commercially affordable," she says.

Laser focus

Top-down proteomics is so named because intact proteins are separated and broken down into smaller and smaller pieces in the MS to determine their sequence and modifications. To do that, researchers can apply any of a number of protein fragmentation methods, and the more options available, the better. "You might want to have a lot of fragmentation tools available to really get the most out of the actual experiment," says Andreas Huhmer, proteomics marketing director at Thermo Fisher Scientific. Thermo's new Orbitrap Fusion Lumos, for instance, offers collision-induced dissociation (CID), in which the peptide backbone is broken by collision with a gas molecule, and the related higher-energy collisional dissociation (HCD). It also enables the popular electron-transfer dissociation, which uses a charged donor molecule to induce fragmentation, as well as hybrid methods, such as electron-transfer and higher-energy collision dissociation (EThcD).

Jennifer Brodbelt, the William H. Wade Endowed Professor of Chemistry at the **University of Texas** at Austin, is developing an alternative fragmentation approach. Ultraviolet photodissocation (UVPD) uses ultraviolet laser pulses to cause proteins to shatter along their backbone, producing a ladder of fragments that vary in size by a single amino acid. That's how other fragmentation methods are supposed to work, too, but according to Brodbelt, most tend to fragment more efficiently at protein termini or near charged residues, providing incomplete sequence coverage. UVPD seems to provide relatively uniform coverage across the entire sequence, at least for proteins up to 40 kDa, including the oft-overlooked protein center. "The fragmentation process does not seem to be as charge-modulated as those other methods," she says.

Brodbelt has worked with Thermo Fisher Scientific to implement the technique on Orbitrap instruments. In one recent paper, she applied the method on an Orbitrap Elite

Featured Participants

Agilent Technologies
www.agilent.com

Bruker
www.bruker.com

National High Magnetic
Field Laboratory
www.nationalmaglab.org

Northwestern University
www.northwestern.edu

The Ohio State University
www.osu.edu

Pacific Northwest
National Laboratory
www.pnnl.gov

The Scripps Research
Institute
www.scripps.edu

Thermo Fisher Scientific
www.thermoscientific.com

University of Pennsylvania
www.upenn.edu

University of Texas Austin
www.utexas.edu

Vanderbilt University
www.vanderbilt.edu

Waters Corp.
www.waters.com

to map the linkages in branched poly-ubiquitin chains. The result was a remarkable series of fragment ions, one for each consecutive amino acid of the ubiquitin chain, terminating at the residue to which the ubiquitin moiety is coupled. By simply counting those ions and watching where they abruptly disappeared, she could determine where the inter-ubiquitin linkages must have occurred.

"You'd see a huge shift, a mass shift when ubiquitin appeared at a particular lysine," Brodbelt explains.

Though still in development, UVPD systems have been installed in several labs. The PNNL 21 T has one. So does John Yates III, the Ernest W. Hahn Professor at the **Scripps Research Institute**, who has mounted the system on an Orbitrap Fusion. Bottom-up proteomics, Yates explains, has long been considered easier than top-down in part because the infrastructure required to do it—the mass spectrometers, the peptide separation methods, and the analytical software—was already mature when the technique was developed. The experiments themselves were thus easier to perform. "For top-down, almost everything has to be reinvented or certainly significantly improved in order to make this whole workflow possible." That, he says, explains his enthusiasm for UVPD. "Hopefully it will get us the kind of fragmentation that we need in order to effectively analyze these things."

From top-down to top-top-down

As top-down adoption grows, so too do the technical developments. One emerging area is what Kelleher calls "top-top-down," or native mass spectrometry. The method allows researchers to examine multiprotein complexes in the MS, and one researcher making significant headway on this approach is Vicki Wysocki, Ohio Eminent Scholar at **Ohio State University**.

Existing fragmentation approaches, such as CID, simply cannot inject enough energy per collision into a protein complex to cause it to fall apart, Wysocki explains. "If you have a very large protein complex …[and] if you are colliding

that into argon with a mass of 40, the amount of energy that you can transfer will be fairly small." Rather than falling apart, a protein in such a complex will simply unfold, she says. So, her group developed an alternative approach, surface-induced dissociation (SID), in which complexes are smashed at high speed into an inert fluorocarbon-coated gold surface.

Using SID, Wysocki says, researchers can work out the topology of protein complexes and subcomplexes, teasing them apart to determine, for instance, which protein-protein interfaces are strong and which are weak. Suppose a given complex is a hexamer, she explains—a dimer of trimers. "We will directly see those trimers as products of the SID," she says. In one recent example, Wysocki's team used that approach to work out the stoichiometry of the *Pyrococcus furiosus* RNAse P complex, an RNA-containing tetramer whose structure was previously unresolved.

Waters has been working with Wysocki's group to offer SID capability to selected investigators on the SYNAPT G2 series qTOFs, and Wysocki has received grant funding to implement the method on Orbitrap and FT-ICR instruments as well. She has also developed more elaborate implementations, including a modified qTOF containing two SID cells flanking Waters' ion mobility separation unit, for performing multiple surface collision events. Ion mobility separation, Wysocki explains, "is sort of like a gas-phase electrophoresis," separating ions by size and shape, and it "has been a huge help in all of this work."

Another emerging development is top-down-based mass spectrometric imaging, Paša-Tolić says. Richard Caprioli at **Vanderbilt University**, and Ron Heeren in the Netherlands have both demonstrated laser ablation-based top-down strategies in the past year using FT-ICR mass analyzers, and Paša-Tolić says she would like to apply such strategies to study the soil rhizosphere, for instance, to determine where different secreted enzymes are located. "If you think about the way we do top-down proteomics right now, it clearly is missing spatial information," Paša-Tolić says. "In many instances, this would be extremely useful to have."

As for Kelleher, he sees a bright future for top-down in clinical research. Indeed, it is in the clinic that one of top-down's biggest successes can already be found. The Bruker BioTyper, a simple matrix-assisted laser desorption/ionization time-of-flight (MALDI-TOF) mass spectrometer for identification of bacterial pathogens based on intact protein masses, "has been a smash success …. Arguably one of the best successes of proteomics in clinical medicine," Kelleher says. Now he hopes to apply that same top-down philosophy to clinical biomarker development for complex disease.

With a growing user community, he won't be alone in that work. But Kelleher remains undaunted. "I'm smiling," he says. "Even if people are telling me they've done it better than my group has, I just say, 'okay, great, it's a big sandbox. Come play!'"

Validated Antibodies

A new product line of PrecisonAb Antibodies has been rigorously validated for use in Western blotting. These antibodies offer superior sensitivity, specificity, and reliability. They also come with the industry's most complete validation data so researchers can accurately assess the antibodies' performance before buying, and a positive control lysate so researchers can optimize the antibodies in their own labs. These are the first of thousands of PrecisonsAb Antibodies Bio-Rad plans to release to help researchers improve their Western blotting results. Scientists have struggled with antibody unreliability for decades because manufacturing standards and quality control vary widely among vendors, targets, and even among antibody lots. PrecisionAb Antibodies are screened using whole-cell lysates from up to 12 different biologically relevant cell lines—by far the industry's most rigorous validation process. Only antibodies that detect endogenous protein levels with high sensitivity and specificity are included in the PrecisionAb product line.

Bio-Rad
For info: 800-424-6723
www.bio-rad.com/precisionabpr

Protein Pegylation Service

Pegylation services are now offered to customers developing protein-based therapeutics and biosimilars through a new collaboration with Celares GmbH. The service offering includes feasibility studies, process and analytical development, and scale-up from milligram to gram quantities required for pilot and subsequent commercial scale. Pegylation, the attachment of polyethylene glycol (PEG) to a molecule, can significantly improve the pharmacological and physicochemical properties of peptide and protein therapeutics and reduce side effects. This well-recognized delivery system for biologics can enhance protein stability, bioavailability, and solubility, overcoming common challenges in the development of these therapeutics. The new services will leverage EMD Millipore's broad range of functionalized PEG products of different molecular weight and activation chemistry, as well as buffers, solvents and excipients, and unit operations employed during the pegylation process and subsequent purification, including tangential and normal flow filtration and chromatography.

EMD Millipore
For info: 800-645-5476
www.emdmillipore.com

Protein Digestion Kit

A new tool for protein digestion, the SMART Digest kit is designed to substantially reduce preparation times and associated errors, facilitating fast, reliable analytical results. Current protein digestion techniques comprise complex procedures requiring determination of protein concentration followed by sample reduction and alkylation prior to digestion with trypsin. To improve this operation, the kit uses a simple three-step, easy-to-implement process that can be automated. Its immobilized trypsin design is formulated for high-quality data with a significantly reduced sample preparation time compared to traditional in-solution digestion methods. The increased reproducibility of digestion possible with this kit should enable users to implement generic, rapid, and robust methods for high-throughput sample processing. The SMART Digest kit is also designed to provide higher sequence coverage while reducing both chemically induced posttranslational modifications and the number of chemicals in the final sample.

Thermo Fisher Scientific
For info: +45-70-23-62-60
www.thermoscientific.com/smartdigest

Conjugated Antibodies

A new range of conjugated antibodies leverages Innova's Lightning-Link and InnovaCoat bioconjugation technologies to provide customers with antibodies conjugated to an extensive range of enzymes, fluorescent dyes, and colloidal gold for improved flexibility in experimental design. The new range comprises 200 antibodies to nearly 30 different cardiac biomarkers, each available directly conjugated to 24 different enzymes, fluorescent dyes, or nanoparticles. In conjunction with the new range, a new corporate website provides customers with easier online ordering facilities, as well as access to a range of resources and support materials. The website also features an Antibody Conjugate Generator tool, which enables customers ordering from the new conjugated antibodies range to select any desired cardiac marker, antibody clone, and label. The online Conjugate Generator provides customers with unprecedented flexibility, speed, and conjugation possibilities, enabling highly tailored reagents to be created at a fraction of the cost of a custom conjugation project.

Innova Biosciences
For info: +44-(0)-1223-496170
www.innovabiosciences.com/products/antibody-conjugates

Host Cell Protein Detection Kit

The Gyrolab CHO-HCP Kit 1 detects and quantifies host cell proteins (HCPs) from Chinese hamster ovary (CHO) cells used in the bioprocessing of biotherapeutics. HCPs are measured throughout the production process, as they may affect the safety and efficacy of the biotherapeutic. The kit has been validated for use on the Gyrolab xP workstation and the new Gyrolab xPlore and is ready to use, eliminating the need for time-consuming assay development. The automation capabilities of Gyrolab systems enable 96 data points to be generated in approximately 1 hour without manual intervention, saving time and reducing errors and repeats. The kit broadens the analytical range from typically two orders of magnitude to four, and therefore requires fewer dilutions and fewer reruns than alternative methods. The kit contains all the reagents needed to produce 96 data points, including a specific Bioaffy CD that has been optimized for this HCP assay.

Gyros
For info: +46-(0)-18-566-300
www.gyros.com

Electronically submit your new product description or product literature information! Go to www.sciencemag.org/products/newproducts.dtl for more information.

Newly offered instrumentation, apparatus, and laboratory materials of interest to researchers in all disciplines in academic, industrial, and governmental organizations are featured in this space. Emphasis is given to purpose, chief characteristics, and availability of products and materials. Endorsement by *Science* or AAAS of any products or materials mentioned is not implied. Additional information may be obtained from the manufacturer or supplier.

The 2015–2016 Keystone Symposia Meetings

Human Nutrition, Environment & Health (T1)
October 14–18, 2015 | Beijing | China

Diabetes: New Insights into Molecular Mechanisms & Therapeutic Strategies (T2)
October 25–29, 2015 | Kyoto | Japan

Systems Immunology: From Molecular Networks to Human Biology (A1)
January 10–14, 2016 | Big Sky, Montana | USA

Cytokine JAK-STAT Signaling in Immunity & Disease (A2)
January 10–14, 2016 | Steamboat Springs, Colorado | USA

Molecular & Cellular Basis of Growth & Regeneration (A3)
January 10–14, 2016 | Breckenridge, Colorado | USA

Nuclear Receptors: Full Throttle (J1)
joint with **Metabolism, Transcription & Disease (J2)**
January 10–14, 2016 | Snowbird, Utah | USA

Biology of Down Syndrome: Impacts Across the Biomedical Spectrum (A4)
January 24–27, 2016 | Santa Fe, New Mexico | USA

Traumatic Brain Injury: Clinical, Pathological & Translational Mechanisms (J3)
joint with **Axons: From Cell Biology to Pathology (J4)**
January 24–27, 2016 | Santa Fe, New Mexico | USA

Drug Discovery for Parasitic Diseases (A5)
January 24–28, 2016 | Tahoe City, California | USA

Small RNA Silencing: Little Guides, Big Biology (A6)
Jan 24–28, 2016 | Keystone, Colorado | USA

Purinergic Signaling (J5) *joint with* **Cancer Immunotherapy: Immunity & Immunosuppression Meet Targeted Therapies (J6)**
January 24–28, 2016 | Vancouver, British Columbia | Canada

Neurological Disorders of Intracellular Trafficking (A7)
January 31–February 4, 2016 | Keystone, Colorado | USA

Cell Biology & Immunology of Persistent Infection (A8)
January 31–February 4, 2016 | Banff, Alberta | Canada

The Cancer Genome (Q1)
joint with **Genomics & Personalized Medicine (Q2)**
February 7–11, 2016 | Banff, Alberta | Canada

Fibrosis: From Basic Mechanisms to Targeted Therapies (Q3)
joint with **Stromal Cells in Immunity (Q4)**
February 7–11, 2016 | Keystone, Colorado | USA

Plant Epigenetics: From Genotype to Phenotype (B1)
February 15–19, 2016 | Taos, New Mexico | USA

Obesity & Adipose Tissue Biology (B2)
February 15–19, 2016 | Banff, Alberta | Canada

Noncoding RNAs in Health & Disease (Q5)
joint with **Enhancer Malfunction in Cancer (Q6)**
February 21–24, 2016 | Santa Fe, New Mexico | USA

G Protein-Coupled Receptors: Structure, Signaling & Drug Discovery (B3)
February 21–25, 2016 | Keystone, Colorado | USA

New Frontiers in Understanding Tumor Metabolism (Q7)
joint with **Immunometabolism in Immune Function & Inflammatory Disease (Q8)**
February 21–25, 2016 | Banff, Alberta | Canada

T Follicular Helper Cells & Germinal Centers (B4)
February 26–March 1, 2016 | Monterey, California | USA

Immunity in Skin Development, Homeostasis & Disease (B5)
February 28–March 2, 2016 | Tahoe City, California | USA

Tuberculosis Co-Morbidities & Immunopathogenesis (B6)
February 28–March 3, 2016 | Keystone, Colorado | USA

Stem Cells & Cancer (C1)
March 6–10, 2016 | Breckenridge, Colorado | USA

Cancer Vaccines: Targeting Cancer Genes for Immunotherapy (X1)
joint with **Antibodies as Drugs (X2)**
March 6–10, 2016 | Whistler, British Columbia | Canada

Ubiquitin Signaling (X3)
joint with **NF-κB & MAP Kinase Signaling in Inflammation (X4)**
March 13–17, 2016 | Whistler, British Columbia | Canada

Islet Biology: From Cell Birth to Death (X5)
joint with **Stem Cells & Regeneration in the Digestive Organs (X6)**
March 13–17, 2016 | Keystone, Colorado | USA

Chromatin & Epigenetics (C2)
March 20–24, 2016 | Whistler, British Columbia | Canada

HIV Persistence: Pathogenesis & Eradication (X7)
joint with **HIV Vaccines (X8)**
March 20–24, 2016 | Olympic Valley, California | USA

Cancer Pathophysiology: Integrating the Host & Tumor Environments (C3)
March 28–Apr 1, 2016 | Breckenridge, Colorado | USA

Modern Phenotypic Drug Discovery: Defining the Path Forward (D1)
April 2–6, 2016 | Big Sky, Montana | USA

Mitochondrial Dynamics (D2)
April 3–7, 2016 | Steamboat Springs, Colorado | USA

Heart Failure: Genetics, Genomics & Epigenetics (Z1)
joint with **Cardiac Development, Regeneration & Repair (Z2)**
April 3–7, 2016 | Snowbird, Utah | USA

Myeloid Cells (D3)
April 10–14, 2016 | Killarney, County Kerry | Ireland

New Therapeutics for Diabetes & Obesity (G1)
April 17–20, 2016 | La Jolla, California | USA

Gut Microbiota, Metabolic Disorders & Beyond (D4)
April 17–21, 2016 | Newport, Rhode Island | USA

Epigenetic & Metabolic Regulation of Aging & Aging-Related Diseases (E1)
May 1–5, 2016 | Santa Fe, New Mexico | USA

Positive-Strand RNA Viruses (N1)
May 1–5, 2016 | Austin, Texas | USA

Nucleic Acid Sensing Pathways: Innate Immunity, Immunobiology & Therapeutics (E2)
May 8–12, 2016 | Dresden | Germany

State of the Brain (R1)
May 22–26, 2016 | Alpbach | Austria

New Approaches to Vaccines for Human & Veterinary Tropical Diseases (M1)
May 22–26, 2016 | Cape Town | South Africa

B Cells at the Intersection of Innate & Adaptive Immunity (E3)
May 29–Jun 2, 2016 | Stockholm | Sweden

Understanding the Function of Human Genome Variation (K1)
May 31–Jun 4, 2016 | Uppsala | Sweden

Autophagy: Molecular & Physiological Mechanisms (V1)
June 5–9, 2016 | Whistler, British Columbia | Canada

Common Mechanisms of Neurodegeneration (Z3)
joint with **Microglia in the Brain (Z4)**
June 12–16, 2016 | Keystone, Colorado | USA

Exosomes/Microvesicles: Novel Mechanisms of Cell-Cell Communication (E4)
June 19–22, 2016 | Keystone, Colorado | USA

www.keystonesymposia.org/meetings

KEYSTONE SYMPOSIA™
on Molecular and Cellular Biology
Accelerating Life Science Discovery

♔ COLUMBIA UNIVERSITY
MEDICAL CENTER
College of Physicians and Surgeons

Chair of the Department of Pharmacology

The Columbia University School of Medicine seeks to fill a position for the chair of the department of Pharmacology. This position will be associated with a tenure-track faculty positions at the Full Professor level. We welcome applications from outstanding scientists, with an international reputation in the fields of pharmacology, chemical biology, or biochemistry whose research interests lie in the following strategic areas of biomedical science:

1. Elucidation of pharmacological targets within signal transduction networks
2. Chemical Biology
3. Systems Pharmacology and Pharmacogenomics
4. Experimental Therapeutics

Applicants should have a Ph.D., MD., M.D./PhD., or equivalent degree, substantial international stature and expertise in managing large-scale research programs, and substantial track record of funded research in the fields described above.

The candidate is expected to develop a new innovative direction for the Columbia University Department of Pharmacology, aligning it with the most recent trends and directions in the elucidation and characterization of molecular targets, genomics of drug response, and other relevant and pertinent research directions for the field. He or she will also be expected to develop a vibrant, externally funded, and leading personal research program in an area related to the above research directions, as well as participating in graduate and medical student teaching. In addition to a generous start-up and recruitment package, an endowed chair is available for this position.

Please send a curriculum vitae, representative reprints, and a statement of current and future research interests, as well as three letters of recomendation. Review of applications will commence on December 15, 2015.

Material should be submitted electronically to **Janiris Jorge, jj318@cumc.columbia.edu**

*Columbia University is an affirmative action/equal opportunity
employer and welcomes applications from women and minorities.*

UTSouthwestern
Medical Center

The Department of Molecular Biology and the Hamon Center for Regenerative Science and Medicine (CRSM) at the University of Texas Southwestern Medical Center invite applications for tenure track faculty positions at the level of Assistant, Associate, or Full Professor. We are seeking interactive individuals with strong research programs focused on mechanistic aspects of gene regulation, cell growth and differentiation, and stem cell biology, including the use of cellular and animal models to study human disease. Attractive recruitment packages, state-of-the-art core facilities, and exceptional laboratory space are available. UT Southwestern has a vibrant graduate program and an atmosphere of collegiality and collaboration. Academic rank will be awarded commensurate with experience.

Applicants should submit a curriculum vitae containing a summary of past research accomplishments, a statement of future objectives, and names of three references via email to: **Dr. Eric N. Olson, Department of Molecular Biology, Hamon Center for Regenerative Science and Medicine, University of Texas Southwestern Medical Center, MolBioSearch@UTSouthwestern. edu**.

UT Southwestern Medical Center is an Affirmative Action/Equal Opportunity Employer. Women, minorities, veterans and individuals with disabilities are encouraged to apply.

OFFER
THE BEST

THE BEST PLACE   Beijing, the capital of China
THE BEST CHANCE   Research Fellow/Postdoc/PI...
THE BEST SALARY   Highly competitive

北京理工大学
www.bit.edu.cn

華北電力大學
www.ncepu.edu.cn

北京航空航天大学
www.buaa.edu.cn

首都師范大學
www.cnu.edu.cn

We offer the scientific dreams
rather than a simple position

For more information, please visit **www.edu.cn/zhaopin**

ASSISTANT/ASSOCIATE/FULL PROFESSOR –
Department of Pharmaceutical Sciences

The College of Pharmacy, Washington State University (WSU) on the Health Sciences campus in Spokane, WA invites applications for a 12 month, full-time, permanent tenure-track faculty position at the rank of Assistant, Associate, or Full Professor (commensurate with experience) in the Department of Pharmaceutical Sciences. Applicants must have an earned terminal advanced degree (Ph.D., PharmD, or M.D. in Pharmacology, Pharmaceutical Sciences, or a related discipline) by the date of hire. The Assistant Professor candidate must possess a track record of accomplishment to demonstrate strong potential to become an outstanding scholar and educator. The Associate Professor candidate must possess a track record of accomplishment demonstrating he/she is an outstanding scholar and educator with an active, nationally recognized, extramurally funded, research program; and have served at least six years as Assistant Professor or equivalent. The Professor candidate must possess a track record of accomplishment demonstrating he/she is an outstanding scholar and educator with an active, internationally recognized, extramurally-funded, research program; and have served at least six years as Associate Professor or equivalent. Areas of special research interest include molecular targets and biomarkers of disease, pharmacogenomics, and drug delivery and development. The successful candidate will be expected to maintain an active extramurally-funded research program, mentor graduate students and fellows, and teach in the graduate courses on topics of pharmacology, biochemistry, and/or molecular biology and, potentially, professional curricula.

Screening of applications will begin September 15, 2015 and will continue until suitable candidates are identified. To see complete position announcement and apply, please visit website: **www.wsujobs.com**. Applications must include the following materials: (1) A cover letter of application describing short and long-term goals, relevant academic preparation, and experience; (2) A current curriculum vitae; and (3) Name, title, organization, phone number and e-mail address for four people willing to serve as employment references.

WSU is an Equal Opportunity/Affirmative Action/ADA Educator and Employer.

The Department of Anatomy & Cell Biology, Brody School of Medicine at East Carolina University (ECU) is seeking applicants for a tenure-track or fixed-term **ASSISTANT/ASSOCIATE PROFESSOR** position in Greenville, North Carolina. Rank will be commensurate with qualifications. We are seeking applicants with a strong interest in graduate student education and enthusiasm and experience in medical education in human gross anatomy and neuroanatomy. Research programs must compliment the strengths of ongoing research in the department (**website: http://www.ecu.edu/anatomy**).

Candidates must apply using the online application process to position #957507 at **website: https://ecu.peopleadmin.com/applicants/jsp/shared/position/JobDetails_css.jsp.**

ECU is a constituent institution of the University of North Carolina and an Equal Opportunity/Affirmative Action University that accommodates the needs of individuals with disabilities.

ASSISTANT/ASSOCIATE PROFESSOR
Ecology and Evolutionary Biology

The Department of Ecology and Evolutionary Biology, Tulane University, invites applications for one TENURE-TRACK POSITION at the level of assistant professor or associate professor. See website: **http://tulane.edu/sse/eebio/about/positions** for details about the position, department, and search. Submit letter of application, curriculum vitae, statements of research and teaching interests, selected publications, and names and addresses of three references to**: e-mail: apply.interfolio.com/30088**. Review of applications will begin **October 15, 2015**, and the search will remain open until the position is filled. *Tulane is an Equal Opportunity Employer/Minorities/Female/Veteran/Disabled employer.*

ASSISTANT PROFESSOR

The Department of Chemistry and Biochemistry and Institute of Molecular Biology at the University of Oregon (websites: **http://chemistry.uoregon.edu; http://molbio.uoregon.edu**) have an opening for a tenure-track biochemistry faculty member at the Assistant Professor level to begin in Fall 2016 or later.

The primary selection criteria will be the potential for establishing a vigorous independent research program addressing fundamental problems in molecular biology, and excellence in teaching at the undergraduate and graduate levels. We will consider applicants working in all areas of molecular biology, including those using cutting-edge approaches to study the mechanisms of cell and genome function, including RNA and protein biochemistry. We seek candidates with a demonstrated commitment to working effectively with students, faculty and staff from diverse backgrounds.

To assure full consideration, apply at website: **https://academicjobsonline.org/ajo/jobs/6024** and upload a curriculum vitae, a statement of research plans and objectives, and a brief statement of teaching philosophy or interests. The candidate should also arrange for three letters of recommendation to be uploaded directly by the recommenders via the preceding URL link by **October 15, 2015**. Review of application materials will continue until the position is filled.

The University of Oregon is an Equal Opportunity, Affirmative Action Institution committed to cultural diversity and compliance with the ADA. The University encourages all qualified individuals to apply, and does not discriminate on the basis of any protected status, including veteran and disability status.

BIOLOGY DEPARTMENT:
ASSISTANT PROFESSOR OF MICROBIOLOGY

Code: tenure track Microbiology Faculty Position. The Department of Biology at Clark University, Worcester Massachusetts website: (**www.clarku.edu/departments/biology/**) invites applications for a tenure track appointment at the rank of Assistant Professor to begin Fall 2016. The successful candidate is expected to develop an externally-funded research program in any field of microbiology, involving PhD, MS, and undergraduate students, and will teach microbiology and courses in their area of expertise. Clark University is especially interested in qualified candidates who can contribute, through their research, teaching, and/or service, to the diversity and excellence of the academic community.

For full consideration, one electronic file with a Curriculum Vitae, research and teaching statements, and three key publications should be received prior to November 1, 2015, as should three letters of reference e-mail: (**microbiology@clarku.edu**). See website **http://www.clarku.edu/offices/hr** for full position description. Inquiries may be directed to Justin Thackeray e-mail: (jthackeray@clarku.edu). *We are an Affirmative Action/Equal Employment Opportunity University and we strongly encourage women and members of minority groups to apply.*

PRINCETON UNIVERSITY DEPARTMENT
OF CHEMISTRY ASSISTANT PROFESSOR

The Department of Chemistry at Princeton University invites applications for a tenure-track assistant professor position in all areas of chemistry. We seek a faculty member who will create a climate that embraces excellence and diversity with a strong commitment to research and teaching that will enhance the work of the department and attract and retain a diverse student body. We strongly encourage applications from members of all underrepresented groups. Candidates are expected to have completed the Ph.D. in chemistry or a related field at the time of appointment. Applicants should submit a description of research interests, curriculum vitae, a list of publications, and contact information for three referees online at website: **https://jobs.princeton.edu/applicants/jsp/shared/position/JobDetails_css.jsp**. The deadline for applications is October 15, 2015.

Princeton University is an Equal Opportunity Employer. All qualified applicants will receive consideration for employment without regard to race, color, religion, sex, national origin, disability status, protected veteran status, or any other characteristic protected by law. This position is subject to the University's background check policy.

ASSISTANT/ASSOCIATE PROFESSOR
Department of Chemistry

The Department of Chemistry at Indiana University invites applications for a position in our Chemical Biology area beginning August 2016, at the rank of Assistant or Associate Professor (tenure-track). The search is open to candidates with interests in all areas of chemical biology, from structural biology and molecular biophysics, to bioanalytical chemistry and metabolic profiling. A Ph.D. in chemistry or a related field and postdoctoral experience are required. Successful candidates will be expected to develop or already have a visible, externally funded research program. Primary teaching assignments will involve graduate-level biochemistry and chemical biology and undergraduate chemistry and biochemistry. The successful candidate will be named a trainer in our NIH-funded Chemistry-Biology Interface graduate training program in Quantitative and Chemical Biology at Indiana University (website: **http://www.chem.indiana.edu/qcb/**). Applications completed by **October 15, 2015** will receive full consideration, but the review will continue until the position is filled. Interested candidates should review the application requirements and submit a complete Curriculum Vitae, a summary of future research plans, and arrange to have four letters of recommendation at website: **https://indiana.peopleadmin.com**). Questions regarding the position or application process can be directed to: **Professor David Giedroc, Chair, Faculty Search Committee, Department of Chemistry, Indiana University, 800 E. Kirkwood Avenue, Bloomington, IN 47405, e-mail: chemchair@indiana.edu**.

Indiana University is an Equal Employment and Affirmative Action Employer and a provider of ADA services. All qualified applicants will receive consideration for employment without regard to age, ethnicity, color, race, religion, sex, sexual orientation or identity, national origin, disability status or protected veteran status.

CHEMISTRY
Assistant, Associate, or Full Professor

The Department of Chemistry at Indiana University invites applications for Tenure/Tenure-track Assistant, Associate, or Full Professor position in Materials Chemistry beginning August 2016. The search is open to all areas of materials chemistry, including theory, modeling, and experimental synthetic approaches to the assembly of inorganic and soft materials as well as the application of analytical and physical chemistry to materials. Candidates with cross-disciplinary research interests are strongly encouraged to apply. A Ph.D. in chemistry or a related field and postdoctoral experience are required. Successful candidates will be expected to develop or have already developed a visible, externally funded research program. Primary teaching assignments will include graduate courses in materials chemistry and undergraduate chemistry. Applications completed by **October 15, 2015** will receive full consideration, but the review will continue until the position is filled. Interested candidates should review the application requirements and submit a complete Curriculum Vitae, a summary of future research plans, and arrange to have four letters of recommendation at the link (website: **https://indiana.peopleadmin.com**). Questions regarding the positions or application process can be directed to: **Professor Sara Skrabalak, Chair, Faculty Search Committee, Department of Chemistry, Indiana University, 800 E. Kirkwood Avenue, Bloomington, IN 47405, e-mail: chemchair@indiana.edu**.

Indiana University is an Equal Employment and Affirmative Action Employer and a provider of ADA services. All qualified applicants will receive consideration for employment without regard to age, ethnicity, color, race, religion, sex, sexual orientation or identity, national origin, disability status or protected veteran status.

myIDP: A career plan customized for you, by you.

For your career in science, there's only one *Science*

my IDP
Science**Careers**

Recommended by leading professional societies and the NIH

Features in myIDP include:

- Exercises to help you examine your skills, interests, and values.

- A list of 20 scientific career paths with a prediction of which ones best fit your skills and interests.

- A tool for setting strategic goals for the coming year, with optional reminders to keep you on track.

- Articles and resources to guide you through the process.

- Options to save materials online and print them for further review and discussion.

- Ability to select which portion of your IDP you wish to share with advisors, mentors, or others.

- A certificate of completion for users that finish myIDP.

Visit the website and start planning today!
myIDP.sciencecareers.org

Science**Careers** In partnership with:

advancing the life sciences
1912-2012

FASEB
Federation of American Societies
for Experimental Biology

UCSF
University of California
San Francisco

MEDICAL COLLEGE OF WISCONSIN

BURROUGHS WELLCOME FUND